

HENRIK ALENIOUS

Broadband Methods in Stability Analysis of Multi-Parallel Grid-Connected Converters

HENRIK ALENIUS

**Broadband Methods in Stability Analysis of
Multi-Parallel Grid-Connected Converters**

ACADEMIC DISSERTATION

To be presented, with the permission of
the Faculty of Information Technology and Communication Sciences
of Tampere University,
for public discussion in the TB109
of Tietotalo, Korkeakoulunkatu 1, Tampere,
on 1 October 2021, at 12 o'clock.

ACADEMIC DISSERTATION

Tampere University, Faculty of Information Technology and Communication Sciences
Finland

*Responsible
supervisor
and Custos*

Assistant Professor
Tomi Roinila
Tampere University
Finland

Pre-examiners

Professor
Xiongfei Wang
Aalborg University
Denmark

Doctor of Science
Anssi Mäkinen
GE Grid Solutions
Finland

Opponent

Associate Professor
Marko Hinkkanen
Aalto University
Finland

The originality of this thesis has been checked using the Turnitin OriginalityCheck service.

Copyright ©2021 Henrik Alenius

Cover design: Roihu Inc.

ISBN 978-952-03-2116-1 (print)

ISBN 978-952-03-2117-8 (pdf)

ISSN 2489-9860 (print)

ISSN 2490-0028 (pdf)

<http://urn.fi/URN:ISBN:978-952-03-2117-8>

PunaMusta Oy – Yliopistopaino
Joensuu 2021

PREFACE

This work has been carried out at the Faculty of Information Technology and Communication Sciences at Tampere University between 2018 and 2021. The work has been funded mostly by Tampere University and Business Finland, along with additional financial support from KAUTE Foundation and Tekniikan Edistämissäätiö.

My first and foremost gratitude goes to Assistant Professor Tomi Roinila for supervising my work and establishing a resourceful and encouraging research environment. His guidance and friendship have been essential during the process. Moreover, I would like to thank Dr. Tech. Tuomas Messo and Professor Teuvo Suntio for their advice and insights in technical aspects of the work.

Thanks to my colleagues at Tampere University, the office has been filled with fascinating discussions and refreshing table tennis matches. The fellow doctoral students in the power electronics research group have provided valuable peer support inside and outside the laboratory. Particular distinction goes to Dr. Tech. Roni Luhtala for sharing many research challenges and thoughts on life in general, within the shared office room.

My sincerest gratitude goes to my friends and family, without whom the doctoral process and life in general would lack a great deal of color and depth. The encouragement from my parents has been essential during my (academic) growth, and my brother, Ilmari, has provided the strongest friendship possible. I would like to also thank my tiny companions, Roope, Luke and Luna, for their enthusiasm and ever-joyful spirit. Finally, thank you, Jenna, for your love and support.

ABSTRACT

The share of power flowing through power electronics is increasing rapidly in modern power systems. Power-electronic converters have become essential in enabling efficient grid connection of renewable energy. Moreover, a simultaneous transformation is taking place in energy distribution and consumption, where converters are applied for high-performance power processing. The high power demands often require multi-parallel configurations of grid-connected converters, thereby modifying the dynamic characteristics of the power grid. Consequently, the power grid is threatened by adverse interactions between the grid and the parallel converters. The interactions may lead to dramatic power quality issues through harmonic resonance and they may even make the system prone to instability.

Previous studies have presented methods for assessing the stability of grid-connected systems through dynamic modeling or impedance-based stability criterion where the terminal impedance characteristics of a grid-connected converter are examined. A major advantage of the impedance-based approach is that the method does not require detailed information of the system parameter values. Assessing the stability of multi-parallel converters is typically challenging as the system configurations are complex and the dynamics change along with the system operation point. Consequently, broadband methods capable of fast measurements are required to minimize the measurement duration and to facilitate real-time analysis and adaptive control schemes.

This thesis presents online methods based on broadband pseudo-random sequences and Fourier techniques for the stability analysis of multi-parallel grid-connected converters. The broadband methods are capable of extracting the required impedance data from such systems rapidly by applying simultaneous multivariable measurements. The presented methods facilitate real-time stability analysis of the system and development of various adaptive controllers. Moreover, the stability assessment is shown to predict the stability of multi-parallel converter configurations, where the impedance-based analysis is enabled through the use of impedance aggregation. The presented methods are validated through a number of experimental measurements.

CONTENTS

1	Introduction	23
1.1	Background	23
1.2	Aim and Scope of the Thesis	28
1.3	Literature Review	31
1.4	Summary of Scientific Contributions	34
1.5	Structure of the Thesis	35
2	Grid-Interfaced Power-Electronic Converters	37
2.1	Synchronous Reference Frame Modeling	37
2.2	Dynamic Modeling and Load Effect	39
2.3	Impedance-Based Stability Analysis	45
2.4	Discussion	47
3	Methods	49
3.1	Frequency-Response Measurements	49
3.2	Stability Analysis of Multi-Parallel Converters	61
4	Experiments	71
4.1	Experimental Setups	73
4.2	Broadband Impedance Measurements	77
4.3	Broadband Stability Analysis	88
4.4	Stability Analysis of Parallel Converters	92
5	Conclusions	105
	References	109
	Publication I	131
	Publication II	143

Publication III	157
Publication IV	175
Publication V	183
Publication VI	193
Publication VII	201
Publication VIII	211

ORIGINAL PUBLICATIONS

- Publication I H. Alenius, T. Roinila, R. Luhtala, T. Messo, A. Burstein, E. de Jong and A. Fabian, "Hardware-in-the-Loop Methods for Stability Analysis of Multiple Parallel Inverters in Three-Phase AC Systems", *IEEE Journal of Emerging and Selected Topics in Power Electronics*, Early Access, pp. 1–10, 2020.
- Publication II H. Alenius, R. Luhtala and T. Roinila, "Combination of Orthogonal Injections in Impedance Measurements of Grid-Connected Systems", *IEEE Access*, vol. 8, pp. 178085–178096, 2020.
- Publication III H. Alenius and T. Roinila, "Impedance-Based Stability Analysis of Paralleled Grid-Connected Rectifiers: Experimental Case Study in a Data Center", *Energies*, no. 8, vol. 13, pp. 1–15, 2020.
- Publication IV H. Alenius, R. Luhtala and T. Roinila, "Amplitude Design of Perturbation Signal in Frequency-Domain Analysis of Grid-Connected Systems", in Proc. *IFAC World Congress*, pp. 1–6, 2020.
- Publication V H. Alenius, M. Berg, R. Luhtala and T. Roinila, "Stability and Performance Analysis of Grid-Connected Inverter Based on Online Measurements of Current Controller Loop", in Proc. *45th Annual Conference of the IEEE Industrial Electronics Society*, pp. 2013–2019, Lisbon, Portugal, 2019.
- Publication VI H. Alenius and T. Roinila, "Analysing the Damping of Grid-Connected Inverter by Applying Impedance-Based Sensitivity Function", in Proc. *46th Annual Conference of the IEEE Industrial Electronics Society*, pp. 1249–1254, Singapore, 2020, pp. 1249–1254, Singapore, 2020.
- Publication VII H. Alenius, M. Berg, R. Luhtala, T. Roinila and T. Messo, "Impedance-Based Stability Analysis of Multi-Parallel Inverters Applying Total Source Admittance", in Proc. *20th Workshop on Control and Modeling for Power Electronics*, pp. 1–8, Toronto, Canada, 2019.

Publication VIII R. Luhtala, H. Alenius, T. Messo and T. Roinila, "Online Frequency Response Measurements of Grid-Connected Systems in Presence of Grid Harmonics and Unbalance", *IEEE Transactions on Power Electronics*, vol. 35, pp. 3343–3347, 2020.

SUMMARY OF PUBLICATIONS

Publication I

The publication contributes to the scientific body of knowledge by presenting online implementation techniques for the stability analysis of multi-parallel grid-connected inverters by applying an experimental power hardware-in-the-loop setup. The stability analysis is performed by applying simultaneous online measurements of the grid impedance, aggregated terminal admittance of the inverters, and inverters' current controller loop gains. The multivariable measurements are performed with broadband orthogonal pseudo-random binary sequences, which enable rapid identification of the system. Consequently, the stability assessment can be implemented in real-time providing a means for online stability monitoring or adaptive control.

Publication II

The publication introduces a novel broadband perturbation signal that is synthesized by combining multiple independently designed orthogonal pseudo-random sequences. As the orthogonal sequences do not have power at common frequencies, the injection amplitude of each sequence can be designed independently. As a result, the combined sequence can be tailored to have a specific spectral power distribution at each frequency band of interest. The adjustable power spectrum provides means for increasing the signal-to-noise ratio of a measurement in comparison to a conventional pseudo-random sequence perturbation.

Publication III

The publication presents a case study on a high-frequency instability phenomenon that occurred in a data center in southern Finland. In this instability incident, multiple paralleled grid-connected rectifiers with total power of 250 kW entered a state of sustained high-frequency resonance. The work presents an experimental approach for characterizing and assessing the stability of such a system by applying terminal admittance measurements of a single rectifier and aggregated impedance-based analysis. The methods can accurately predict the system stability and the resonant modes of the system with a varying number of parallel converters, thereby giving insight into the hosting capacity of the grid for multi-parallel converters. The scientific contribution of this publication is two-fold, where an example of typical instability incident related to multi-parallel converters is presented, and an analysis method that is capable of predicting such incidents is proposed.

Publication IV

The publication discusses the amplitude selection on a broadband perturbation applied in the online impedance measurements of grid-connected systems. The inherent trade-offs between the measurement performance against the measurement duration and grid-side disturbances are considered, where the grid disturbances are quantified by the total harmonic distortion (THD) of grid currents and voltages. A design algorithm for choosing a suitable injection amplitude is presented to minimize the grid waveform pollution during online impedance measurements. The main contribution of the publication is to emphasize the fundamental trade-offs in amplitude selection of perturbation injection and to propose design methods for the utilization of broadband online measurements of grid-connected systems.

Publication V

The publication presents a stability analysis method based on assessment of the load-affected loop gain of the innermost current control loop. The method provides an efficient way to analyse the stability in local scope either through modeling approach or online loop gain measurements. Additionally, the method is shown to predict the interactions resulting from the phase-locked loop dynamics. The proposed method contributes to the field of power electronics by providing a readily usable measurement-based tool for stability analysis of grid-connected converters.

Publication VI

The publication presents an extension to the conventional impedance-based stability criterion, where the system stability margins are quantified by applying a sensitivity function. The method extracts the critical system damping and resonant mode from the terminal impedance data, which can be utilized in the prediction of instability issues. Consequently, the contribution of this publication lies in extracting quantitative stability data from conventional impedance-based methods. The terminal impedance data is extracted from both the grid and the grid-connected converter by applying a quadratic-residue binary sequence.

Publication VII

The publication proposes a straightforward method for the stability analysis of multi-parallel converters by applying an impedance aggregation technique. A generalized Nyquist criterion is applied on the aggregated total admittance of the converters, which is supplemented by the polar analysis and impedance-based sensitivity function. The method can be applied to predict the maximum capacity of parallel converters at a certain grid interface, which is the main contribution of the publication.

Publication VIII

The main contribution of the publication is a presented design method for broadband impedance measurements, where the distortion caused by unbalanced grid voltages and harmonic voltages is mitigated. In the method, the number of averaged periods of the periodic perturbation sequence is designed so that the spectral leakage of harmonic voltages is minimized. The method is shown to drastically improve the measurement performance especially in distorted grid conditions.

Author's contribution

The author was the main contributor for implementing and developing the methods presented in Publications I-VII. In Publication VIII, the author was responsible for the configuration of the experimental hardware-in-the-loop setup. The author carried out all the writing in Publications I-VII. Assistant Professor Tomi Roinila, the supervisor of the thesis, provided counsel during the doctoral work and insight in aspects related to system identification. Dr. Tech. Tuomas Messo assisted in topics related to control and dynamic analysis of power electronics with his expertise. The co-authors in the publications assisted with the laboratory measurements and commented on the manuscript drafts.

SYMBOLS

A	Excitation signal time-domain amplitude
C_{dc}	DC-link capacitor capacitance
C_f	CL-filter capacitance
d	Duty ratio
d	Distance between eigencontour point and critical point
d'	Complementary duty ratio
D_d	Duty ratio d-component steady-state value
D_q	Duty ratio q-component steady-state value
ΔT	Time difference
e	Excitation signal
f_{bw}	Bandwidth of pseudo-random perturbation
f_{gen}	Generation frequency of pseudo-random perturbation
f_g	Grid frequency
f_p	Frequency of periodic disturbance
f_{res}	Frequency resolution of pseudo-random perturbation
f_{sw}	Switching frequency
G_{ci}	Control-to-input transfer function
G_{co}	Control-to-output transfer function
G_{est}	Estimated transfer function
G_{io}	Input-to-output transfer function
G_{PI}	PI-controller transfer function
i_{in}	Input current
i_L	Inductor current
I_{Ld}	Inductor current d-component steady-state value

I_{Lq}	Inductor current q-component steady-state value
I_{od}	Output current d-component steady-state value
I_{oq}	Output current q-component steady-state value
j	Imaginary unit
k	A positive integer
K_C	Clarke's transformation coefficient
K_{CC-P}	Current controller proportional gain
K_{CC-I}	Current controller integral gain
K_{PLL-P}	Phase-locked loop proportional gain
K_{PLL-I}	Phase-locked loop integral gain
L	L-filter inductance
L_2	CL-filter inductance
L_{tf}	Transformer inductance
λ	System eigenvalue
λ_1	First eigenvalue of 2x2 matrix
λ_2	Second eigenvalue of 2x2 matrix
M_S	Sensitivity peak
N	Sequence length
n	Shift register length for maximum-length binary sequence generation
N_{QRBS}	Sequence length of quadratic-residue binary sequence
n_u	Input noise signal
n_y	Output noise signal
P	Number of averaged periods
p	A complex system pole
Φ_m	Minimum phase margin
r	Reference signal
R_{L2}	CL-filter inductor resistance
R_d	CL-filter damping resistance
R_L	L-filter inductor parasitic resistance
r_L	L-filter inductor parasitic resistance
R_{tf}	Transformer resistance

s	Laplace variable
S_n	Nominal power
σ^2	Measurement variance
t	Time
T_{dt}	Switching deadtime
T_{meas}	Measurement duration
T_{MLBS}	Period duration of maximum-length binary sequence
T_{oi}	Output-to-input transmittance
θ	Dq-frame angle
u	Input signal
$U_{j\omega}$	Fourier-transformed noise-affected input signal
ω	Angular frequency
ω_c	Critical angular frequency
ω_g	Fundamental grid angular frequency
v_{dc}	DC-link voltage
V_{dc}	DC-link voltage steady-state value
v_g	Grid voltage
V_g	Grid phase voltage
v_L	Inductor voltage

A	State space matrix A
B	State space matrix B
C	State space matrix C
D	State space matrix D
d	Multivariable duty ratio
G	Transfer function matrix
G_{cc}	Current control matrix
G_{ci}	Control-to-input transfer function matrix
G_{co}	Control-to-output transfer function matrix

\mathbf{G}_{dec}	Decoupling gain matrix
\mathbf{G}_{io}	Input-to-output transfer function matrix
\mathbf{H}	Hadamard matrix
\mathbf{I}	Identity matrix
\mathbf{i}_{in}	Multivariable input current
\mathbf{i}_{L}	Multivariable load current
\mathbf{i}_{L}	Multivariable inductor current
\mathbf{i}_{o}	Multivariable output current
\mathbf{i}_{S}	Multivariable source current
\mathbf{L}	Multivariable loop gain
\mathbf{T}_{oi}	Output-to-input transmittance matrix
\mathbf{u}	Input vector in state space
\mathbf{v}_{g}	Multivariable grid voltage
\mathbf{v}_{in}	Multivariable input voltage
\mathbf{v}_{o}	Multivariable output voltage
\mathbf{v}_{S}	Multivariable source voltage
\mathbf{x}	State vector in state space
\mathbf{y}	Output vector in state space
\mathbf{Y}_{in}	Input admittance matrix
\mathbf{Y}_{o}	Output admittance matrix
$\mathbf{Y}_{\text{o-tot}}$	Aggregated total terminal admittance
\mathbf{Y}_{S}	Multivariable source admittance
\mathbf{Z}_{g}	Multivariable grid impedance
\mathbf{Z}_{L}	Multivariable load impedance
\mathbf{v}_{L}	Multivariable inductor voltage

Superscripts

$\hat{}$	Linearized variable
L	Load-affected variable
$*$	Unperturbed signal

Subscripts

a	Phase A component
abc	Three-phase phase-domain variable
α	Alpha component
b	Phase B component
β	Beta component
c	Phase C component
d	D component
in	Input signal
L	Load subsystem signal
max	Maximum value
meas	Measured value
min	Minimum value
n	Noise component
out	Output signal
q	Q component
ref	Reference value
s	Signal component
S	Source subsystem signal
z	Zero component (dq-domain)
0	Zero component ($\alpha\beta$ -domain)
1	First component of vector
2	Second component of vector
11	First direct component of matrix
12	First cross-coupling component of matrix
21	Second cross-coupling component of matrix
22	Second direct component of matrix

ABBREVIATIONS

AC	Alternating current
COS	Combined orthogonal sequence
DC	Direct current
DFT	Discrete Fourier transformation
GHG	Greenhouse gas
GNC	Generalized Nyquist criterion
IRS	Inverse-repeat sequence
LHP	Left-hand plane
LTl	Linear time invariant
MIMO	Multi-input multi-output
MLBS	Maximum-length binary sequence
OBS	Orthogonal binary sequence
PCC	Point-of-common coupling
PHIL	Power hardware-in-the-loop
PLL	Phase-locked loop
PRS	Pseudo-random sequence
PSU	Power supplying unit
PV	Photovoltaic
QRBS	Quadratic-residue binary sequence
RHP	Right-hand plane
SISO	Single-input single-output
SNR	Signal-to-noise ratio
SVD	Singular value decomposition
THD	Total harmonic distortion

UNFCCC	United Nations Framework Convention on Climate Changes
XOR	Excluding-or -operation
ZOH	Zero-order hold

1 INTRODUCTION

1.1 Background

Climate change is among the major challenges of the 21st century. An overwhelming body of evidence has presented rising threats that result from the changes in our climate [1]–[3], which induce a number of ecological and economical threats [4]–[7]. The scientific community has widely accepted the role of human actions in advancing climate change, where greenhouse gas (GHG) emissions are the main contributor to the increase in global temperatures [8]. During recent decades, GHG emissions have risen at a rapid pace and, consequently, immediate actions are required to halt climate change. As a result, authorities have taken action and environmental policies have been adopted. In the Paris Agreement of 2015, 196 nations belonging to the United Nations Framework Convention on Climate Changes (UNFCCC) signed an agreement to limit the increase in global average temperature below 2 °C and to pursue a limit of 1.5 °C [9]. The parties that signed the agreement represent 97 % of global GHG emissions. Moreover, detailed environmental strategies and objectives are being adopted at nation levels.

The global energy sector is responsible for the majority of GHG emissions and therefore it plays an essential role in the reduction of emissions. Despite the recent progress in renewable alternatives, fossil fuels are still responsible for the majority of primary energy sources [10]. Dramatic reduction in GHG emissions could be achieved by replacing production based on fossil fuels with GHG-free renewable sources. Consequently, many modern environmental policies involve utilization of renewable energy sources; for example, the European Union’s binding target for 2030 is to produce at least 32 % of its energy from renewable sources [11]. Simultaneously with the policy changes, the cost of installing renewable energy has decreased drastically and become a price-competitive alternative [12], [13]; for example, the cost of newly installed photovoltaic (PV) production has declined by 82 % over 2010-2019 [14]. Consequently, more than half of the renewable energy capacity installed in 2019 achieved lower energy costs than newly installed coal power [14]. Additionally, renewable energy offers a way to energize poverty stricken locations through cheap and readily available production, such as small-scale solar panels. As a result, in 2019 the share of renewable energy in the new installments of global generating capacity was 72 % [14]. Of

all the emerging renewable technologies, wind and PV power have been deemed the most prominent [15], [16].

The increments in the share of renewable energy production produce challenges to energy infrastructure [17]–[19]. The fundamental differences in the properties of renewable energy production in comparison to conventional production often limit the hosting capacity of the power system for renewable production, as the dynamics of the grid integration are drastically different [20], [21]. Conventional electricity production typically utilizes the combustion of fossil fuels in centralized large-scale plants, where the produced steam rotates a synchronous generator. The generator interfaces the generated power to the electric grid by coupling the rotating magnetic field to the grid voltages [22]. Consequently, the rotating mass of the generation is synchronized with the fundamental grid voltages. The coupled system is robust against disturbances due to the inertia of the rotating mass and long time constants that resist changes [22]. On the other hand, renewable electricity is typically generated in significantly smaller units, such as photovoltaic (PV) plants or wind turbines. Interfacing the renewable resources to the grid is more challenging in comparison to conventional combustion-based resources [23], [24]. In PV plants and variable-speed wind turbines, the generated power must be accommodated to a suitable form for the power system, that is, fixed-frequency alternating current (AC). In addition, the primary source of energy, such as solar irradiation or wind, may inherently fluctuate and a controller is required to maximize the energy yield [25]–[27]. A conventional synchronous generator is incapable of the power conversion required in such applications and therefore a different type of interfacing device is required. Semiconductor-based power-electronic converters have offered a solution for systems that require advanced power processing [28], [29], as the currents and voltages can be manipulated by changing the switching state of semiconductor switches [30]. As the semiconductors involve no moving parts and energy loss during switching is very low, the switching state can be changed very quickly, enabling an advanced capability for power processing. Grid-connected power-electronic devices, also known as converters, can be divided into two categories; inverters convert direct current (DC) to AC; and rectifiers convert AC to DC ¹. Due to the favorable characteristics of converters, such as a high degree of controllability and fast dynamic performance, the majority of PV and wind power is interfaced to the grid through a three-phase inverter that accommodates the power produced in the primary energy source to the AC power system [31], [32]. Consequently, grid-connected power electronics play an essential role in the grid integration of renewable energy resources.

Simultaneously with the rise of inverter-interfaced renewable energy production, electricity consumption is also increasingly interfaced to the power grid through power electronics [28]. In modern society, an increasing share of power consumption takes place in applications that require precise power processing, such as electronics, data centers, variable-

¹While also DC-DC and AC-AC converters exist, the main focus on this work is on AC-DC rectifiers and DC-AC inverters which represent the majority of grid-connected converters.

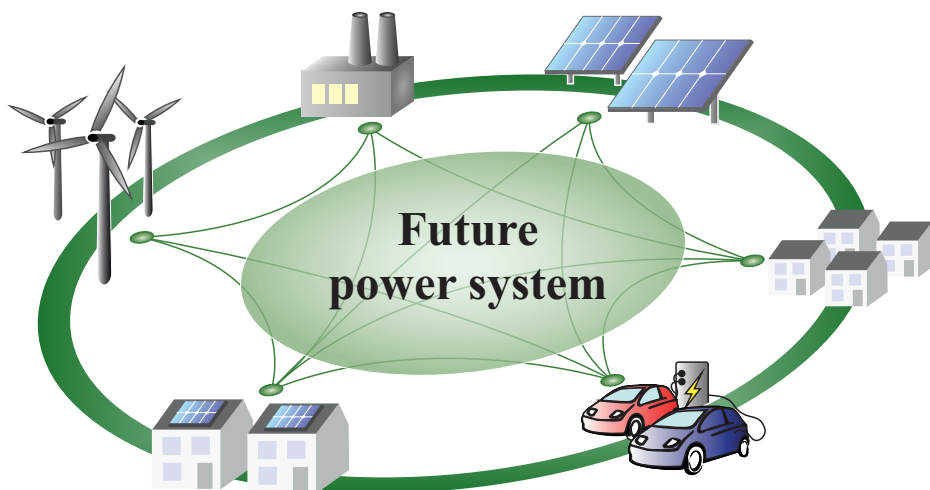


Figure 1.1 Illustration of a future electric system known as a smart grid.

speed motor drives, and electric vehicles [33]. Through these changes in power production and consumption, the modern power grid is experiencing a change towards a decentralized converter-penetrated system [18], [19], [34]–[36]. In such a system, the power no longer flows radially from centralized synchronous generators to consumption - instead, production is decentralized among the consumption and the meshed topology is mainly converter-based [30]. This change both requires and allows smart metering of the system [37]–[39] and use of demand response [40]–[42], as the converters enable both auxiliary grid-supporting functions and communication between devices [43]–[48]. An intelligent system where the power flows and power quality are constantly optimized through distributed resources is known as a smart grid [49], [50]. Fig. 1.1 presents a future electric system, a smart grid, which can be operated either in standalone-mode or connected to the main grid.

1.1.1 Stability issues emerging from power electronics

The high power processing performance of power-electronic converters has a drawback; the fast internal dynamics and lack of physical coupling with the grid induce control challenges. Unlike synchronous generators that have strong physical coupling and high rotational inertia that resists changes in grid synchronization, grid-connected converters lack these inherently stabilizing phenomena [51], [52]. A grid-connected converter is controlled by multiple high-bandwidth control loops, and consequently, the converter interacts with the grid over a wide frequency range [53]. As a result, the converter is prone to stability issues resulting from the dynamics of the interfacing system [54]–[56].

The power grid that interfaces a grid-connected converter affects the stability of the con-

verter. Consequently, one of the major challenges in the stability analysis of grid-connected systems is caused by versatility and variations in grid dynamics [56], [57]. The dynamics of the power grid may vary drastically and unpredictably, which makes stability prediction difficult and location dependent. The load impedance of a grid-connected inverter is the equivalent terminal impedance of the grid seen at the interface, which depends on the location and grid-connection type. The grid impedance can vary over a wide range, which increases the risk of stability issues resulting from detrimental interactions between the inverter controllers and the interfacing grid [58], [59]. In high-impedance grids, an adverse dynamic interaction may occur between the converter and the grid, which pollutes the grid voltages with harmonic content, decreases power quality, and can even lead to system shut down [54]. The grid connected converters are especially prone to stability issues due to dynamic effect of the interfacing grid system. To tackle this challenge, the control systems of grid-connected converters are often designed to ensure robustness even for interfaces with high grid impedance [60]–[63]. However, ensuring robustness easily leads to overly conservative controller design for the majority of systems, as the controllers are designed based on the worst-case scenario, which leads to decreased system performance in low-impedance grids. As a conclusion, the optimization between the system performance and robustness necessitates methods to assess the system stability margins at a given interface.

Additional challenges for the power system emerge when the penetration of power-electronic converters increases [23], [64]–[67]. When multiple converters are connected close to each other, as is the case in converter-based smart grids, the converters interact with each other in addition to interacting with the grid [68]–[70]. The additional interaction between the multiple subsystems further increases the risk of stability issues, and consequently, the systems that contain multiple parallel converters are more prone to stability issues in comparison to a single grid-connected converter. Instability incidents have been reported from systems that have high penetration of grid-interfaced converters, such as PV plants [71], wind farms [72]–[74], data centers [75], and systems with a high share of distributed generation [68], [76]. In addition to the higher risk of stability issues, the stability analysis of systems with multiple converters is also more complex due to the increased number of interacting subsystems.

The stability analysis of the power grid is conventionally performed by assessing the large signal stability of the system through an analysis of the rotor angle stability, voltage stability and frequency stability of the system [77]–[79]. However, the large-signal stability examination is insufficient for addressing the stability issues in grid-connected converters, where the stability can be lost due to a dynamic interaction between the converter and the source/load at any frequency [80]. Therefore, other methods are required to consider the dynamic small-signal stability of the grid-connected converter. The small-signal stability can be assessed by considering the impact of source/load effect on the controller dynamics or by examining the compatibility of the terminal impedances of the converter and the interfacing

grid. The latter method is known as impedance-based stability analysis, which is one of the most common methods for stability analysis of grid-connected converters [81]. The main advantage of impedance-based analysis is that, in addition to impedance modeling, the terminal impedances can be extracted by measurements without having detailed information on the subsystem dynamics. However, examining the stability of a grid-connected converter by applying the impedance-based stability criterion may lose accuracy when multiple converters are present in the system. The impedance-based analysis is interface specific² and provides analysis only in the local scope [82]. Therefore, stability analysis methods for systems that involve multiple parallel converters are required to enable the emergence of smart grids and to advance the rise of renewable energy production.

1.1.2 Broadband methods

The stability of a grid-connected converter depends not only on the internal dynamics of the device but also on the dynamics of the system the converter is connected to [51]. For grid-connected converters, the exact dynamics of the grid at the point of common coupling are rarely known in detail. The lack of system information is especially typical for systems that include multiple converters, as the other devices are often black-box systems where the internal dynamics are protected by the manufacturer. Therefore, the stability analysis of a grid-connected converter often requires experimental studies to account for the uncertainties present in most systems [64].

A common method to extract system dynamics is to apply frequency-response measurements, where the small-signal response of the system to an excitation is identified on multiple frequencies [83]. Typically, the system is excited by an external perturbation signal and the system response is measured, and the frequency-response is obtained by comparing the frequency components of input and response signals [84]. The performance of a frequency-response measurement is highly dependent on the applied perturbation signal [85]. Broadband perturbation signals, where multiple frequencies are excited simultaneously, have demonstrated multiple favorable attributes for measurements on grid-connected converters [86]–[88]. Recently, a class of periodic and deterministic perturbations known as pseudo-random sequences (PRS) has become popular in identification of grid-connected converters [86], [89]–[91]. In comparison to conventional broadband perturbations, such as multi-sine or impulse, the PRS perturbations have demonstrated multiple favorable characteristics for online measurements including low crest factor and ease of generation.

The accurate analysis of grid-connected converters necessitates that the measurements are performed online during the nominal operation of the system, as the small-signal dynamics depend on the steady state operation point [88]. In such a measurement configuration, the

²Observability limitations may lead to erroneous conclusions on system stability.

perturbation signal acts as a disturbance to the power grid and, consequently, the design of the perturbation must be performed so that the disturbance to the grid is minimized without compromising the quality of obtained measurements. Thus, the time-domain amplitude and frequency-domain spectrum of the perturbation signal must be carefully designed, depending on the grid-connected system under study.

In systems that consist of multiple grid-connected devices, the stability analysis requires detailed information about the system. The required information must often be extracted through frequency-response measurements that are performed online during normal system operation. In such measurements, rapid measurement duration and negligible system disturbance combined with high measurement accuracy are essential. Consequently, broadband methods offer attractive attributes that can be utilized in the stability analysis of multi-parallel grid-connected converters. Broadband stability analysis enables multiple advanced control and protection features, such as adaptive control of inverters or predictive system protection based on stability margins, as most of the applications necessitate a measurement-based approach and rapid identification time. For example, an adaptive controller that mitigates the stability issues resulting from grid impedance variation can be implemented into a grid-connected converter by applying a continuous real-time stability assessment.

1.2 Aim and Scope of the Thesis

The goal of this work is to provide broadband methods for stability analysis of grid-connected systems that consist of multiple parallel converters. The methods enable the robust design of systems that include high penetration of grid-connected converters, thereby advancing the deployment of a smart power grid and improving the renewable production hosting capacity of the power system. Moreover, the methods can be applied continuously online in real-time stability monitoring, which facilitates the adaptive control and online system optimization. The methods can be applied simultaneously in local and global scope, providing holistic oversight of the system stability.

This thesis presents broadband identification methods to extract the required information for the stability analysis of multi-parallel converters. The methods are based on periodic pseudo-random sequences, which allow rapid identification of multivariable systems. A design method for the injection amplitude design is presented based on quantifying the disruption on the system under measurement. Moreover, the thesis presents a novel perturbation sequence generated by combining several pseudo-random sequences, which enables versatile spectral design that allows optimization of signal-to-noise ratio in the measurements.

The introduced methods produce stability criteria for systems that consist of multiple parallel connected inverters by applying impedance aggregation of parallel devices. The impedance aggregation allows the stability analysis to be performed at the common interface of

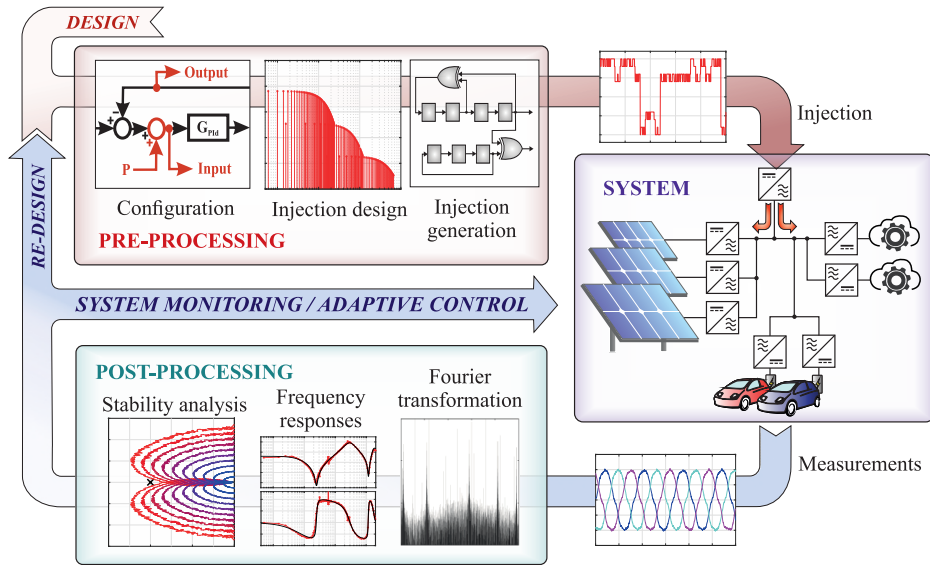


Figure 1.2 Graphical abstract of the thesis.

the parallel converters, thus improving the observability of the system. Moreover, a real-time implementation of the stability analysis method is presented by applying a power hardware-in-the-loop method for parallel inverters. The real-time analysis enables advanced control schemes and online system optimization based on the system stability margins without requiring device-to-device communication.

Fig. 1.2 presents a graphical abstract of this work. In the illustration, the system under study consists of multiple sources and loads, all of which are interfaced to the grid through a power-electronic converter. The system is continuously monitored by injecting a low-amplitude perturbation signal and measuring the resulting currents and voltages. The measured signals are transformed into the frequency domain, and the frequency-responses are computed from the system inputs and responses. The system stability margins and dynamic characteristics are extracted, and used in real-time for system monitoring, adaptive control, or other control objectives.

The main contributions in the thesis can be summarized as follows:

- Impedance-based analysis method for multi-parallel converters based on impedance aggregation.
- Real-time implementation of stability analysis for multi-parallel converters.
- A novel perturbation sequence that increases measurement performance by optimizing excitation spectrum.
- A design process for selecting the injection amplitude and measurement duration for

broadband impedance measurement of grid-connected systems.

1.2.1 Research challenges

The stability assessment of converter-penetrated systems involves a number of challenges. Although many of the challenges are general for dynamic analysis and system identification, some of the challenges particularly occur in grid-connected systems. The primal challenge in the assessment of multi-converter systems is the inherent complexity and versatility of such systems. The fluctuating nature of power flows, connection of loads and devices, and other varying phenomena causes the power system to be in a state of constant change, affecting the equivalent grid impedance at the interface of a grid-connected converter [51]. Consequently, the system stability margins vary along with the fluctuating operation conditions, as the impact of grid impedance on the stability of a grid-connected device has been rigorously proven [54], [64]. The stability analysis methods must be able to keep up with the changing operation conditions, and as a result, the methods must be fast to implement to re-evaluate the stability. Thus, approaches based on repeatable measurements are favorable over static modeling-based approaches.

Another challenge emerges from the limited amount of information in the analysis of systems that consist of multiple converters. The system often has a complex structure, which makes it difficult to identify the interfaces suitable for stability assessment. Moreover, some of the subsystems (for example, individual converters) may have completely unknown internal dynamics, as the detailed control structure of each converter is typically not known. Also, the exact parameters of transmission lines, transformers, and other passive components may have uncertainties. Consequently, parametric methods are impractical and arduous for such systems.

While measurements are often required to extract the dynamic characteristics of the system, measuring the frequency responses for stability analysis involves practical difficulties. As the dynamics of many devices (such as converters) depend on the system operation point, the measurements must be performed online during the nominal operation of the system. However, the measurements typically require a perturbation injection which acts as a disturbance for the grid. Thus, an inherent trade-off between measurement accuracy against uninterrupted system operation and power quality exists.

Lastly, more challenges are related to the realization of the system identification required for the measurement-based stability analysis methods. The first challenge is to implement the measurements by applying existing grid-connected devices so that external measurement hardware is not required. Secondly, the location of the measurement interfaces affects the stability indicators as the observability of some dynamics may be limited depending on the location. Therefore, achieving a holistic outlook on the stability of a multi-converter sys-

tem may require multiple measurements or the combination of local and global stability assessment methods.

1.2.2 Research Questions

The research questions in this thesis can be summarized as follows:

- What are the limitations in applying the modeling-based and measurement-based stability analysis methods for systems that consist of multiple paralleled converters?
- How can the stability of a grid-connected multi-parallel converter system be evaluated by the system frequency-response measurements?
- How can the amplitude of a broadband perturbation be automatically designed for frequency-response measurement of a grid-connected multi-parallel converter system?
- How can the signal-to-noise ratio of a broadband perturbation be increased within constraints of the perturbation time-domain amplitude?
- How can the aggregated source admittance be utilized in the stability analysis of grid-connected multi-parallel converter system?
- How can the system stability margins be quantified from the impedance data?

1.3 Literature Review

The first reports of instability in power-electronic converters were reported in the early 1970s, when an instability phenomenon was observed in DC-DC converters with input-side filters [92], [93]. The dynamic modeling based on the source- and load-effect in [94], [95] indicated that the instability emerged from the interaction between the LC-filter and the converter. Consequently, the terminal impedance characteristics became an essential tool in the stability assessment of DC-DC converters. The method was extended to dq-frame three-phase inverters in [96], where the source-load interactions were assessed for AC systems that contained regulated constant-power loads. In [81], the method of examining the source and load impedance ratios was named as an impedance-based stability criterion.

Contrary to conventional power system stability analysis, where large-signal transients are the focus, the converter-penetrated systems are especially prone to small-signal instability [82], [97]–[100]. The small-signal stability analysis can be performed through multiple approaches. The most accurate approach is through non-linear analysis where the non-linear characteristics of the system are modeled in great detail, for example by applying Lyapunov stability criterion [101], [102] or bifurcation [103], [104]. However, the methods are impractical in the assessment of systems that contain, for example, multiple converters [105].

In the state-space analysis, the dynamics of the system are captured by first-order differential equations that describe the relations of input, output, and state variables. The stability of the system can be obtained straightforwardly by calculating the system eigenvalues [77], and the eigenvalue-based approach has been extensively applied for the stability analysis of grid-connected converters [106]–[112], parallel converters [113]–[119], and microgrids [99], [120]–[122]. However, the state-space approach requires detailed information on each building block of the system, which is not always available [82], [118], [123]. Moreover, the scalability of the state-space methods is limited [118], [124] and the approach has limited applicability on complex systems with a high number of converters.

In systems that include multiple converters with unknown internal dynamics, the approaches based on system modeling are rendered unwieldy as the set of information is not sufficient and the models cannot be derived [82]. The measurement-based approaches are able to tackle this limitation, as the required information for the analysis can be extracted from the frequency-response measurements [123], [125]–[127]. In the loop-gain based analysis, the stability is assessed by examining a control loop gain of converter [128]. The method is typically applied for the stability assessment of a single converter, and therefore the method excels in the local-scope stability analysis. Moreover, the loop-gain method is highly applicable for real-time stability monitoring [126], [129], [130] or adaptive control of a converter [90], [131], [132].

The most widely applied method for the stability assessment is the impedance-based analysis, where the stability of two interconnected systems is examined by the equivalent impedances of both subsystems at the interface [55], [81], [95], [133]. The impedance-based analysis has been thoroughly applied for the stability analysis of grid-connected inverters [100], [127], [134]–[140], back-to-back connected converters [82], [141], [142], and parallel converters [75], [124], [130], [143]–[146]. Multiple methods have been presented for extracting the stability indications from the impedance data, such as sensitivity analysis [55], [147]–[149], (generalized) Nyquist criterion [82], [100], [127], [134]–[137], [142], [144], [145], [150], [151], transfer function fitting [143], [144], and impedance crossover analysis [130], [138]–[140], [152]. Table 1.1 summarizes the advantages and disadvantages of the presented impedance-based stability analysis methods.

In recent years, an increasing research effort has been focused on the stability analysis of systems that consist of multiple converters. The eigenvalue-based approaches have been extended to assess the stability of systems that consists of multiple parallel converters in [99], [113]–[118], [120]–[122]. However, the eigenvalue-method requires detailed information on the system configuration and internal device dynamic and, as a result, lacks applicability to practical systems. In [143], [144], a vector-fitting approach was applied to extract the system poles from the modeled impedances. In [75], the impedance-based analysis was applied to a data center consisting of multiple rectifiers interconnected in complex configuration by modeling the converters and the distribution network. An approach based on global ad-

Method	Description	Advantages	Disadvantages
Impedance crossover	Examine the phase difference of intersecting subsystem impedances	<ul style="list-style-type: none"> • Intuitive • Quantifies margins 	<ul style="list-style-type: none"> • Infeasible for 3-P systems • Ignores RHP zeros
Sensitivity analysis	Derives sensitivity function from the closed-loop impedance ratio	<ul style="list-style-type: none"> • Characterizes margins • Predicts system response 	<ul style="list-style-type: none"> • Requires auxiliary method to examine absolute stability
Generalized Nyquist criterion	Plots the minor loop eigenvalues as contours in complex plane	<ul style="list-style-type: none"> • Most common method • Easy to apply 	<ul style="list-style-type: none"> • Does not quantify stability margins
Transfer function fitting	Numerically fits transfer functions on minor loop	<ul style="list-style-type: none"> • Yields detailed system quantification 	<ul style="list-style-type: none"> • Computationally demanding • Prone to misfitting • Requires high-quality measurements

Table 1.1 Comparison of impedance-based stability analysis methods.

mittance of parallel inverters was proposed in [124], [146], where the total admittance of multiple inverters was modeled, and the Nyquist criterion was applied on the single-input single-output (SISO) impedance ratio. However, the same shortcomings seen in eigenvalue-methods occur in these modeling-based implementations of impedance-based analysis, as the methods assume detailed system information. Moreover, assumptions on known transmission line impedance were also made in [153], where the cross-coupling elements were also omitted. In [154], a comparison between impedance-based assessment in dq-domain and sequence domain was performed, and the impedances were obtained by impedance sweeps and transformation into a global reference frame. However, the work in [154] focused on detailed comparisons between stability assessment methods, and the implementation of measurement methods required to obtain the impedances was not included in the scope of the work.

Measuring the frequency response of a system is an efficient method for characterizing the dynamics of the system, and consequently, it has been commonly applied in the identification of grid-connected systems [64]. The stability analysis of grid-connected converters has been performed based on measurements on converter terminal admittances [153], [155], [156], grid impedances [157], [158], or stand-alone on-board systems [125], [126], [159], [160]. In the early implementations, the grid impedance was measured by introducing drastic transients to the system in order to perturb the currents and voltages [161], [162]. However, the impulse-like transients may disrupt the system operation, especially in grid-connected applications. To reduce the grid disturbances, the measurement method was improved in [163], [164] where the impulse perturbation was replaced by controllable sinusoids that were injected into the system. In [165], the measurements were further improved by utilizing the grid-connected device itself in the perturbation injection, which removed the

need for an additional measurement device.

Multiple studies have proposed methods for measuring the impedance of the three-phase system; phase impedance measurements were presented in [166], sequence-domain measurements were obtained in [167], and the first dq-domain measurement implementations were proposed in [168], [169]. In [81], the terminal impedances of a single-phase inverter and interfacing grid were measured, and the stability was predicted based on the impedance measurements. In [123], the dq-domain impedance measurements were applied to predict the stability of interconnected converters. Moreover, the method was extended to parametric identification of multi-converter systems in [127]. In [170], an impedance operator was proposed for the stability analysis of multi-converter systems, where the converters do not share a common frame of reference.

The latest advance in frequency-response measurements has been the emergence of real-time implementations. In real-time implementations, measurements are applied in a continuous manner to achieve very fast response rates, which have been applied to adaptive control [149], [171], [172] and system protection [173]–[176]. Often in the adaptive control, the controller parameters are continuously updated based on real-time measurements on the grid impedance [88], [149], [172], [177], [178], which in turn improves control performance or system stability. On the other hand, the system protection schemes often require very fast reaction times, and therefore the real-time frequency-response measurements can be applied in the system monitoring. In [136], a real-time stability assessment method for a grid-connected inverter was implemented based on real-time grid-impedance measurements, whereas in [126], a similar method was implemented based on real-time identification of controller loops. The work in [129] proposed a real-time stability assessment method for a DC distribution system based on online monitoring of bus impedance. However, the real-time methods have not been adequately extended to three-phase systems that consist of parallel grid-connected converters.

1.4 Summary of Scientific Contributions

The scientific contributions of this thesis can be summarized as follows

- An aggregation method for applying the impedance-based stability analysis to multiple converters.
- A measurement-based method for predicting the hosting capacity for parallel converters at a certain grid-interface.
- Power hardware-in-the-loop implementation of a real-time stability assessment of multiple inverters based on online measurements.
- Design method for perturbation signal with adjustable Fourier amplitude spectrum

based on combined orthogonal sequences.

- Design procedure for injection amplitude and measurement duration of broadband measurement.
- A method for quantifying the stability margins and predicting dynamic response for multi-parallel converter systems.

1.5 Structure of the Thesis

This thesis consists of five chapters and eight publications, [P1]-[P8]. The contents of the chapters can be summarized as follows.

Chapter 2: Grid-Interfaced Power-Electronic Converters

In Chapter 2, the theoretical background of dynamical analysis of grid-interfaced power electronics is discussed. The introduction to small-signal modeling starts by presenting the synchronous reference frame (dq-frame), where the analysis presented in this thesis takes place. Moreover, a dynamical model of a three-phase grid-connected inverter is presented in the dq-domain, and the origin of load effect that results from the grid impedance is presented analytically. Based on the load effect and its resemblance to feedback control systems, the impedance-based stability criterion is presented.

Chapter 3: Methods

Chapter 3 presents the methods that are derived and applied in this work, divided into two sections: measurement methods; and stability analysis methods. In the first section, the methods for the design of perturbation signals for the identification of power-electronic systems are discussed. First, a general overview of frequency-response measurements of dynamic systems is presented. Then, the pseudo-random binary sequences, which are applied in most of the measurements presented in this thesis, are introduced. Moreover, the orthogonal perturbation sequences are presented along with their application in multivariable measurements. The next subsection presents the contributions of this work on the design of broadband measurements with respect to grid-connected systems. Lastly, the thesis presents a novel method for the design of perturbations sequences: a combined orthogonal sequence (COS). The COS is a highly adjustable perturbation sequence that enables the optimization of the perturbation amplitude spectrum so that the signal-to-noise ratio can be improved over a wide frequency-range without increasing the time-domain amplitude of the injection.

The second section presents the stability analysis methods for multi-parallel converters

that are constructed within this thesis. A method for extending the conventional impedance-based stability criterion on multiple parallel converters is shown, where the impedance aggregation of the parallel devices enables the assessment of the grid hosting capacity for the paralleled devices. Moreover, the impedance-based stability criterion is further extended by deriving the impedance-based sensitivity function that is capable of quantifying and predicting the system stability margins. Next, a different approach is taken for the stability analysis: instead of global-scope impedance analysis, the analysis takes place in the local scope by assessing the load-affected loop gains of converters. Lastly, the chapter presents real-time methods for implementing the methods in a power hardware-in-the-loop (PHIL) setup, where a dual identification scheme is also presented, enabling simultaneous identification of an inverter's terminal grid impedance and innermost controller loop gain.

Chapter 4: Experiments

In Chapter 4, the methods proposed in this thesis are implemented on experimental setups. Consequently, this chapter summarizes the experiments performed in the original publications that form the foundation of this thesis. The experimental results verify the performance and applicability of the proposed methods in kilowatt scale, where the methods are tested in realistic conditions.

Chapter 5: Conclusions

Chapter 5 draws conclusions that summarize the thesis. The presented methods are given a critical review, where limitations and potential challenges in the presented methods are discussed. Moreover, the discussion considers also the general challenges in the stability assessment of complex systems that have high penetration of grid-connected converters. The last section is dedicated for discussing the potential future research topics based on the results of this thesis.

2 GRID-INTERFACED POWER-ELECTRONIC CONVERTERS

This chapter introduces the theoretical background for the dynamical analysis of grid-interfaced three-phase power electronics. First, a synchronous reference frame (dq-domain) is established to facilitate the dynamic analysis of three-phase systems. Then, a dynamic model of a three-phase grid-connected inverter is derived and the impact of non-zero grid impedance on the inverter dynamics is considered through load-effect modeling. Based on the load-affected transfer functions, an impedance-based stability criterion is presented where the stability of a grid-connected converter is assessed by an equivalent feedback system that consists of the two subsystems.

Power electronics are inherently non-linear and time-discontinuous due to the switched-mode operation between two (or more) subcircuits. Multiple approaches have been taken in the dynamic modeling of power electronics to address this non-linearity and time-discontinuity. Discrete-time analysis can be applied to model the dynamics without loss of accuracy [179], [180]. However, due to the complexity of discrete-time methods, the use of averaging theory is preferred for the analysis of complex systems [181], [182]. With the state-space averaging, the switching between circuits can be averaged over a switching period [183]. However, the averaging over switching period limits the applicable frequency range of the method; the accuracy of the model dynamics begins to deteriorate after one tenth of the switching frequency [182]. By applying averaged modeling, the set of differential equations that describe the system can be made time-continuous, but the non-linear characteristics persist. Further simplification can be achieved by linearizing the equations, either around a state-state equilibrium point [54] or by linearizing the equations around a periodic trajectory [184]–[186]. In this thesis, the systems are considered linear time invariant (LTI) systems by applying averaged modeling and linearization at an equilibrium point.

2.1 Synchronous Reference Frame Modeling

In the analysis of power-electronic systems, small-signal modeling is a frequently used technique to analyze the dynamics of a non-linear system around an operation point [187]. In

small-signal modeling, small-magnitude AC signals are approximated with a first-order linear approximation around the DC operation point. As a result, an AC equivalent circuit that is linear can be applied, which enables the use of linear modeling by applying, for example, Laplace transform. This technique allows linear analysis of non-linear systems without significant loss of accuracy, given that the superimposed AC signal has sufficiently low magnitude so that the operation point remains unchanged.

The dynamic small-signal analysis of DC systems is intuitive and straightforward, as the signals can be considered as scalar variables. However, for multivariable three-phase AC systems, two inherent challenges emerge: the system must be depicted as matrices; and the system does not have an equilibrium point in terms of small-signal analysis as the signals oscillate with the fundamental frequency [187]. In order to address the first challenge, the signals can be transformed to the stationary reference frame ($\alpha\beta$ -frame) through Clarke's transformation, where the signals are expressed as a rotating space vector [188]. For a three-phase signal $\mathbf{x}_{abc}(t) = [x_a(t), x_b(t), x_c(t)]^T$, the Clarke's transformation can be performed as

$$\begin{bmatrix} x_\alpha(t) \\ x_\beta(t) \\ x_0(t) \end{bmatrix} = K_C \begin{bmatrix} 1 & -1/2 & -1/2 \\ 0 & \sqrt{3}/2 & -\sqrt{3}/2 \\ 1/2 & 1/2 & 1/2 \end{bmatrix} \begin{bmatrix} x_a(t) \\ x_b(t) \\ x_c(t) \end{bmatrix} \quad (2.1)$$

where K_C is the transformation coefficient (for a power-invariant transformation $K_C = \sqrt{2/3}$ and for an amplitude-invariant transformation $K_C = 2/3$) and $x_\alpha(t)$, $x_\beta(t)$, and $x_0(t)$ are the alpha, beta, and zero components, respectively. The zero can be omitted in balanced three-phase systems, and consequently, the Clarke's transformation can depict the three AC signals with two AC signals.

The analysis can be further simplified by rotating the reference frame along with the rotating space vector. The frame can be aligned with the space vector by applying Park's transformation, where the reference frame rotates with the fundamental grid frequency ω_g [189]. As the reference frame rotates along with the space vectors, the fundamental oscillating components appear as constant signals; orthogonal DC-valued d- and q-components can fully represent the three balanced AC signals. Consequently, the synchronous-reference frame representation provides the equilibrium point required for the small-signal analysis for three-phase AC systems. The Park's transformation can be given as

$$\begin{bmatrix} x_d(t) \\ x_q(t) \\ x_z(t) \end{bmatrix} = K_C \begin{bmatrix} \cos(\theta) & \sin(\theta) & 0 \\ -\sin(\theta) & \cos(\theta) & 0 \\ 0 & 0 & 1 \end{bmatrix} \begin{bmatrix} x_\alpha(t) \\ x_\beta(t) \\ x_0(t) \end{bmatrix} \quad (2.2)$$

where θ is the frame angle and $x_d(t)$, $x_q(t)$, and $x_z(t)$ are the direct (d), quadrature (q), and zero (z) components, respectively [189]. By combining the Clarke's and Park's transforma-

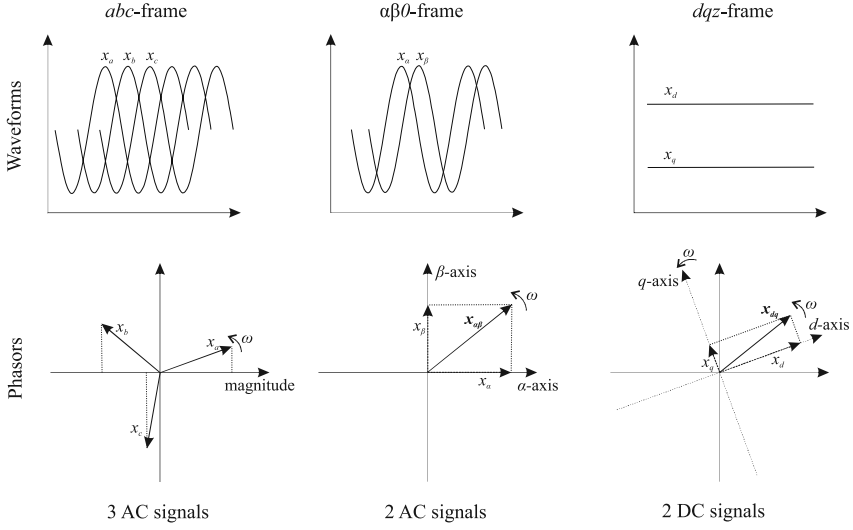


Figure 2.1 Illustration of three-phased signals in the stationary and synchronous reference frame.

tions, the balanced phase signals can be directly transformed to the dq-frame by applying

$$\begin{bmatrix} x_d(t) \\ x_q(t) \end{bmatrix} = K_C \begin{bmatrix} \cos(\theta) & \cos(\theta - \frac{2\pi}{3}) & \cos(\theta + \frac{2\pi}{3}) \\ -\sin(\theta) & -\sin(\theta - \frac{2\pi}{3}) & -\sin(\theta + \frac{2\pi}{3}) \end{bmatrix} \begin{bmatrix} x_a(t) \\ x_b(t) \\ x_c(t) \end{bmatrix} \quad (2.3)$$

Fig. 2.1 demonstrates the signal waveforms and phasors in the three domains. Another approach is to model the system in the sequence domain and apply harmonic linearization to obtain the equilibrium point. In literature, both sequence domain and dq-domain are applied in the analysis of three-phase systems. The domains are closely related, and stability analysis results are similar in both domains [142]. In this work, the analysis will be performed in the dq-domain as the domain directly provides the equilibrium point for the small-signal analysis.

2.2 Dynamic Modeling and Load Effect

Fig. 2.2 presents the power stage of a three-phase grid-connected inverter, where subscripts a, b and c denote the phases, S_1 - S_6 are the power switches, d and d' the duty ratio and its complement, L and R_L the filter inductance and parasitic resistance, i_{in} and i_L the input and inductor currents, and v_{dc} , v_g and v_L are the DC, grid, and inductor voltages, respectively. The inverter injects currents to the grid by manipulating the switching state of the six

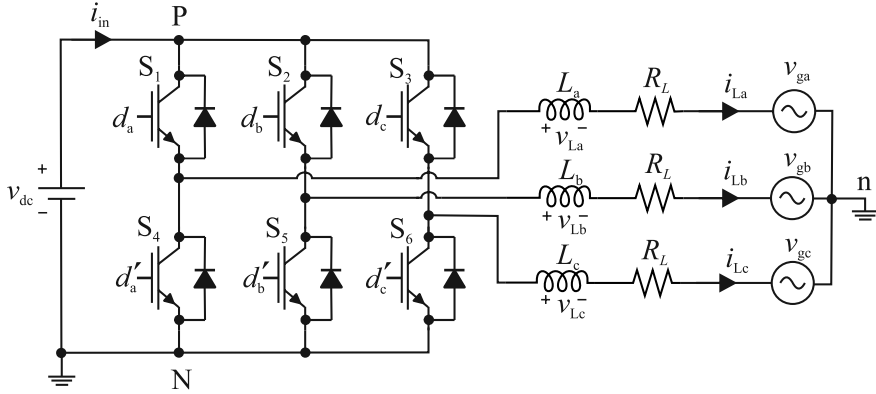


Figure 2.2 Power stage of a two-level three-phase inverter.

switches, where a lower and upper switch exist for each phase leg. This topology is known as the two-level voltage-sourced inverter, which is a common inverter type. The switches are controlled through space-vector modulation, where a rotating space vector defines the switching sequence. The averaged voltages over the inductors can be given as

$$\begin{bmatrix} v_{La} \\ v_{Lb} \\ v_{Lc} \end{bmatrix} = \begin{bmatrix} d_A \\ d_B \\ d_C \end{bmatrix} \langle v_{dc} \rangle - R_L \begin{bmatrix} i_{La} \\ i_{Lb} \\ i_{Lc} \end{bmatrix} - \begin{bmatrix} v_a \\ v_b \\ v_c \end{bmatrix} - \begin{bmatrix} v_{nN} \\ v_{nN} \\ v_{nN} \end{bmatrix} \quad (2.4)$$

where d_A , d_B , and d_C are the duty ratios of the upper switches and the brackets denote averaged variables. The derivative of the inductor current can be given as

$$\frac{d\langle \mathbf{i}_L \rangle}{dt} = \frac{1}{L} \langle \mathbf{v}_L \rangle \quad (2.5)$$

and consequently, the inductor current derivatives can be given in the synchronous reference frame as

$$\frac{d\langle i_{Ld} \rangle}{dt} = \frac{1}{L} \left(d_d \langle v_{dc} \rangle + \omega_s L \langle i_{Lq} \rangle - r_L \langle i_{Ld} \rangle - \langle v_{od} \rangle \right) \quad (2.6)$$

$$\frac{d\langle i_{Lq} \rangle}{dt} = \frac{1}{L} \left(d_q \langle v_{dc} \rangle - \omega_s L \langle i_{Ld} \rangle - r_L \langle i_{Lq} \rangle - \langle v_{oq} \rangle \right) \quad (2.7)$$

Additionally, the input current can be given as

$$\langle i_{in} \rangle = \frac{3}{2} \left(d_d \langle i_{Ld} \rangle + d_q \langle i_{Lq} \rangle \right) \quad (2.8)$$

and output current d- and q-components are equal to inductor current components

$$\langle i_{od} \rangle = \langle i_{Ld} \rangle \quad (2.9)$$

$$\langle i_{oq} \rangle = \langle i_{Lq} \rangle \quad (2.10)$$

Linearization of the equations occurs around the equilibrium point, where the DC-component of the signals remains unchanged. The equilibrium point can be solved from the averaged equations by setting the derivative terms equal to zero and solving the steady state, given as

$$\begin{cases} I_{Ld} = I_{od} \\ I_{Lq} = I_{oq} \\ D_d = \frac{V_{od} + r_L I_{Ld} - \omega_s L I_{Lq}}{V_{dc}} \\ D_q = \frac{V_{oq} + r_L I_{Lq} + \omega_s L I_{Ld}}{V_{dc}} \\ I_{in} = \frac{3}{2} (D_d I_{Ld} + D_q I_{Lq}) \end{cases} \quad (2.11)$$

where uppercase letters denote the steady-state values. Equations (2.6-2.10) can be linearized around the equilibrium point given in (2.11) by applying first-order Taylor's series approximation, yielding

$$\begin{cases} \frac{d\hat{i}_{Ld}}{dt} = -\frac{r_L}{L} \hat{i}_{Ld} + \omega_s \hat{i}_{Lq} + \frac{D_d}{L} \hat{v}_{in} - \frac{1}{L} \hat{v}_{od} + \frac{V_{dc}}{L} \hat{d}_d \\ \frac{d\hat{i}_{Lq}}{dt} = -\frac{r_L}{L} \hat{i}_{Lq} - \omega_s \hat{i}_{Ld} + \frac{D_q}{L} \hat{v}_{in} - \frac{1}{L} \hat{v}_{oq} + \frac{V_{dc}}{L} \hat{d}_q \\ \hat{i}_{in} = \frac{3D_d}{2} \hat{i}_{Ld} + \frac{3D_q}{2} \hat{i}_{Lq} + \frac{3I_{Ld}}{2} \hat{d}_d + \frac{3I_{Lq}}{2} \hat{d}_q \\ \hat{i}_{od} = \hat{i}_{Ld} \\ \hat{i}_{oq} = \hat{i}_{Lq} \end{cases} \quad (2.12)$$

where the linearized variables are denoted with a hat.

The linearized equations form the state-space representation of the system, which is commonly used in control engineering to model a physical system by first-order differential equations consisting of input, output, and state variables [54]. The state-space representation can be written in the matrix form as

$$\frac{d}{dt} \underbrace{\begin{bmatrix} \hat{i}_{Ld} \\ \hat{i}_{Lq} \end{bmatrix}}_{\mathbf{x}} = \underbrace{\begin{bmatrix} -\frac{r_L}{L} & \omega_s \\ -\omega_s & -\frac{r_L}{L} \end{bmatrix}}_{\mathbf{A}} \underbrace{\begin{bmatrix} \hat{i}_{Ld} \\ \hat{i}_{Lq} \end{bmatrix}}_{\mathbf{x}} + \underbrace{\begin{bmatrix} \frac{D_d}{L} & -\frac{1}{L} & 0 & \frac{V_{dc}}{L} & 0 \\ \frac{D_q}{L} & 0 & -\frac{1}{L} & 0 & \frac{V_{dc}}{L} \end{bmatrix}}_{\mathbf{B}} \underbrace{\begin{bmatrix} \hat{v}_{in} \\ \hat{v}_{od} \\ \hat{v}_{oq} \\ \hat{d}_d \\ \hat{d}_q \end{bmatrix}}_{\mathbf{u}} \quad (2.13)$$

$$\underbrace{\begin{bmatrix} \hat{i}_{in} \\ \hat{i}_{od} \\ \hat{i}_{oq} \end{bmatrix}}_{\mathbf{y}} = \underbrace{\begin{bmatrix} \frac{3D_d}{2} & \frac{3D_q}{2} \\ 1 & 0 \\ 0 & 1 \end{bmatrix}}_{\mathbf{C}} \underbrace{\begin{bmatrix} \hat{i}_{Ld} \\ \hat{i}_{Lq} \end{bmatrix}}_{\mathbf{x}} + \underbrace{\begin{bmatrix} 0 & 0 & 0 & \frac{3I_{Ld}}{2} & \frac{3I_{Lq}}{2} \\ 0 & 0 & 0 & 0 & 0 \\ 0 & 0 & 0 & 0 & 0 \end{bmatrix}}_{\mathbf{D}} \underbrace{\begin{bmatrix} \hat{v}_{in} \\ \hat{v}_{od} \\ \hat{v}_{oq} \\ \hat{d}_d \\ \hat{d}_q \end{bmatrix}}_{\mathbf{u}} \quad (2.14)$$

where \mathbf{A} , \mathbf{B} , \mathbf{C} , and \mathbf{D} are the state-space matrices, and \mathbf{x} , \mathbf{u} , and \mathbf{y} are the state, input, and output vectors, respectively. The transfer functions from system inputs to outputs can be directly obtained from the state space by transforming the state space to the frequency domain. The transfer function matrix \mathbf{G} can be calculated as

$$\mathbf{G} = \mathbf{C}(s\mathbf{I} - \mathbf{A})^{-1}\mathbf{B} + \mathbf{D} \quad (2.15)$$

where s is the Laplace variable and \mathbf{I} is an 2-by-2 identity matrix. Consequently, the transfer functions for all input-output pairs can be given as

$$\underbrace{\begin{bmatrix} \hat{i}_{in} \\ \hat{i}_{od} \\ \hat{i}_{oq} \end{bmatrix}}_{\mathbf{y}} = \underbrace{\begin{bmatrix} Y_{in} & T_{oid} & T_{oiq} & G_{cid} & G_{ciq} \\ G_{iod} & -Y_{odd} & -Y_{oqd} & G_{codd} & G_{coqd} \\ G_{ioq} & -Y_{odq} & -Y_{oqq} & G_{codq} & G_{coqq} \end{bmatrix}}_{\mathbf{G}} \underbrace{\begin{bmatrix} \hat{v}_{in} \\ \hat{v}_{od} \\ \hat{v}_{oq} \\ \hat{d}_d \\ \hat{d}_q \end{bmatrix}}_{\mathbf{u}} \quad (2.16)$$

which are known as Y-parameters of the system [190] where the subscripts denote the components in dq domain and the property of the transfer function; for example, G_{coqd} refers to control-to-output transfer function qd-component (from control q component \hat{d}_q to output d component \hat{i}_{od}). The transfer function matrix shown in (2.16) can be presented in

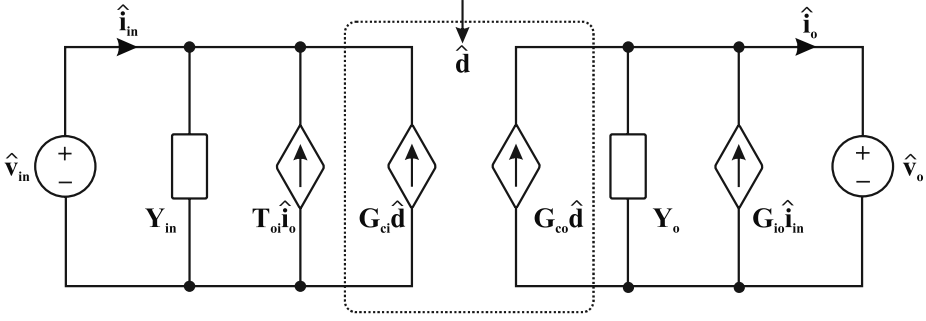


Figure 2.3 Two-port model of a three-phase inverter.

multivariable form, where the transfer functions are grouped into 2-by-2 submatrices

$$\begin{bmatrix} \hat{i}_{in} \\ 0 \\ \hat{i}_{od} \\ \hat{i}_{oq} \end{bmatrix} = \begin{bmatrix} Y_{in} & 0 \\ 0 & 0 \\ G_{iod} & 0 \\ G_{ioq} & 0 \end{bmatrix} - \begin{bmatrix} T_{oid} & T_{oiq} \\ 0 & 0 \\ Y_{odd} & Y_{oqd} \\ Y_{odq} & Y_{oqq} \end{bmatrix} \begin{bmatrix} G_{cid} & G_{ciq} \\ 0 & 0 \\ G_{codd} & G_{coqd} \\ G_{codq} & G_{coqq} \end{bmatrix} \begin{bmatrix} \hat{v}_{in} \\ 0 \\ \hat{v}_{od} \\ \hat{v}_{oq} \\ \hat{d}_d \\ \hat{d}_q \end{bmatrix} \quad (2.17)$$

The denotation can be compressed by grouping the submatrices into elements given as

$$\begin{bmatrix} \hat{i}_{in} \\ \hat{i}_o \end{bmatrix} = \begin{bmatrix} \mathbf{Y}_{in} & \mathbf{T}_{oi} & \mathbf{G}_{ci} \\ \mathbf{G}_{io} & -\mathbf{Y}_o & \mathbf{G}_{co} \end{bmatrix} \begin{bmatrix} \hat{v}_{in} \\ \hat{v}_o \\ \hat{d} \end{bmatrix} \quad (2.18)$$

The multivariable-form transfer function can be further represented as a multivariable linear circuit, which is known as the two-port model of the inverter dynamics. Fig. 2.3 presents a two-port model of the grid-connected inverter, where the elements denote multivariable transfer function matrices.

The modeling above considers the unterminated converter dynamics, where the source and load are considered as ideal voltage or current sources. The equivalent series impedance of an ideal voltage source equals zero, whereas an ideal current source incorporates an infinite parallel impedance. However, real systems may deviate drastically from the ideal considerations. In grid-connected systems, the equivalent grid impedance (load impedance) is particularly interesting as the impact of grid impedance on the converter dynamics have been rigorously demonstrated [54], [55], [110], [177], [191], [192]. The dynamical impact

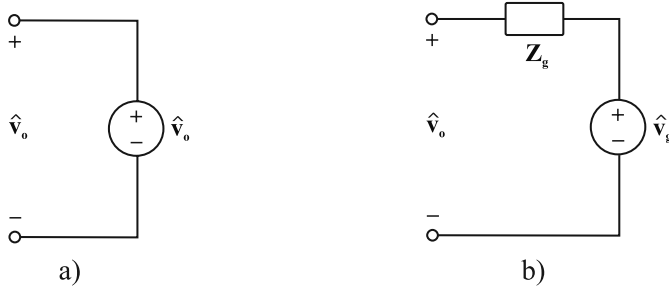


Figure 2.4 Grid represented as a) ideal voltage source and b) Thevenin equivalent.

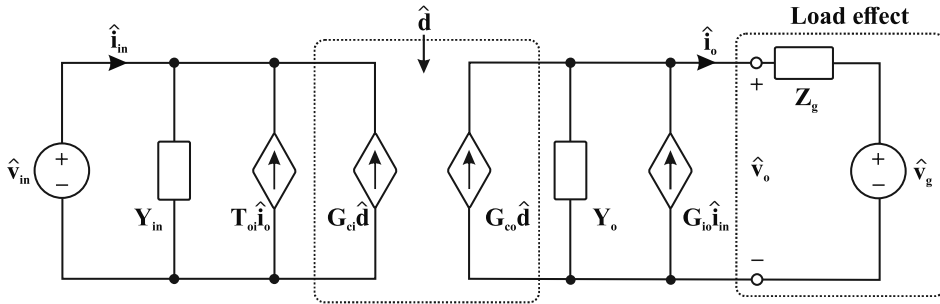


Figure 2.5 Two-port model of a three-phase inverter connected to grid with non-zero impedance.

can be accounted for through the use of load-effect modeling, where the ideal voltage source (load) is replaced by a Thevenin equivalent of the grid comprising a voltage source and equivalent series impedance [54]. Fig. 2.4 illustrates the ideal grid connection (a) and realistic grid connection (b). It should be noted that the grid impedance may consist of multiple series and parallel elements, and the shape of the frequency-dependent impedance may be highly complex [191], [193]–[195].

Fig. 2.5 presents the two-port model of the grid-connected converter, when the ideal load has been replaced with a grid connection that has a non-zero grid impedance. The load voltage at the grid interface can be written as

$$\hat{v}_o = \hat{v}_g + Z_g \hat{i}_o \quad (2.19)$$

Substituting (2.19) into (2.18) and solving with respect to \hat{v}_g , which is the new input variable for the system, yields the load-affected transfer function matrix

$$\begin{bmatrix} \hat{i}_{in} \\ \hat{i}_o \end{bmatrix} = \begin{bmatrix} Y_{in} + T_{oi}Z_g[I + Y_oZ_g]^{-1}G_{io} & T_{oi} - T_{oi}Z_g[I + Y_oZ_g]^{-1}Y_o & G_{ci} + T_{oi}Z_g[I + Y_oZ_g]^{-1}G_{co} \\ G_{io}[I + Y_oZ_g]^{-1} & -Y_o[I + Y_oZ_g]^{-1} & G_{co}[I + Y_oZ_g]^{-1} \end{bmatrix} \begin{bmatrix} \hat{v}_{in} \\ \hat{v}_g \\ \hat{d} \end{bmatrix} \quad (2.20)$$

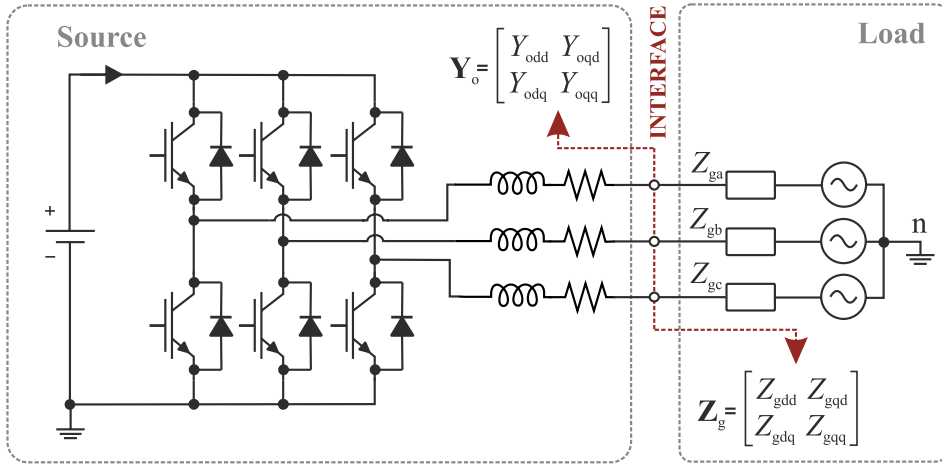


Figure 2.6 Terminal impedance characteristics of a grid-connected inverter with non-zero grid impedance.

The load-affected dynamics (that is, the impact of grid impedance on dynamics) can be assessed based on (2.20).

2.3 Impedance-Based Stability Analysis

The impedance-based stability analysis determines the stability of two interconnected systems by examining the ratio of the terminal impedances/admittances of the two systems. Fig. 2.6 presents a three-phase inverter connected to a grid that has non-zero grid impedance, and the stability analysis can be performed based on the impedance characteristics observable from the point-of-common coupling (PCC). The impedance-based stability criterion originates from the load effect, which is discussed in detail in Section 2.2. The load-affected transfer functions, presented in (2.20), share common poles introduced by the term $[\mathbf{I} + \mathbf{Y}_o \mathbf{Z}_g]^{-1}$ that occurs in each transfer function submatrix. Consequently, assuming the system is stable when connected to an ideal grid, examining $[\mathbf{I} + \mathbf{Y}_o \mathbf{Z}_g]^{-1}$ is both a necessary and sufficient condition for system stability.

In order to simplify the analysis, a small-signal equivalent of the grid-connected inverter system can be constructed from a Norton equivalent, representing the inverter, and Thevenin equivalent representing the power grid, as shown in Fig. 2.7. Fig. 2.8 presents the duality between the small-signal equivalent circuit of interconnected subsystems and a negative-feedback system. The current flowing to the system can be obtained as

$$\hat{\mathbf{i}}_L = [\mathbf{I} + \mathbf{Y}_S \mathbf{Z}_L]^{-1} [\hat{\mathbf{i}}_S - \mathbf{Y}_S \hat{\mathbf{v}}_S] \quad (2.21)$$

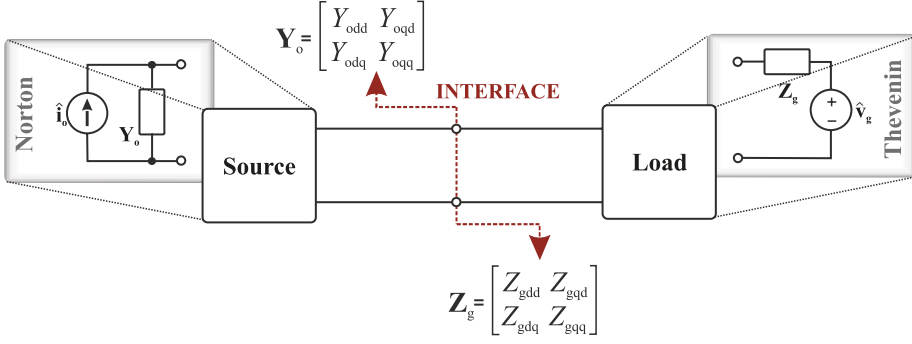


Figure 2.7 Equivalent source-load system based on Norton and Thevenin equivalents.

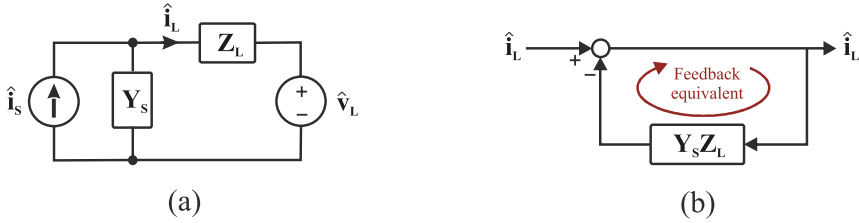


Figure 2.8 Equivalence between small-signal source-load system and feedback system.

where subscript S denotes source subsystem (inverter), and L denotes load subsystem. The poles (that is, the stability) of the small-signal equivalent circuit are equivalent to the poles of the system obtained through the load-effect modeling. Thus, the equivalence between the simplified interconnected subsystems and detailed modeling of the system dynamics is validated.

The matrix term $[\mathbf{I} + \mathbf{Y}_S \mathbf{Z}_L]^{-1}$ resembles the transfer function of a negative-feedback closed-loop system, where the transfer function of the feedback loop is

$$\mathbf{L} = \mathbf{Y}_S \mathbf{Z}_L \quad (2.22)$$

which is also known as the *minor loop gain*. Based on this observation, the stability of the grid-connected system can be evaluated similarly than the stability of a conventional feedback system. A straightforward method for determining the stability of such a system is to apply the Nyquist criterion on the loop gain. As the minor loop gain is a matrix instead of a scalar, the use of a generalized Nyquist criterion (GNC) is required [96]. In the GNC, the eigenvalues of the multivariable loop gain are calculated by solving the eigenvalues from

$$\det(\mathbf{L}(j\omega) - \lambda(j\omega)\mathbf{I}) = 0 \quad (2.23)$$

In dq-domain, the loop \mathbf{L} is a 2-by-2 matrix, and consequently, two eigenvalues ($\lambda_1(j\omega)$ and $\lambda_2(j\omega)$) are obtained. In the GNC, the frequency-dependent eigenvalues are plotted in the complex plane, and the stability of the system can be determined by examining the contour encirclements around the critical point $(-1, 0)$.

2.4 Discussion

This chapter has established the theoretical background for the small-signal assessment of grid-connected converters in the dq-domain. Moreover, the theoretical origin of the source-load interaction that occurs between a grid-connected converter and the grid is presented. The theory lays the foundation for the broadband stability analysis methods presented later in this thesis. The presented methods are based on the small-signal dynamics of grid-connected systems in a synchronous reference frame, and a considerable share of the stability analysis methods are based on the impedance interactions between the source-load system.

3 METHODS

This chapter presents the methods applied in the thesis. The chapter is divided into two sections: the first discusses the methods used in the design of frequency-response measurements; the second presents the methods for the stability analysis of multiple parallel converters. The first section starts by introducing the implementation of experimental frequency-response measurements in power-electronic systems. The following subsections discuss the perturbation signals, with an emphasis on pseudo-random sequences, and introduce multivariable measurements by applying orthogonal sequences. Moreover, the design of injection amplitude and the measurement duration are presented in the next subsection. Lastly, a method for designing a novel perturbation sequence that has a highly adjustable excitation spectrum is presented.

In the second section, an impedance aggregation method is first introduced to simplify the impedance-based analysis of multi-converter systems. Then, the impedance-based approach is complemented by applying a sensitivity function to quantify the system stability margins. Additionally, a parallel stability analysis method is presented based on the load-affected loop gain measurements, enabling the simultaneous local scope analysis of each converter. Finally, the chapter is concluded by implementing the presented methods in real-time for continuous stability assessment of parallel converters.

3.1 Frequency-Response Measurements

The dynamic characteristics of grid-connected systems can typically be considered as linear time invariant (LTI) for small-signal variations around the steady state operation point. Based on control theory, such systems can be characterized by their time-domain impulse response function and frequency-domain frequency response function, which are equivalent and interchangeable [83]. The frequency response is the Fourier transformation of the impulse response. In the frequency response function, the system is evaluated at a number of frequency points, which together form the frequency response function.

Fig. 3.1 presents a generalized overview of a frequency-response measurement, where a system plant $G(j\omega)$ is characterized in the frequency domain. An excitation signal $e(t)$ is injected into the reference signal $r(t)$, which controls the system actuator. The actuator gen-

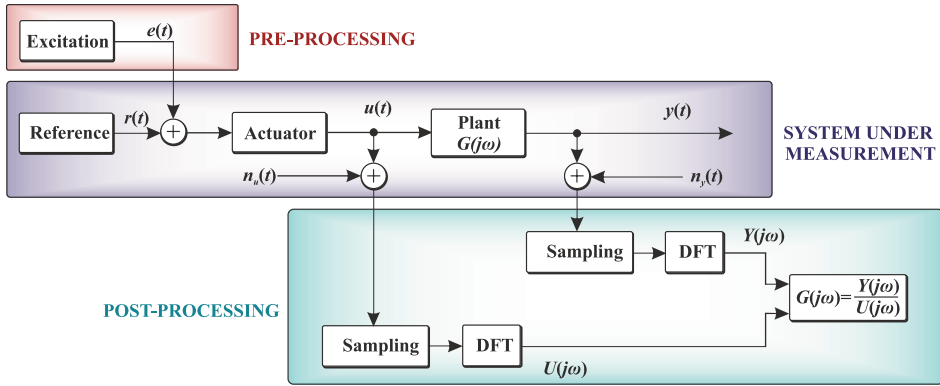


Figure 3.1 Generalized setup for frequency-response measurement.

erates the system input signal $u(t)$ that produces the output signal $y(t)$ in the system plant. The measured signals are corrupted by noise, $n_u(t)$ and $n_y(t)$ for the input and output noise, respectively. The measured signals are sampled and transformed to the frequency domain by applying discrete Fourier transformation (DFT). The frequency response function is calculated as

$$G(j\omega) = \frac{Y(j\omega)}{U(j\omega)} \quad (3.1)$$

where $U(j\omega)$ and $Y(j\omega)$ are the Fourier-transformed noise-affected input and output signals, respectively.

3.1.1 Pseudo-Random Binary Sequences

The performance of a frequency-response measurement method is directly related to the characteristics of the perturbation signal [85]. A single-tone sine wave is a trivial excitation signal, where all the excitation energy occurs at a single frequency, resulting in a maximal signal-to-noise (SNR) ratio [85]. However, when using the single-tone sine, multiple sequential measurements are required to obtain the frequency response in a wide band. As a result, the measurement time may become very long [127]. To decrease the measurement duration, multiple sine waves can be combined to form a multi-tone sine [196]. Despite multiple advantages, the multi-tone sine has limited suitability on power-electronic devices as the large number of signal levels makes it difficult to implement on low-cost hardware [197]. Additionally, combining multiple sine waves increases the crest factor of the signal, and the high amplitude time-domain peaking may disrupt sensitive systems [83].

Recently, pseudo-random sequences (PRS) have been adopted for frequency-response measurements of power-electronic converters [89], [125], [160], [198], [199]. PRS are a class of deterministic and periodic broadband signals that typically have two signal levels [85].

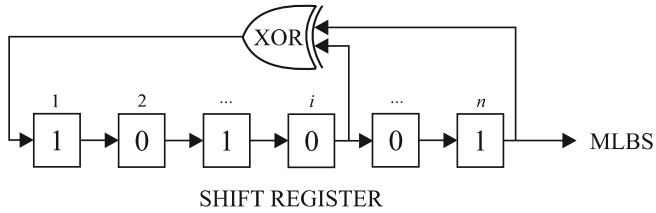


Figure 3.2 MLBS generator implemented with shift registers.

The ease of implementation combined with a low crest factor, controllable measurement bandwidth and frequency resolution have made the PRS a particularly attractive alternative to other types of broadband perturbations.

The most common PRS is the maximum-length binary sequence (MLBS) [200]. The MLBS exists for sequence lengths of $N = 2^n - 1$, where n is a positive integer. The sequence is easy to implement as it can be generated in hardware by applying shift registers [201]. Fig. 3.2 presents an n -stage-long shift register with excluding-or (XOR) feedback that generates an MLBS signal. The shift registers are populated by bits 0 and 1, where the starting configuration can be anything except all 0s. Mapping the resulting signal levels to $-A$ and A changes the signal into a symmetric perturbation with a DC-value of almost zero. The MLBS has an evenly spaced power spectrum with frequency resolution of

$$f_{\text{res}} = \frac{f_{\text{gen}}}{N} \quad (3.2)$$

where f_{gen} is the generation frequency (the frequency with which the shift registers change value). The MLBS is periodic with a duration of

$$T_{\text{MLBS}} = \frac{N}{f_{\text{gen}}} \quad (3.3)$$

and consequently, the measurements can be averaged over multiple periods to increase the measurement SNR. Fig. 3.3 presents the continuous time-domain signal and power spectrum of a 31-bit-long MLBS generated at 1 kHz. The zero-order-hold (ZOH) nature of the practical implementation causes a decrease in the power of the signal and, consequently, the usable bandwidth of the excitation is below the generation frequency. Typically, the bandwidth of the MLBS excitation is considered to be the frequency range where the spectral lines have not dropped below half of the maximum power, which is approximately $f_{\text{bw}} \approx 0.44f_{\text{gen}}$ [202].

One constraint in applying the MLBS is the limited number of signal lengths. As the available sequence lengths are defined as $N = 2^n - 1$, each sequence is approximately twice as long as the previous sequence. Consequently, tuning the frequency resolution of the perturbation signal becomes difficult. To tackle this limitation, a quadratic-residue binary sequence

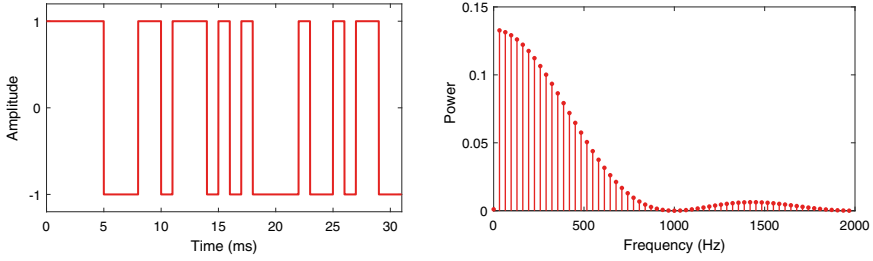


Figure 3.3 (a) Time-domain waveform and (b) frequency-domain power spectrum of a MLBS signal.

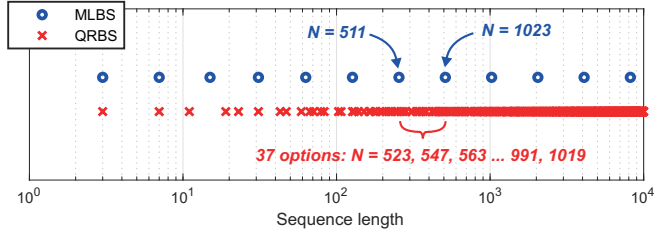


Figure 3.4 Signal length options for for MLBS (blue) and QRBS (red).

(QRBS) can be applied [P6]. The QRBS is another sequence from the PRS class and shares the same attractive characteristics as the MLBS. The QRBS exists for sequence lengths of

$$N_{\text{QRBS}} = 4k - 1 \quad (3.4)$$

where N_{QRBS} is a prime number and k is a positive integer. Therefore, the QRBS offers significantly more alternatives for the sequence length in comparison to the MLBS. Fig. 3.4 demonstrates the available signal length options up to a maximum sequence length of 10000 [P6]. The design of QRBS perturbation can be summarized as follows [200]:

1. Choose signal length $N = 4k - 1$, where N is a prime and k a positive integer
2. Form sequence up to $(N - 1)/2$,
 $[1 \ 2 \ \dots \ (N - 1)/2]$
3. Square the sequence,
 $[1^2 \ 2^2 \ \dots \ ((N - 1)/2)^2]$
4. Take modulo N of all the values,
 $[1_{\text{mod } N} \ 2_{\text{mod } N} \ \dots \ ((N - 1)/2)_{\text{mod } N}]$
5. Generate a sequence of zeros with length N
6. Set the values in empty sequence to one based on the modulo sequence (that is, if the modulo sequence in (4) contains a number 1, the first element of the sequence full of zeros is replaced with one).

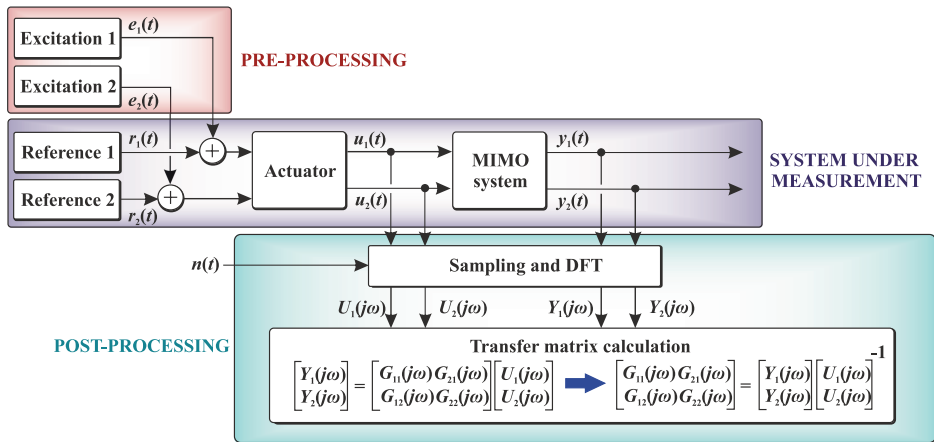


Figure 3.5 Generalized multivariable system identification setup.

7. From the obtained sequence, map values of 0 to $-A$ and values of 1 to A , where A is the desired injection amplitude.

3.1.2 Multivariable Identification with Orthogonal Sequences

Grid-connected systems are typically multivariable systems with multiple inputs and multiple outputs. Such multi-input multi-output (MIMO) systems are characterized by $n \times m$ transfer function matrices, where n is the number of system inputs and m is the number of outputs. An example of such a system is a dq-domain model of a grid-connected converter terminal impedance with $n = 2$ and $m = 2$ modeled as

$$\begin{bmatrix} y_d(s) \\ y_q(s) \end{bmatrix} = \underbrace{\begin{bmatrix} G_{dd}(s) & G_{qd}(s) \\ G_{dq}(s) & G_{qq}(s) \end{bmatrix}}_{\mathbf{G}(s)} \begin{bmatrix} u_d(s) \\ u_q(s) \end{bmatrix} \quad (3.5)$$

where u and y are the system input and output, respectively, $\mathbf{G}(s)$ is the transfer matrix, and subscripts d and q are the signal direct and quadrature components. In the 2x2 transfer matrix, the diagonal components represent the d and q channels of the system, whereas the off-diagonal components are the cross-couplings between the channels.

Fig. 3.5 presents a generalized transfer matrix identification configuration for a multivariable system with two inputs and two outputs. Identifying the transfer matrix requires measurements on each individual transfer function. The simplest way to identify such system is to apply a superposition theorem by sequentially perturbing each input while measuring all the output responses for each input [84]. However, sequential measurements require

n identification cycles, which makes the process time consuming. Moreover, such a technique is prone to changes in the operation point of the grid-connected system. The results become unreliable when some of the transfer functions are measured in different operation conditions.

Instead of sequential measurements for each input, orthogonal perturbation signals can be applied for simultaneous identification of the complete transfer matrix. The orthogonal perturbations are uncorrelated and share no common excited frequency, and consequently, the inputs can be perturbed uncorrelated to each other [200]. Therefore, the perturbation in the q channel does not affect the measurements on d channel, provided that the system is linear or almost linear, as the measurements occur on different frequencies. Orthogonal measurements reduce identification duration and enable measuring the system frequency responses under the same operating conditions [P8].

A major advantage of PRS signals is that corresponding orthogonal signals are easy to generate. One of the methods for producing orthogonal signals is the Hadamard modulation, where orthogonal sequences are formed from a PRS (for example, any MLBS or QRBS). The PRS that acts as the original sequence is the first orthogonal binary sequence (OBS), and higher order OBS can be formed by Hadamard modulating the first OBS. In the Hadamard modulation, the Hadamard matrix is a square matrix of size $2^k \times 2^k$ that is populated by values -1 and 1, which can be formed recursively by applying

$$\mathbf{H}_{2^k} = \begin{bmatrix} \mathbf{H}_{2^{k-1}} & \mathbf{H}_{2^{k-1}} \\ \mathbf{H}_{2^{k-1}} & -\mathbf{H}_{2^{k-1}} \end{bmatrix} \quad (3.6)$$

where k is the index of Hadamard matrix. The zero-order Hadamard matrix is $\mathbf{H}_{k=0} = [1]$ from which the sequential matrices are formed. An OBS of order $k + 1$ is generated by concatenating the k^{th} order OBS (the previous orthogonal sequence) twice and performing an element-wise multiplication of vector containing the concatenated sequence and vector containing repeated k^{th} row of \mathbf{H}_k . The second-order OBS is commonly known as the inverse-repeat sequence (IRS). As the formulation of subsequent OBS requires concatenating the original sequence twice, the length of each OBS is doubled in comparison to the previous sequence.

Fig. 3.6 presents the time-domain signals and frequency spectra for two orthogonal sequences formed by the Hadamard modulation: a 31-bit-long OBS_1 and a corresponding 62-bit-long OBS_2 (where the OBS_1 is the MLBS shown in Fig. 3.3). A complete 2x2 dq-domain transfer matrix can be identified simultaneously by injecting the OBS_1 into the first input (u_d) and OBS_2 into the second input (u_q) as illustrated in Fig. 3.5. As the inputs are excited with different distinct frequencies, the corresponding responses to each input can be separated from the output signals (assuming that the system is linear). Consequently, all the transfer functions of the multivariable system are identified simultaneously.

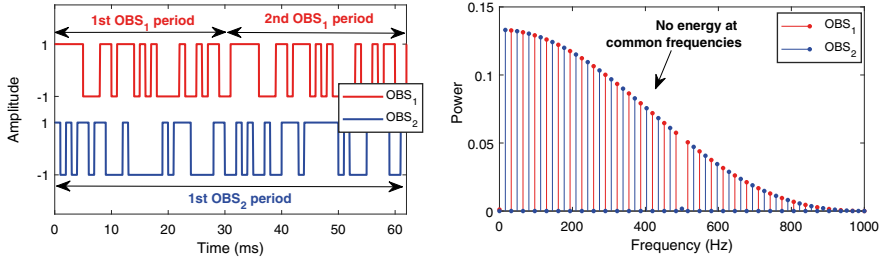


Figure 3.6 (a) Time-domain waveform and (b) frequency-domain power spectrum of OBS₁ (red) and OBS₂ (blue) signals.

3.1.3 Broadband Measurement Design

The design process of a broadband frequency-response measurement begins with specifying the measurement specification parameters. The specification parameters define the desired measurement features and consist of:

- Measurement bandwidth (f_{bw})
- Measurement duration (T_{meas})
- Frequency resolution (f_{res})
- Measurement accuracy (quantified by signal-to-noise ratio (SNR) or variance (σ^2))
- Measurement disturbance on the system under measurement

The selection of the specification parameters depends on the objective of the measurement and system characteristics. Next, the design parameters are selected based on the objective defined by the specification parameters. The design parameters are qualities of the PRS perturbation and measurement implementation that include:

- Generation frequency (f_{gen})
- Sequence length (N)
- Number of averaged periods (P)
- Perturbation amplitude (A)

As the frequency-response is typically measured on multiple frequency points, the fundamental first step is to design the frequency bandwidth (f_{bw}) and frequency resolution (f_{res}) suitable for the application. Moreover, another fundamental design parameter is the desired measurement accuracy, which depends on the objective of the measurement; in some experiments, a more crude identification accuracy is adequate, whereas some applications necessitate very high-quality measurements. However, the measurement design involves inherent

trade-offs between the measurement performance against measurement duration (T_{meas}), frequency spectrum, and injection amplitude (A) [P4].

The measurement quality can be assessed by considering the signal-to-noise ratio (SNR) of the measurement describing the ratio of a desired signal to the power of background noise in the system, given as

$$\text{SNR} = \frac{P_s}{P_n} = \frac{A_s^2}{A_n^2} \quad (3.7)$$

where P_s and P_n are the power and A_s and A_n are the amplitude of the signal and noise components, respectively. Hence, the SNR of the system perturbation can be applied to represent the noise-rejection capabilities of the measurement by comparing the power of excitation to the power of background distortions. Additionally, the measurement variance (σ^2) can be used to numerically assess the measurement performance. The variance can be calculated by comparing the measured frequency response to a known reference

$$\sigma^2 = (G_{\text{ref}}(j\omega) - G_{\text{meas}}(j\omega))^2 \quad (3.8)$$

where $G_{\text{ref}}(j\omega)$ is a known reference and $G_{\text{meas}}(j\omega)$ is the measured transfer function.

In grid-connected systems, where the frequency-response measurements are performed online, special characteristics impose constraints on the measurement design. The perturbation signal injected into the system acts as a disturbance, and consequently, pollutes the grid voltages and currents with harmonic and inter-harmonic content. Additionally, a high injection amplitude may excite the non-linear dynamics of the system and distort the measurements. Increasing the injection amplitude, however, directly improves the SNR enhancing the measurement performance. Therefore, the injection amplitude and measurement duration are especially crucial design parameters in the identification of grid-connected systems. The adverse impact of the perturbation injection on the grid can be considered directly by assessing the total harmonic distortion (THD) in currents and voltages [P4].

Perturbation signals based on PRS are deterministic and periodic, and consequently, the broadband measurements can be averaged over multiple injection periods (P), which mitigates the impact of non-periodic distortions, such as measurement noise. In logarithmic averaging procedure [84], the frequency response can be obtained by applying

$$G(j\omega) = \left(\prod_{k=1}^P \frac{Y_k(j\omega)}{U_k(j\omega)} \right)^{1/P} \quad (3.9)$$

In the method, the measurements of inputs and outputs are segmented and Fourier-transformed, after which (3.9) is applied. While averaging over multiple periods mitigates the impact of uncorrelated noise, it also increases the measurement duration proportional to P .

The transformation to frequency domain required in frequency-response measurements

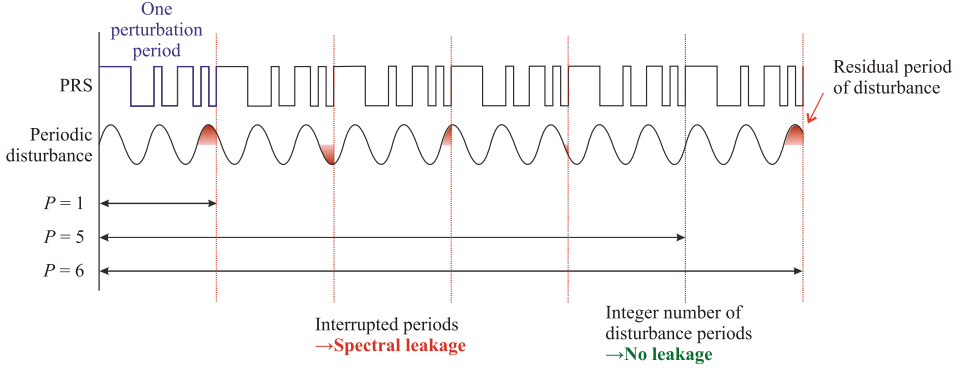


Figure 3.7 Illustration of origin of spectral leakage from periodic disturbances.

is typically performed by applying DFT, where a finite-length sampled signal is transformed into the frequency domain. In general, the DFT window length that determines the discrete frequency resolution must be synchronized with the excited frequencies in order to avoid spectral leakage that corrupts the measurements. In other words, the DFT frequency vector must include the excited frequencies. In systems with periodic disturbances, also the periodic disturbances may also cause measurement deterioration through spectral leakage. In grid-connected systems, the periodic disturbances typically are a result of the fundamental grid signals and their harmonics. Additionally, an unbalance between the three-phase voltages causes a periodic oscillation in the dq-frame signals, occurring on twice the fundamental frequency. The adverse impact of these periodic oscillations on measurement accuracy can be mitigated by designing the measurement duration so that the measurement time consists of an integer number of fundamental cycles, which mitigates the spectral leakage from periodic disturbances to the frequencies that are measured [P8].

Fig. 3.7 illustrates the measurement design where, by adjusting the number of averaged periods of perturbation, the spectral leakage from periodic disturbances is avoided. As seen from the figure, the periods of the disturbance and PRS are not equal, and as the DFT window is determined by the PRS period, many selections for the number of averaged periods result in interrupting the period of the disturbance, resulting in spectral leakage. However, the impact of spectral leakage can be minimized by selecting the DFT window so that an integer number of periods for both the PRS and periodic disturbance are captured. In the example, such a design is achieved by setting $P = 5$ (or an integer multiple of five). The spectral leakage of a periodic disturbance is reduced by minimizing the time difference (ΔT) between the measurement duration (DFT window length) and the nearest full period of the disturbance. For a PRS measurement, the time difference can be given as

$$\Delta T = \left| \frac{N}{f_{\text{gen}}} P f_p - \text{nint} \left(\frac{N}{f_{\text{gen}}} P f_p \right) \right| \frac{1}{f_p} \quad (3.10)$$

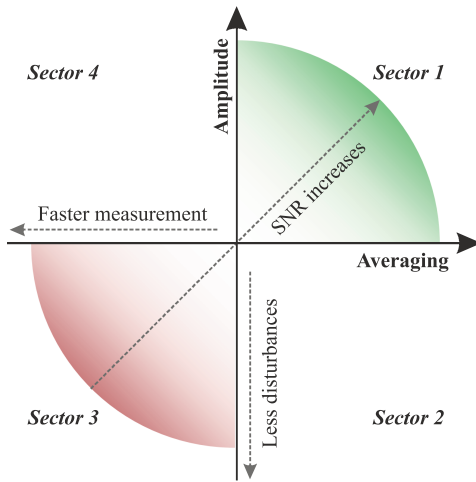


Figure 3.8 Illustration of inherent trade-offs in measurement design.

where N is the length and f_{gen} the generation frequency of the PRS, P is the number of averaged periods, f_p is the frequency of periodic distortion, and int is an operation that yields the nearest integer [P8].

As the majority of periodic disturbances in grid-connected systems are a result of the fundamental system frequency and its harmonics, it is sufficient to consider the fundamental frequency as the periodic disturbance¹. In [P8], the following design procedure is proposed to mitigate the spectral leakage in measurements on grid-connected systems:

1. Select $f_{\text{gen}} = m(2f_g)$, where m is a positive integer and f_g is the fundamental grid frequency
2. Choose $P = a(f_{\text{gen}}/f_g)$, where a is a positive integer.
3. Select N to achieve the desired frequency resolution.

Fig. 3.8 illustrates the inherent trade-offs in the measurement design of grid-connected systems. The SNR, and therefore the measurement accuracy, can be improved by increasing amplitude or number of averaged periods. However, increasing the injection amplitude increases the disturbances experienced by the remainder of the system, and increasing the number of averaged periods increases the measurement duration. Consequently, the optimal parameter selection is highly dependent on the application and desired performance. In the figure, four different sections with different emphases are identified, where example applications can be given as follows [P4]:

Section 1: High-accuracy measurement suitable for applications that require maximum accuracy, such as detailed stability analysis.

¹An integer number of fundamental cycles also means an integer number of harmonic cycles.

Section 2: Medium-accuracy measurement suitable for identification of sensitive systems, such as online power system monitoring.

Section 3: Low-accuracy measurement suitable for time-critical applications where measurement defects can be tolerated.

Section 3: Medium-accuracy measurement suitable for time-critical online applications, such as adaptive control or system protection.

3.1.4 Combined Orthogonal Sequences

While the MLBS and QRBS demonstrate many desirable characteristics, these PRS perturbations also have shortcomings. The perturbations have evenly spaced frequency resolution, and the shape of the excitation spectrum is fixed. In the impedance (admittance) measurements of grid-connected systems, the frequency range is typically wide and the frequency response exhibits drastically different magnitude in different frequency ranges. The low-frequency impedance (admittance) especially is often small and, consequently, the response to the perturbation is weak, making the SNR poor in these regions. With the PRS, the excitation spectrum cannot be focused into certain frequency ranges, as increasing the injection amplitude increases the excitation energy evenly on all frequencies.

One method to adjust the injection energy spectrum at certain frequency ranges is to apply combined orthogonal sequences (COS) [P2]. In this method several orthogonal binary sequences (OBS) are summed up to form a single perturbation. The COS can be adjusted to have different frequency resolution and different excitation amplitude in different frequency ranges. This allows the SNR to be enhanced without an increase of the injection time-domain amplitude, as the excitation energy is focused more adequately (that is, a high-power excitation is applied for the low-magnitude frequency ranges without increasing the power of excitation at the frequency ranges that already have high SNR in the system response) [P2]. Consequently, the impedance measurements performed with COS can achieve significantly higher measurement accuracy in comparison to measurements with equal-amplitude MLBS perturbation [P2].

The COS can be designed by applying the following steps (an example is shown for three OBS) [P2]:

1. Design an MLBS so that the generation frequency is twice as high as the highest frequency to be identified and choose the sequence length so that a sufficient frequency resolution is achieved for the high-frequency range. The MLBS acts as the first OBS.
2. Produce a second OBS from the MLBS and choose a lower generation frequency to target the middle-range frequencies.
3. Produce a third OBS and choose an even lower generation frequency to target the

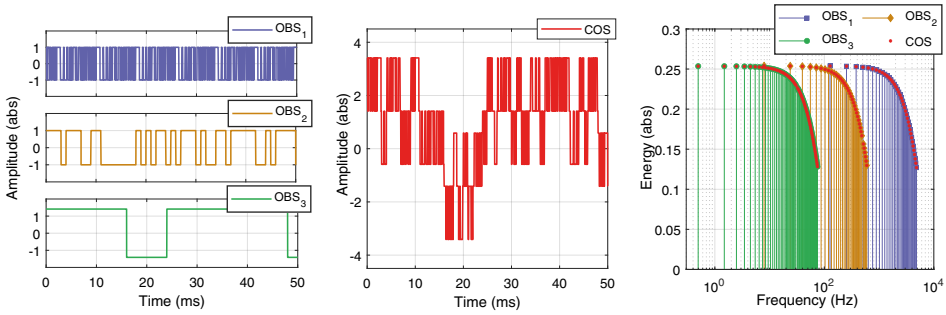


Figure 3.9 A third-order COS shown in time domain and frequency domain for both individual OBS and the COS.

low-frequency range.

4. Choose the excitation amplitude independently for each sequence based on, for example, assumed shape of impedance (admittance) under measurement or by iterative adjustments.
5. Combine the sequences by summing them up.

Fig. 3.9 presents an example implementation of a third-order COS with three OBS, where (a) shows the individual sequences in the time domain, (b) shows the COS in the time domain, and (c) shows the frequency spectral for both OBS and COS.

In order to preserve the orthogonality of the sequences, the generation frequencies must be integer multiples of each other, and each new sequence must have lower generation frequency compared to the previous sequence. The measurement duration is determined by the sequence that has the lowest generation frequency (the highest-order OBS), and the other OBSs occur for multiple periods within the total duration. As the perturbation sequence consists of multiple sequences, the excited frequencies must be chosen from the frequency vector obtained by the DFT for the frequency-response calculation. The DFT analysis can be performed as follows

1. Inject b -order COS into the system (consisting of $OBS_1, OBS_2, \dots, OBS_b$) at corresponding generation frequencies $f_{\text{gen}-1}, f_{\text{gen}-2}, \dots, f_{\text{gen}-b}$ (in descending order).
2. Measure input and output signals.
3. Perform a k -point DFT on the signals, where $k = N_b * f_s / f_{\text{gen}-h}$ where f_s is the sampling frequency and N_b is the length of the highest order OBS.
4. For the highest-order sequence (OBS_b), select the harmonics that satisfy

$$(i - 1) \bmod 2 = 0 \quad (3.11)$$

where i is the order of harmonic.

5. For the first sequence (OBS_1), select the harmonics that satisfy

$$(i - 4 * f_{\text{gen-1}}/f_{\text{gen-b}}) \bmod (4 * f_{\text{gen-1}}/f_{\text{gen-b}}) = 0 \quad (3.12)$$

6. For the remaining OBS, select the harmonics that satisfy

$$(i - 2 * f_{\text{gen-j}}/f_{\text{gen-b}}) \bmod (4 * f_{\text{gen-j}}/f_{\text{gen-b}}) = 0 \quad (3.13)$$

where j is the order of the OBS in the range from 2 to $b - 1$.

7. From each OBS, omit the harmonics above 44 % of the corresponding generation frequency (a 6 dB decrease in power).
8. Calculate the impedance from the output-to-input ratio of signals at the selected frequencies.

3.2 Stability Analysis of Multi-Parallel Converters

In a system that consists of multiple parallel converters, the converters interact with the grid impedance and, additionally, with each other. The term "parallel converters" typically refers to devices that are directly connected to the same point-of-common coupling (PCC), but it may also refer to converters that are connected into proximity with each other in the same system. In such systems, it is imperative to consider the system stability in terms of both local and global scope. Depending on the system configuration, the assessment may be impaired by limited observability of some system states that are prone to instability. Especially in impedance-based methods, the selection of measurement interfaces has a drastic impact on the obtained stability indication.

3.2.1 Aggregated Impedance-Based Stability Criterion

Fig. 3.10 presents a system of n parallel photovoltaic inverters connected to the same PCC. In such a system, assessing the stability of each inverter individually at the local interfaces is insufficient. Instead, the shared grid interface of the inverters at the PCC must be applied for the stability assessment. The shared grid interface is known as the global interface (in terms of the n parallel inverters). It should be noted that this approach assumes the interconnection impedances between the inverters to be negligible. If interconnection impedance between the converters is considerable in comparison to the grid impedance, the complexity of the analysis increases, and generalized impedance-based method cannot be derived.

The stability analysis at the global interface can be performed straightforwardly by applying impedance (admittance) aggregation for the paralleled converters [P3, P7]. The im-

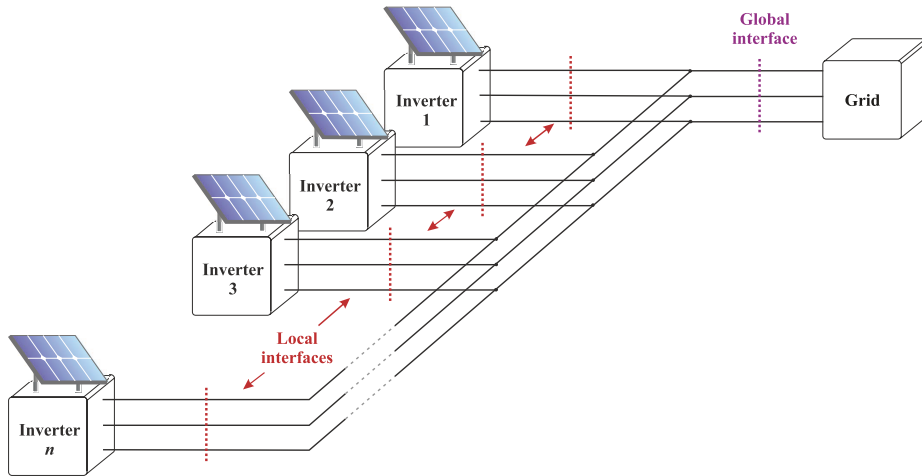


Figure 3.10 Multi-parallel grid-connected inverters in a photovoltaic plant.

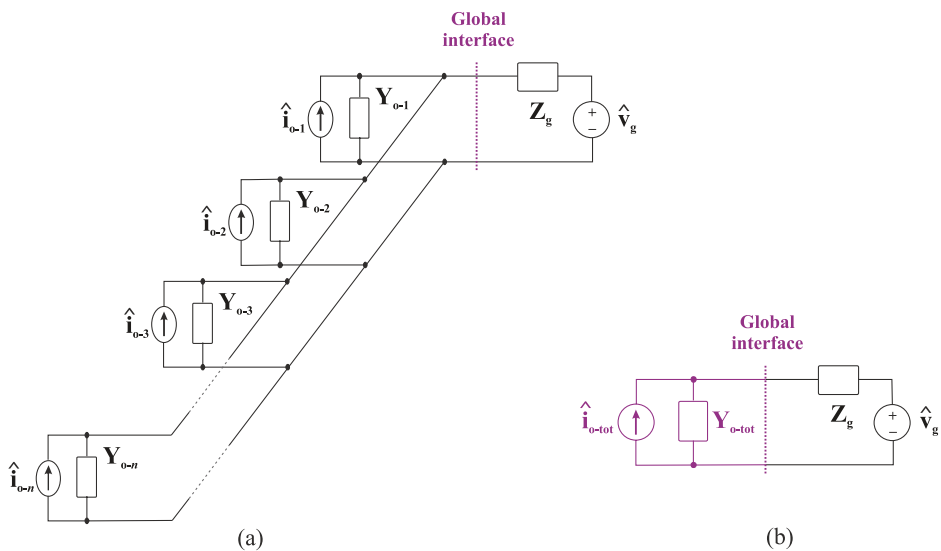


Figure 3.11 (a) Equivalent source-load circuit of parallel inverters and (b) equivalent aggregated source-load circuit.

pedance aggregation enables extending the impedance-based stability analysis from a single converter to multi-parallel converters. Fig. 3.11 (a) presents an equivalent source-load connection of multi-parallel converters as in Fig. 2.7 in Section 2.3 for a single converter. By applying circuit theory, the Norton equivalents representing the parallel sources can be combined as shown in Fig. 3.11 (b). The aggregated source admittance is given by

$$\mathbf{Y}_{o\text{-tot}} = \sum_{k=1}^n \mathbf{Y}_{o-k} \quad (3.14)$$

where \mathbf{Y}_{o-k} is the terminal output admittance of the k^{th} parallel converter [P7]. The equation is further simplified in the special case where the inverters are identical or almost identical and have equal terminal admittance of \mathbf{Y}_o for each inverter. For such a system the aggregated source admittance can be given as [P3]

$$\mathbf{Y}_{o\text{-tot}} = n \mathbf{Y}_o \quad (3.15)$$

By applying the aggregated total impedance (admittance) of the converters, the stability analysis can be performed like that of a single grid-connected converter.

A major benefit of the aggregation method is the low requirement on prior information about the system. For a system with close to identical converters, the analysis can be performed accurately by utilizing only the terminal impedance of the grid and the terminal admittance of a single converter [P3]. In case of unknown grid or converter dynamics, frequency-response measurements can be applied to extract the terminal impedance (admittance) [P3],[P7]. Consequently, the aggregation method can be applied to estimate the hosting capacity of the grid PCC for multi-parallel grid-connected converters and, therefore, to predict and mitigate the stability issues that result from the multiple parallel devices [P3].

3.2.2 Assessment of Stability Margins

The stability margin describes system robustness by quantifying the proximity of instability, which is essential in system design. Although the impedance-based stability analysis has many favorable features, it requires auxiliary methods to quantify the system stability margins. This thesis presents methods for quantifying the system stability margins from terminal impedance data.

Impedance-Based Sensitivity Function

The sensitivity function approach is an extension to the forbidden region method [203], [204], where a graphical analysis based on the Nyquist contours and restricted areas of the complex plane is applied. The sensitivity function has been proposed for single-input single-

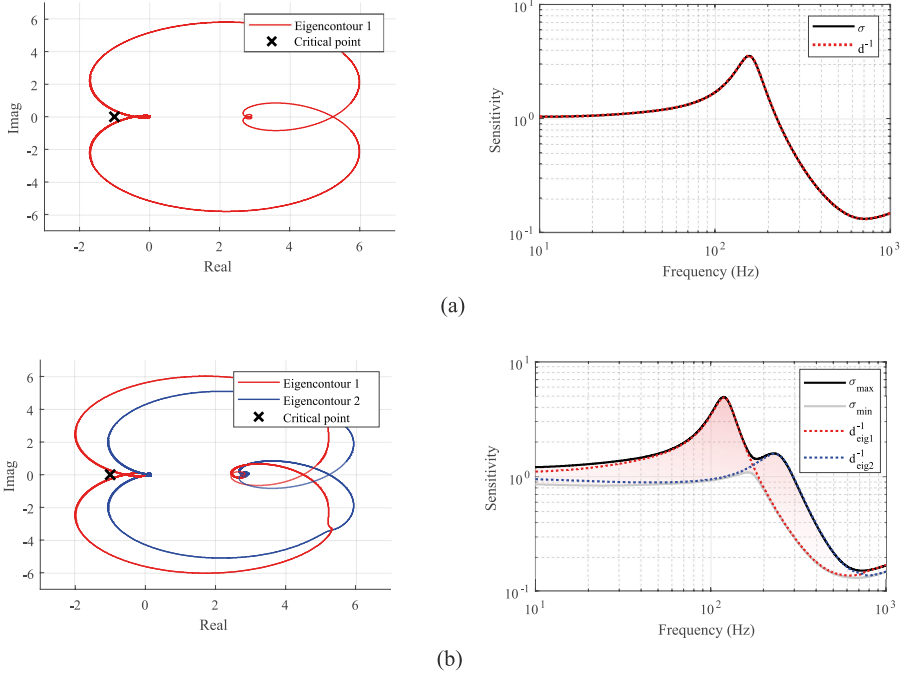


Figure 3.12 Nyquist diagram (left) and sensitivity function (right) for (a) SISO system and (b) MIMO system.

output (SISO) systems in [147], [148], where the sensitivity function is equal to the distance between the Nyquist contour and the critical point $(-1, 0)$. However, the method cannot be directly applied for MIMO systems, as such systems produce multiple eigencontours in the complex plan. The work in [P7] proposes an impedance-based sensitivity criterion for MIMO system, which formulates a sensitivity function from the singular value decomposition (SVD) of the closed-loop minor loop gain. The impedance-based sensitivity function of a multivariable system is the upper singular value obtained by

$$\sigma_{\max} = \overline{\text{SVD}}((\mathbf{I} + \mathbf{L})^{-1}) \quad (3.16)$$

where \mathbf{I} is a 2×2 identity matrix, \mathbf{L} is the minor loop gain ($\mathbf{L} = \mathbf{Y}_o \mathbf{Z}_g$), and $\overline{\text{SVD}}$ denotes the maximum singular value calculation [P7].

The sensitivity function describes the maximum disturbance amplification of the system and, consequently, the system robustness. However, the sensitivity function is an auxiliary method that does not indicate the absolute stability. Therefore, a method such as generalized Nyquist criterion (GNC) must be applied prior to applying the sensitivity function to determine the stability of the system. Fig. 3.12 illustrates the equivalence between the (generalized) Nyquist diagram and sensitivity function for stable example SISO and MIMO systems.

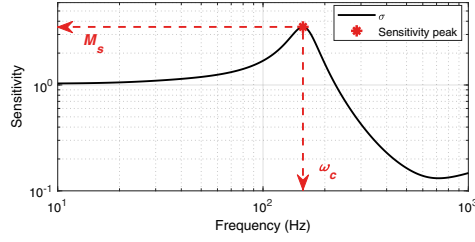


Figure 3.13 Parameter extraction from the sensitivity peak of a SISO sensitivity function.

For both systems, the equivalence can be demonstrated by calculating the reciprocal of the distance between a point in an eigencontour and critical point (d^{-1}) and by calculating the singular value(s) (σ) given as (3.16). A SISO system is represented by a single eigencontour and singular value, whereas MIMO systems are represented by two eigencontours and upper and lower singular values (σ_{\max} and σ_{\min} , respectively). In SISO systems, the singular value and reciprocal of the distance are equal and, consequently, the sensitivity function can be directly obtained by assessing the proximity of the eigencontour to the critical point. However, the analysis is not as straightforward for MIMO systems. For a 2x2 MIMO system, the reciprocal of distance can be calculated for both eigencontours (d_{eig1}^{-1} and d_{eig2}^{-1}) like that of SISO systems. However, these values represent the direction-dependent sensitivities, and the main interest typically lies in the *worst-case sensitivity* of the system². The worst-case sensitivity is equal to the upper singular value (σ_{\max}) obtained (3.16), which consequently represents the MIMO system sensitivity function.

Estimation of System Damping Factor

The work in [P6] proposes a method for estimation of the system damping factor from the terminal impedance data. In the method, a sensitivity function is calculated from the grid impedance and inverter output admittance of the critical channel³. Moreover, the frequency (ω_c) and magnitude (M_s) of the sensitivity peak (that is, the maximum sensitivity) are identified as shown in Fig. 3.13. The corresponding minimum phase margin, is calculated by applying

$$\Phi_m = 2\text{asin}\left(\frac{1}{2M_s}\right) \quad (3.17)$$

which yields the minimum for the phase margin of the Nyquist contour by assuming that the closest point from the Nyquist contour to the critical point is the point where the contour

²Often, the sensitivity peak is dominated by one of the eigenvalues, and applying distance-based assessment as for SISO systems produces only a small error. However, this is not always the case, and therefore, the SVD-based approach should be applied.

³The method assumes that a critical channel can be identified. For grid-connected inverters, the critical channel is often the q-channel due to PLL interactions [151].

breaches the unity circle [P6]. Consequently, the method yields the worst-case damping, and the actual system may have a slightly higher phase margin. From the obtained minimum phase margin, the system damping ratio (ζ) can be obtained by solving

$$\Phi_m = \text{atan}\left(2 \frac{\zeta}{\sqrt{-2\zeta^2 + \sqrt{1 + 4\zeta^4}}}\right) \quad (3.18)$$

which can be approximated by $\zeta = 0.01\Phi_m$ when $\Phi_m < \pi/3$ [P6]. Moreover, the natural resonant frequency of the system can be obtained as

$$\omega_n = \frac{\omega_c}{\sqrt{1 - \zeta^2}} \quad (3.19)$$

The critical damping ratio and natural resonant frequency can be applied in intuitive quantification of system stability. Moreover, the critical system dynamics can be approximated with a general second-order transfer function

$$G_{\text{est}}(s) = \frac{\omega_n^2}{s^2 + 2\zeta\omega_n s + \omega_n^2} \quad (3.20)$$

Pole-Zero Fitting

Another approach for assessing the stability margins is through transfer-function fitting and pole-zero analysis [205]–[207]. In [P7], the transfer-function fitting was performed on the closed-loop minor loop gain $(\mathbf{I} + \mathbf{Y}_o \mathbf{Z}_g)^{-1}$, where the grid impedance \mathbf{Z}_g and aggregated converter terminal admittance \mathbf{Y}_o was identified with frequency-response measurements. The stability was assessed by examining the closed-loop poles of the system terminal impedances. A similar approach was taken in [P3], where closed-loop poles were extracted by fitting a transfer function on the closed-loop minor loop gain. The closed-loop poles both address the absolute stability of the system and indicate the system stability margins, where the damping factor and natural resonant frequency can be given as

$$\zeta = \frac{\Re\{p\}}{|p|} \quad (3.21)$$

$$\omega_n = |p| \quad (3.22)$$

where p is a complex pole and $\Re\{p\}$ is the real part of the pole.

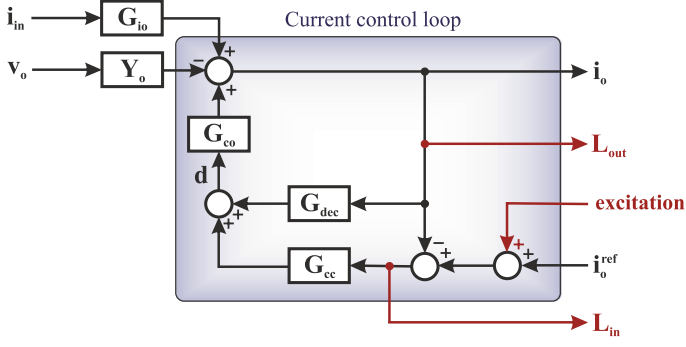


Figure 3.15 Block diagram of an online current controller loop gain measurement.

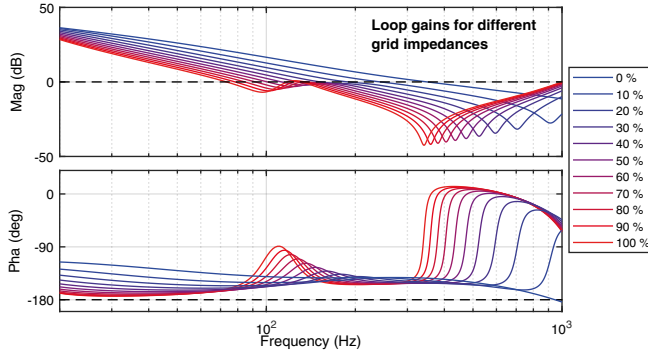


Figure 3.16 Illustration of load effect on current control loop for grid impedance varying from 0 to 100 %.

and the loop frequency response is obtained from the input (L_{in}) and output (L_{out}) signals.

The transfer function from the control signal to output current (G_{co}) is the plant for the current controller. As discussed in Section II, the grid impedance affects the open-loop transfer functions through the load effect. By comparing equations (2.18) and (2.20), the load-affected control-to-output transfer function can be written as

$$G_{co}^L = G_{co} [I + Y_o Z_g]^{-1} \quad (3.24)$$

and consequently, the impedance-based interaction between the inverter and the grid is incorporated into the current control loop. Moreover, the impact of other control loops is incorporated into the innermost loop through the closed-loop system dynamics (the other control loops affect the output admittance of the inverter, which affects impedance-based interaction in the load effect). Fig. 3.16 illustrates the impact of grid impedance on the load-affected current control loop, where the increasing grid impedance simultaneously decreases the control bandwidth and phase margin [P5].

troller (Injection point), and the frequency responses are obtained from the measurements shown in red: voltage vector $\mathbf{v} = [v_d, v_q]^T$, input current vector $\mathbf{i}_{in} = [i_{in-d}, i_{in-q}]^T$, and actual current vector $\mathbf{i}_o = [i_d, i_q]^T$. The load-affected current controller loop gain is extracted by considering the input current vector \mathbf{i}_{in} as the system input and actual current vector \mathbf{i}_o as the system output, whereas for the impedance measurements, the input vector is the actual current vector \mathbf{i}_o and output vector is the resulting voltage vector \mathbf{v} . Therefore, the measurements are obtained simultaneously with only one injection.

4 EXPERIMENTS

This chapter presents the implementation and experimental results of the proposed methods. The first section introduces three experimental setups that are applied in the experimental validation of the proposed methods. The experiments are divided into three sections: broadband measurement methods; broadband stability analysis; and stability analysis of parallel converters. The experiments can be summarized as follows.

Broadband Impedance Measurements

The first set of experiments focuses on the characteristics and performance of broadband frequency-response measurements performed on power-electronic systems in the synchronous reference frame. The experiments present validation for the design methods introduced in Section 3.

Experiment 1: Averaging Design of Broadband Measurement [P8]

The work in [P8] presents a method for designing the number of averaged PRS periods in an impedance measurement to minimize the measurement performance degradation that results from periodic disturbances in the grid signals. The method mitigates the effect of unbalance and harmonics in grid voltages and currents by designing the measurement duration so that the spectral leakage is avoided [P8]. The performance of the method is verified by experimental impedance measurements under unbalanced and distorted grid conditions.

Experiment 2: Amplitude Design of Broadband Perturbation [P4]

The detrimental impact of online impedance measurement of a grid-connected device on the remainder of the grid is discussed in [P4], where the grid-side disturbance is quantified by the total-harmonic distortion (THD) in grid voltages and currents. Moreover, [P4] proposes a method for selecting the amplitude of a broadband PRS perturbation and number of averaged periods with respect to measurement accuracy and grid disturbance. The experimental impedance measurements validate the proposed methodology.

Experiment 3: Combined Orthogonal Sequences [P2]

Broadband frequency-response measurements are performed for grid impedance and terminal admittance of a grid-connected inverter by applying an MLBS perturbation and the proposed combined orthogonal sequence (COS) perturbation [P2]. The results illustrate the enhanced measurement performance of the COS resulting from the improved excitation spectrum [P2].

Broadband Stability Analysis

The second set of experiments validates the performance of the proposed stability analysis methods based on online loop-gain measurement and stability margin quantification.

Experiment 4: Load-Affected Control Loop Analysis [P5]

The stability assessment of a grid-connected converter based on online measurement of the load-affected innermost control loop, proposed in [P5], is verified by measurements in this experiment. First, simulation results illustrate how the loop measurements can be applied to predict the control robustness. Then, experimental results validate the applicability of the load-affected loop gain analysis.

Experiment 5: Impedance-Based Sensitivity Function [P6]

In this experiment, the stability margin quantification through impedance-based sensitivity function is validated. The impedance-based sensitivity function is shown to predict the robustness of a grid-connected inverter, which is described by systemic damping factor and critical oscillation frequency [P6]. The sensitivity function is derived by experimental terminal impedance measurements performed with a quadratic-residue binary sequence (QRBS) injection [P6].

Stability Analysis of Parallel Converters

The third set of experiments implement the proposed methods in the stability assessment of multi-parallel converters. In the experiments, the stability analysis is performed by applying broadband impedance and loop gain measurements, and the accuracy is validated by step response tests and waveform assessment.

Experiment 6: Impedance Aggregation [P7]

Experimental terminal impedance measurements are applied to verify the impedance aggregation method [P7]. The stability of multi-parallel converters is assessed based on the aggregation method, and the decrease in stability margins resulting from more parallel devices is illustrated.

Experiment 7: Hosting Capacity Analysis [P3]

In the experiment, terminal admittance measurements of a single-phase grid-connected rectifier are applied to facilitate aggregated impedance-based stability assessment of multi-parallel power-supplying units [P3]. The experiments accurately predict the instability event that occurred in a data center when 96 equivalent PSUs were connected in parallel [P3].

Experiment 8: Real-Time Broadband Stability Analysis [P1]

The last experiment presents a real-time implementation of the methods discussed in this thesis by applying a power hardware-in-the-loop (PHIL) setup. The methods are shown to be capable of predicting the impedance-based interactions for parallel inverters by applying online measurements [P1]. In addition, the experiments demonstrate the proposed method for simultaneous loop and impedance measurements [P1].

4.1 Experimental Setups

The experiments section of this thesis is performed by applying three different experimental setups:

Experimental setup 1 is a scaled-down (2.7 kVA) prototype of a grid-connected three-phase photovoltaic inverter.

Experimental setup 2 is a high-power (200 kVA) setup consisting of multiple parallel amplifiers that are set to emulate parallel inverters and an AC grid.

Experimental setup 3 is an admittance measurement setup for a grid-connected rectifier (2.4 kVA).

The first two experimental setups are power hardware-in-the-loop (PHIL) setups where actual hardware is (partially) controlled within a real-time simulation. The third setup consists of hardware source and load to enable the terminal admittance measurements in varying operation points.

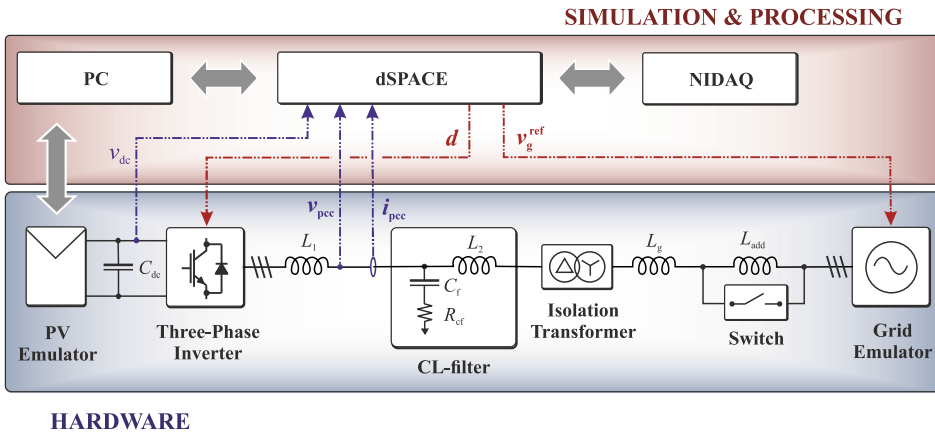


Figure 4.1 Experimental power hardware-in-the-loop setup 1.

4.1.1 Experimental Setup 1

The experimental verification of the measurement and analysis methods for a three-phase grid-connected inverter are performed with a 2.7 kVA PHIL setup as shown in Fig. 4.1. The setup consists of

- a three-phase linear voltage amplifier (*Spitzenberger & Spies PAC 15000*) that acts as a grid emulator
- a three-phase inverter with insulated-gate bipolar-transistor switches (*Myway Plus MWINV-9R144*)
- a photovoltaic emulator (*Spitzenberger & Spies PVS 7000*) that provides the DC power for the inverter
- an isolation transformer between the grid emulator and the inverter
- passive components including an external CL-filter and inductors that act as the grid impedance.

The inverter and grid emulator are controlled within a real-time simulation (dSPACE) in order to enable rapid prototyping of identification and control schemes on real hardware. In some of the identification methods, a data-acquisition card (NIDAQ USB-3636) is utilized to record measured signals. Fig. 4.2 presents a photograph of the experimental setup.

The experimental setup operates with nominal power of 2.7 kVA with 120 V fundamental voltage and 60 Hz fundamental grid frequency. The controller parameters and passive component configuration both change experiment-to-experiment. The fixed parameters are given in Table 4.1.

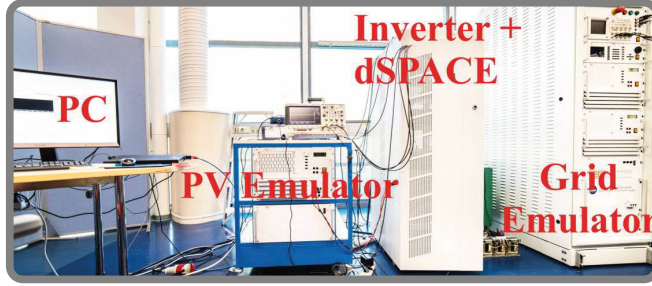


Figure 4.2 Photograph of Experimental Setup 1.

Table 4.1 Parameters of Experimental Setup 1.

Parameter	Symbol	Value
Grid frequency	f_g	60 Hz
Grid phase voltage	V_g	120 V
Inverter nominal power	S_n	2.7 kVA
Switching frequency	f_{sw}	8 kHz
Power factor	$\cos\phi$	1.0
Switching deadtime	T_{dt}	4.0 μs
DC voltage	V_{dc}	414.3 V
DC input current	I_{dc}	6.577 A
DC capacitor capacitance	C_{dc}	1.5 mF
L-filter inductance	L	2.2 mH
L-filter resistance	R_L	100 m Ω
CL-filter inductance	L_2	0.6 mH
CL-filter resistance	R_{L2}	40 m Ω
CL-filter capacitance	C_f	10 μF
CL-filter damping resistance	R_d	1.8 Ω
Transformer inductance	L_{tf}	0.3 mH
Transformer resistance	R_{tf}	400 m Ω

4.1.2 Experimental Setup 2

The experiments on parallel inverters were performed with a high-power (200 kVA) PHIL setup at DNV GL Flexible Power Grid Lab. Fig. 4.3 presents the overview of the laboratory setup configuration. The setup is powered by a 200 kVA power amplifier that is fed from a 10 kV grid through an input filter, which connects to the common DC-link of four 50 kVA power amplifiers that are capable of bidirectional power flow. The power amplifiers are controlled by an OPAL-RT real-time simulator that enables rapid prototyping of control and identification schemes. Moreover, the power amplifiers consist of six parallel half-bridge converters with an equivalent switching frequency of 125 kHz resulting in 5 kHz closed-loop

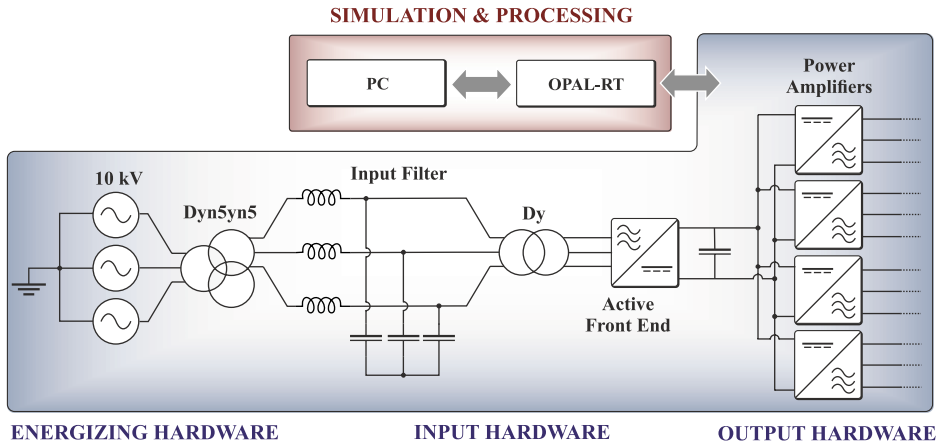


Figure 4.3 Power hardware-in-the-loop setup at DVN GL Flexible Power Grid Lab (Experimental Setup 2).

bandwidth. Consequently, the amplifiers can be set to emulate the grid connection of multi-parallel converters, where a single amplifier acts as a grid and others emulate three-phase inverters (as shown in detail in [208]). Passive components, such as inductors, can be placed in between the amplifiers to act as filters or to emulate the grid impedance.

4.1.3 Experimental Setup 3

The third experimental setup applied in [P3] facilitates the terminal admittance measurement of a 2.4 kVA power-supplying unit (PSU), which is a single-phase grid-connected rectifier. The measurement setup uses largely the same hardware as Experimental Setup 1. Fig. 4.4 presents an overview of Experimental Setup 3, which consists of the grid emulator (*Spitzenberger & Spiess PAC 15000*), the PSU, and an adjustable resistive DC power load. The grid emulator provides 230V/50Hz single-phase voltage, providing the input power source for the rectifier unit. In order to measure the rectifier in varying loading state, a modular resistive power sink is connected to the output side that has nominal voltage of 12.5 V. Fig. 4.5 presents a photograph of the PSU connected to the load. The passive load unit consists of 10 parallel ceramic power resistors ($R = 0.8 \Omega$) each rated for 300 W power dissipation. With the 12.5 V output voltage, each resistor consumes 200 W, and consequently, the load can be operated in the power range of 200 to 2000 W. As a result, the terminal admittance measurements can be performed over a wide loading range up to 80 % of nominal power, which is assumed to be the typical loading state.

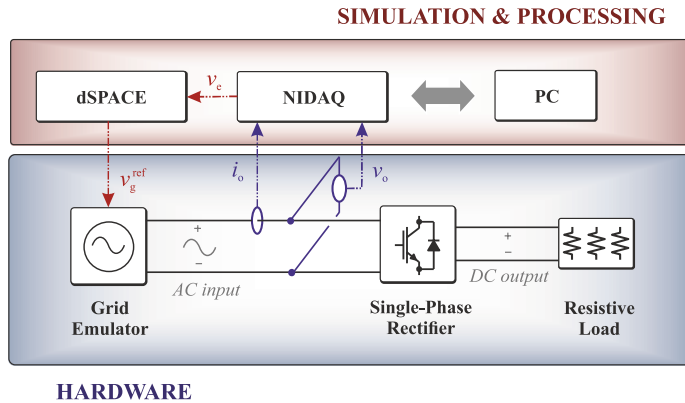


Figure 4.4 Experimental setup for measuring the terminal admittance of a single-phase rectifier (Experimental Setup 3).



Figure 4.5 Photograph of the adjustable passive load in Experimental Setup 3.

4.2 Broadband Impedance Measurements

4.2.1 Experiment 1: Averaging Design of Broadband Measurement [P8]

Fig. 4.6 presents a broadband measurement configuration for measuring the multivariable grid impedance as seen by a grid-connected three-phase inverter, where the lower part of the schematic (grey) is the control structure of the inverter and the upper part (blue) is the signal processing for the impedance identification. The excitation injection is highlighted in red, where two uncorrelated perturbation signals (OBS_1 and OBS_2) are injected into the current references (\hat{i}_{dq-ref}) [P8]. Consequently, the inverter produces the perturbations in its output

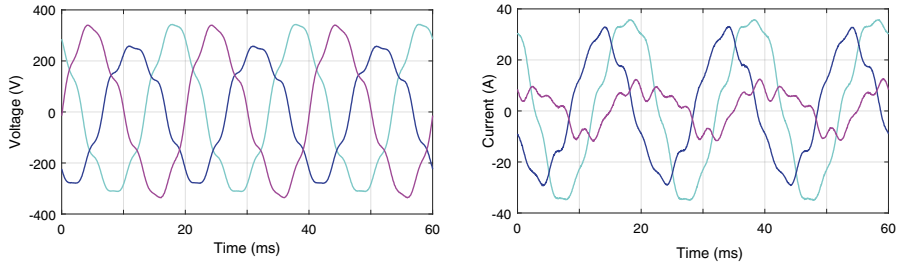


Figure 4.7 Distorted grid currents and voltages during nominal operation without perturbation injection.

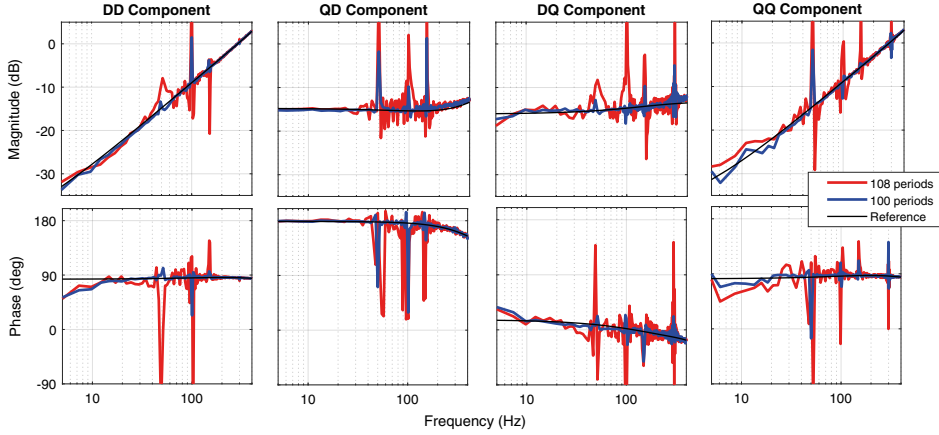


Figure 4.8 Grid impedance measurements by applying 100 averaged periods (blue) and 108 averaged periods (red).

sequence component exists in 2nd and 7th harmonic (100 and 350 Hz) and a 5 % negative sequence component exists in 2nd and 5th harmonic (100 and 250 Hz). In the dq-frame rotating at 50 Hz, periodic oscillations occur at 50, 100, 150, and 300 Hz. Fig. 4.7 presents the distorted grid waveforms during nominal system operation before the perturbation injection is enabled.

The identification is performed by injecting two uncorrelated sequences, OBS_1 and OBS_2 , into the system. OBS_1 is a 2047-bit-long MLBS injected into the d-channel, and OBS_2 is 4094-bit-long sequence produced by applying Hadamard modulation and injected into the q-channel. Both sequences are generated at 5 kHz and the measurement frequency resolution is consequently 2.44 Hz. The currents and voltages are dq-transformed into the synchronous reference frame produced by the slow measurement PLL, and the signals are captured by a measurement card (NI USB-6363).

Fig. 4.8 presents the complete multivariable grid impedance measurements that are obtained by applying different number of averaged perturbation periods. The measurement averaged over $P = 100$ periods (blue) is designed by applying the proposed method, where the spectral leakage from periodic oscillations is mitigated by selecting P in a manner that

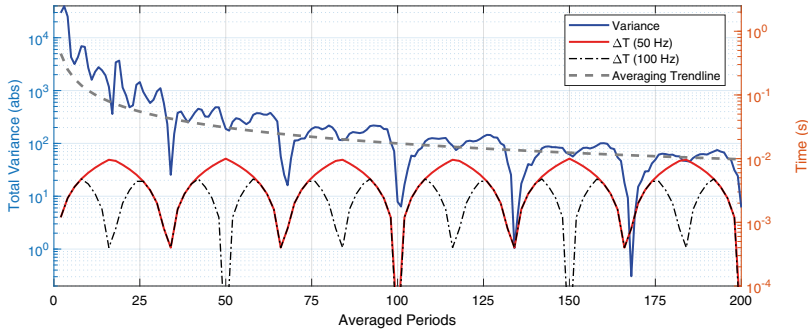


Figure 4.9 Total measurement variance as a function of number of averaged periods.

the measurement window encompasses an integer number of fundamental periods (and thus also an integer number of harmonic periods). Another design is presented ($P = 108$, red line) for comparison, where the number of averaged periods is increased, thereby increasing the measurement SNR. However, this design does not comply with the proposed design method of including the integer number of fundamental periods, and consequently a significant spectral leakage occurs from the periodic disturbances. As a result, the measurement performance is greatly deteriorated.

A more comprehensive test was performed by performing a high-duration measurement with $P = 200$ and separating the obtained signals into different length data sets. Consequently, the frequency-response calculation could be performed by applying a wide range of averaged periods, $P = 2 : 2 : 200$. A data set with corresponding length is selected for each P ; for example, calculation with $P = 10$ utilizes the first 10 periods of the measured signals (1/20 of the complete data set). From each obtained impedance, the total measurement variation (sum of variance of all four components) is calculated. Fig. 4.9 presents the total variation (blue), an averaging trendline (grey), and the time differences (3.10) to the nearest integer period of fundamental frequency (red) and second harmonic (black). As seen from the figure, the measurement performance gradually increases along with the averaging trendline as the number of averaged periods increases. However, the measurement performance also clearly exhibits a pattern of repeating local minimums simultaneously with the minimums of the time difference to the nearest fundamental period, where the spectral leakage from the periodic disturbances is mitigated. Therefore, it is highly beneficial to select the number of averaged periods to match the local minimums instead of arbitrarily increasing the number of averaged periods. Such design can be achieved by complying with the design method presented in Section 3.1.3 [P8].

The impact of spectral leakage on variance (measurement accuracy) is further illustrated by comparing the variance of three measurements with a different number of averaged periods. Fig. 4.10 presents the measurement variance of three measurements:

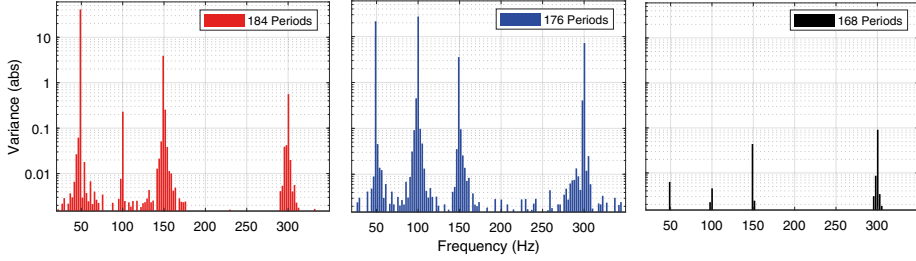


Figure 4.10 Measurement variance spectrum with varying measurement designs.

- $P = 168$ (black) selected to the local minimum of time difference to the nearest fundamental period.
- $P = 184$ (red) selected to the local minimum of time difference to the nearest second harmonic period.
- $P = 176$ (blue) selected from between the other measurements without consideration of spectral leakage.

As seen from the figure, the measurement with $P = 176$ (blue) has the highest measurement variance (i.e. the poorest measurement accuracy), as the spectral leakage is not considered. The measurement with $P = 184$ (red) is selected to the local minimum of time difference to 100 Hz (dashed black line in Fig. 4.9) and it mitigates the spectral leakage from the second harmonic and its integer multiples (100 Hz, 200 Hz, 300 Hz, ...), and consequently the measurement variance is smaller in comparison to $P = 176$ around the periodic disturbances at 100 and 300 Hz. Lastly, the measurement with $P = 168$ is designed in accordance with the presented method by selecting the number of averaged periods to the local minimum of time difference to 50 Hz (red line in Fig. 4.9). With the proposed design, the spectral leakage is mitigated from all the periodic oscillations resulting from the unbalance and grid harmonics, and therefore the measurement performance is drastically improved.

4.2.2 Experiment 2: Amplitude Design of Broadband Perturbation [P4]

The experiments on the amplitude design of broadband perturbation injection are performed with Experimental Setup 1. A similar system configuration is applied as in Experiment 1, where a grid-connected inverter is applied in the grid impedance measurements. The experiments were performed for grids of various strength, as characterized by the short-circuit ratio (SCR), and special interest was placed on the impact of perturbation injection on the quality of grid currents and voltages [P4]. Moreover, the effect of perturbation amplitude on the achieved measurement performance is presented.

The measurements are performed with an MLBS excitation, where the injection ampli-

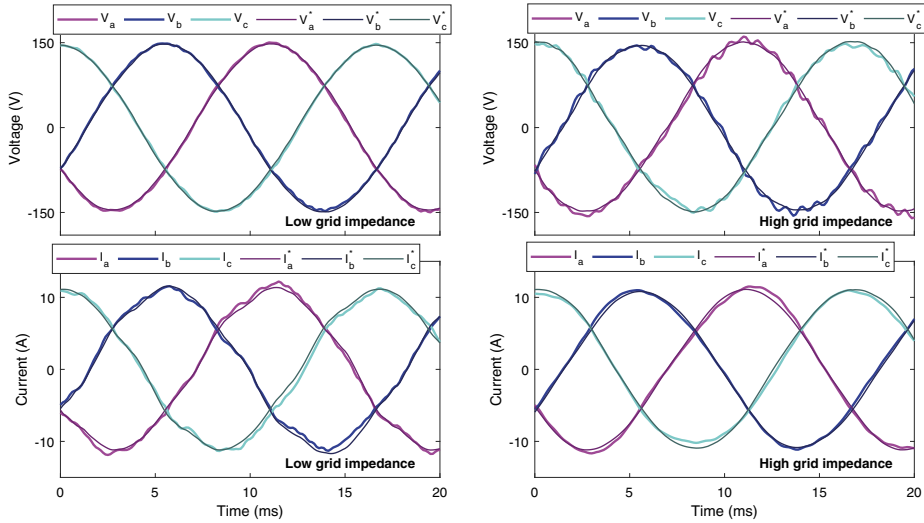


Figure 4.11 Three-phase currents and voltages with and without perturbation in low impedance and high impedance grids.

tude was varied between 0.5 and 5 % of the nominal inverter output current. The multivariable impedance is identified by applying sequential measurements, where the perturbation is injected first into the d-channel to obtain the impedance dd- and dq-components, and then into the q-channel to obtain the impedance qd- and qq-components¹.

Fig. 4.11 presents the unperturbed (denoted with *) and perturbed grid currents and voltages with a 5 % injection amplitude during the measurement of a low impedance grid (SCR= 22) and high impedance grid (SCR= 3.9). The waveforms demonstrate the effect of a current perturbation on the grid, where the perturbation pollutes the fundamental grid components with distortions and increases the total harmonic distortion (THD) in currents and voltages. Moreover, the grid strength determines the way the distortions are divided into currents and voltages: in low impedance grids, the voltage response is weak and the distortions are weighted towards the currents; whereas in high impedance grids, the impedance acts as a filtering component for the currents while the voltage response is strengthened and more distorted [P4]. Table 4.2 presents the measured THD from the grid currents and voltages for varying perturbation injection amplitudes in grids of different strength.

Fig. 4.12 presents the measurement variance as a function of the number of averaged periods for different perturbation amplitudes (like in Section 4.2.1). For all the experiments, the measurement accuracy increases along with the number of averaged periods. However, a low injection amplitude cannot be fully compensated by increasing the measurement averaging, as demonstrated by drastic improvement in measurement performance when the injection

¹The impedance calculation is performed through calculating the impedance matrix by applying two independent measurements.

Table 4.2 Measured THD values of currents and voltages with varying perturbation injection amplitude.

	Injection amplitude					
	0.0 %	0.5 %	1.0 %	3.0 %	5.0 %	
SCR = 22	5.41 %	5.42 %	5.47 %	6.03 %	7.03 %	Current
SCR = 7.1	2.91 %	2.90 %	2.96 %	3.50 %	4.41 %	
SCR = 3.9	2.15 %	2.15 %	2.19 %	2.70 %	3.54 %	
SCR = 22	1.17 %	0.99 %	1.11 %	1.42 %	1.29 %	Voltage
SCR = 7.1	2.02 %	1.94 %	2.05 %	2.33 %	3.21 %	
SCR = 3.9	2.38 %	2.45 %	2.17 %	2.99 %	3.74 %	

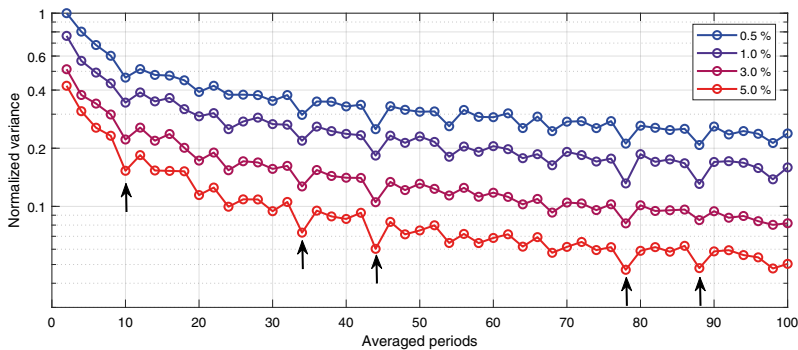


Figure 4.12 Total measurement variance as a function of the number of averaged periods for different perturbation injection amplitudes.

amplitude is increased [P4]. For example, achieving normalized variance of 0.3 (although normalized variance is non-descriptive, it allows easy comparison of performance) requires approximately:

- 4 measurement periods for 5.0 % injection amplitude
- 8 measurement periods for 3.0 % injection amplitude
- 20 measurement periods for 1.0 % injection amplitude
- 34 measurement periods for 0.5 % injection amplitude²

The measurement variance also exhibits distinct numbers of averaged periods where the variance is significantly lower (at 10, 34, 44, 78, 88), as illustrated by arrows in the figure. These designs correspond to the design proposed for minimizing the spectral leakage presented in

²If the effect of minimized spectral leakage is taken into account. If this effect is omitted and only the measurement SNR is compared, achieving similar accuracy takes 50 measurement periods.

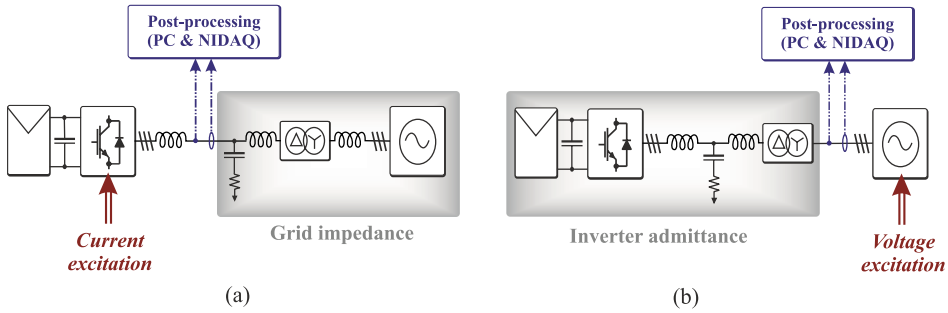


Figure 4.13 Measurement configuration for (a) grid impedance measurements and (b) terminal admittance measurements.

Section 3.1.3 and experimentally verified in Section 4.2.1.³

The perturbation amplitude design of a broadband measurement depends on multiple parameters, such as system sensitivity, desired measurement accuracy, and desired measurement duration. Consequently, the design involves multiple trade-offs that must be weighted for each case.

4.2.3 Experiment 3: Combined Orthogonal Sequences [P2]

The performance of the impedance measurements achieved by applying combined orthogonal sequences (COS) is experimentally verified through impedance measurements with Experimental Setup 1 [P2]. In the experiments, the impedance measurements are performed by applying both the proposed COS perturbation and an MLBS perturbation, thereby enabling comparison of measurement performance. Fig. 4.13 presents the experimental configuration where (a) grid impedance is measured by applying a current injection from the inverter and (b) terminal admittance is measured by applying a voltage excitation from the grid emulator.

The terminal admittance measurements are performed by applying both the conventional MLBS and the COS [P2]. The perturbations are designed to have an equal bandwidth, measurement duration, and time-domain injection amplitude. Moreover, the low-frequency resolution is designed to be equal. Due to the characteristics of the orthogonal sequences in COS, the MLBS is averaged over two periods for each COS period to achieve equal measurement duration. The measurements are performed by superimposing a voltage-type perturbation into the grid voltage references of the grid emulator during normal operation, and the results are shown for the admittance d-component. The total terminal admittance is assumed to have multiple resonant peaks resulting from the passive LCL-components and the

³It should be noted that the spectral leakage mitigation is considerably more difficult for systems that have fundamental frequency of 60 Hz as opposed to 50 Hz systems, as the fundamental period involves a recurring decimal $1/60 \text{ Hz} = 16.\bar{6} \text{ ms}$.

Table 4.3 Sequence parameters for terminal admittance measurements with MLBS and COS.

	N	f_{gen} (Hz)	A (V)	f_{res} (Hz)	P	T_m (s)
OBS ₁	63	4000	0.1	63.5	128	2.016
OBS ₂	126	500	0.2	7.94	8	2.016
OBS ₃	252	125	0.7	0.99	1	2.016
COS	411	125..4000	1	0.99..64	1	2.016
MLBS	4095	4000	1	0.98	2	2.048

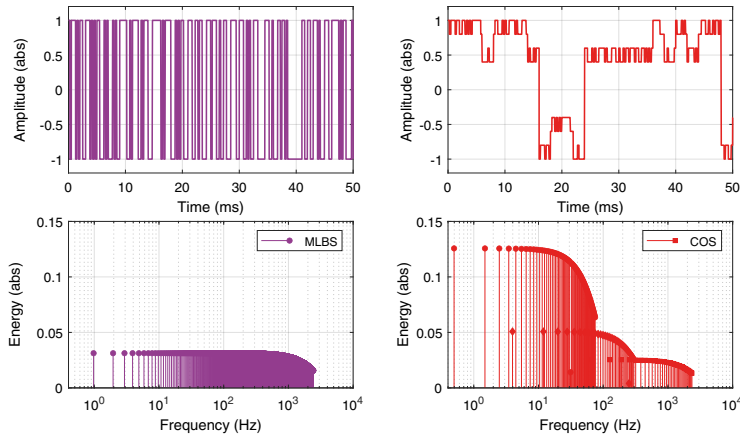


Figure 4.14 Time domain waveform and frequency domain spectrum for the MLBS (purple) and the COS (red) designed for admittance measurement.

inverter's control loops and, consequently, a fine measurement resolution is also required in the low frequency range. Consequently, the COS is designed to consist of three orthogonal sequences in order to achieve sufficient frequency resolution and excitation energy over a wide frequency range. As the low-frequency characteristics are often more challenging to identify accurately, the majority of the COS perturbation energy is directed towards the low frequencies by setting the amplitude of the highest-order OBS to the highest. Table 4.3 summarizes the signal parameters for each OBS individually, the resulting COS, and the conventional MLBS.

Fig. 4.14 presents the time domain waveforms and energy spectra of the applied perturbations. As seen from the figure, the COS is designed to have significantly more energy in the specific frequencies in comparison to the MLBS when the time-domain amplitudes are designed to be equal. Fig. 4.15 shows the measured terminal admittance of the system when both the MLBS and the COS are applied as the excitation perturbation, along with the analytically obtained admittance as a reference. The results show the enhanced measurement accuracy when using the proposed COS, as the measurement follows the reference more

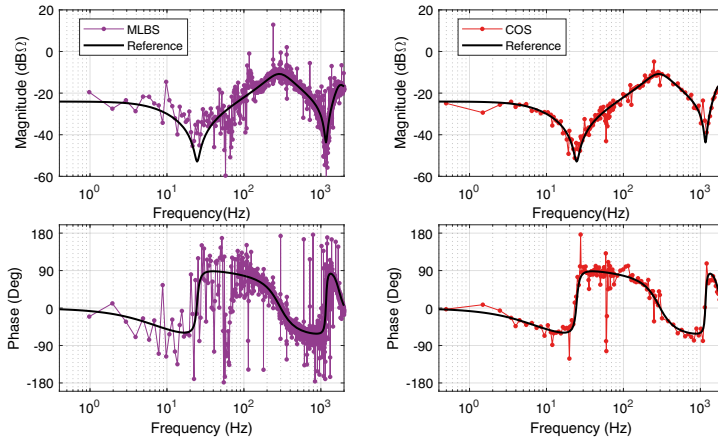


Figure 4.15 Terminal admittance measurement by applying the MLBS (purple) and the COS (red).

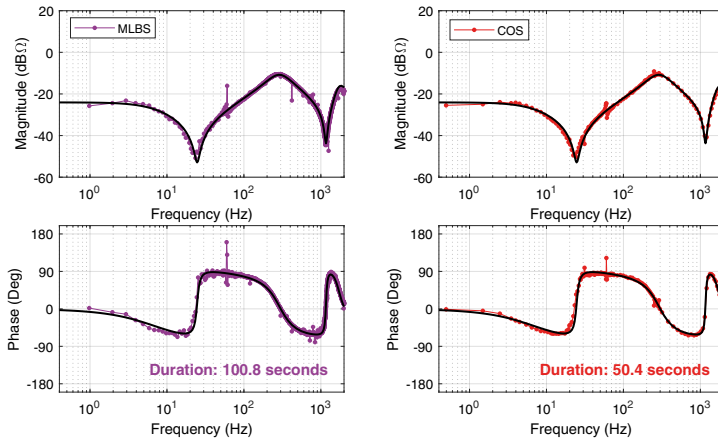


Figure 4.16 Long duration terminal admittance measurement by applying the MLBS (purple) and the COS (red).

accurately over the wide bandwidth and especially in the resonant peaks that are poorly identified with the conventional MLBS [P2]. With the COS, the SNR can be significantly increased to overcome the deteriorating effects of noise, grid harmonics, and nonlinearities that corrupt the MLBS measurement.

The measurement results obtained with a single perturbation sequence ($T_{\text{meas}} = 2.0$ s) can be further improved by averaging the measurements over multiple injection periods. Fig. 4.16 presents long-duration measurements of the terminal admittance, where the MLBS perturbation is averaged over 100 excitation periods and the COS over 25 periods. Consequently, the measurement durations are 100.8 s for the MLBS and 50.4 s for the COS. As seen from the results, applying the COS achieves similar (or even better) accuracy in significantly shorter measurement duration.

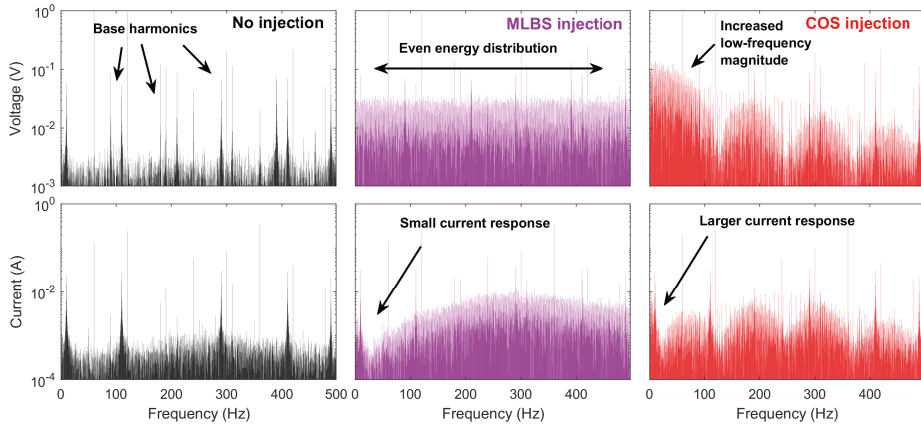


Figure 4.17 Spectra of the d-channel voltages (upper) and currents (lower) when no injection is applied (black), when the MLBS injection is applied (purple), and when the COS injection is applied (red).

In order to provide further validation of the proposed COS performance, a spectral analysis is performed on the grid currents and voltages. Fig. 4.17 presents the measured d-channel voltages (upper) and currents (lower) for the three cases: during normal operation without injection (black), during the MLBS injection (purple), and during the COS injection (red). The left-most subplot shows the baseline spectrum, where the system noise and harmonic voltages and currents are present, whereas the other subplots show the waveforms during the voltage-type perturbation injection. With the MLBS injection, the excitation spectrum superimposed on the nominal operation is evenly distributed as designed. However, the current response spectrum shows that the low-frequency anti-resonance at 25 Hz especially produces only a weak current response; in this case, the admittance magnitude is only $-50 \text{ dB}\Omega$ and the current response is only approximately 0.3 % of the voltage response. The COS perturbation is designed to augment the excitation energy towards the low frequencies, as seen from the right-most subplot. Therefore, the current response is also magnified, leading to superior measurement performance.

Lastly, the impact of perturbation on the system is quantified by measuring the THD of the currents and voltages during different injections. Table 4.4 presents the phase current and voltage THDs for the three cases. As the injection amplitude is selected to be small, the perturbation has only a minor impact on the THDs, as the base level when no perturbation is injected is close to the THD during the measurements. It should be noted that the COS disturbs the system marginally less than the MLBS.

Table 4.4 Total harmonic distortions in phase currents and voltages.

	Voltage THD	Current THD
No excitation	0.3 %	6.47 %
MLBS excitation	0.54 %	6.91 %
COS excitation	0.45 %	6.60 %

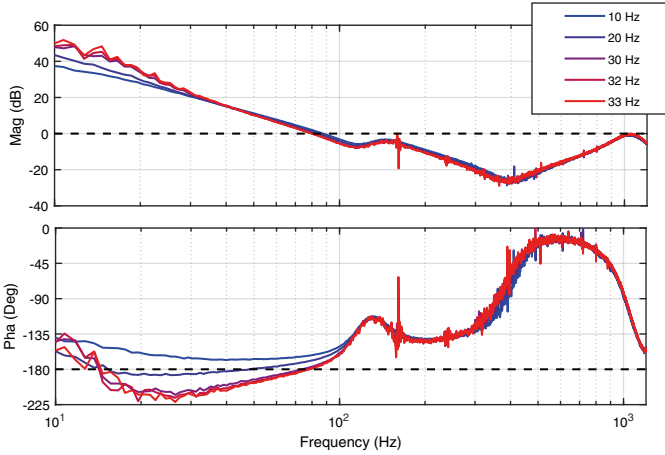


Figure 4.18 Measured current controller loop q-channel loop gains with different PLL bandwidths.

4.3 Broadband Stability Analysis

4.3.1 Experiment 4: Load-Affected Control Loop Analysis [P5]

In Experiment 4, the load-affected current controller, which is the innermost controller, loops of a grid-connected inverter are measured online [P5]. The experiments are performed with Experimental Setup 1, where the inverter is connected into a high-impedance grid by connecting an additional inductor (12 mH) to emulate the grid impedance. The impact of varying grid impedance on the current control loop was demonstrated in [P5] and in [132]. In this experiment, analysing the impact of phase-locked loop (PLL) bandwidth on system stability through the load-affected current control loop is presented.

The PLL affects the current control loop through modifying the inverter output admittance, which in turn modifies the load effect on the control-to-output transfer function [P5]. Fig. 4.18 presents the measured q-channel current control loops for five different PLL bandwidth tunings, where the low-frequency phase declines as the PLL bandwidth increases. Moreover, the loop gain is a non-minimum phase system that has an open-loop RHP pole,

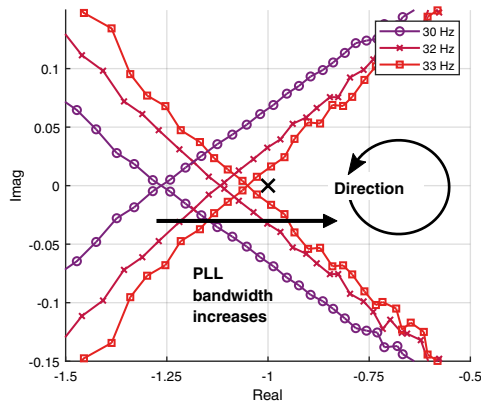


Figure 4.19 Nyquist loci for different PLL tunings.

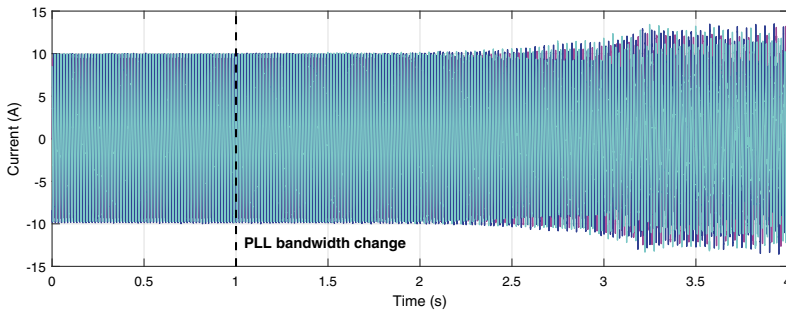


Figure 4.20 Three-phase currents when the PLL bandwidth is change at $t = 1$ s.

and consequently the Nyquist contour must encircle the critical point once, anticlockwise, in order for the system to be stable. Fig. 4.19 presents the corresponding Nyquist plots where an anticlockwise encirclement is observed for each system. However, the increase in PLL bandwidth shifts the crossing point of each contour towards the critical point. Based on the trend, it can be assumed that a system with 34 Hz PLL would no longer encircle the critical point, which would indicate instability.

Fig. 4.20 presents the phase currents of the inverter when the PLL bandwidth is changed from 33 Hz to 34 Hz at $t = 1$ s, where zoomed-in steady state waveforms for both 33 Hz PLL and 34 Hz PLL are shown in Fig. 4.21. The currents show that within seconds from the PLL bandwidth change, the system enters the state of sustained resonance indicating instability or marginal stability. Consequently, the stability indication from the load-affected loop analysis accurately predicted the stability of the system, when the instability is mainly caused by interaction between the inverter’s PLL and grid impedance [P5].

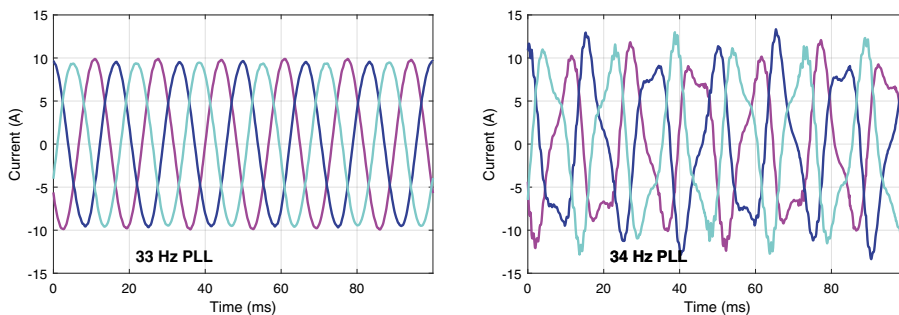


Figure 4.21 Three-phase current waveforms in steady state.

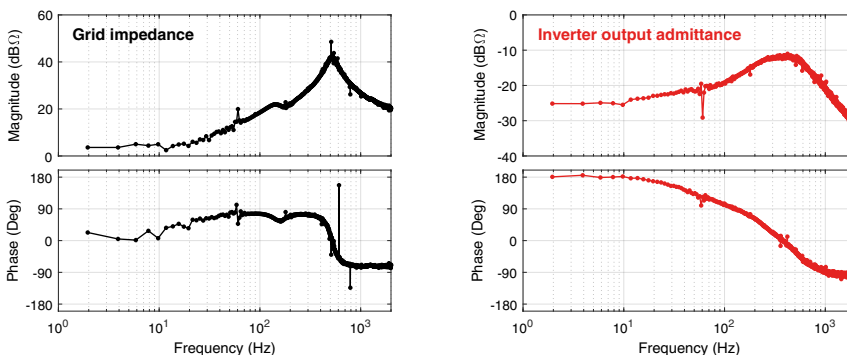


Figure 4.22 Measured q-component grid impedance (left) and inverter output admittance (right).

4.3.2 Experiment 5: Impedance-Based Sensitivity Function [P6]

The method for predicting the robustness of a grid-connected system based on an impedance-based sensitivity function is experimentally verified by applying Experimental Setup 1. In the experiment, the terminal q-channel impedances at a point-of-common coupling are measured with a broadband perturbation and the system stability is assessed by extracting the predicted stability margins from the impedance data [P6]. The measurements are performed by applying a 1999-bit-long quadratic-residue binary sequence (QRBS) that is generated at 8 kHz and averaged over 50 measurement periods resulting in 2 Hz frequency resolution. First, the inverter output admittance is measured by injecting a 2 V voltage perturbation from the grid emulator. Then, an additional inductor is connected to the system to emulate the grid impedance, and the grid impedance is measured by injecting a 0.2 A current perturbation from the inverter. Fig. 4.22 presents the measured q-channel grid impedance and inverter output admittance.

Fig. 4.23 presents the Nyquist contour of the q-component impedance ratio. The contour does not encircle critical point indicating stable operation. However, the contour trav-

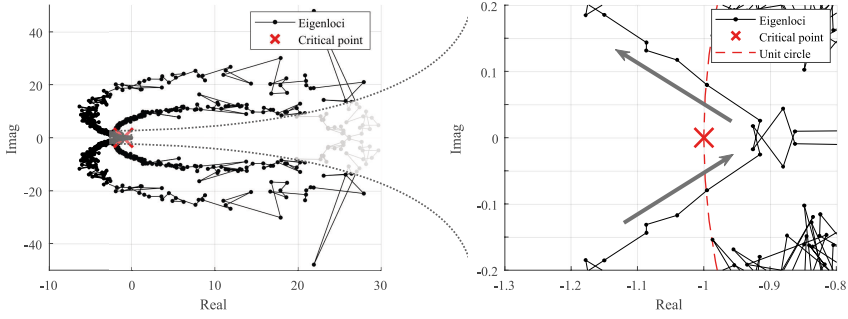


Figure 4.23 Nyquist contour of the impedance ratio.

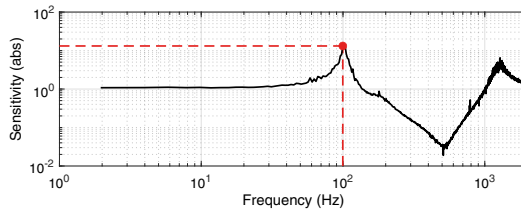


Figure 4.24 Impedance-based sensitivity function with sensitivity peak indicated in red.

els from the proximity of the critical point and, as a consequence, the system stability margins may be low. To quantify the stability margins, the method proposed in Section 3.2.2 is applied. Fig. 4.24 presents the impedance-based sensitivity function calculated from the measured terminal impedances. From the sensitivity function, the sensitivity peak is identified resulting in $M_s = 13.1$ where the corresponding angular frequency is $\omega_c = 626.2$ rad/s. By applying (3.17-3.20), the system equivalent phase margin is $\Phi_m = 4.36^\circ$ and damping is $\zeta = 0.038$ [P6].

The achieved stability margins can be experimentally validated by performing a transient response experiment. In the experiment, the estimated second-order transfer function is applied to predict the step response, which is compared to the actual dynamic response of the system. The system is disturbed by performing a step change to the q-current reference of the inverter. Fig. 4.25 presents the predicted and measured dynamic responses to a step-like transient. The oscillatory response confirms the estimated stability margins, as the oscillatory frequency and damping factor are accurately reflected by the analytically obtained prediction [P6]. It should be noted that the proposed method applies the *minimum phase margin* in (3.17), and consequently the actual damping ratio may be slightly higher. However, the resulting error is small, and the method yields the worst-case stability margin.

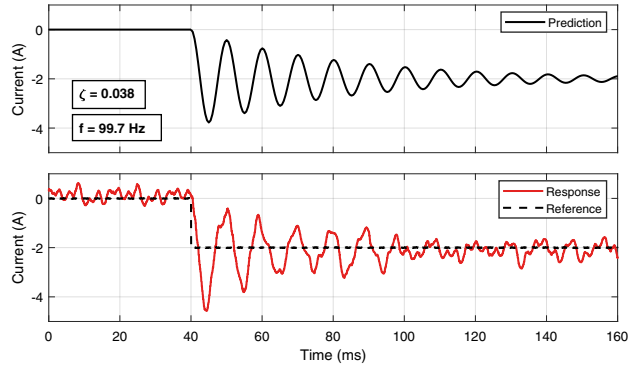


Figure 4.25 Predicted dynamic performance based on estimated stability margins (upper) and actual dynamic performance (lower).

Table 4.5 Perturbation parameters in the multivariable admittance measurements.

Parameter		OBS ₁	OBS ₂
Sequence length	(N)	2047	4094
Generation frequency	(f_{gen})	5 kHz	5 kHz
Injection amplitude	(A)	1.0 %	1.0 %
Number of periods	(P)	100	50
Measurement duration	(T_{meas})	40.9 s	40.9 s

4.4 Stability Analysis of Parallel Converters

4.4.1 Experiment 6: Impedance Aggregation [P7]

The experimental validation of the impedance aggregation method is performed by applying Experimental Setup 2. The setup is configured to emulate a system of three parallel inverters that connect to a shared point-of-common coupling and inject power to the fourth unit that acts as an ideal grid [P7]. The multivariable terminal admittance is measured for the inverters independently as well as for the total terminal admittance of the multi-parallel inverters. The measurements apply a MIMO measurement scheme, where two orthogonal sequences are injected to the d- and q-components of the grid voltages. Table 4.5 presents the measurement parameters.

Fig. 4.26 presents the terminal multivariable admittance of each converter, where the admittances are not equal due to different current controller parameters and different filter parameters. Based on the impedance aggregation method presented in Section 3.2.1, the

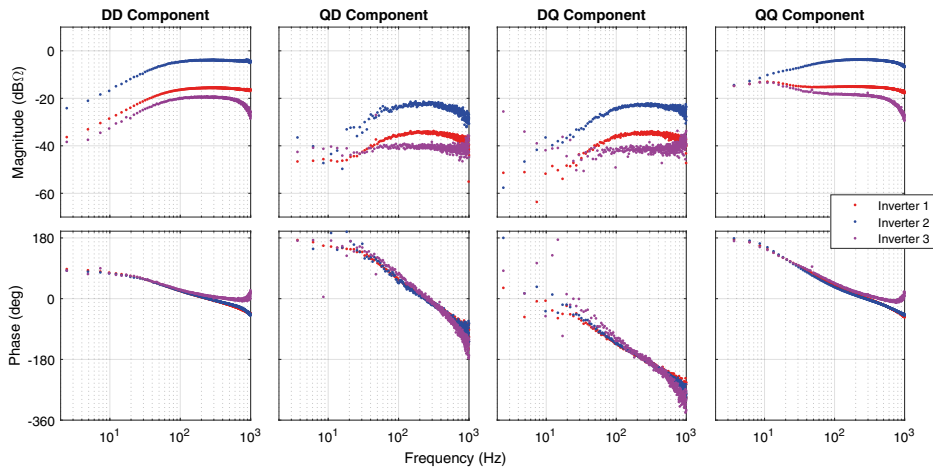


Figure 4.26 Separately measured multivariable terminal admittances of three inverters.

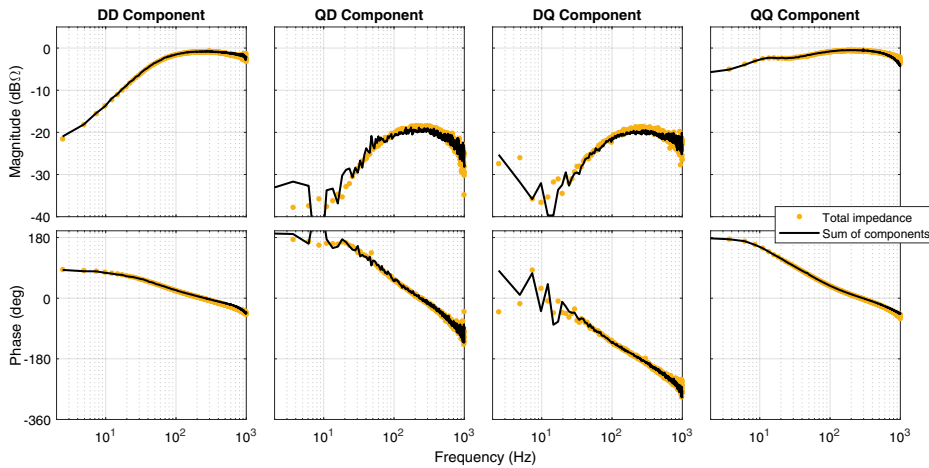


Figure 4.27 Measured (orange) and aggregated (black) total admittance of parallel inverters.

total terminal admittance of inverters that share the point-of-common coupling is equal to the sum of each inverters' terminal admittance. Consequently, the method can be validated by comparing the sum of admittances measured independently to the total admittance measured from the multi-parallel configuration. Fig. 4.27 shows the measured total admittance of the inverters' (orange) and the sum of components (black)⁴, where the results are uniform. Differences occur in the low frequency range of the cross-couplings, where the magnitude of the admittance is very low and the measurements are noisy.

Assuming the interconnection impedances between the parallel devices are small, the sta-

⁴The black line is formed by summing the three admittance components in Fig. 4.26.

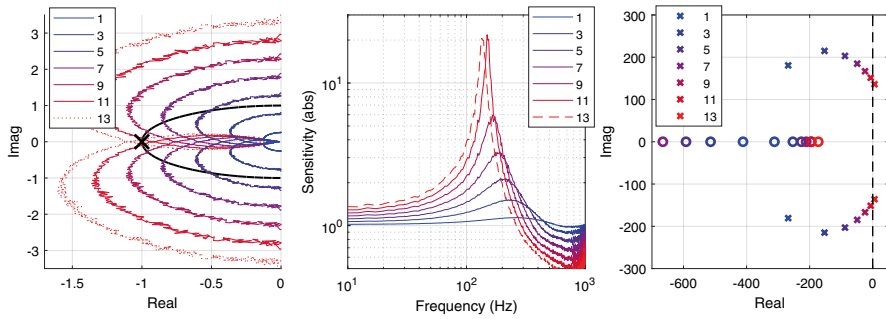


Figure 4.28 Aggregated stability assessment of multi-parallel inverters by applying generalized Nyquist criterion (left), sensitivity function (middle) and pole-zero map (right).

bility analysis of multi-parallel converters can be applied based on the terminal admittances of each device. In the case of identical devices, the analysis is further simplified, and the total terminal admittance is simply the admittance of a single device multiplied by the number of parallel devices. Consequently, assessing the stability and maximum hosting capacity of a grid at a certain point becomes straightforward and convenient. Moreover, measuring the total terminal admittance of multiple parallel inverters is often inconvenient or even impossible for practical systems, as the measurement would require a very specific hardware configuration and measurement devices.

To demonstrate the stability assessment based on aggregated impedance-based stability criterion, an example case study is presented. The study presents the stability analysis for a varying number of parallel identical inverters, which is performed by applying the aggregation method on the measured terminal admittance of Inverter 3 (purple line in Fig. 4.26). Fig. 4.28 presents the generalized Nyquist loci⁵ (left), sensitivity function (middle), and pole-zero map of critical poles (right) for 1...13 parallel inverters. As seen from the Nyquist loci, the stability margins decrease along with an increasing number of paralleled inverters, until the stability is lost at 13 parallel devices. Consequently, the absolute hosting capacity is 12 parallel devices (without consideration of safety margins). Similarly, the sensitivity function shows an increasing sensitivity peak that shifts towards lower frequencies when the number of parallel units increases. By applying transfer function fitting, the critical poles and zeros located in the (2,2)-component of the closed-loop minor loop gain are obtained. The critical pole pair shifts towards the imaginary axis when the number of parallel devices is increased, where the pole pair shifts into the right-hand plane (RHP) for 13 parallel devices, indicating instability. Similar conclusions can be drawn from the different assessment methods for the system stability and hosting capacity.

⁵Only the critical contour closer to the critical point is shown for illustrative purposes.

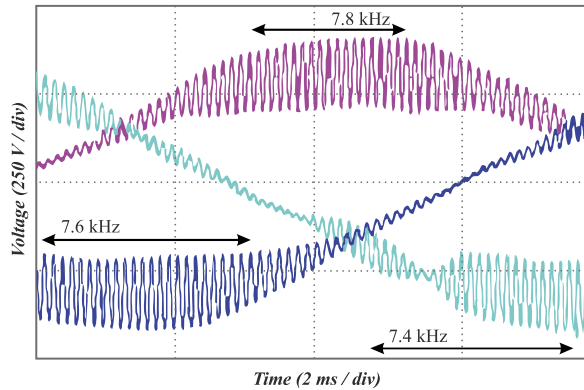


Figure 4.29 Distorted phase voltages during instability incident in a data center.

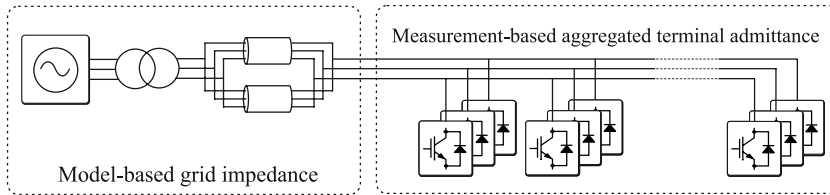


Figure 4.30 Grid connection schematic of the data center.

4.4.2 Experiment 7: Hosting Capacity Analysis [P3]

In Experiment 7, the presented aggregation method for stability assessment of multi-parallel converters is utilized in a case study of a real-life instability incident [P3]. In November 2017, a new data center in southern Finland expressed unstable operation through a drastic sustained harmonic resonance. Fig. 4.29 presents the measured on-site phase voltages at the point-of-common coupling during the resonance. As seen from the figure, the fundamental voltages are corrupted by a major harmonic distortion occurring in a high-frequency range around 7-8 kHz with a peak-to-peak amplitude of 31 % of fundamental voltages. The harmonic resonance damaged electrical equipment of other consumers in the proximity of the data center. The data center was energized by 96 parallel power supplying units (PSUs) that were 2.4 kVA single-phase rectifiers with a total power of approximately 240 kVA. The rectifiers were connected to the power grid through two parallel underground cables and a 500 kVA transformer (20.5/0.41 kV). The effect of other electric loads of the data center, such as lighting or air conditioning, is assumed negligible, and the rectifiers are assumed to be identical. Fig. 4.30 presents the simplified system configuration, and the parameters are shown in Table 4.6.

Table 4.6 Grid connection parameters for grid impedance model.

	Parameter	Value
Cable	Length	88 m
	Resistance	0.20 Ω /km
	Capacitance	0.28 μ F/km
	Inductance	0.26 mH/km
Transformer	Nominal power	500 kW
	Voltage	20.5/0.41 kV
	Resistance	1.064 %
	Reactance	4.420 %

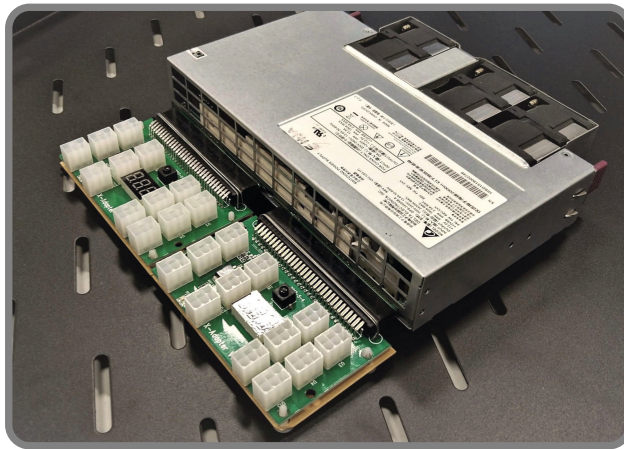


Figure 4.31 Photograph of a 2400 W single-phase PSU.

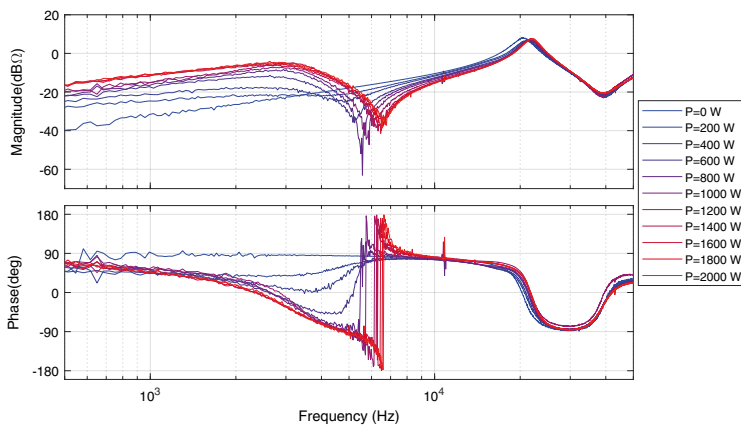


Figure 4.32 Measured terminal admittance of a PSU for power range from 0 to 2000 W.

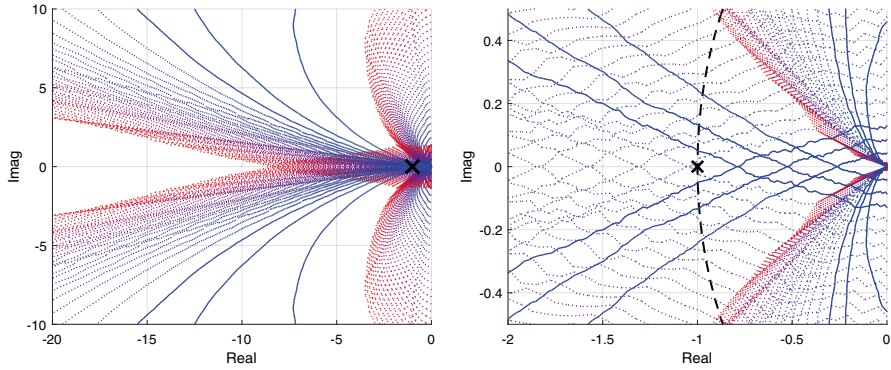


Figure 4.33 Nyquist loci for varying number of parallel PSUs (stable systems shown with solid line, unstable systems with dashed line).

In the following analysis, the origin of instability is explained through an impedance-based analysis of the system, where the terminal admittance of a PSU obtained from the data center (a photograph shown in Fig. 4.31) is measured by applying broadband methods and an impedance aggregation method is applied. The measurements are performed by applying Experimental Setup 3. The terminal admittance of the PSU was measured by injecting an MLBS perturbation to the grid voltages produced by the grid emulator. A 2047-bit-long MLBS was generated at 140 kHz generation frequency — consequently, the measurement frequency resolution was 68 Hz and duration of a single period was 14.6 ms. The measurements were averaged over 2000 perturbation periods making the total measurement duration 29.2 s. The voltage-type excitation was injected with 2 V amplitude that is approximately 1 % of the nominal voltages. The terminal admittance was measured in different loading states (0...2000 W) by modifying the number of parallel resistors in the passive load. Fig. 4.32 presents the measured terminal admittance of the PSU. The grid impedance was modeled based on the known parameters of the transformer and cables.

The stability analysis was performed by aggregation method for a varying number of parallel units that are assumed to be balanced between the three phases. Fig. 4.33 presents the zoomed-in Nyquist loci for various number of parallel converters. As seen from the figure, the contour shifts to encircle the critical point indicating existing instability when the number of parallel devices is increased from 9 to 12. Moreover, similar results are obtained through a complementary analysis method that is performed by utilizing transfer function fitting and pole-zero analysis. Fig. 4.34 shows the closed-loop poles of the system that are obtained through transfer function fitting. Increasing the number of parallel converters shifts the critical pole pair from the left-hand plane (LHP) into the right-hand plane (RHP), which in turn indicates instability for the system. The stability boundary obtained through transfer function fitting differs slightly from the boundary obtained through Nyquist criterion,

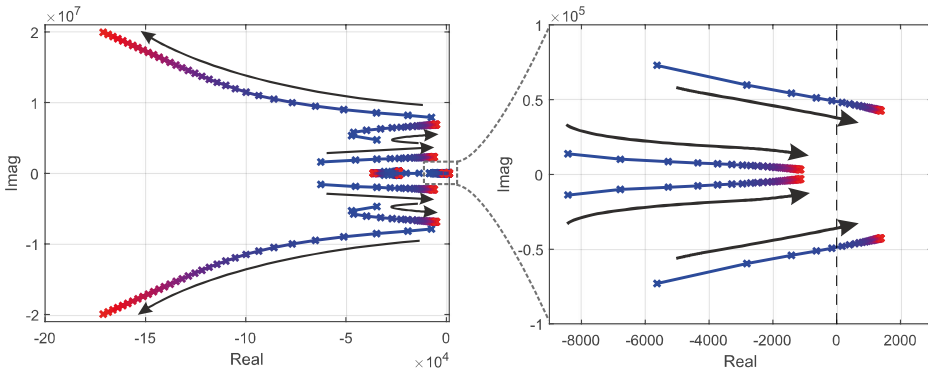


Figure 4.34 Closed-loop poles for varying number of parallel PSUs (blue: 3 converters, red: 96 converters).

as the poles indicate that the stability is lost when the number of converters is increased from 12 to 15. This is a result of minor inaccuracies that occur during the numerical transfer function fitting. However, the pole-zero analysis is an auxiliary method for quantifying the stability margins and the primary analysis on absolute stability should be assessed by applying Nyquist criterion. The system stability margins are obtained by assessing the critical pole pair of the system, shown in Table 4.7, where the analysis predicts unstable operation at frequency range of 7...8 kHz when more than 15 converters are connected in parallel. Consequently, the broadband stability assessment that was performed predicted both the instability and the resonance frequency by applying only a coarse grid impedance model and measured terminal admittance of a single PSU [P3].

Table 4.7 Critical poles of multi-parallel PSUs.

Parallel PSUs	Critical pole pair (1000 rad/s)	Frequency (Hz)	Damping factor
3	$-5.197 \pm 72.761i$	11609.8	0.0714
6	$-2.216 \pm 59.83i$	9528.8	0.0370
9	$-0.871 \pm 54.448i$	8666.8	0.0160
12	$-0.147 \pm 51.515i$	8198.9	0.0029
15	$0.293 \pm 49.674i$	7906	-0.0059
18	$0.583 \pm 48.412i$	7705.6	-0.0120
21	$0.786 \pm 47.493i$	7559.8	-0.0166
24	$0.936 \pm 46.794i$	7449.0	-0.0200
27	$1.049 \pm 46.246i$	7362.2	-0.0227
30	$1.139 \pm 45.803i$	7292.0	-0.0249
33	$1.210 \pm 45.439i$	7234.4	-0.0266
36	$1.269 \pm 45.134i$	7186.1	-0.0281
39	$1.317 \pm 44.874i$	7145.0	-0.0294
42	$1.358 \pm 44.651i$	7109.7	-0.0304
45	$1.393 \pm 44.458i$	7079.2	-0.0313
48	$1.424 \pm 44.287i$	7052.1	-0.0321
51	$1.450 \pm 44.137i$	7028.4	-0.0328
54	$1.473 \pm 44.003i$	7007.2	-0.0335
57	$1.494 \pm 43.883i$	6988.2	-0.0340
60	$1.512 \pm 43.775i$	6971.2	-0.0345
63	$1.528 \pm 43.677i$	6955.7	-0.0350
66	$1.543 \pm 43.588i$	6941.6	-0.0354
69	$1.556 \pm 43.506i$	6928.6	-0.0358
72	$1.568 \pm 43.431i$	6916.8	-0.0361
75	$1.579 \pm 43.362i$	6905.9	-0.0364
78	$1.590 \pm 43.299i$	6895.9	-0.0367
81	$1.599 \pm 43.239i$	6886.4	-0.0370
84	$1.608 \pm 43.185i$	6877.9	-0.0372
87	$1.616 \pm 43.134i$	6869.8	-0.0375
90	$1.623 \pm 43.086i$	6862.2	-0.0377
93	$1.630 \pm 43.041i$	6855.1	-0.0379
96	$1.636 \pm 42.999i$	6848.5	-0.0381

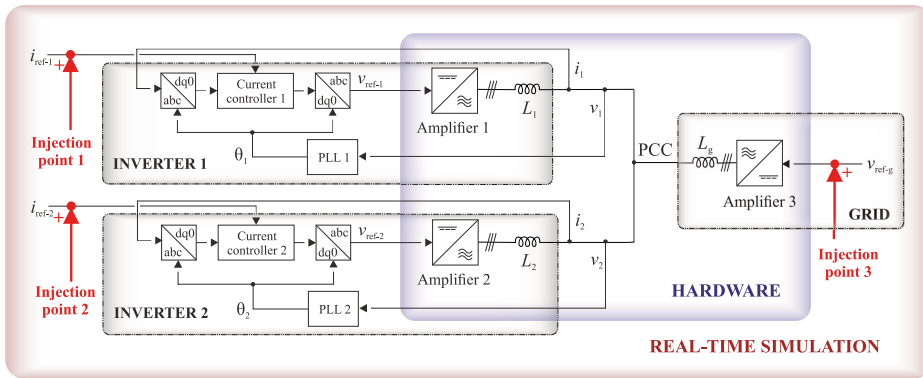


Figure 4.35 Conceptual diagram of the experimental setup and injection points.

4.4.3 Experiment 8: Real-Time Broadband Stability Analysis [P1]

The real-time implementation of the broadband stability analysis was tested through Experimental Setup 2. The setup configuration is realized by three amplifier groups, where two amplifiers were set to emulate parallel three-phase grid-connected inverters and the third group acted as the grid [P1]. The output filters of the inverters and grid impedance were physically implemented with three-phase inductors. Fig. 4.35 presents the schematic of the system configuration — the parameters are shown in Table 4.8.

The real-time broadband measurements were implemented as MIMO measurements by applying two orthogonal perturbations. Moreover, the same perturbations were applied in simultaneous identification of load-affected current control loops and terminal impedances, as illustrated in Fig. 3.18 in Section 3.2.4. The first orthogonal sequence was a 2047-bit-long maximum-length binary sequence (MLBS) and the second orthogonal sequence was a 4094-bit-long inverse repeat sequence (IRS). Both sequences were generated at 5 kHz and the injection amplitudes were adjusted so that the currents and voltages did not deviate from their nominal values more than 5%. The measurements were averaged over 100 periods for the MLBS and 50 periods for the IRS. Increasing the PLL bandwidth in a high-impedance grid makes the system prone to instability [151], and therefore, the PLL tunings were chosen for alteration to test the method in versatile conditions. Three sets of experiments were performed, where the phase-locked loop (PLL) bandwidth (shared by the inverters) was tuned differently, to 20, 60, or 85 Hz.

The experiments were performed by utilizing the different injection points shown in Fig. 4.35. The aggregated terminal admittance of the inverters can be measured by applying Injection Point 3. Moreover, the grid impedance and load-affected loops can be measured by applying Injection Points 1 and 2. In this work, sequential measurements were performed for the inverters to avoid interaction between perturbations injected from Inverters 1 and 2.

Table 4.8 Parameters of the Experimental Setup 2.

Parameter	Symbol	Value
Grid frequency	f_g	50 Hz
Nominal main voltage (RMS)	V_n	400 V
Output power of inverters	P_{sp}	24.4 kW
Power factor of inverters	$\cos(\phi)$	1.00
D-current reference	i_d^*	50 A
Grid inductance	L_g	2.0 mH
Inverter 1 L-filter inductance	L_1	0.5 mH
Inverter 2 L-filter inductance	L_2	3.2 mH
Inverter 1 CC proportional gain	K_{CC1-P}	1.6514
Inverter 1 CC integral gain	K_{CC1-I}	518.8
Inverter 2 CC proportional gain	K_{CC2-P}	10.070
Inverter 2 CC integral gain	K_{CC2-I}	3162
20 Hz PLL proportional gain	$K_{PLL20-P}$	1.30
20 Hz PLL integral gain	$K_{PLL20-I}$	75.2
60 Hz PLL proportional gain	$K_{PLL60-P}$	3.90
60 Hz PLL integral gain	$K_{PLL60-I}$	676.4
85 Hz PLL proportional gain	$K_{PLL85-P}$	5.52
85 Hz PLL integral gain	$K_{PLL85-I}$	1358

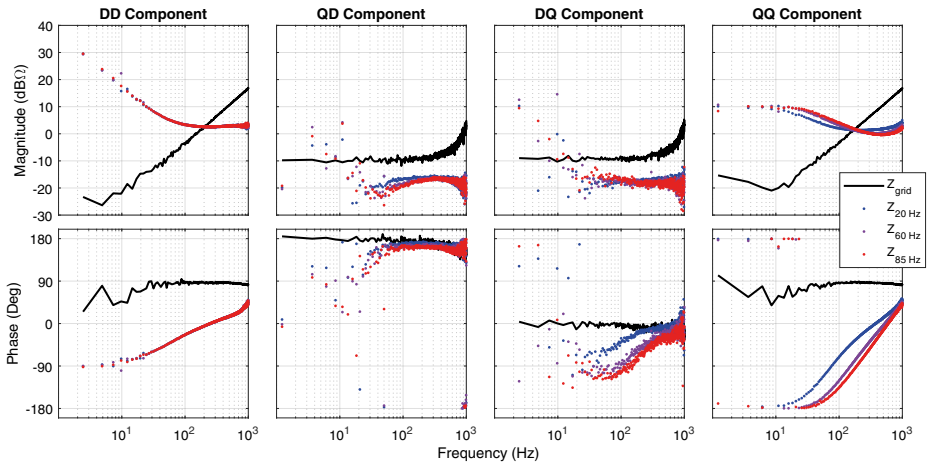


Figure 4.36 Grid impedance (black) and aggregated inverter admittance for varying PLL parameters.

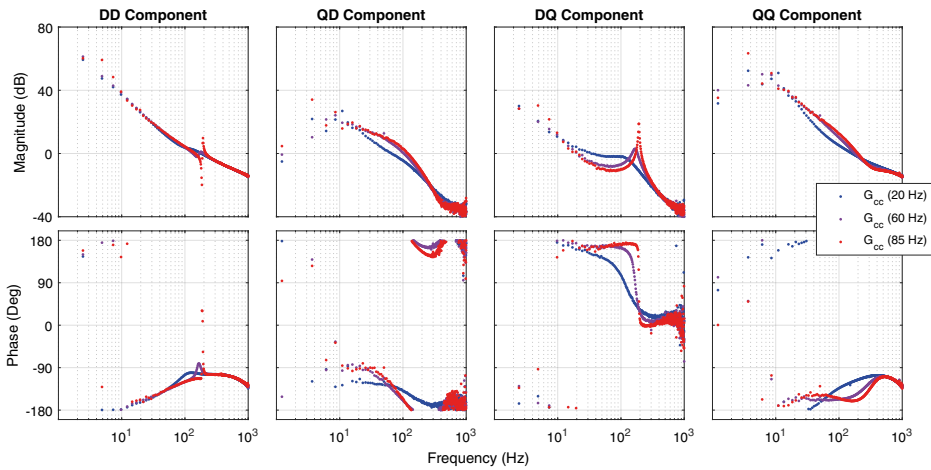


Figure 4.37 Inverter 1 load-affected current controller loop gain for varying PLL parameters.

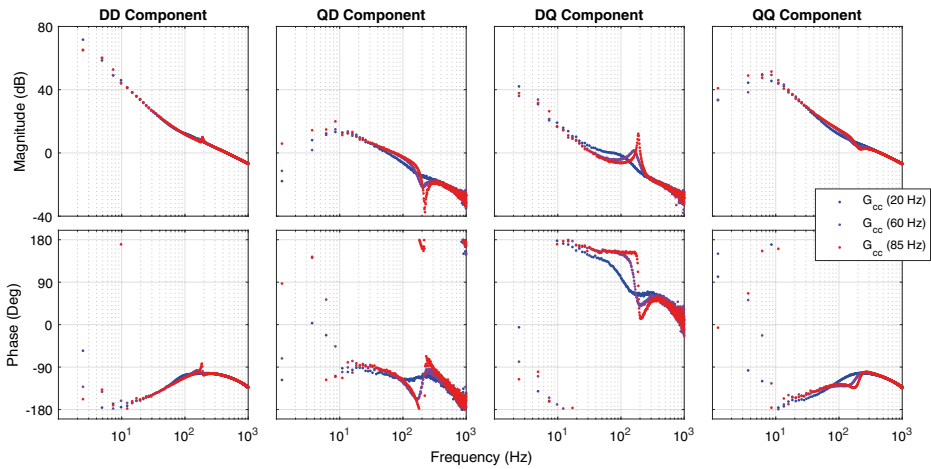


Figure 4.38 Inverter 2 load-affected current controller loop gain for varying PLL parameters.

Fig. 4.36 presents the measured grid impedance and aggregated terminal impedance of the inverters for varying PLL tunings. Similarly, Fig. 4.37 and Fig. 4.38 present the load-affected current control loop gains for Inverters 1 and 2, respectively.

The stability assessment could be performed similarly for the obtained internal loop gains and for the minor loop gain formed by the terminal impedances. In this implementation, generalized Nyquist criterion (GNC) is applied for the impedance data and pole-zero analysis for both loop gains and impedances. Fig. 4.39 presents the GNC loci of the minor loop gain for different PLL tunings. As seen from the figure, the second eigenvalue remains largely unchanged, but the first eigenvalue experiences a drastic shift towards the critical point when the PLL bandwidth is increased. The system is close to marginal stability when the PLL

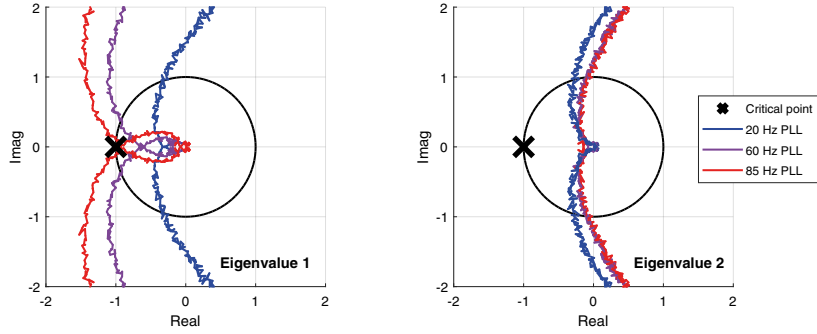


Figure 4.39 Impedance-based GNC analysis for varying PLL parameters.

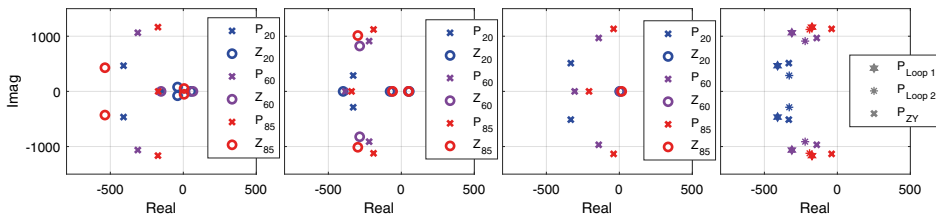


Figure 4.40 Pole-zero maps based on measured minor loop gain and inverter current controller loops.

bandwidth is set to 85 Hz. In the pole-zero analysis, the measurement data is continuously fitted to a parametric model. Fig. 4.40 presents the obtained poles and zeros for the system. As seen from the figure, the critical poles experience a similar shift towards the imaginary axis in both internal loop gains and in impedance-based analysis [P1].

Lastly, the obtained analysis is validated against transient experiments in offline analysis. The fitted parametric model can be utilized to predict the time-domain operation. In the validation, the step responses of the parametric model obtained from the minor loop

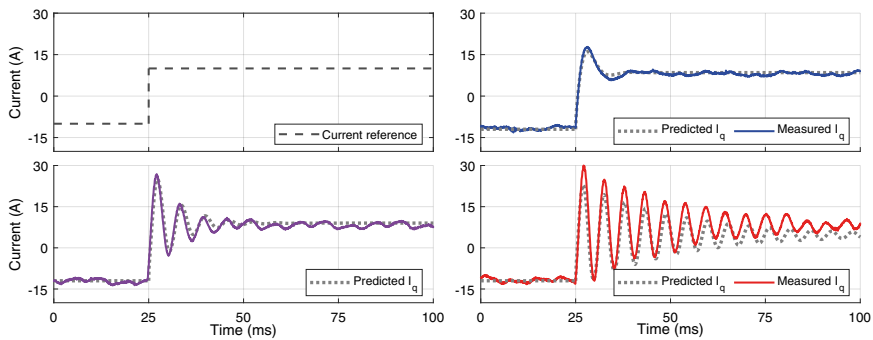


Figure 4.41 Comparison between the predicted system transient responses and experimental responses.

gain (that is, the terminal impedances) are compared against actual system step responses, where the current reference q-component of Inverter 1 is abruptly changed from -10 to 10 A. The experiment was repeated for all test parameter sets. Fig. 4.41 presents the predicted transient responses in comparison to actual system responses. As seen from the figure, the obtained parametric model accurately captures the dynamic performance of the system in all three experiment sets. Consequently, the performed real-time stability assessment based on broadband measurements achieved high fidelity in the assessment of two parallel grid-connected inverters.

5 CONCLUSIONS

The global energy scenario has experienced a paradigm shift during the past few decades, where an increasing amount of energy processing has taken place in power electronics. The transition has occurred simultaneously across energy production, distribution, and consumption, driven by the rapid rise of grid-connected renewable energy sources and drastic increments in power-electronic based energy consumption. Consequently, the power-electronic converters have become an essential technology in the modern power system, as such converters enable advanced power processing capabilities. The high penetration of grid-connected power electronics introduces emerging challenges to the stability and power quality of the power system.

The stability analysis of grid-connected power electronics has become a vital procedure in the design of systems that connect to the grid through power-electronic converters. Previous studies have presented methods for assessing the stability of such systems by applying state-space modeling or impedance-based stability criteria, where the stability is analyzed based on terminal impedances at the interface. However, the grid-connected systems often include multiple unknown parameters, and the detailed dynamics of some subsystems are often unknown, therefore model-based approaches are often impractical. Moreover, the small-signal dynamics depend on the operation point and as the operational conditions typically vary over time, a static analysis becomes insufficient.

This thesis has presented broadband stability analysis methods that can be applied in the assessment of systems that consist of multiple parallel converters. The methods utilize on-line frequency-response identification based on pseudo-random broadband sequences. The contributions of this thesis can be summarized in three categories:

- Design methods for amplitude and averaging selection of broadband measurements of grid-connected systems are presented. Moreover, multivariable measurement techniques are presented by applying orthogonal sequences. Lastly, the thesis presents a novel perturbation sequence constructed from multiple orthogonal sequences, which enables more versatile excitation design where a single broadband sequence can facilitate different frequency resolutions and excitation energies for different frequency ranges.
- Stability analysis based on load-affected loop gain measurements are proposed, where

the stability of each grid-connected converter is individually assessed based on a measured innermost control loop. The thesis also proposes a multivariable impedance-based sensitivity function that is formulated by applying singular value decomposition on terminal impedance data. The sensitivity function can be applied to quantify the stability margins, thereby extending generalized Nyquist criterion analysis.

- Broadband stability analysis methods for multi-parallel grid-connected converters are proposed. An impedance aggregation technique is proposed to assess the stability of parallel converters based on total terminal admittance, which is shown to predict the hosting capacity (maximum number of parallel converters) at a given grid interface. A major advantage of the proposed method is its applicability to systems with very limited amounts of information, as the required information can be extracted through terminal measurements. Lastly, a real-time implementation of stability analysis for parallel converters is shown.

The presented measurement and analysis methods have been validated through extensive testing by applying multiple hardware setups in power range between 2.5 and 200 kVA. In the experiments, power hardware-in-the-loop configurations were utilized, where some of the controllers were implemented on a real-time simulation whereas physical hardware is applied. The presented broadband identification techniques were shown to achieve accurate results within very short measurement durations. The stability analysis methods were shown to accurately predict the system stability and stability margins in various configurations.

Discussion and Criticism

An inherent difficulty in stability analysis of converter-penetrated systems is the complexity and versatility of such systems. The power system configuration varies drastically from location to location, and the state of the system undergoes constant evolution as subsystems, such as factories or local production, are connected, disconnected, and updated. Consequently, the analysis methods are required to perform in very different configurations where no assumptions on the power system can be made in a larger scope. As a result, measurement-based approaches are highly desired and especially rapid broadband methods perform well in online applications.

The presented methods depend on terminal impedance (admittance) measurements of subsystems. The main advantage — the reliance on system identification — is also the main obstacle in applying the methods: performing the measurements requires either special hardware or access to the control structure of existing hardware in the system. The presented methods enable the use of grid-connected converters directly in the measurements as they can be utilized in the perturbation injection. The converter control structure must support

perturbation injection, which is typically not the case in commercial devices. Additionally, the applied broadband perturbations are prone to non-linear distortions when the system under measurement has a high degree of non-linearity. In this thesis, the issues related to system non-linearity are assumed to be negligible and thus omitted. Another challenge is related to the complexity of the grid structure, where the optimal measurement locations depend on the grid configuration and engineer insight is required in selection of the interfaces. However, this challenge is largely universal for all stability analysis methods.

Another important aspect in online identification of grid-connected systems is the impact of perturbation on the system. The perturbation, required in active identification techniques, acts as a disturbance to the system, and therefore the regulations imposed by the grid code must also consider such methods. While this thesis has presented design methods for minimizing the impact on the grid, the detrimental impact on the grid cannot be completely neglected. Moreover, simultaneous excitation of the same frequencies from multiple sources may result in interactions that corrupt the measurements. To tackle this issue, sequential identification schemes or communication between devices is required if such measurement-based methods are to be applied in the vicinity of each other.

Future work

This thesis proposes solutions to a specific area of stability analysis, as per the limited scope of the work, and the generalization of the presented methods and derivation of further analysis tools remains a future research topic. To conclude this thesis, the future research aspects and challenges are discussed in order to spark further research on this essential dimension of power system analysis. Several challenges remain in the holistic stability assessment of converter-penetrated power system: generalization of analysis methods on increasingly complex systems, efficient utilization of a communication network over multiple devices, and stability enhancements for grid-connected devices.

A primal objective for the future research is to implement the assessment methods on more complex power systems that consist of multi-parallel converters connected over multiple buses. Further research is required to generalize the analysis towards such systems where identification of critical system interfaces is difficult or impossible. The conventional approach, where extensive effort is focused on deriving system state space through system modeling or system-wide simulations, suffers from time-consuming implementation and poor compatibility with black-box subsystems. Based on the performance of broadband methods presented in this thesis, an attractive alternative for analysis of such systems could be incorporating small-signal impedance into methods based on nodal admittance matrix. Such approach would enable combining measurement-based data into model-based approach, while preserving the possibility of holistic stability analysis in large scope through the use of, for

example, polar fitting to predict the modal stability data. Moreover, methods that are capable of reducing the order of system model and extracting the critical characteristics and modes from the bulk of data are highly valuable future research pathways.

Further future research topics involve the utilization of communication in both device-to-device level and in system level, along with improvements on converter design to achieve higher levels of robustness. Ideally, performing stability analysis would not be essential as the building blocks of the system, such as synchronous generators and power-electronic-based resources, were designed to be highly robust. Methods such as passivity-based design of converters and adaptive controllers have been proposed to increase the resilience against harmful interactions. However, these approaches often either deteriorate dynamic performance through overly conservative controller tunings or disturb the system by applying injection signals used for measurements. Consequently, further scientific advances are required to increase the system robustness without compromising performance.

REFERENCES

- [1] J. Hansen, R. Ruedy, M. Sato and K. Lo, "Global Surface Temperature Change", *Reviews of Geophysics*, vol. 48, no. 4, pp. 1–29, Dec. 2010.
- [2] D. Coumou and S. Rahmstorf, "A decade of weather extremes", *Nature Climate Change*, vol. 2, no. 7, pp. 491–496, 2012.
- [3] B. C. Douglas, "Global sea level rise", *Journal of Geophysical Research*, vol. 96, no. C4, pp. 6981, 1991.
- [4] C. Bellard, C. Bertelsmeier, P. Leadley, W. Thuiller and F. Courchamp, "Impacts of climate change on the future of biodiversity", *Ecology Letters*, vol. 15, no. 4, pp. 365–377, 2012.
- [5] M. Springmann, D. Mason-D’Croz, S. Robinson, T. Garnett, H. C. J. Godfray, D. Gollin, M. Rayner, P. Ballon and P. Scarborough, "Global and regional health effects of future food production under climate change: a modelling study", *The Lancet*, vol. 387, no. 10031, pp. 1937–1946, May 2016.
- [6] C. Raleigh and H. Urdal, "Climate change, environmental degradation and armed conflict", *Political Geography*, vol. 26, no. 6, pp. 674–694, Aug. 2007.
- [7] M. Kahn, K. Mohaddes, R. Ng, M. Pesaran, M. Raissi and J.-C. Yang, "Long-Term Macroeconomic Effects of Climate Change", *International Monetary Fund Working Papers*, pp. 1–59, 2019.
- [8] J. Cook, N. Oreskes, P. T. Doran, W. R. Anderegg, B. Verheggen, E. W. Maibach, J. S. Carlton, S. Lewandowsky, A. G. Skuce, S. A. Green, D. Nuccitelli, P. Jacobs, M. Richardson, B. Winkler, R. Painting and K. Rice, "Consensus on consensus: A synthesis of consensus estimates on human-caused global warming", *Environmental Research Letters*, vol. 11, no. 4, 2016.
- [9] United Nations, "Paris Agreement", *United Nations Treaty Collection, Chapter XXVII 7D*, 2015.
- [10] F. Johnsson, J. Kjärstad and J. Rootzén, "The threat to climate change mitigation posed by the abundance of fossil fuels", *Climate Policy*, vol. 19, no. 2, pp. 258–274, 2019.

- [11] "Directive (EU) 2018/2001 of the European Parliament and of the Council of 11 december 2018 on the promotion of the use of energy from renewable", *Official Journal of the European Union*, 2018.
- [12] G. He, J. Lin, F. Sifuentes, X. Liu, N. Abhyankar and A. Phadke, "Rapid cost decrease of renewables and storage accelerates the decarbonization of China's power system", *Nature Communications*, vol. 11, no. 1, pp. 1–9, 2020.
- [13] T. Braunschweig, M. Sharmina, E. Manderson, C. McLachlan, M. Hannon, J. Hardy and S. Mander, "Business models and financial characteristics of community energy in the UK", *Nature Energy*, vol. 5, no. 2, pp. 169–177, 2020.
- [14] International Renewable Energy Agency, "Renewable Power Generation Costs in 2019", 2020.
- [15] F. Blaabjerg and K. Ma, "Future on power electronics for wind turbine systems", *IEEE Journal of Emerging and Selected Topics in Power Electronics*, vol. 1, no. 3, pp. 139–152, 2013.
- [16] M. Liserre, T. Sauter and J. Hung, "Future Energy Systems: Integrating Renewable Energy Sources into the Smart Power Grid Through Industrial Electronics", *IEEE Industrial Electronics Magazine*, vol. 4, no. 1, pp. 18–37, Mar. 2010.
- [17] A. Etxegarai, P. Eguia, E. Torres, A. Iturregi and V. Valverde, "Review of grid connection requirements for generation assets in weak power grids", *Renewable and Sustainable Energy Reviews*, vol. 41, pp. 1501–1504, 2015.
- [18] Q. Peng, Q. Jiang, Y. Yang, T. Liu, H. Wang and F. Blaabjerg, "On the Stability of Power Electronics-Dominated Systems: Challenges and Potential Solutions", *IEEE Transactions on Industry Applications*, vol. 55, no. 6, pp. 7657–7670, 2019.
- [19] A. Khan, M. Hosseinzadehtaher, M. B. Shadmand, S. Bayhan and H. Abu-Rub, "On the Stability of the Power Electronics-Dominated Grid: A New Energy Paradigm", *IEEE Industrial Electronics Magazine*, vol. 14, no. 4, pp. 65–78, Dec. 2020.
- [20] F. Ding and B. Mather, "On Distributed PV Hosting Capacity Estimation, Sensitivity Study, and Improvement", *IEEE Transactions on Sustainable Energy*, vol. 8, no. 3, pp. 1010–1020, Jul. 2017.
- [21] H. Al-Saadi, R. Zivanovic and S. F. Al-Sarawi, "Probabilistic Hosting Capacity for Active Distribution Networks", *IEEE Transactions on Industrial Informatics*, vol. 13, no. 5, pp. 2519–2532, Oct. 2017.
- [22] I. Boldea, "Synchronous Generators", 2nd edition. Taylor & Francis, 2015, 504 pages.
- [23] X. Liang, "Emerging Power Quality Challenges Due to Integration of Renewable Energy Sources", *IEEE Transactions on Industry Applications*, vol. 53, no. 2, pp. 855–866, 2017.

- [24] S. R. Sinsel, R. L. Riemke and V. H. Hoffmann, "Challenges and solution technologies for the integration of variable renewable energy sources—a review", *Renewable Energy*, vol. 145, pp. 2271–2285, 2020.
- [25] M. Järvelä, S. Valkealahti, E. Ka and .-. Cheng, "Ideal operation of a photovoltaic power plant equipped with an energy storage system on electricity market", *Applied Sciences*, vol. 7, no. 7, 2017.
- [26] M. Anvari, G. Lohmann, M. Wächter, P. Milan, E. Lorenz, D. Heinemann, M. R. R. Tabar and J. Peinke, "Short term fluctuations of wind and solar power systems", *New Journal of Physics*, vol. 18, no. 6, 2016.
- [27] J. H. Enslin, M. S. Wolf, D. B. Snyman and W. Swiegers, "Integrated photovoltaic maximum power point tracking converter", *IEEE Transactions on Industrial Electronics*, vol. 44, no. 6, pp. 769–773, 1997.
- [28] B. Bose, "Global Energy Scenario and Impact of Power Electronics in 21St. Century", *IEEE Transactions on Industrial Electronics*, vol. 60, no. 7, pp. 2638–2651, 2013.
- [29] M. A. Hannan, M. S. Lipu, P. J. Ker, R. A. Begum, V. G. Agelidis and F. Blaabjerg, "Power electronics contribution to renewable energy conversion addressing emission reduction: Applications, issues, and recommendations", *Applied Energy*, vol. 251, no. December 2018, pp. 113404, 2019.
- [30] F. Blaabjerg, Y. Yang, K. Ma and X. Wang, "Power electronics - the key technology for renewable energy system integration", in *Proc. 2015 International Conference on Renewable Energy Research and Applications*, pp. 1618–1626, Palermo, Italy, 2015.
- [31] J. M. Carrasco, L. G. Franquelo, J. T. Bialasiewicz, E. Galván, R. C. Portillo Guisado, M. Á. M. Prats, J. I. León and N. Moreno-Alfonso, "Power-electronic systems for the grid integration of renewable energy sources: A survey", *IEEE Transactions on Industrial Electronics*, vol. 53, no. 4, pp. 1002–1016, 2006.
- [32] F. Blaabjerg, Z. Chen and S. Kjaer, "Power Electronics as Efficient Interface in Dispersed Power Generation Systems", *IEEE Transactions on Power Electronics*, vol. 19, no. 5, pp. 1184–1194, Sep. 2004.
- [33] B. K. Bose, "Power Electronics in Smart Grid and Renewable Energy Systems", *Proceedings of the IEEE*, vol. 105, no. 11, pp. 2007–2010, 2017.
- [34] N. Maïzi and V. Mazauric, "From centralized to decentralized power systems: The shift on finitude constraints", *Energy Procedia*, vol. 158, pp. 4262–4267, 2019.
- [35] A. Kargarian, J. Mohammadi, J. Guo, S. Chakrabarti, M. Barati, G. Hug, S. Kar and R. Baldick, "Toward Distributed/Decentralized DC Optimal Power Flow Implementation in Future Electric Power Systems", *IEEE Transactions on Smart Grid*, vol. 9, no. 4, pp. 2574–2594, 2018.

- [36] Q. C. Zhong, "Power-Electronics-Enabled Autonomous Power Systems: Architecture and Technical Routes", *IEEE Transactions on Industrial Electronics*, vol. 64, no. 7, pp. 5907–5918, 2017.
- [37] J. Lloret, J. Tomas, A. Canovas and L. Parra, "An Integrated IoT Architecture for Smart Metering", *IEEE Communications Magazine*, vol. 54, no. 12, pp. 50–57, 2016.
- [38] Q. Chen, D. Kaleshi, Z. Fan and S. Armour, "Impact of Smart Metering Data Aggregation on Distribution System State Estimation", *IEEE Transactions on Industrial Informatics*, vol. 12, no. 4, pp. 1426–1437, 2016.
- [39] J. M. Guerrero, "Guest Editorial Special Issue on Power Quality in Smart Grids", *IEEE Transactions on Smart Grid*, vol. 8, no. 1, pp. 379–381, 2017.
- [40] D. Li and S. K. Jayaweera, "Distributed smart-home decision-making in a hierarchical interactive smart grid architecture", *IEEE Transactions on Parallel and Distributed Systems*, vol. 26, no. 1, pp. 75–84, 2015.
- [41] S. L. Arun and M. P. Selvan, "Intelligent Residential Energy Management System for Dynamic Demand Response in Smart Buildings", *IEEE Systems Journal*, vol. 12, no. 2, pp. 1329–1340, Jun. 2018.
- [42] S. Bahrami and A. Sheikhi, "From Demand Response in Smart Grid Toward Integrated Demand Response in Smart Energy Hub", *IEEE Transactions on Smart Grid*, vol. 7, no. 2, pp. 650–658, 2016.
- [43] E. Ancillotti, R. Bruno and M. Conti, "The role of communication systems in smart grids: Architectures, technical solutions and research challenges", *Computer Communications*, vol. 36, no. 17-18, pp. 1665–1697, 2013.
- [44] M. Erol-Kantarci and H. T. Mouftah, "Energy-Efficient Information and Communication Infrastructures in the Smart Grid: A Survey on Interactions and Open Issues", *IEEE Communications Surveys and Tutorials*, vol. 17, no. 1, pp. 179–197, 2015.
- [45] V. Gungor and F. Lambert, "A survey on communication networks for electric system automation", *Computer Networks*, vol. 50, no. 7, pp. 877–897, May 2006.
- [46] V. C. Gungor, D. Sahin, T. Kocak, S. Ergut, C. Buccella, C. Cecati and G. P. Hancke, "Smart Grid Technologies: Communication Technologies and Standards", *IEEE Transactions on Industrial Informatics*, vol. 7, no. 4, pp. 529–539, Nov. 2011.
- [47] X. Zhao, L. Chang, R. Shao and K. Spence, "Power System Support Functions Provided by Smart Inverters - A Review", *CPSS Transactions on Power Electronics and Applications*, vol. 3, no. 1, pp. 25–35, 2018.
- [48] Q. Liu, S. Member, T. Caldognetto and S. Buso, "Review and Comparison of Grid-Tied Inverter Controllers in Microgrids", *IEEE Transactions on Power Electronics*, vol. 35, no. 7, pp. 7624–7639, 2019.

- [49] R. Bayindir, I. Colak, G. Fulli and K. Demirtas, "Smart grid technologies and applications", *Renewable and Sustainable Energy Reviews*, vol. 66, pp. 499–516, Dec. 2016.
- [50] X. Yu, C. Cecati, T. Dillon and M. Simões, "The New Frontier of Smart Grids", *IEEE Industrial Electronics Magazine*, vol. 5, no. 3, pp. 49–63, Sep. 2011.
- [51] L. Meegahapola, A. Sguarezi, J. S. Bryant, M. Gu, E. R. Conde D. and R. B. A. Cunha, "Power System Stability with Power-Electronic Converter Interfaced Renewable Power Generation: Present Issues and Future Trends", *Energies*, vol. 13, no. 13, pp. 3441, Jul. 2020.
- [52] A. Ulbig, T. S. Borsche and G. Andersson, "Impact of Low Rotational Inertia on Power System Stability and Operation", in *Proc. IFAC Proceedings Volumes*, vol. 47, no. 3, pp. 7290–7297, Cape Town, South Africa, 2014.
- [53] Z. Shuai, D. Liu, J. Shen, C. Tu, Y. Cheng and A. Luo, "Series and parallel resonance problem of wideband frequency harmonic and its elimination strategy", *IEEE Transactions on Power Electronics*, vol. 29, no. 4, pp. 1941–1952, 2014.
- [54] T. Suntio, T. Messo and J. Puukko, "*Power Electronics Converters - Dynamics and Control in Conventional and Renewable Energy Applications*". Wiley-VCH, 2017, 720 pages.
- [55] T. Suntio, T. Messo, M. Berg, H. Alenius, T. Reinikka, R. Luhtala and K. Zenger, "Impedance-Based Interactions in Grid-Tied Three-Phase Inverters in Renewable Energy Applications", *Energies*, vol. 12, no. 464, 2019.
- [56] W. Du, Q. Fu, X. Wang and H. Wang, "Small-signal stability analysis of integrated VSC-based DC/AC power systems – A review", *International Journal of Electrical Power & Energy Systems*, vol. 103, pp. 545–552, Dec. 2018.
- [57] H. Alenius, T. Messo, T. Reinikka and T. Roinila, "Aggregated Modeling and Power Hardware-in-the-Loop Emulation of Grid Impedance", in *Proc. 2018 IEEE Energy Conversion Congress and Exposition*, pp. 4179–4186, Portland, USA, 2018.
- [58] M. Liserre, R. Teodorescu and F. Blaabjerg, "Stability of Photovoltaic and Wind Turbine Grid-Connected Inverters for a Large Set of Grid Impedance Values", *IEEE Transactions on Power Electronics*, vol. 21, No. 1, 2006.
- [59] H. Alenius, "*Modeling and Electrical Emulation of Grid Impedance for Stability Studies of Grid-Connected Converters*". Master's thesis, 2018, 67 pages.
- [60] Y. A. R. I. Mohamed, "Suppression of low- and high-frequency instabilities and grid-induced disturbances in distributed generation inverters", *IEEE Transactions on Power Electronics*, vol. 26, no. 12, pp. 3790–3803, 2011.
- [61] Y. A.-R. I. Mohamed, "Mitigation of Converter-Grid Resonance, Grid-Induced Distortion, and Parametric Instabilities in Converter-Based Distributed Generation", *IEEE Transactions on Power Electronics*, vol. 26, no. 3, pp. 983–996, Mar. 2011.

- [62] D. Pan, X. Ruan, C. Bao, W. Li and X. Wang, "Optimized Controller Design for LCL-Type Grid-Connected Inverter to Achieve High Robustness Against Grid-Impedance Variation", *IEEE Transactions on Industrial Electronics*, vol. 62, no. 3, pp. 1537–1547, Mar. 2015.
- [63] Y. He, X. Wang, X. Ruan, D. Pan, X. Xu and F. Liu, "Capacitor-Current Proportional-Integral Positive Feedback Active Damping for LCL -Type Grid-Connected Inverter to Achieve High Robustness Against Grid Impedance Variation", *IEEE Transactions on Power Electronics*, vol. 34, no. 12, pp. 12423–12436, Dec. 2019.
- [64] Y. Han, M. Yang, H. Li, P. Yang, L. Xu, E. A. A. Coelho and J. M. Guerrero, "Modeling and Stability Analysis of LCL-Type Grid-Connected Inverters: A Comprehensive Overview", *IEEE Access*, vol. 7, pp. 114975–115001, 2019.
- [65] K. Gu, F. Wu and X. P. Zhang, "Sub-synchronous interactions in power systems with wind turbines: A review", *IET Renewable Power Generation*, vol. 13, no. 1, pp. 4–15, 2019.
- [66] X. Wang, M. G. Taul, H. Wu, Y. Liao, F. Blaabjerg and L. Harnefors, "Grid-Synchronization Stability of Converter-Based Resources—An Overview", *IEEE Open Journal of Industry Applications*, vol. 1, pp. 115–134, 2020.
- [67] M. Ahmed, L. Meegahapola, A. Vahidnia and M. Datta, "Stability and Control Aspects of Microgrid Architectures-A Comprehensive Review", *IEEE Access*, vol. 8, pp. 144730–144766, 2020.
- [68] J. Enslin and P. Heskes, "Harmonic interaction between a large number of distributed power inverters and the distribution network", *IEEE Transactions on Power Electronics*, vol. 19, no. 6, pp. 1586–1593, 2004.
- [69] J. L. Agorreta, M. Borrega, J. López and L. Marroyo, "Modeling and control of N-parallel grid-connected inverters with LCL filter coupled due to grid impedance in PV plants", *IEEE Transactions on Power Electronics*, vol. 26, no. 3, pp. 770–785, 2011.
- [70] J. He, Y. W. Li, D. Bosnjak and B. Harris, "Investigation and Active Damping of Multiple Resonances in a Parallel-Inverter-Based Microgrid", *IEEE Transactions on Power Electronics*, vol. 28, no. 1, pp. 234–246, Jan. 2013.
- [71] C. Li, "Unstable Operation of Photovoltaic Inverter from Field Experiences", *IEEE Transactions on Power Delivery*, vol. 33, no. 2, pp. 1013–1015, 2017.
- [72] H. Liu, X. Xie, J. He, T. Xu and Z. Yu, "Subsynchronous Interaction Between Direct-Drive PMSG Based Wind Farms and Weak AC Networks", *IEEE Transactions on Power Systems*, vol. 32, no. 6, pp. 4708–4720, 2017.
- [73] L. Wang, X. Xie, Q. Jiang, H. Liu, Y. Li and H. Liu, "Investigation of SSR in Practical DFIG-Based Wind Farms Connected to a Series-Compensated Power System", *IEEE Transactions on Power Systems*, vol. 30, no. 5, pp. 2772–2779, 2015.

- [74] L. C. . Gross, "Sub-Synchronous Grid Conditions: New Event, New Problem, and New Solutions", in Proc. *37th Annual Western Protective Relay Conference*, pp. 1–19, Spokane, USA, 2010.
- [75] J. Sun, M. Xu, M. Cespedes, D. Wong and M. Kauffman, "Modeling and analysis of data center power system stability by impedance methods", in Proc. *2019 IEEE Energy Conversion Congress and Exposition*, pp. 107–116, Baltimore, USA, 2019.
- [76] R. Yan, N. Al-Masood, T. Kumar Saha, F. Bai and H. Gu, "The anatomy of the 2016 South Australia blackout: A catastrophic event in a high renewable network", *IEEE Transactions on Power Systems*, vol. 33, no. 5, pp. 5374–5388, 2018.
- [77] P. Kundur, "*Power System Stability and Control*". McGraw-Hill, 1994, 1176 pages.
- [78] P. Kundur, J. Paserba, V. Ajarapu, G. Andersson, A. Bose, C. Canizares, N. Hatzia-rygiou, D. Hill, A. Stankovic, C. Taylor, T. Van Cutsem and V. Vittal, "Definition and classification of power system stability", *IEEE Transactions on Power Systems*, vol. 19, no. 3, pp. 1387–1401, 2004.
- [79] J. Machowski, Z. Lubosny, J. W. Bialek and J. R. Bumby, "*Power System Dynamics: Stability and Control*". Wiley, 2020, 888 pages.
- [80] X. Wang, F. Blaabjerg and W. Wu, "Modeling and Analysis of Harmonic Stability in an AC Power-Electronics-Based Power System", *IEEE Transactions on Power Electron-ics*, vol. 29, no. 12, pp. 6421–6432, Dec. 2014.
- [81] J. Sun, "Impedance-based stability criterion for grid-connected inverters", *IEEE Trans-actions on Power Electronics*, vol. 26, no. 11, pp. 3075–3078, 2011.
- [82] M. Amin and M. Molinas, "Small-Signal Stability Assessment of Power Electronics based Power Systems: A Discussion of Impedance- and Eigenvalue-based Methods", *IEEE Transactions on Industry Applications*, vol. 53, no. 5, pp. 5014–5030, 2017.
- [83] J. Schoukens, K. Godfrey and M. Schoukens, "Nonparametric Data-Driven Modeling of Linear Systems: Estimating the Frequency Response and Impulse Response Func-tion", *IEEE Control Systems*, vol. 38, no. 4, pp. 49–88, 2018.
- [84] R. Pintelon and J. Schoukens, "*System Identification - A Frequency Domain Approach*". John Wiley & Sons, 2001, 787 pages.
- [85] K. Godfrey, "*Perturbation Signals for System Identification*". Prentice Hall, UK, 1993, 421 pages.
- [86] T. Roinila, M. Vilkkko and J. Sun, "Broadband methods for online grid impedance measurement", in Proc. *2013 IEEE Energy Conversion Congress and Exposition*, pp. 3003–3010, Denver, USA, 2013.

- [87] Z. Liu, J. Liu and Z. Liu, "Analysis, Design, and Implementation of Impulse-Injection-Based Online Grid Impedance Identification with Grid-Tied Converters", *IEEE Transactions on Power Electronics*, vol. 35, no. 12, pp. 12959–12976, 2020.
- [88] M. Cespedes and J. Sun, "Online grid impedance identification for adaptive control of grid-connected inverters", in Proc. *2012 IEEE Energy Conversion Congress and Exposition*, pp. 914–921, Raleigh, USA, 2012.
- [89] D. Martin, E. Santi and A. Barkley, "Wide Bandwidth System Identification of AC System Impedances by Applying Perturbations to an Existing Converter", in Proc. *2011 IEEE Energy Conversion Congress and Exposition*, pp. 2549–2556, Phoenix, USA, 2011.
- [90] T. Roinila, H. Abdollahi, S. Arrua and E. Santi, "Adaptive Control of DC Power Distribution Systems: Applying Pseudo-Random Sequences and Fourier Techniques", in Proc. *2018 International Power Electronics Conference*, pp. 1719–1723, Niigata, Japan, 2018.
- [91] T. Messo, T. Roinila, A. Aapro and P. Rasilo, "Evaluation of Dead-Time Effect of Grid-Connected Inverters Using Broadband Methods", in Proc. *IFAC PapersOnLine*, vol. 51, no. 15, pp. 449–454, Stockholm, Sweden, 2018.
- [92] N. O. Sokal, "System oscillations from negative input resistance at power input port of switching-mode regulator, amplifier, DC/DC converter, or DC/DC inverter", in Proc. *1973 IEEE Power Electronics Specialists Conference*, pp. 138–140, Pasadena, USA, 1973.
- [93] Y. Yu and J. J. Biess, "Some design aspects concerning input filters for DC-DC converters", in Proc. *1971 IEEE Annual Power Electronics Specialists Conference*, no. 2, pp. 66–76, Pasadena, USA, 1971.
- [94] A. G. J. Macfarlane and I. Postlethwaite, "The generalized nyquist stability criterion and multivariable root loci", *International Journal of Control*, vol. 25, no. 1, pp. 81–127, 1977.
- [95] D. Middlebrook, "Input filter considerations in design and applications of switching regulators", pp. 91–107, 1976.
- [96] M. Belkhat, "Stability criteria for AC power systems with regulated loads", Doctoral thesis, Purdue University, 1997, pages 1–122.
- [97] B. Wen, D. Boroyevich, R. Burgos, P. Mattavelli and Z. Shen, "Analysis of D-Q Small-Signal Impedance of Grid-Tied Inverters", *IEEE Transactions on Power Electronics*, vol. 31, no. 1, pp. 675–687, 2016.
- [98] E. A. A. Coelho, P. C. Cortizo and P. F. D. Garcia, "Small-signal stability for parallel-connected inverters in stand-alone AC supply systems", *IEEE Transactions on Industry Applications*, vol. 38, no. 2, pp. 533–542, 2002.

- [99] G. O. Kalcon, G. P. Adam, O. Anaya-lara, S. Lo and K. Uhlen, "Small-Signal Stability Analysis of Multi-Terminal VSC-Based DC Transmission Systems", *IEEE Transactions on Power Electronics*, vol. 27, no. 4, pp. 1818–1830, 2012.
- [100] T. Messo, R. Luhtala, A. Aapro and T. Roinila, "Accurate Impedance Model of Grid-Connected Inverter for Small-Signal Stability Assessment in High-Impedance Grids", Niigata, Japan, 2018.
- [101] B. Shakerighadi, E. Ebrahimzadeh, F. Blaabjerg and C. L. Bak, "Lyapunov- and Eigenvalue-based Stability Assessment of the Grid-connected Voltage Source Converter", in Proc. *2018 IEEE International Power Electronics and Application Conference and Exposition*, pp. 18–23, Shenzhen, China, 2018.
- [102] A. M. Lyapunov, "The general problem of the stability of motion", *International Journal of Control*, vol. 55, no. 3, pp. 531–534, Mar. 1992.
- [103] Z. Shuai, Y. Hu, Y. Peng, C. Tu and Z. J. Shen, "Dynamic Stability Analysis of Synchronverter-Dominated Microgrid Based on Bifurcation Theory", *IEEE Transactions on Industrial Electronics*, vol. 64, no. 9, pp. 7467–7477, Sep. 2017.
- [104] V. Ajjarapu and B. Lee, "Bifurcation theory and its application to nonlinear dynamical phenomena in an electrical power system", *IEEE Transactions on Power Systems*, vol. 7, no. 1, pp. 424–431, 1992.
- [105] A. U. Rahman, I. Syed and M. Ullah, "Small-Signal Stability Criteria in AC Distribution Systems — A Review", *Electronics*, vol. 8, no. 2, pp. 1–18, 2019.
- [106] G. C. Verghese, F. C. Scheweppe, E. Power and S. Engineering, "Selective Modal Analysis With Applications to Electric Power Systems, Part II: The Dynamic Stability Problem", *IEEE Transactions on Power Apparatus and Systems*, vol. PAS-101, no. 9, pp. 3126–3134, 1982.
- [107] Y. Wang, X. Wang, F. Blaabjerg and Z. Chen, "Harmonic instability assessment using state-space modeling and participation analysis in inverter-fed power systems", *IEEE Transactions on Industrial Electronics*, vol. 64, no. 1, pp. 806–816, 2017.
- [108] D. Yang and X. Wang, "Unified Modular State-Space Modeling of Grid-Connected Voltage-Source Converters", *IEEE Transactions on Power Electronics*, vol. 35, no. 9, pp. 9700–9715, 2020.
- [109] M. Amin, J. A. Suul, S. D'Arco, E. Tedeschi and M. Molinas, "Impact of state-space modelling fidelity on the small-signal dynamics of VSC-HVDC systems", in Proc. *11th IET International Conference on AC and DC Power Transmission*, pp. 1–11, Birmingham, UK, 2015.
- [110] J. Z. Zhou, H. Ding, S. Fan, Y. Zhang and A. M. Gole, "Impact of short circuit ratio and phase locked loop parameters on the small signal behavior of a VSC HVDC converter", *IEEE Transactions on Power Delivery*, vol. 29, no. 5, pp. 2287–2296, 2014.

- [111] M. Lu, A. Al-Durra, S. M. Muyeen, S. Leng, P. C. Loh and F. Blaabjerg, "Benchmarking of Stability and Robustness against Grid Impedance Variation for LCL-Filtered Grid-Interfacing Inverters", *IEEE Transactions on Power Electronics*, vol. 33, no. 10, pp. 9033–9046, 2018.
- [112] G. Yan, Y. Cai, Q. Jia, Y. Li and S. Liang, "Stability analysis and operation control of photovoltaic generation system connected to weak grid", in Proc. *2017 IEEE Conference on Energy Internet and Energy System Integration*, pp. 1–6, Beijing, China, 2017.
- [113] Y. Wang, X. Wang, F. Blaabjerg and Z. Chen, "Small-Signal Stability Analysis of Inverter-Fed Power Systems Using Component Connection Method", *IEEE Transactions on Smart Grid*, vol. 9, no. 5, pp. 5301–5310, 2017.
- [114] A. Rodríguez-Cabero and M. Prodanovic, "Stability analysis for weak grids with power electronics interfaces", in Proc. *42nd Annual Conference of the IEEE Industrial Electronics Society*, pp. 2402–2407, Florence, Italy, 2016.
- [115] E. Ebrahimzadeh, F. Blaabjerg, X. Wang and C. L. Bak, "Harmonic Stability and Resonance Analysis in Large PMSG-Based Wind Power Plants", *IEEE Transactions on Sustainable Energy*, vol. 9, no. 1, pp. 12–23, 2017.
- [116] J. R. Massing, G. G. Koch, A. T. Pereira, H. Pinheiro, V. F. Montagner and R. C. Oliveira, "Modeling and stability analysis of current controllers for multi-paralleled grid-connected converters with LCL-filter", in Proc. *18th Workshop on Control and Modeling for Power Electronics*, pp. 1–7, Stanford, USA, 2017.
- [117] J. Beerten, S. D'Arco and J. A. Suul, "Identification and Small-Signal Analysis of Interaction Modes in VSC MTDC Systems", *IEEE Transactions on Power Delivery*, vol. 31, no. 2, pp. 888–897, 2016.
- [118] F. Ackermann, N. Bihler and S. Rogalla, "Stability prediction and stability enhancement for large-scale PV Power plants", in Proc. *7th International Symposium on Power Electronics for Distributed Generation Systems*, pp. 1–7, Vancouver, Canada, 2016.
- [119] Z. Yang, C. Bendfeld, J. Qiang, B. Mortimer and R. W. De Doncker, "Stability Investigation of Large-Scale PV Parks with Eigenvalue-Based Method", in Proc. *22nd European Conference on Power Electronics and Applications*, pp. 1–10, Lyon, France, 2020.
- [120] N. Pogaku, M. Prodanović and T. C. Green, "Modeling, analysis and testing of autonomous operation of an inverter-based microgrid", *IEEE Transactions on Power Electronics*, vol. 22, no. 2, pp. 613–625, 2007.
- [121] A. Rodríguez-Cabero and M. Prodanovic, "Stability analysis for weak meshed networks with power electronics-based distributed generation", in Proc. *43rd Annual Conference of the IEEE Industrial Electronics Society*, pp. 1569–1574, Beijing, China, 2017.

- [122] A. Rodriguez-Cabero, J. Roldan-Perez and M. Prodanovic, "Small-Signal Modelling and Control Design of VSCs in Multi-Terminal Railway Applications", in Proc. *2018 IEEE Energy Conversion Congress and Exposition*, pp. 2222–2227, Portland, USA, 2018.
- [123] B. Wen, D. Boroyevich, R. Burgos, P. Mattavelli and Z. Shen, "Small-Signal Stability Analysis of Three-Phase AC Systems in the Presence of Constant Power Loads Based on Measured d-q Frame Impedances", *IEEE Transactions on Power Electronics*, vol. 30, no. 10, pp. 5952–5963, 2015.
- [124] W. Cao, K. Liu, S. Wang, H. Kang, D. Fan and J. Zhao, "Harmonic Stability Analysis for Multi-Parallel Inverter-Based Grid-Connected Renewable Power System Using Global Admittance", *Energies*, vol. 12, no. 14, pp. 2687, Jul. 2019.
- [125] A. Riccobono, M. Cupelli, A. Monti, E. Santi, T. Roinila, H. Abdollahi, S. Arrua and R. A. Dougal, "Stability of shipboard dc power distribution: Online impedance-based systems methods", *IEEE Electrification Magazine*, vol. 5, no. 3, pp. 55–67, 2017.
- [126] T. Roinila, T. Messo, R. Luhtala, R. Scharrenberg, E. C. De Jong, A. Fabian and Y. Sun, "Hardware-in-the-Loop Methods for Real-Time Frequency-Response Measurements of on-Board Power Distribution Systems", *IEEE Transactions on Industrial Electronics*, vol. 66, no. 7, pp. 5769–5777, 2019.
- [127] A. Riccobono, M. Mirz and A. Monti, "Noninvasive Online Parametric Identification of Three-Phase AC Power Impedances to Assess the Stability of Grid-Tied Power Electronic Inverters in LV Networks", *IEEE Journal of Emerging and Selected Topics in Power Electronics*, vol. 6, no. 2, pp. 629–647, 2018.
- [128] R. D. Middlebrook, "Measurement of loop gain in feedback systems", *International Journal of Electronics*, vol. 38, no. 4, pp. 485–512, Apr. 1975.
- [129] H. Abdollahi, A. Khodamoradi, E. Santi and P. Mattavelli, "Online Bus Impedance Estimation and Stabilization of DC Power Distribution Systems: A Method Based on Source Converter Loop-Gain Measurement", in Proc. *2020 IEEE Applied Power Electronics Conference and Exposition*, pp. 3371–3378, New Orleans, USA, 2020.
- [130] T. Roinila, H. Abdollahi, S. Arrua and E. Santi, "Real-Time Stability Analysis and Control of Multiconverter Systems by Using MIMO-Identification Techniques", *IEEE Transactions on Power Electronics*, vol. 34, no. 4, pp. 3948–3957, Apr. 2019.
- [131] M. Shirazi, R. Zane and D. Maksimovic, "An Autotuning Digital Controller for DC–DC Power Converters Based on Online Frequency-Response Measurement", *IEEE Transactions on Power Electronics*, vol. 24, no. 11, pp. 2578–2588, Nov. 2009.
- [132] R. Luhtala, H. Alenius and T. Roinila, "Adaptive Optimization of Current-Control Loop for Grid-Connected Inverters", in Proc. *2020 IEEE Applied Power Electronics Conference and Exposition*, pp. 1897–1903, New Orleans, USA, 2020.

- [133] Y. Hu, S. Bu, B. Zhou, Y. Liu and C.-W. Fei, "Impedance-Based Oscillatory Stability Analysis of High Power Electronics-Penetrated Power Systems—A Survey", *IEEE Access*, vol. 7, pp. 120774–120787, 2019.
- [134] B. Wen, D. Boroyevich, R. Burgos, P. Mattavelli and Z. Shen, "Inverse Nyquist Stability Criterion for Grid-Tied Inverters", *IEEE Transactions on Power Electronics*, vol. 32, no. 2, pp. 1548–1556, 2017.
- [135] M. Amin and M. Molinas, "A Gray-Box Method for Stability and Controller Parameter Estimation in HVDC-Connected Wind Farms Based on Nonparametric Impedance", *IEEE Transactions on Industrial Electronics*, vol. 66, no. 3, pp. 1872–1882, Mar. 2019.
- [136] R. Luhtala, T. Roinila and T. Messo, "Implementation of Real-Time Impedance-Based Stability Assessment of Grid-Connected Systems Using MIMO-Identification Techniques", *IEEE Transactions on Industry Applications*, vol. 54, no. 5, pp. 5054–5063, 2018.
- [137] T. Reinikka, H. Alenius, T. Roinila and T. Messo, "Power Hardware-in-the-Loop Setup for Stability Studies of Grid-Connected Power Converters", in Proc. *2018 International Power Electronics Conference*, pp. 1704–1710, Niigata, Japan, 2018.
- [138] J. Xu, B. Zhang, Q. Qian, X. Meng and S. Xie, "Robust Control and Design Based on Impedance- Based Stability Criterion for Improving Stability and Harmonics Rejection of Inverters in Weak Grid", in Proc. *2017 IEEE Applied Power Electronics Conference and Exposition*, pp. 3619–3624, Tampa, USA, 2017.
- [139] D. Yang, X. Ruan and H. Wu, "Impedance shaping of the grid-connected inverter with LCL filter to improve its adaptability to the weak grid condition", *IEEE Transactions on Power Electronics*, vol. 29, no. 11, pp. 5795–5805, 2014.
- [140] C. Zou, H. Rao, S. Xu, Y. Li, W. Li, J. Chen, X. Zhao, Y. Yang and B. Lei, "Analysis of Resonance between a VSC-HVDC Converter and the AC Grid", *IEEE Transactions on Power Electronics*, vol. 33, no. 12, pp. 10157–10168, 2018.
- [141] B. Wen, D. Boroyevich, P. Mattavelli, Z. Shen and R. Burgos, "Experimental verification of the Generalized Nyquist stability criterion for balanced three-phase ac systems in the presence of constant power loads", in Proc. *2012 IEEE Energy Conversion Congress and Exposition*, pp. 3926–3933, Raleigh, USA, 2012.
- [142] A. Rygg, M. Molinas, C. Zhang and X. Cai, "On the equivalence and impact on stability of impedance modelling of power electronic converters in different domains", *IEEE Journal of Emerging and Selected Topics in Power Electronics*, vol. 5, no. 4, pp. 1444–1454, 2017.

- [143] M. Bakhshizadeh, C. Yoon, J. Hjerrild, C. L. Bak, Ł. H. Kocewiak, F. Blaabjerg and B. Hesselbæk, "The Application of Vector Fitting to Eigenvalue-Based Harmonic Stability Analysis", *IEEE Journal of Emerging and Selected Topics in Power Electronics*, vol. 5, no. 4, pp. 1487–1498, 2017.
- [144] M. K. Bakhshizadeh, F. Blaabjerg, J. Hjerrild, Ł. Kocewiak and C. Leth Bak, "Improving the Impedance Based Stability Criterion by Using the Vector Fitting Method", *IEEE Transactions on Energy Conversion*, vol. 33, no. 4, pp. 1739–1747, Dec. 2018.
- [145] X. Zou, X. Du and G. Wang, "Modeling and stability analysis for multiple parallel grid-connected inverters system", in Proc. *2018 IEEE Applied Power Electronics Conference and Exposition*, pp. 2431–2436, San Antonio, USA, 2018.
- [146] W. Cao, S. Wang, H. Kang, K. Liu, Q. Wang and J. Zhao, "Inherent interaction analysis for harmonic oscillations in the multi-paralleled grid-connected inverter system using a sum type criterion: Global admittance (GA)", *IEEE Access*, vol. 8, pp. 8275–8285, 2020.
- [147] S. Vesti, T. Suntio, J. A. Oliver, R. Prieto and J. A. Cobos, "Impedance-based stability and transient-performance assessment applying maximum peak criteria", *IEEE Transactions on Power Electronics*, vol. 28, no. 5, pp. 2099–2104, 2013.
- [148] T. Reinikka, T. Roinila, R. Luhtala and T. Messo, "Impedance-Based Sensitivity-Criterion for Grid-Connected Three-Phase Inverters", in Proc. *2018 IEEE Energy Conversion Congress and Exposition*, pp. 4173–4178, Portland, USA, 2018.
- [149] R. Luhtala, H. Alenius and T. Roinila, "Practical Implementation of Adaptive SRF-PLL for Three-Phase Inverters Based on Sensitivity Function and Real-Time Grid-Impedance Measurements", *Energies*, vol. 13, no. 5, pp. 1173, Mar. 2020.
- [150] R. Burgos, D. Boroyevich, F. Wang, K. Karimi and G. Francis, "On the Ac stability of high power factor three-phase rectifiers", in Proc. *2010 IEEE Energy Conversion Congress and Exposition*, pp. 2047–2054, Atlanta, USA, 2010.
- [151] T. Messo, J. Jokipii, A. Mäkinen and T. Suntio, "Modeling the grid synchronization induced negative-resistor-like behavior in the output impedance of a three-phase photovoltaic inverter", in Proc. *4th IEEE International Symposium on Power Electronics for Distributed Generation Systems*, pp. 1–7, Rogers, USA, 2013.
- [152] T. Roinila, T. Messo and E. Santi, "MIMO-identification techniques for rapid impedance-based stability assessment of three-phase systems in DQ Domain", *IEEE Transactions on Power Electronics*, vol. 33, no. 5, pp. 4015–4022, 2018.
- [153] Y. Cho, K. Hur, Y. C. Kang and E. Muljadi, "Impedance-based stability analysis in grid interconnection impact study owing to the increased adoption of converter-interfaced generators", *Energies*, vol. 10, no. 9, 2017.

- [154] A. Rygg, "Impedance-based methods for small-signal analysis of systems dominated by power electronics", Ph.D. dissertation, Norwegian University of Science and Technology, 2018.
- [155] H. Gong, D. Yang and X. Wang, "Identification of the DQ impedance model for three-phase power converter considering the coupling effect of the grid impedance", in Proc. *2019 IEEE Applied Power Electronics Conference and Exposition*, pp. 120–126, Anaheim, USA, 2019.
- [156] H. Gong, X. Wang and D. Yang, "DQ-Frame Impedance Measurement of Three-Phase Converters Using Time-Domain MIMO Parametric Identification", *IEEE Transactions on Power Electronics*, vol. 36, no. 2, pp. 2131–2142, Feb. 2021.
- [157] X. Chen, J. Chen, C. Gong and H. Wang, "Impedance-based analysis of grid-connected inverter in high impedance grids", in Proc. *8th Conference on Industrial Electronics and Applications*, pp. 1284–1289, Melbourne, Australia, 2013.
- [158] A. Suarez, C. Blanco, P. Garcia, A. Navarro-Rodriguez, J. Manuel and C. Rodriguez, "Online Impedance Estimation in AC Grids Considering Parallel-Connected Converters", in Proc. *2018 IEEE Energy Conversion Congress and Exposition*, pp. 5912–5919, Portland, USA, 2018.
- [159] M. Jaksic, Z. Shen, I. Cvetkovic, D. Boroyevich, R. Burgos, C. DiMarino and F. Chen, "Medium-Voltage Impedance Measurement Unit for Assessing the System Stability of Electric Ships", *IEEE Transactions on Energy Conversion*, vol. 32, no. 2, pp. 829–841, 2017.
- [160] J. Siegers, E. Santi and A. Barkley, "Wide bandwidth system identification of MVDC distribution system by applying perturbations to an existing converter", in Proc. *2013 IEEE Electric Ship Technologies Symposium*, pp. 434–441, Arlington, USA, 2013.
- [161] A. S. Morched and P. Kundur, "Identification and Modelling of Load Characteristics at High Frequencies", *IEEE Transactions on Power Systems*, vol. 2, no. 1, pp. 153–159, 1987.
- [162] A. Girgis and R. McManis, "Frequency domain techniques for modeling distribution or transmission networks using capacitor switching induced transients", *IEEE Transactions on Power Delivery*, vol. 4, no. 3, pp. 1882–1890, Jul. 1989.
- [163] M. Harris, A. Kelley, J. Rhode and M. Baran, "Instrumentation for measurement of line impedance", in Proc. *1994 IEEE Applied Power Electronics Conference and Exposition*, pp. 887–893, Orlando, USA, 1994.
- [164] J. Rhode, A. Kelley and M. Baran, "Complete characterization of utilization-voltage power system impedance using wideband measurement", *IEEE Transactions on Industry Applications*, vol. 33, no. 6, pp. 1472–1479, 1997.

- [165] B. Palethorpe, M. Sumner and D. Thomas, "Power system impedance measurement using a power electronic converter", in Proc. *Ninth International Conference on Harmonics and Quality of Power Proceedings*, pp. 208–213, Orlando, USA, 2000.
- [166] M. Nagpal, W. Xu and J. Sawada, "Harmonic impedance measurement using three-phase transients", *IEEE Transactions on Power Delivery*, vol. 13, no. 1, pp. 272–277, 1998.
- [167] M. Cespedes and J. Sun, "Three-phase impedance measurement for system stability analysis", in Proc. *IEEE 14th Workshop on Control and Modeling for Power Electronics*, Salt Lake City, USA, 2013.
- [168] G. Francis, R. Burgos, D. Boroyevich, F. Wang and K. Karimi, "An algorithm and implementation system for measuring impedance in the D-Q domain", in Proc. *2011 IEEE Energy Conversion Congress and Exposition*, pp. 3221–3228, Phoenix, USA, 2011.
- [169] J. Huang, K. A. Corzine and M. Belkhaty, "Small-Signal Impedance Measurement of Power-Electronics-Based AC Power Systems Using Line-to-Line Current Injection", *IEEE Transactions on Power Electronics*, vol. 24, no. 2, pp. 445–455, 2009.
- [170] C. Zhang, M. Molinas, A. Rygg and X. Cai, "Impedance Network of Interconnected Power Electronics Systems: Impedance Operator and Stability Criterion", 2018.
- [171] R. Luhtala, T. Messo and T. Roinila, "Adaptive Control of Grid-Voltage Feedforward for Grid-Connected Inverters based on Real-Time Identifications of System Stability Margins", in Proc. *2018 International Power Electronics Conference*, pp. 1–8, Niigata, Japan, 2018.
- [172] M. Cespedes and J. Sun, "Adaptive control of grid-connected inverters based on on-line grid impedance measurements", *IEEE Transactions on Sustainable Energy*, vol. 5, no. 2, pp. 516–523, 2014.
- [173] Z. Staroszczyk, "A method for real-time, wide-band identification of the source impedance in power systems", *IEEE Transactions on Instrumentation and Measurement*, vol. 54, no. 1, pp. 377–385, 2005.
- [174] P. Garcia, M. Sumner, A. Navarro-Rodriguez, J. M. Guerrero and J. Garcia, "Observer-Based Pulsed Signal Injection for Grid Impedance Estimation in Three-Phase Systems", *IEEE Transactions on Industrial Electronics*, vol. 65, no. 10, pp. 7888–7899, 2018.
- [175] V. Behjat, A. Vahedi, A. Setayeshmehr, H. Borsi and E. Gockenbach, "Diagnosing shorted turns on the windings of power transformers based upon online FRA using capacitive and inductive couplings", *IEEE Transactions on Power Delivery*, vol. 26, no. 4, pp. 2123–2133, 2011.
- [176] Y. Lee and S. Han, "Real-Time Voltage Stability Assessment Method for the Korean Power System Based on Estimation of Thévenin Equivalent Impedance", *Applied Sciences*, vol. 9, no. 8, pp. 1671, Apr. 2019.

- [177] X. Chen, Y. Zhang, S. Wang, J. Chen and C. Gong, "Impedance-Phased Dynamic Control Method for Grid-Connected Inverters in a Weak Grid", *IEEE Transactions on Power Electronics*, vol. 32, no. 1, pp. 274–283, Jan. 2017.
- [178] H. Alenius, R. Luhtala, T. Messo and T. Roinila, "Autonomous reactive power support for smart photovoltaic inverter based on real-time grid-impedance measurements of a weak grid", *Electric Power Systems Research*, vol. 182, pp. 106207, 2020.
- [179] G. C. Verghese, M. E. Elbuluk and J. G. Kassakian, "A General Approach to Sampled-Data Modeling for Power Electronic Circuits", *IEEE Transactions on Power Electronics*, vol. PE-1, no. 2, pp. 76–89, 1986.
- [180] D. Maksimovic and R. Zane, "Small-signal discrete-time modeling of digitally controlled PWM converters", *IEEE Transactions on Power Electronics*, vol. 22, no. 6, pp. 2552–2556, 2007.
- [181] X. Yue, X. Wang and F. Blaabjerg, "Review of Small-Signal Modeling Methods Including Frequency-Coupling Dynamics of Power Converters", *IEEE Transactions on Power Electronics*, vol. 34, no. 4, pp. 3313–3328, 2018.
- [182] D. Maksimovic, A. M. Stankovic, V. Joseph Thottuvelil and G. C. Verghese, "Modeling and Simulation of Power Electronic Converters", *Proceedings of the IEEE*, vol. 89, no. 6, pp. 898–912, 2001.
- [183] R. D. Middlebrook and S. Cuk, "A general unified approach to modelling switching-converter power stages", in *Proc. 1976 IEEE Power Electronics Specialists Conference*, vol. 21, no. 1, pp. 18–34, Cleveland, USA, 1976.
- [184] N. M. Wereley and S. R. Hall, "Linear Time Periodic Systems: Transfer Function, Poles, Transmission Zeroes and Directional Properties", in *Proc. 1991 American Control Conference*, pp. 1179–1184, Boston, USA, 1991.
- [185] J. Kwon, X. Wang, C. L. Bak and F. Blaabjerg, "Harmonic instability analysis of single-phase grid connected converter using Harmonic State Space (HSS) modeling method", in *Proc. 2015 IEEE Energy Conversion Congress and Exposition*, pp. 2421–2428, Montreal, Canada, 2015.
- [186] N. M. Wereley, "Analysis and control of linear periodically time varying systems", Doctoral thesis, Massachusetts Institute of Technology, 1990.
- [187] J. Sun, "Small-signal methods for AC distributed power systems-A review", *IEEE Transactions on Power Electronics*, vol. 24, no. 11, pp. 2545–2554, 2009.
- [188] E. Clarke, "Circuit Analysis of A-C Power Systems; Symmetrical and Related Components". Wiley, 1943, 540 pages.

- [189] R. H. Park, "Two-reaction theory of synchronous machines generalized method of analysis-part I", *Transactions of the American Institute of Electrical Engineers*, vol. 48, no. 3, pp. 716–727, Jul. 1929.
- [190] C. K. Tse, "*Linear Circuit Analysis*". Addison-Wesley, 1998, 328 pages.
- [191] L. Jessen and F. W. Fuchs, "Investigation of renewable energy generation and load impact on the grid impedance at different points of connection in public low voltage grids to support grid integration of renewable energies", in Proc. *18th European Conference on Power Electronics and Applications*, Karlsruhe, Germany, 2016.
- [192] D. Dong, B. Wen, D. Boroyevich, P. Mattavelli and Y. Xue, "Analysis of phase-locked loop low-frequency stability in three-phase grid-connected power converters considering impedance interactions", *IEEE Transactions on Industrial Electronics*, vol. 62, no. 1, pp. 310–321, 2015.
- [193] F. Barakou, M. H. Bollen, S. Mousavi-Gargari, O. Lennerhag, P. A. Wouters and E. F. Steennis, "Impact of load modeling on the harmonic impedance seen from the transmission network", in Proc. *17th International Conference on Harmonics and Quality of Power*, pp. 283–288, Belo Horizonte, Brazil, 2016.
- [194] J. Meyer, P. Schegner, R. Stiegler, I. Röder and A. Belger, "Harmonic Resonances in Residential Low Voltage Networks Caused by Consumers Electronics", in Proc. *24th International Conference on Electricity Distribution*, pp. 1–5, 2017.
- [195] A. Knop and F. W. Fuchs, "High frequency grid impedance analysis by current injection", in Proc. *35th Annual Conference of IEEE Industrial Electronics*, pp. 536–541, Porto, Portugal, 2009.
- [196] J. Schoukens, P. Guillaume and Pinte, "Design of multisine excitations", in Proc. *International Conference on Control 1991*, pp. 638–643, Edinburgh, UK, 1991.
- [197] T. Roinila, M. Vilkkö, J. Sun and S. Member, "Online Grid Impedance Measurement Using Discrete-Interval Binary Sequence Injection", *IEEE Journal of Emerging and Selected Topics in Power Electronics*, vol. 2, no. 4, pp. 985–993, 2014.
- [198] T. Roinila, T. Messo, T. Suntio and M. Vilkkö, "Pseudo-Random Sequences in DQ-Domain Analysis of Feedforward Control in Grid-Connected Inverters", in Proc. *IFAC PapersOnLine*, vol. 48, no. 28, pp. 1301–1306, Beijing, China, 2015.
- [199] J. Koppinen, J. Kukkola and M. Hinkkanen, "Plug-In Identification Method for an LCL Filter of a Grid Converter", *IEEE Transactions on Industrial Electronics*, vol. 65, no. 8, pp. 6270–6280, 2018.
- [200] A. H. Tan and K. Godfrey, "*Industrial Process Identification: Perturbation Signal Design and Applications*". Springer, 2019, 217 pages.

- [201] W. Davies, "Using the binary maximum length sequence for the identification of system dynamics", *Proceedings of the Institution of Electrical Engineers*, vol. 114, no. 10, 1582–1584, 1967.
- [202] K. Godfrey, "Introduction to binary signals used in system identification", in *Proc. International Conference on Control 1991*, pp. 161–166, Edinburgh, UK, 1991.
- [203] C. Wildrick, F. Lee, B. Cho and B. Choi, "A method of defining the load impedance specification for a stable distributed power system", *IEEE Transactions on Power Electronics*, vol. 10, no. 3, pp. 280–285, May 1995.
- [204] Xiaogang Feng, Jinjun Liu and F. Lee, "Impedance specifications for stable DC distributed power systems", *IEEE Transactions on Power Electronics*, vol. 17, no. 2, pp. 157–162, Mar. 2002.
- [205] B. Gustavsen and A. Semlyen, "Rational Approximation of Frequency Domain Responses by Vector Fitting", *IEEE Transactions on Power Delivery*, vol. 14, no. 3, pp. 1052–1061, 1999.
- [206] B. Gustavsen, "Computer Code for Rational Approximation of Frequency Dependent Admittance Matrices", *IEEE Power Engineering Review*, vol. 22, no. 6, pp. 64, 2002.
- [207] B. Gustavsen and A. Semlyen, "A Robust Approach for System Identification in the Frequency Domain", *IEEE Transactions on Power Delivery*, vol. 19, no. 3, pp. 1167–1173, 2004.
- [208] T. Messo, R. Luhtala, T. Roinila, E. de Jong, R. Scharrenberg, T. Caldognetto, P. Mattavelli, Y. Sun and A. Fabian, "Using High-Bandwidth Voltage Amplifier to Emulate Grid-Following Inverter for AC Microgrid Dynamics Studies", *Energies*, vol. 12, no. 3, pp. 379, Jan. 2019.
- [209] R. Luhtala, T. Messo, T. Roinila, H. Alenius, E. de Jong, A. Burstein and A. Fabian, "Identification of Three-Phase Grid Impedance in the Presence of Parallel Converters", *Energies*, vol. 12, no. 14, pp. 2674, Jul. 2019.
- [210] H. Alenius, T. Roinila, R. Luhtala, T. Messo, A. Burstein, E. de Jong and A. Fabian, "Hardware-in-the-Loop Methods for Stability Analysis of Multiple Parallel Inverters in Three-Phase AC Systems", *IEEE Journal of Emerging and Selected Topics in Power Electronics*, Early Access, pp. 1–10, 2020.
- [211] H. Alenius, R. Luhtala and T. Roinila, "Combination of Orthogonal Injections in Impedance Measurements of Grid-Connected Systems", *IEEE Access*, vol. 8, pp. 178085–178096, 2020.
- [212] H. Alenius and T. Roinila, "Impedance-Based Stability Analysis of Paralleled Grid-Connected Rectifiers: Experimental Case Study in a Data Center", *Energies*, no. 8, vol. 13, pp. 1–15, 2020.

- [213] H. Alenius, R. Luhtala and T. Roinila, "Amplitude Design of Perturbation Signal in Frequency-Domain Analysis of Grid-Connected Systems", in Proc. *IFAC World Congress*, pp. 1–6, 2020.
- [214] H. Alenius, M. Berg, R. Luhtala and T. Roinila, "Stability and Performance Analysis of Grid-Connected Inverter Based on Online Measurements of Current Controller Loop", in Proc. *45th Annual Conference of the IEEE Industrial Electronics Society*, pp. 2013–2019, Lisbon, Portugal, 2019.
- [215] H. Alenius and T. Roinila, "Analysing the Damping of Grid-Connected Inverter by Applying Impedance-Based Sensitivity Function", in Proc. *46th Annual Conference of the IEEE Industrial Electronics Society*, pp. 1249–1254, Singapore, 2020, pp. 1249–1254, Singapore, 2020.
- [216] H. Alenius, M. Berg, R. Luhtala, T. Roinila and T. Messo, "Impedance-Based Stability Analysis of Multi-Parallel Inverters Applying Total Source Admittance", in Proc. *20th Workshop on Control and Modeling for Power Electronics*, pp. 1–8, Toronto, Canada, 2019.
- [217] R. Luhtala, H. Alenius, T. Messo and T. Roinila, "Online Frequency Response Measurements of Grid-Connected Systems in Presence of Grid Harmonics and Unbalance", *IEEE Transactions on Power Electronics*, vol. 35, pp. 3343–3347, 2020.

PUBLICATIONS

PUBLICATION

I

”Hardware-in-the-Loop Methods for Stability Analysis of Multiple Parallel Inverters in Three-Phase AC Systems”

H. Alenius, T. Roinila, R. Luhtala, T. Messo, A. Burstein, E. de Jong and A. Fabian

IEEE Journal of Emerging and Selected Topics in Power Electronics, Early Access, pp. 1–10, 2020

Publication reprinted with the permission of the copyright holders

Hardware-in-the-Loop Methods for Stability Analysis of Multiple Parallel Inverters in Three-Phase AC Systems

Henrik Alenius, *Member, IEEE*; Tomi Roinila, *Member, IEEE*; Roni Luhtala, *Member, IEEE*; Tuomas Messo, *Member, IEEE*; Andrew Burstein, *Member, IEEE*; Erik de Jong, *Senior Member, IEEE*; Alejandra Fabian

Abstract—Modern electric distribution systems typically contain several feedback-controlled parallel inverters that together form a complex power distribution system. Consequently, a number of issues related to stability arise due to interactions among multiple inverter subsystems. Recent studies have presented methods where the stability and other dynamic characteristics of a paralleled inverter system can be effectively analyzed using impedance measurements. This paper presents implementation techniques for a comprehensive online stability analysis of grid-connected paralleled inverters using power hardware-in-the-loop measurements based on an OPAL-RT real-time simulator. The analysis is based on simultaneous online measurements of current control loop gains of the inverters and the grid impedance, and aggregated terminal admittance measurements of the inverters. The analysis includes the measurement of the inverters' aggregated output impedance, inverters' loop gains, global minor loop gain, and grid impedance. The presented methods make it possible to rapidly evaluate the system on both global and local level in real time, thereby providing means for online stability monitoring or adaptive control of such systems. Experimental measurements are shown from a high-power energy distribution system recently developed at DNV GL, Arnhem, Netherlands.

Index Terms—Parallel inverters, Three-phase electric power, Power system stability, Frequency-domain analysis, Stability analysis.

I. INTRODUCTION

AN increasing number of applications of AC-distributed power systems have been made possible due to advances in semiconductor technologies and inverter topologies. These applications can be found in several new and emerging fields, including renewable energy generation [1], hybrid and electric vehicles [2], smart grids [3], electric aircrafts [4], and electric ships [5].

AC-distributed power systems are most often dependent on the operation of paralleled inverters. In some applications, such as large-scale photovoltaic or wind power plants, the system may include hundreds or even thousands of inverters operating in parallel for scaling up the total power generation capacity. Fig. 1 shows a typical configuration of multi-paralleled inverters connected to a power grid through a

point of common coupling (PCC). Usually, the inverters are individually designed based on the stability requirements of the inverter standalone operation. However, the use of multiple inverters in parallel results in dynamic interaction causing system performance degradation or even instability [6], as reported from distribution systems that include photovoltaic plants [7], wind power systems [8], [9], and data centers [10].

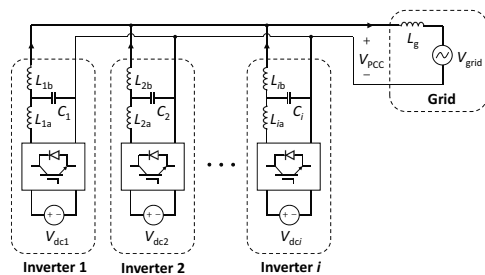


Fig. 1: Parallel grid-connected inverters.

Stability issues involved in multi-paralleled grid-connected inverters have been studied extensively in recent years. In [11], a small-signal stability assessment method was presented, where the stability is assessed based on the outermost voltage and frequency droops while neglecting the inner controller dynamics. The work in [12] presented a method in which multiple paralleled inverters were modeled as a multivariable system, where an equivalent inverter described the totality of multiple inverters. The work in [12] was based on the hypothesis that all of the current references of each inverter are the same. However, considering that the reference of each inverter is independently controlled, such as in a PV plant where current references vary along with maximum-power-point-tracking algorithm, the presented model lacks some essential physical significance and cannot comprehensively describe the characteristics of a PV plant. The authors in [13] applied a similar approach and presented models based on interactive current and common current to describe the interaction among multiple paralleled inverters.

Impedance-based small-signal analysis provides another method to evaluate the system stability [14], [15]. In this method, the impedances of source and load subsystems are measured and Nyquist stability criterion is applied to assess the system stability. While this method is characterized by

H. Alenius and T. Messo are with the Faculty of Information Technology and Communication Sciences, Tampere, Finland, email: henrik.alenius@tuni.fi; tuomas.messo@tuni.fi

T. Roinila and R. Luhtala are with the Faculty of Engineering and Natural Sciences, Tampere University, Tampere, Finland, email: tomi.roinila@tuni.fi; roni.luhtala@tuni.fi

A. Burstein, E. de Jong and A. Fabian are with the DNV GL, Arnhem, Netherlands, email: andrew.burstein@dnvgl.com; erik.dejong@dnvgl.com; alejandra.fabian@dnvgl.com

simplicity, it does not provide any information on the system internal stability poles [16]. The system's internal stability was considered by the authors in [17], which provided an interpretation of the stability analysis presented in [12] using the source and load impedances. An alternative method for the impedance-based analysis was presented in [18], where the stability of a grid-connected inverter was characterized by the measured load-affected current controller loop.

In many modern distribution systems, the high share of renewable production combined with multiple parallel inverters introduce changes to the power system [19]. Especially in micro grids, the system operation status and configuration may fluctuate along with changes in loading state, power generation, or grid topology. As a consequence, it may become challenging to predict the detailed system characteristics required in most stability analysis methods. In highly fluctuating conditions, a stability analysis based on typical operation status may be insufficient. To tackle this issue, real-time analysis methods based on continuous online measurements are highly desirable. The real-time stability indications can be applied in advanced system monitoring, fault prevention, or adaptive control. The online identification and analysis can be integrated into the inverter controllers applying digital analyzer techniques [20], [21].

The present paper considers real-time stability analysis of paralleled grid-connected inverters by utilizing an OPAL-RT power hardware-in-the-loop (PHIL) setup that was developed recently at DNV GL, Arnhem, Netherlands. The OPAL-RT is a multi-purpose real-time simulator that is widely used in real-time analysis and control of various power-electronics applications including wind-turbine emulation [22], fuel-cell modeling [23], and analysis of smart-grid performance [24]. A PHIL setup consists of a hardware-in-the-loop simulator, such as OPAL-RT, and power hardware, such as physical power cables and devices [25]. Recently, PHIL setups have been applied in versatile experimenting of various power-electric systems [26]–[28].

The primary goal of this work is to provide detailed steps towards implementing a comprehensive real-time stability analysis for a system that has multiple paralleled inverters connected to a grid. The second goal of the work is to present the proof-of-concept for online stability analysis performed with parallel approaches simultaneously, and to compare the obtained stability indications. The method includes simultaneous use of loop gain analysis and impedance-based analysis applying an online multivariable measurement. The concept is applied to an experimental system at 50 kW power level.

The remainder of the paper is organized as follows. Section II reviews the theory of the frequency-response identification using orthogonal wideband techniques applied in the paper. Section III introduces the experimental high-power PHIL setup recently developed at DNV GL and presents the implementation of the online frequency-response measurement method. Section IV presents experimental results based on paralleled high-power inverters connected to a high-impedance grid and operated with different controller tunings. Finally, Section V draws conclusions.

II. METHODS

A. Frequency-response measurement in the dq domain

Direct-quadrature (dq) transformation rotates the reference frame of three-phase systems in order to simplify the analysis of three-phase circuits. In the case of balanced three-phase circuits, the transformation reduces three AC quantities to two DC quantities, which makes it possible to utilize controllers with simpler structures and lower dynamic orders [29]. The dq-frame representation allows straightforward small-signal analysis as the non-linear characteristics can be linearized around the steady-state operation point [30].

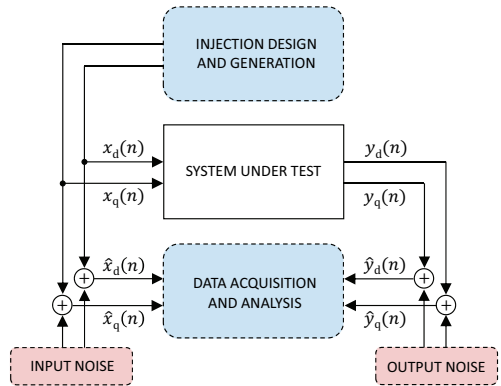


Fig. 2: Typical measurement setup.

Fig. 2 shows a typical measurement setup where the system under test is to be identified in the dq domain [31]. Examples of such identification include the output impedance of a three-phase inverter, inverter loop gain(s), and grid impedance [29]. In the setup, the system is perturbed by d- and q-component injections $x_d(n)$ and $x_q(n)$, which yield the corresponding output responses $y_d(n)$ and $y_q(n)$. The measured input and output signals, $[\hat{x}_d(n), \hat{x}_q(n)]$ and $[\hat{y}_d(n), \hat{y}_q(n)]$, are corrupted by input noise and output noise, respectively. The noise signals are assumed to resemble white noise and are uncorrelated with the other system variables. All of the signals are assumed to be zero mean sequences. The measured signals are buffered and segmented, and the signals are transformed to the frequency-domain by applying discrete Fourier transformation (DFT), given as

$$\hat{X}(j\omega) = \mathcal{F}\{\hat{x}(n)\} \quad (1)$$

where $\hat{X}(j\omega)$ is the signal transformed to the frequency domain. From the Fourier-transformed input and output signals, the frequency response (impedance or loop gain) can be obtained for each input/output pair by applying

$$G(j\omega) = \frac{\hat{Y}(j\omega)}{\hat{X}(j\omega)} \quad (2)$$

where $\hat{X}(j\omega)$ is the Fourier-transformed input signal and $\hat{Y}(j\omega)$ is the Fourier-transformed output signal. In impedance measurements, for example, the input is a current signal

(containing the nominal current and injected current perturbation) and the output is the resulting voltage signal. In noisy environments, the logarithmic averaging procedure [31] is often applied to compute the frequency response between desired variables as

$$G_{\log}(j\omega) = \left(\prod_{k=1}^P \frac{\hat{Y}_k(j\omega)}{\hat{X}_k(j\omega)} \right)^{1/P} \quad (3)$$

where P denotes the number of injected excitation periods. The method tends to cancel out the effect of uncorrelated noise from both input and output sides, so that the frequency response is obtained more accurately compared to conventional cross-correlation techniques [31]. In the dq-domain analysis the method is applied to each input-output couple, resulting in a 2×2 frequency-response matrix that represents a frequency response from each input (input d and q component) to each output (output d and q component). That is, the matrix includes the direct components as well as the cross-coupling components.

B. Maximum-length binary sequence

The perturbation design plays a very important role in obtaining the desired frequency response (or any other parametric or nonparametric system model) through the experiment described in Fig. 2. An optimal design leads to maximally informative experiments that is, experiments that extract the maximum amount of information and reduces operational costs associated with the identification procedure. For a linear-system identification of sensitive systems, a binary signal such as maximum-length pseudo-random binary sequence (MLBS) most often offers the best possible choice in terms of maximizing signal power within time-domain-amplitude constraints [32]. The MLBS is a periodic broadband signal that has a largely controllable spectral energy distribution, and consequently, the measurements can be averaged over multiple periods to increase the signal-to-noise ratio [32]. The averaging procedure enables accurate online measurements even with very small injection amplitude, which may be a requirement in sensitive systems where large injection amplitude, such as in impulse injection, may disrupt the system operation. Another major advantage of the MLBS over the other types of signals such as sinusoids is that the sequence can be implemented with a low-cost system whose output can only generate a small number of signal levels. Due to the several favorable characteristics, the MLBS has become a popular perturbation signal in stability analysis of both AC and DC power distribution systems [33]–[37].

C. Orthogonal perturbations

Considering the multiple-input-multiple-output (MIMO) system in Fig. 2, the inputs and outputs are most often coupled. For such a system, the conventional approach is to apply the superposition theorem to the frequency-response measurements, where the excitation signal is separately injected to each system input one at a time, and all the output responses are measured for each input excitation [31]. Then, (3) is applied to

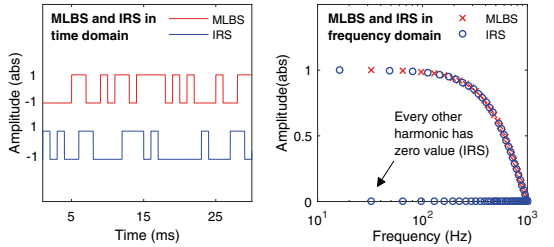


Fig. 3: Two orthogonal sequences (MLBS and IRS) in time and frequency domain.

each combination of input and output. However, the superposition approach requires multiple consecutive measurements, which increases the measurement time and may make the results prone to variations in the system under measurement. In this work, the MIMO system is measured applying orthogonal binary sequences, where multiple orthogonal injections are used to simultaneously excite all the system inputs. As the injections are orthogonal (that is, they have energy at different frequencies), the injections do not disturb each other and the MIMO system can be identified simultaneously within one measurement cycle [38]. Consequently, the technique has considerable advantages over the method using superposition theorem and sequential perturbations, as all the frequency responses are measured simultaneously under the same system operation conditions.

The synthesis of orthogonal (periodic) binary sequences has been well documented [32]. One of the most popular techniques is to apply a modulation with rows of a Hadamard matrix [38]–[40]. In this method, a periodic binary sequence, such as the maximum-length binary sequence (MLBS), is used as a base signal. The second signal is obtained by adding, modulo 2, the sequence $[0 \ 1 \ 0 \ 1 \ \dots]$ to the MLBS. The third signal is obtained by adding the sequence $[0 \ 0 \ 1 \ 1 \ 0 \ 0 \ 1 \ 1 \ \dots]$ to the MLBS, and so on. Note, that the sequence length of the i^{th} orthogonal sequence is doubled compared to the length of the $(i - 1)^{\text{th}}$ sequence.

Fig. 3 shows an example of two orthogonal binary sequences generated by the method. The length of the MLBS is 63 bits, and generated at 1 kHz. The second sequence is known as an inverse-repeat binary sequence (IRS) because the modulation inverts every other digit of the MLBS. As Fig. 3 shows, the energy of every other harmonic has zero value in the IRS, which means that the MLBS and IRS have energy at different frequencies.

III. SETUP IMPLEMENTATION

The power hardware-in-the-loop (PHIL) setup shown in Fig. 5 at DNV GL Flexible Power Grid Lab is made up of an Egston digital power amplifier and an OPAL-RT real-time digital simulator. The simulator is utilized to control the power amplifier, which consists of four groups of four single-phase units. The units have closed-loop bandwidth of 5 kHz and total rated power of 200 kVA. The individual digital power amplifier unit is implemented with six interleaved parallel half-bridge converters that have an equivalent switching frequency

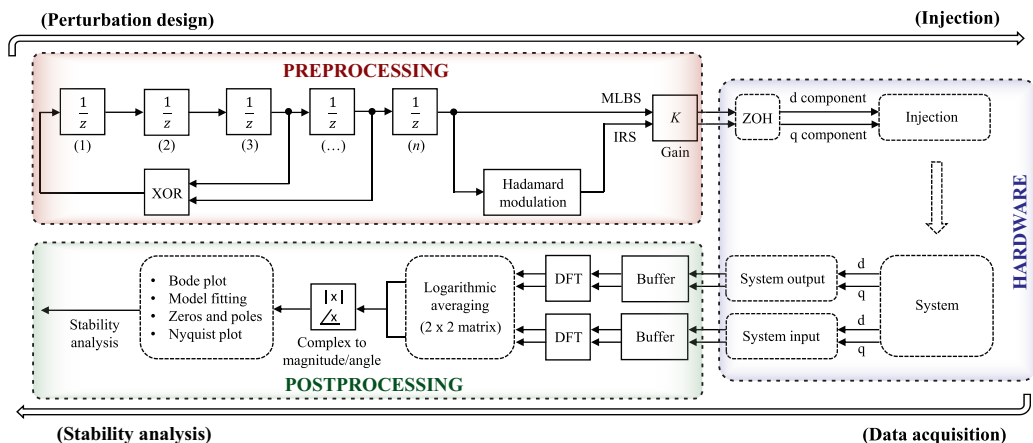


Fig. 4: Schematic of the pre- and postprocessing for the proposed real-time analysis method.

of 125 kHz. For the closed-loop PHIL setup, the high-speed communication link is established between real-time simulator and power amplifier. The current and voltage measurements are acquired from the output terminal of the digital amplifier to OPAL-RT every $4 \mu\text{s}$ while the voltage and current control signal setpoints are sent to Egston digital input/output box. A host PC is connected via asynchronous Ethernet to the OPAL-RT target PC. As shown in Fig. 5, the power amplifiers are isolated from the mains by a Dy transformer and 200 kW

active front-end. The power amplifiers can be freely configured to act as sources or loads depending on what kind of power system architecture is studied.

A. PHIL Implementation

Fig. 4 presents a schematic diagram of the proposed real-time method for system stability analysis, which is implemented in OPAL-RT. The diagram consists of three sections: preprocessing, actual hardware, and postprocessing. The preprocessing section is responsible for the injection design and synthesis, where the orthogonal wideband perturbation signals are generated. The MLBS is implemented through shift registers and exclusive-or feedback, where the unit-delay blocks have a delay that corresponds to the generation frequency [41]. The orthogonal inverse-repeated sequence (IRS) is similarly generated in shift registers by processing the MLBS through Hadamard modulation [32]. Then, the perturbations are simultaneously injected to the physical system to d and q components, and the input and output signals are continuously measured and buffered. The injection point is the current- or voltage-references of the device used in measurements; for example, the loop and grid impedance measurements are performed by superimposing the perturbation to the current reference of an inverter. In the postprocessing, the data sequences are Fourier-transformed and averaged by using (3) yielding the frequency-response data. The obtained frequency-response matrix is then (simultaneously) used to complete the Bode plot(s), Nyquist contour(s), system loop gains, and system poles and zeros. The refresh rate of the frequency-response matrix is PN/f_g , where P is the number of injection periods, N is the injection(s) length, and f_g is the injection(s) generation frequency. In this implementation, the postprocessing takes place in the OPAL-RT. In real implementations, however, the postprocessing can be integrated on the inverter controller structure, which also enables easy system scaling for higher number of inverters, as the computational effort for an independent inverter is unchanged. Online techniques

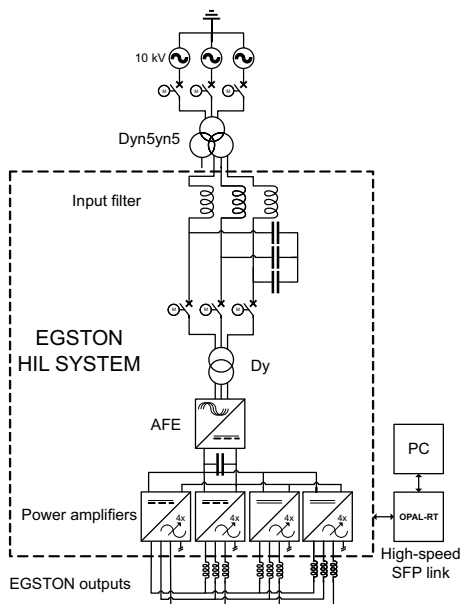


Fig. 5: PHIL setup in DNV GL Flexible Power Grid Lab.

and currents did not deviate from their nominal values by more than 5%. Considering the inherent harmonics present in most grids, the injection can be designed so that the decrease in power quality is negligible.

Three sets of experiments were performed to analyze the system stability in different conditions. In the experiments, the inverters' PLL bandwidth was tuned differently: in the first experiment the bandwidth was set to 20 Hz, in the second to 60 Hz, and finally in the last experiment to 85 Hz. As previously reported [43], increasing the PLL bandwidth in weak grid generally decreases the system robustness, and altering the PLL tuning was chosen so that the proposed approach can be tested in versatile stability conditions. In all experiments, the full 2x2 frequency-response matrix including the direct components (d and q) and cross-coupling components (dq and qd) was measured.

The experiments were performed by first utilizing the inverters in measurements (injection points 1 and 2 in Fig. 6), and then performing the grid measurements (injection point 3). The injection point in the inverter measurements allows measuring both the current controller loop gains and grid impedance simultaneously with the same injection. As a consequence, this process eliminates the need for separate measurements for loop gains and grid impedance. In the loop gain measurements, the input vector is the current controller reference $\mathbf{i}_{in} = [i_{in-d}, i_{in-q}]^T$ and the output vector is the current response $\mathbf{i}_o = [i_d, i_q]^T$ (as shown in Fig. 7). Similarly, in the grid impedance measurements, the output current \mathbf{i}_o is the excitation and the output vector is the voltage response $\mathbf{v}_{pcc} = [v_d, v_q]^T$. The measurements are sampled at 10 kHz and the impedances and loop gains are extracted from the measured signals by applying equations (1)-(3) to each input/output pair. In order to avoid spectral leakage, the measured signals are segmented to consist of 4094 samples for the MLBS-perturbed signals and 8188 samples for the IRS-perturbed signals (as the sampling frequency is twice as high as the generation frequency of the perturbations). At first, Inverter 2 was disconnected and the loop and impedance measurements were performed with Inverter 1. After this, Inverter 2 was reconnected and the injection was applied to Injection Point 2 to obtain the current control loop of the second inverter. It would have been possible to simultaneously measure the current loop gains from both inverters but this approach would have required the use of four orthogonal sequences. Finally, the injections were applied to Injection Point 3 for obtaining the aggregated output impedance of the paralleled inverters. In all measurements, (1) was applied over 100 injection periods for the MLBS and over 50 injection periods for the IRS (as the length of the IRS is doubled compared to the MLBS). The refreshment rate, which is equal to the duration of averaged measurement cycle, is 41 seconds during which the computation is performed. With modern inverter controllers, transfer function calculation and stability analysis can be easily performed within this time frame enabling real-time stability assessment. When very fast (millisecond range) measurement cycles are applied, the computational requirements become stricter and the hardware performance must be considered in the method tuning.

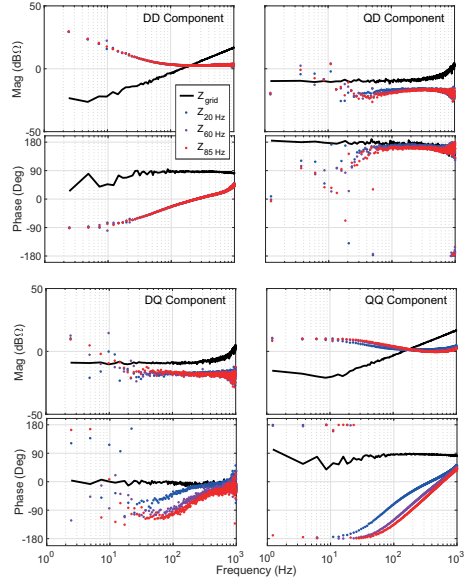


Fig. 8: Measured impedances of the grid (black) and the inverters with different PLL bandwidth tunings.

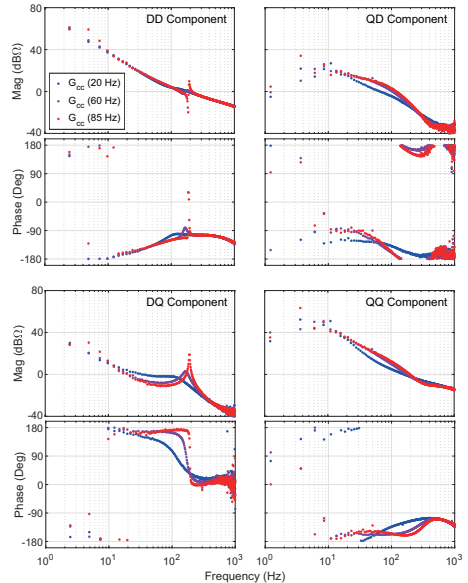


Fig. 9: Measured inverter 1 current controller loop gain with different PLL tunings.

Fig. 8 shows the measured inverters' aggregated output impedance and the grid impedance at the PCC for all the three different experiments. A simple approximate of the system robustness can be obtained by examining the qq-component of the impedances, where the phase margin at the intersection frequency indicates system stability margins. For

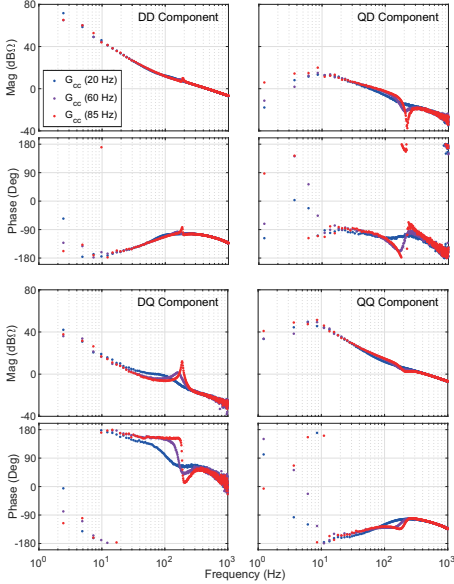


Fig. 10: Measured inverter 2 current controller loop gain with different PLL tunings.

the system with 20 Hz PLL bandwidths, the phase margin is approximately 57 degrees at the intersection frequency around 190 Hz. Increasing the bandwidth to 60 Hz reduces the phase margin to 13 degrees, and increase to 85 Hz decreases phase margin to 4 degrees indicating almost marginal stability. However, this single-input-single-output consideration ignores the inherent multivariable nature of the system, and reliable analysis requires the use of complete 2×2 matrices [6], which is presented in the following section. Similarly, the 2×2 matrices of the load-affected internal current control loops are shown in Fig. 9 for Inverter 1 and in Fig. 10 for Inverter 2.

C. Stability analysis

The stability analysis can be performed on the measured PCC impedances or internal loop gains, where similar methods can be applied. In this work, the stability analysis is performed by generalized Nyquist criterion (GNC) for the impedances, and pole-zero fitting for the internal loop gains. These methods can be applied simultaneously, as the measurements can be obtained with a single injection cycle as discussed previously. In the GNC, the distance from the eigenvalue contour to the critical point shows the system robustness. Fig. 11 presents the eigenvalue contours for the system for different experiments. A drastic change towards instability is seen when the PLL bandwidth is increased as the eigenvalue 1 contour shifts towards the critical point. With 85 Hz PLL bandwidth, the system is almost marginally stable.

In addition to the impedance-based GNC analysis, the system stability was analyzed through system poles and zeros. The poles and zeros were continuously calculated from the same impedance data, and additionally, from the internal

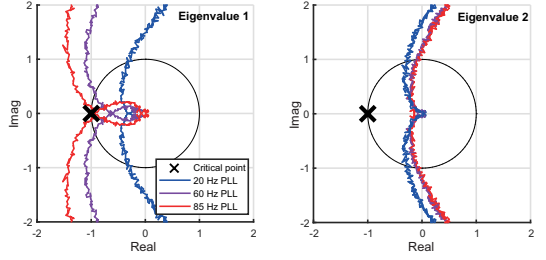


Fig. 11: Impedance-based Nyquist contours with different PLL tunings.

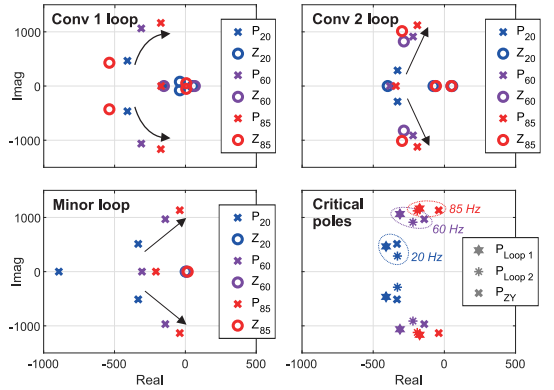


Fig. 12: Pole-zero maps based on measured minor loop gain and inverter current controller loops.

current controller loops for each inverter. Consequently, the method enabled the use of two parallel approaches. For evaluating the values of zeros and poles, parametric models were continuously estimated based on the measured loop gains [44]. Fig. 12 shows the estimated poles and zeros based on the minor loop (impedance ratio) and loop gains from inverters 1 and 2. The critical poles shown in bottom right subfigure shift towards the imaginary axis and approximately the same stability margins can be obtained through all the methods.

The use of parallel approaches increases the flexibility and usability of the stability analysis method, as both approaches have their advantages. The impedance-based approach excels in system-level analysis and monitoring, but becomes more time consuming in very complex systems with many inverters. On the other hand, the loop-gain-based analysis is readily available even in such systems, and additionally provides detailed information on individual-inverter level. This local data can be utilized in, for example, fault prevention by identifying the low-stability devices or in independent adaptive control of the inverters.

D. Time-domain verification

The presented methods assess the stability in the frequency domain, as the frequency-domain results are significantly more straightforward to derive. However, ultimately the interest on

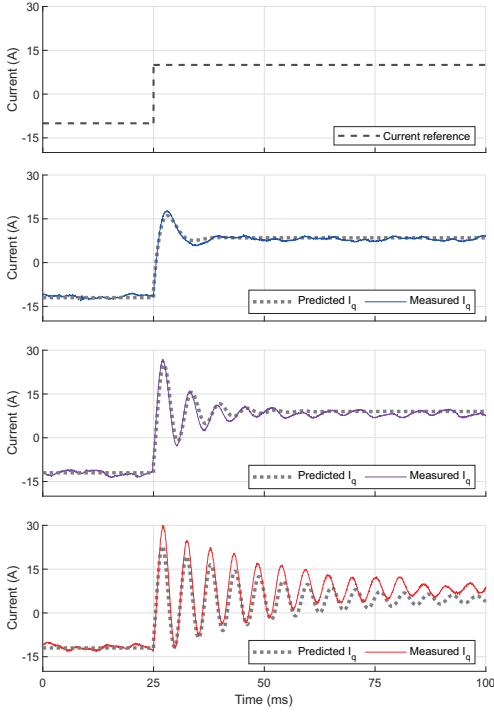


Fig. 13: Step response comparison.

system performance often relies in the time domain operation, and the frequency domain is applied as an auxiliary domain. In order to validate the obtained stability margins and to verify the proposed methodology, a comparison between transient performance of the actual system and the predicted stability margins is performed in the time domain. In the following analysis, the minor loop (impedance ratio) poles and zeros were used to construct the corresponding dynamics in the time domain by predicting the time-domain step response from the obtained frequency-domain margins. The validation was performed offline by first constructing transfer functions from the pole zero data (as shown in (4) in the footnote for the 85 Hz PLL system). Then, the time-domain prediction was obtained by applying MATLAB step-function on the pole-zero data, where the step response of a transfer function is calculated numerically. The calculated response is compared to the actual response of the experimental system which shown in Fig. 6.

Fig. 13 presents the predicted system behavior and the actual response to a step change in the current reference of the Inverter 1. The q channel current reference is changed from -10

$$G(s) = \frac{2.03e05 * (s + 3.57e03)(s + 1.99e03)}{(s + 1.31e06)(s + 3.89e01 + j1.15e03)(s + 3.89e01 - j1.15e03)} \\ = \frac{2.03e05s^2 + 1.13e09s + 1.45e12}{s^3 + 1.31e06s^2 + 1.03e08s + 1.74e12} \quad (4)$$

to 10 A, and the response is measured for all the test parameter sets. The figure shows that the actual system response is very accurately predicted with the proposed method, as both the oscillatory frequency and the damping ratio closely match the experimental waveform. A steady state error that persists after the oscillations have settled results from the minor deviations in the fitted locations of the poles and zeros, which accumulate to the DC-gain of the system. From the stability perspective, the significant characteristics that quantify the system stability are the overshoot, oscillatory frequency, and the damping ratio (that is, the rate of decay in the oscillations). With the proposed methods, these were accurately predicted even for the system that was close to marginal stability.

V. CONCLUSIONS

Paralleled inverters play an important role in the operation of most grid-connected system. A number of stability issues arise from the interactions among multiple inverter subsystems and the power grid. Recent studies have presented techniques, such as impedance-based analysis, to assess the stability and dynamic characteristics of multi-inverter systems. Frequency-response measurements are often required to extract information from these systems, as the internal dynamics of some subsystems may be unknown. Especially online methods for measurements are analysis are highly desirable, in order to provide real-time data on the system status, which can be utilized in advanced system monitoring, fault protection, and adaptive control. This paper has presented a practical real-time approach to perform a comprehensive stability analysis of a three-phase grid-connected system containing paralleled inverters by applying a power hardware-in-the-loop platform. The method applies orthogonal injections for multivariable system identification and utilizes parallel approaches for stability analysis by applying impedance-based analysis and loop-gain assessment simultaneously. Consequently, a detailed information can be obtained from both local and global point of view for holistic stability assessment. Experimental measurements were shown from a high-power energy distribution system recently developed at DNV GL, Arnhem, Netherlands. The presented methods can be used to modify various system characteristics, such as impedance behavior and control dynamics, in real time, thereby providing means for several stability and adaptive control design tools for grid-connected systems containing paralleled inverters.

ACKNOWLEDGEMENTS

This research and testing has been performed using the ERIGrid Research Infrastructure and is part of a project that has received funding from the European Union's Horizon 2020 Research and Innovation Programme under Grant Agreement No. 654113. The support of the European Research Infrastructure ERIGrid and its partner DNVGL is very much appreciated. The work was also supported in part by the Academy of Finland.

APPENDIX: EXPERIMENTAL SYSTEM SPECIFICATIONS

TABLE I: Parameters of the experimental setup.

Parameter	Symbol	Value
Grid frequency	f_g	50 Hz
Nominal main voltage (RMS)	V_n	400 V
Output power of inverters	P_{sp}	24.4 kW
Power factor of inverters	$\cos(\phi)$	1.00
D-current reference	i_d^*	50 A
Grid inductance	L_g	2.0 mH
Inverter 1 L-filter inductance	L_1	0.5 mH
Inverter 2 L-filter inductance	L_2	3.2 mH
Inverter 1 CC proportional gain	K_{CC1-P}	1.6514
Inverter 1 CC integral gain	K_{CC1-I}	518.8
Inverter 2 CC proportional gain	K_{CC2-P}	10.070
Inverter 2 CC integral gain	K_{CC2-I}	3162
20 Hz PLL proportional gain	$K_{PLL20-P}$	1.30
20 Hz PLL integral gain	$K_{PLL20-I}$	75.2
60 Hz PLL proportional gain	$K_{PLL60-P}$	3.90
60 Hz PLL integral gain	$K_{PLL60-I}$	676.4
85 Hz PLL proportional gain	$K_{PLL85-P}$	5.52
85 Hz PLL integral gain	$K_{PLL85-I}$	1358

REFERENCES

- [1] R. Karasani, V. Borghate, P. Meshram, H. Suryawanshi, and S. Sabyasachi, "A three-phase hybrid cascaded modular multilevel inverter for renewable energy environment," *IEEE Transactions on Power Electronics*, vol. 32, pp. 1070–1087, 2017.
- [2] T. Windisch and W. Hofmann, "A novel approach to MTPA tracking control of AC drives in vehicle propulsion systems," *IEEE Transactions on Vehicular Technology*, vol. 67, pp. 9294–9302, 2018.
- [3] F. Peng, "Flexible AC transmission systems (FACTS) and resilient AC distribution systems (RACDS) in smart grid," *Proceedings of the IEEE*, vol. 105, pp. 2099–2115, 2017.
- [4] V. Madonna, P. Giangrande, and M. Galea, "Electrical power generation in aircraft: Review, challenges, and opportunities," *IEEE Transactions on Transportation and Electrification*, vol. 4, pp. 646–659, 2018.
- [5] W. Liu, T. Tarasiuk, M. Gorniak, M. Savaghebi, J. Vasquez, C.-L. Su, and J. Guerrero, "Power quality assessment in shipboard microgrids under unbalanced and harmonic AC bus voltage," *IEEE Transactions on Industry Applications*, vol. 55, pp. 765–775, 2019.
- [6] T. Suntio, T. Messo, M. Berg, H. Alenius, T. Reinikka, R. Luhtala, and K. Zenger, "Impedance-Based Interactions in Grid-Tied Three-Phase Inverters in Renewable Energy Applications," *Energies*, vol. 12, no. 464, 2019.
- [7] C. Li, "Unstable operation of photovoltaic inverter from field experiences," *IEEE Transactions on Power Delivery*, vol. 33, pp. 1013–1015, 2017.
- [8] H. Liu, X. Xie, J. He, T. Xu, and Z. Yu, "Subsynchronous Interaction Between Direct-Drive PMSG Based Wind Farms and Weak AC Networks," *IEEE Transactions on Power Systems*, vol. 32, no. 6, pp. 4708–4720, 2017.
- [9] L. Wang, X. Xie, Q. Jiang, H. Liu, Y. Li, and H. Liu, "Investigation of SSR in Practical DFIG-Based Wind Farms Connected to a Series-Compensated Power System," *IEEE Transactions on Power Systems*, vol. 30, no. 5, pp. 2772–2779, 2015.
- [10] H. Alenius and T. Roinila, "Impedance-Based Stability Analysis of Paralleled Grid-Connected Rectifiers: Experimental Case Study in a Data Center," *Energies*, vol. 13, no. 2109, 2020.
- [11] E. A. A. Coelho, P. C. Cortizo, and P. F. D. Garcia, "Small-signal stability for parallel-connected inverters in stand-alone AC supply systems," *IEEE Transactions on Industry Applications*, vol. 38, no. 2, pp. 533–542, 2002.
- [12] J. Agorreta, M. Borrega, J. Lopez, and L. Marroyo, "Modeling and control of N-paralleled grid-connected inverters with LCL filter coupled due to grid impedance in PV plants," *IEEE Transactions on Power Electronics*, vol. 26, pp. 770–785, 2011.
- [13] M. Lu, X. Wang, F. Blaabjerg, and C. Loh, "An analysis method for harmonic resonance and stability of multi-paralleled lcl-filtered inverters," in *Proc. IEEE International Symposium on Power Electronics for Distributed Generation Systems*, 2015, pp. 1–6.
- [14] J. Sun, "Impedance-based stability criterion for grid-connected inverters," *IEEE Transactions on Power Electronics*, vol. 26, pp. 3075–3078, 2011.
- [15] T. Roinila and T. Messo, "Online grid-impedance measurement using ternary-sequence injection," *IEEE Transactions on Industry Applications*, vol. 54, pp. 5097–5103, 2018.
- [16] M. Amin and M. Molinas, "Small-Signal Stability Assessment of Power Electronics based Power Systems: A Discussion of Impedance- and Eigenvalue-based Methods," *IEEE Transactions on Industry Applications*, vol. 53, no. 5, pp. 5014–5030, 2017.
- [17] F. Cavazzana, P. Mattavelli, M. Corradin, and I. Toigo, "On the stability analysis of multiple parallel inverters using the impedance multiplication effect," in *Proc. IET International Conference on Power Electronics, Machines and Drives*, 2016, pp. 1–6.
- [18] H. Alenius, M. Berg, R. Luhtala, and T. Roinila, "Stability and Performance Analysis of Grid-Connected Inverter Based on Online Measurements of Current Controller Loop," in *Proc. Annual Conference of the IEEE Industrial Electronics Society*, 2019, pp. 2013–2019.
- [19] B. Bose, "Global Energy Scenario and Impact of Power Electronics in 21st Century," *IEEE Transactions on Industrial Electronics*, vol. 60, no. 7, pp. 2638–2651, 2013.
- [20] A. Barkley and E. Santi, "Online monitoring of network impedances using digital network analyzer techniques," in *Proc. Applied Power Electronics Conference and Exposition*, 2009, pp. 440–446.
- [21] A. Riccobono, M. Mirz, and A. Monti, "Noninvasive online parametric identification of three-phase ac power impedances to assess the stability of grid-tied power electronic inverters in lv networks," *IEEE Journal of Emerging and Selected Topics in Power Electronics*, vol. 6, no. 2, pp. 629–647, 2018.
- [22] A. Merabet, K. Tawfique, M. Islam, S. Enebeli, and R. Beguenane, "Wind turbine emulator using OPAL-RT real-time HIL/RCP laboratory," in *Proc. International Conference on Microelectronics*, 2014, pp. 192–195.
- [23] E. Breaz, F. Gao, D. Paire, and R. Tirnovan, "Fuel cell modeling with dSPACE and OPAL-RT real time platforms," in *Proc. IEEE Transportation Electrification Conference and Expo*, 2014, pp. 1–6.
- [24] D. Bian, M. Kuzlu, M. Pipattanasoporn, S. Rahman, and Y. Wu, "Real-time co-simulation platform using OPAL-RT and OPNET for analyzing smart grid performance," in *Proc. IEEE Power and Energy society General Meeting*, 2015, pp. 1–5.
- [25] P. C. Kotsampopoulos, F. Lehffuss, G. F. Lauss, B. Bletterie, and N. D. Hatziaargyriou, "The limitations of digital simulation and the advantages of PHIL testing in studying distributed generation provision of ancillary services," *IEEE Transactions on Industrial Electronics*, vol. 62, no. 9, pp. 5502–5515, 2015.
- [26] C. Yin, B. Ye, X. Wang, and L. Dai, "Power hardware-in-the-loop simulation of a distributed generation system connected to a weak grid," in *IEEE Conference on Energy Internet and Energy System Integration*, 2017, pp. 1–6.
- [27] H. Alenius, T. Messo, T. Reinikka, and T. Roinila, "Aggregated Modeling and Power Hardware-in-the-Loop Emulation of Grid Impedance," in *IEEE Energy Conversion Congress and Exposition 2018*, 2018, pp. 4179–4186.
- [28] T. Reinikka, H. Alenius, T. Roinila, and T. Messo, "Power Hardware-in-the-Loop Setup for Stability Studies of Grid-Connected Power Converters," *2018 International Power Electronics Conference, IPEC-Niigata - ECCE Asia 2018*, pp. 1704–1710, 2018.
- [29] T. Suntio, T. Messo, and J. Puukko, *Power Electronic Converters: Dynamics and Control in Conventional and Renewable Energy Applications*. Wiley-VCH, 2017.
- [30] L. Harnefors, "Modeling of three-phase dynamic systems using complex transfer functions and transfer matrices," *IEEE Transactions on Industrial Electronics*, vol. 54, no. 4, pp. 2239–2248, 2007.
- [31] R. Pintelon and J. Schoukens, *System Identification - A Frequency Domain Approach*. The Institute of Electrical and Electronics Engineers, Inc. New York, 2001.
- [32] A. Tan and K. Godfrey, *Industrial Process Identification - Perturbation Signal Design and Applications*. Springer Nature Switzerland, 2019.
- [33] T. Roinila, M. Vilkkö, and J. Sun, "Broadband methods for online grid impedance measurement," in *Proc. IEEE Energy Conversion Congress and Exposition*, 2013, pp. 3003–3010.
- [34] T. Roinila, H. Abdollahi, S. Arrua, and E. Santi, "Adaptive control of interconnected multi-converter systems: Applying pseudo-random

sequences and fourier techniques,” in *Proc. International Power Electronics Conference*, 2018, pp. 1719–1723.

- [35] A. Riccobono, M. Cupelli, A. Monti, E. Santi, T. Roinila, H. Abdollahi, S. Arrua, and R. Dougal, “Stability of shipboard DC power distribution: Online impedance-based systems methods,” *IEEE Electrification Magazine*, vol. 5, pp. 55–67, 2017.
- [36] H. Abdollahi, S. Arrua, T. Roinila, and E. Santi, “A novel DC power distribution system stabilization method based on adaptive resonance-enhanced voltage controller,” *IEEE Transactions on Power Electronics*, vol. 66, pp. 5653–5662, 2019.
- [37] R. Luhtala, H. Alenius, T. Messo, and T. Roinila, “Online Frequency Response Measurements of Grid-Connected Systems in Presence of Grid Harmonics and Unbalance,” *IEEE Transactions on Power Electronics*, vol. 35, no. 4, pp. 3343–3347, 2020.
- [38] T. Roinila, T. Messo, and E. Santi, “MIMO-identification techniques for rapid impedance-based stability assessment of three phase systems in dq domain,” *IEEE Transactions on Power Electronics*, vol. 3, pp. 4015–4022, 2018.



Henrik Alenius (S’18) received his M.Sc. degree in electrical engineering from Tampere University of Technology, Tampere, Finland, in 2018. Since then, he has worked as a doctoral student with the Faculty of Information Technology and Communication Sciences at Tampere University. His research interests include impedance-based interactions in grid-connected systems, broadband methods in impedance measurements, and stability analysis of multi-parallel inverters.



Tomi Roinila (M’10) received the M.Sc. (Tech.) and Dr.Tech. degrees in automation and control engineering from Tampere University of Technology, in Finland, in 2006 and 2010, respectively. He is currently an Associate Professor in the Faculty of Information Technology and Communications Sciences in Tampere University, in Finland. His main research interests include modeling and control of grid-connected power-electronics systems, and modeling of multiconverter systems.



Roni Luhtala (S’17) received his M.Sc. in electrical engineering from the Tampere University of Technology, Tampere, Finland, in 2017. Since then, he has been working as a doctoral student in the Faculty of Engineering and Natural Sciences at Tampere University. His main research interests include real-time identification and adaptive control of grid-connected systems.



Tuomas Messo (M’14) received his Dr.Tech. degree in electrical engineering from Tampere University of Technology, Tampere, Finland, in 2014. He is currently with GE Grid Solutions and holds the position of Adjunct Professor at Tampere University in the field of power electronics, where he also worked as an Assistant Professor between 2016 and 2019. His research interests include grid-connected three-phase power converters for renewable energy applications and microgrids, dynamic modeling, control design, impedance-based interactions in three-phase systems, and impedance design of grid-connected inverters.

- [39] R. Luhtala, T. Roinila, and T. Messo, “Implementation of real-time impedance-based stability assessment of grid-connected systems using mimo-identification techniques,” *IEEE Transactions on Industry Applications*, vol. 54, pp. 5054–5063, 2018.
- [40] T. Roinila, H. Abdollahi, S. Arrua, and E. Santi, “Real-time stability analysis and control of multi-converter systems by using MIMO-identification techniques,” *IEEE Transactions on Power Electronics*, vol. 34, pp. 3948–3957, 2019.
- [41] K. Godfrey, *Perturbation Signals for System Identification*. Prentice Hall, UK, 1993.
- [42] T. Roinila, H. Abdollahi, S. Arrua, and E. Santi, “Online measurement of bus impedance of interconnected power electronic systems: Applying orthogonal sequences,” in *Proc. IEEE Energy Conversion Congress and Exposition*, 2017, pp. 5783–5788.
- [43] T. Messo, J. Jokipii, A. Mäkinen, and T. Santio, “Modeling the grid synchronization induced negative-resistor-like behavior in the output impedance of a three-phase photovoltaic inverter,” in *Proc. IEEE International Symposium on Power Electronics for Distributed Generation Systems*, 2013, pp. 1–7.
- [44] L. Ljung, *System Identification-Theory for the User*. Prentice Hall PTR, USA, 1999.



Erik de Jong (M ’05, SM ’12) received a cum laude B.Eng. and a cum laude M.Eng. degree in electric and electronic engineering from the Rand Afrikaans University, Johannesburg, South Africa in 2001 and 2003, respectively. He received a Ph.D. degree from Delft University of Technology, Delft, The Netherlands, in 2007. Since 2007, he has been with DNV GL/Energy, Arnhem, The Netherlands, as a technical professional, specializing and providing consultancy services in power electronics and its applications in utility grids. Since 2008, he is also with the Flex Power Grid Laboratory as general manager responsible for all operations regarding medium-voltage grid inverter research, testing and certification. In 2010 he received the prestigious Hidde Nijland award for his contributions in the field of testing utility-interactive power electronics. Since 2013, he is also senior researcher in the field of power electronics and power cybernetics with DNV GL’s Strategic Research and Innovation department. He serves as expert in the IEC 61400-21 standardisation maintenance team (TC88) for revision 3 on Power Quality, is industry member of the DERLab association and is the Dutch delegate for the Smart Grid International Research Facility Network (IEA-ISGAN-SIRFN) activities. As part-time associate professor at the Technical University of Eindhoven, Electrical Energy Systems group, he directs research programs and guides PhD students in the field of power electronics dominated (smart) grids. He is very active in publishing scientific research results in peer reviewed international conferences and journals.



Andrew Burstein (M’13) received a cum laude BS in electrical engineering technology: smart grids at the State University College of New York at Buffalo, USA, in 2013, and a cum laude MSc in sustainable energy technology from Eindhoven University of Technology, The Netherlands, in 2015. He is currently a researcher at DNV GL Power and Renewables, Arnhem, The Netherlands. His main focus is working in the Flex Power Grid Laboratory and is interested in developing leading cutting edge testing services for grid-connected power electronics.



Alejandra Fabian received her B.Sc. degree in Electronics Technology from Monterey Institute of Technology and Higher Education, Estado de Mexico, Mexico in 2011, and the M.Sc. degree in Sustainable Energy Technology from Eindhoven University of Technology, Eindhoven, Netherlands in 2016. She is currently a researcher at DNV GL Group Technology & Research, Arnhem, Netherlands. Her research interests are in hardware in the loop methods, power systems and control applications for renewable energy integration.

PUBLICATION

II

**”Combination of Orthogonal Injections in Impedance Measurements of
Grid-Connected Systems”**

H. Alenius, R. Luhtala and T. Roinila

IEEE Access, vol. 8, pp. 178085–178096, 2020

Publication reprinted with the permission of the copyright holders

Received August 12, 2020, accepted September 21, 2020, date of publication September 25, 2020, date of current version October 8, 2020.

Digital Object Identifier 10.1109/ACCESS.2020.3026727

Combination of Orthogonal Injections in Impedance Measurements of Grid-Connected Systems

HENRIK ALENIUS¹, (Graduate Student Member, IEEE),
RONI LUHTALA², (Graduate Student Member, IEEE),
AND TOMI ROINILA¹, (Member, IEEE)

¹Faculty of Information Technology and Communication Sciences, Tampere University, 33720 Tampere, Finland

²Faculty of Engineering and Natural Sciences, Tampere University, 33720 Tampere, Finland

Corresponding author: Henrik Alenius (henrik.alenius@tuni.fi)

ABSTRACT Impedance-based stability criterion has become a popular method in determining the stability of grid-connected systems. Recent studies have presented the utilization of various pseudo-random-sequence (PRS) perturbations for rapidly and accurately obtaining the impedances required for the stability analysis. A major drawback of the PRS is, however, that the signal power is linearly distributed over many harmonic frequencies. As the injection amplitude must be kept small to avoid too strong nonlinear distortions, it becomes challenging to provide enough power to the whole frequency band of interest. This work proposes a novel perturbation that is synthesized by summing up several independently designed orthogonal PRS injections. As the orthogonal sequences do not have power at common frequencies, the resulting combined signal can be tailored to have a specific spectral-power distribution at each frequency band of interest. As a consequence, the system impedances can be accurately measured over a wide frequency band. The performance of the method is verified through experimental measurements of a 2.7 kW grid-connected system, where grid impedance measurements and terminal inverter output admittance measurements are performed.

INDEX TERMS Impedance measurement, system identification, broadband perturbation, orthogonal sequences.

I. INTRODUCTION

The rapid increase in grid-connected power electronics has disrupted the dynamics of most power systems and exposed challenges in the system compatibility and stability [1]. The detailed structure of the power system is often unknown, and the precise internal dynamics of commercial devices are often protected by the manufacturer. Consequently, impedance measurements are often the only option to identify the system dynamics. Recently, the impedance measurements have been applied for many purposes, such as stability analysis [2]–[6], controller design [7], and adaptive control [8]–[10].

Past studies have presented various measurement techniques to obtain the terminal impedance of the grid or grid-connected subsystem [2]–[4], [9], [11]. Particularly,

broadband methods have become popular due to short measurement time where a broadband perturbation such as a pseudo-random sequence (PRS) or an impulse is placed, for example, on top of the system's controller reference signal [9], [12]–[19]. The resulting responses in the system output voltages and currents are measured, and Fourier techniques are applied to extract the impedance information.

One of the most widely applied broadband sequence has been the maximum-length binary sequence (MLBS) which can be easily implemented, as the sequence has only two signal levels [20]. The MLBS exhibits multiple desirable characteristics, such as controllable frequency bandwidth and resolution, and low crest factor [21]. However, the MLBS suffers from very limited number of available signal lengths, as the sequence length is defined as $2^n - 1$ where n is a positive integer [21]. In addition, the spectral power of the MLBS is linearly distributed over many harmonic frequencies, which

The associate editor coordinating the review of this manuscript and approving it for publication was Guangya Yang^{1b}.

causes challenges in the identification of wide frequency bands where both the high- and low-frequency characteristics are important to be measured. In many grid-connected systems, especially the low-frequency impedance (admittance) can be small resulting in a very weak response to the applied perturbation. Such systems include inductive transmission grids [22] and converter systems where control loops shape the terminal characteristics [23]. In order to increase the signal-to-noise ratio, either the injection amplitude has to be increased or more injection periods have to be applied and averaged to reduce the effect of noise. Both methods may become difficult in practice; increasing the amplitude may drift the system out of its linear region or disturb the normal operation of the system, whereas increasing the injection periods requires more computing power and memory storage [24].

Recent studies have presented perturbation signals that have adjustable spectral energies at specific frequency ranges. The authors in [24] applied the discrete-interval binary sequence (DIBS). The DIBS is a computer-optimized binary signal, where the goal of the optimization is to force as much power as possible into the specified (user-defined) harmonic frequencies without increasing the signal time-domain amplitude. In the DIBS, however, a significant amount of the signal total power appears in non-specified harmonics [21]. In addition, the iterative sequence design through computer optimization can be very complex. Another solution would be using a multi-sine perturbation, where multiple sinusoids with different frequencies are summed up [25]–[27]. However, the multi-sine typically has a large number of signal levels making it difficult to implement the signal with a low-cost application [24]. In addition, the multi-sine often exhibits large signal peaks in its time-domain waveform, making it unsuitable for sensitive systems [28]. The multisine crest factor can be minimized by phase optimization algorithms, such as in [29], however, these processes require high computational effort and affect the magnitude spectrum.

This work proposes a novel perturbation-design method to overcome the drawbacks of the MLBS. The proposed method is based on combined sequences where several orthogonal binary sequences are designed and summed up to form a single perturbation. The orthogonal sequences do not have power at common frequencies, and therefore, it is possible to independently design each sequence in the summation so that the spectral power of the sequences is distributed into specific frequency ranges. Summing up the sequences produces a near-binary signal which has a high degree of freedom in terms of signal length and spectral power distribution compared to the MLBS. As a result, the frequency-specific excitation power can be drastically increased without increasing the signal time-domain amplitude, and the system impedance(s) can be measured significantly more accurately compared to a similar-amplitude MLBS. In addition, as the frequency resolution of each orthogonal sequence in the combined signal can be separately selected, one can adjust the resolution to

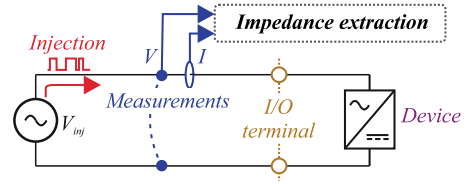


FIGURE 1. Schematic of a converter terminal impedance measurement.

a very fine value within a specific frequency range so that possible resonances can be accurately measured. Otherwise the produced signal has the same attractive properties than the conventional MLBS.

The remainder of the work is organized as follows. Section II reviews the theoretical background for impedance measurements using pseudo-random sequences. Section III presents the proposed design method for multiple orthogonal sequences. Section IV presents experimental validation based on a 2.7 kW three-phase grid-connected inverter system. Section V concludes the work.

II. IMPEDANCE MEASUREMENTS WITH PSEUDO-RANDOM SEQUENCES

A. MEASURING TERMINAL IMPEDANCE

Fig. 1 presents a simplified diagram of a typical broadband-measurement setup for a power-electronic device for obtaining the terminal impedance, where V_{inj} denotes the voltage injection and V and I are the measured terminal voltage and current. The perturbation is injected to the system as a voltage- or current-type excitation, for example by applying the current references of an inverter. The voltages and currents are measured, and transformed to the frequency domain through discrete Fourier transformation (DFT)

$$\hat{X}(j\omega) = \mathcal{F}\{\hat{x}(t)\} \quad (1)$$

where $\hat{x}(t)$ is a measured time-domain signal and $\hat{X}(j\omega)$ is the corresponding frequency-domain signal. The frequency response (impedance or admittance) can be extracted from the frequency-domain input and output signals [14]

$$G(j\omega) = \frac{\hat{Y}(j\omega)}{\hat{X}(j\omega)} \quad (2)$$

where $\hat{X}(j\omega)$ is the input signal and $\hat{Y}(j\omega)$ is the output signal.

In three-phase AC systems, the impedance measurements are typically performed in the dq-domain, where the system can be transformed from time-periodic AC trajectories to time-invariant DC operating points [30]. However, the system becomes a multivariable system with two input signals and two output signals which are coupled through cross-coupling elements. To address this coupling effect in the impedance measurements, two independent sets of measurements are required [31], [32]. The complete impedance matrix can be

obtained from

$$\begin{bmatrix} Z_d & Z_{qd} \\ Z_{dq} & Z_q \end{bmatrix} = \begin{bmatrix} V_{d1} & V_{d2} \\ V_{q1} & V_{q2} \end{bmatrix} \begin{bmatrix} I_{d1} & I_{d2} \\ I_{q1} & I_{q2} \end{bmatrix}^{-1} \quad (3)$$

where subscripts “1” and “2” are the two independent measurements. The independent measurements can be performed by, for example, sequentially injecting the perturbation to first d-channel and then to q-channel.

B. MAXIMUM-LENGTH BINARY SEQUENCE

Maximum-length binary sequence (MLBS) is a class of pseudo-random signals that can be straightforwardly generated using shift registers [20]. The MLBS is a periodic and deterministic binary sequence that exists for sequence lengths of $N = 2^n - 1$, where n is an integer larger than 2. Because the MLBS has only two different signal levels, the sequence is easy to generate in low-cost hardware. The frequency spectrum of the MLBS is linearly spaced with a resolution of $f_{\text{res}} = f_{\text{gen}}/N$, where f_{gen} is the signal generation frequency. The measurement duration of a single period is $T_m = 1/f_{\text{res}}$, and due to the signal periodicity, the MLBS can be averaged over multiple periods to increase the signal-to-noise ratio.

C. ORTHOGONAL SEQUENCES

Orthogonal sequences are signals that are uncorrelated with each other, that is, they have no power at same frequencies. Such sequences have been typically applied in systems that have multiple inputs and outputs. Using the orthogonal sequences as injections makes it possible to simultaneously measure the frequency responses between several (coupled) inputs and outputs [4]. In the present work, however, the orthogonal sequences are applied to form a single perturbation sequence.

Various techniques have been presented to implement orthogonal broadband sequences. One of the most common approach is the use of Hadamard modulation [21], where the conventional MLBS is used as a first sequence. The second (orthogonal) sequence is formed by modulating the MLBS with a 2-bit sequence [0 1], which results in a sequence whose length is doubled and all the even-order harmonics are suppressed. Similarly, the third sequence is formed by modulating the MLBS with a sequence [0 0 1 1]. Further orthogonal sequences can be formed by continuing this modulation pattern for an arbitrary number of sequences. Detailed instructions for applying the modulation can be found in [21]. Fig. 2 presents three orthogonal binary sequences in the frequency domain, generated by the Hadamard modulation. The sequences have different amplitudes for illustration, they are generated at 1 kHz and have lengths of 31 for sequence 1, 62 for sequence 2, and 124 for sequence 3. As the figure shows, the sequences have no power at common frequencies.

III. COMBINING MULTIPLE ORTHOGONAL SEQUENCES

This work proposes a novel application for orthogonal sequences; a combined orthogonal sequence (COS) is

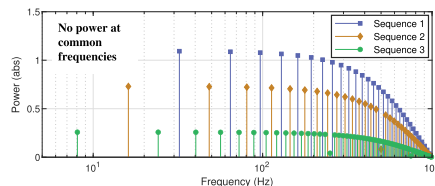


FIGURE 2. Power spectra of three orthogonal sequences.

generated by summing up multiple orthogonal binary sequences (OBS). This provides added degrees of freedom in the perturbation design as each of the orthogonal sequences can be independently designed for a specific frequency range. The COS is a near-binary sequence in which the spectral power is significantly increased at specific frequency ranges compared to the MLBS. Additionally, the frequency resolution of the produced sequence can be selected differently for specific frequency ranges thus enabling accurate evaluation of, for example, resonance peaks.

A. DESIGNING THE COS

The COS can be designed by using the following steps (an example by using three orthogonal sequences)

- 1) Design an MLBS so that the generation frequency is twice higher than highest frequency to be identified, and choose the sequence length so that a sufficient frequency resolution is achieved for the high-frequency range.
- 2) Produce a second orthogonal sequence from the MLBS, and choose a lower generation frequency to target the middle-range frequencies.
- 3) Produce a third orthogonal sequence and choose even lower generation frequency to target the low-frequency range.
- 4) Choose the excitation amplitude for each sequence.
- 5) Combine the sequences by summing them together.

In order to preserve the orthogonality of the sequences, the generation frequencies must be integer multiples of each other, and each new sequence must have lower generation frequency compared to the previous sequence. The measurement duration of the COS is determined by the sequence that has the lowest generation frequency (the last OBS). The other OBS, which have shorter duration for a single period, occur multiple periods within the total duration. As a consequence, each individual sequence is applied with integer number of periods and the sequence periodicity is preserved.

The impedance calculation through Fourier methods is straightforward and two approaches exist. The first approach is to calculate a separate discrete Fourier transformation (DFT) for each of the OBS, where the impedance can be obtained similarly than in conventional broadband sequence analysis. However, this approach requires the use of multiple DFTs, which may increase the required calculation power.

Alternatively, a single DFT can be performed and the analysis is performed by the following steps:

- 1) Inject h orthogonal sequences to the system ($OBS_1, OBS_2, \dots, OBS_h$) at corresponding generation frequencies $f_{gen}^1, f_{gen}^2, \dots, f_{gen}^h$ (at a descending order). Measure the input and output signals.
- 2) Perform a k -point DFT on the signals, where $k = n * f_s / f_{gen}^h$, where f_s is the sampling frequency and n is the length of the highest order OBS that is generated at the lowest frequency.
- 3) For the last orthogonal sequence (OBS_h), select the harmonics that satisfy

$$(i - 1) \bmod 2 = 0 \quad (4)$$

where i is the order of the harmonic.

- 4) For the first orthogonal sequence (OBS_1), select the harmonics that satisfy

$$(i - 4 * f_{gen}^1 / f_{gen}^h) \bmod (4 * f_{gen}^1 / f_{gen}^h) = 0 \quad (5)$$

- 5) For the remaining orthogonal sequences, select the harmonics that satisfy

$$(i - 2 * f_{gen}^j / f_{gen}^h) \bmod (4 * f_{gen}^j / f_{gen}^h) = 0 \quad (6)$$

where j is the order of the OBS in the range from 2 to $h - 1$

- 6) For each OBS, remove the harmonics that are above 60.3 % of the corresponding generation frequency (a 6 dB decrease in the excitation amplitude).

This procedure selects the excited frequencies from the spectrum, and the impedance can be obtained from the output-to-input ratio.

The major benefit of the proposed COS is that the perturbation can be flexibly optimized to extract information from systems that are challenging to measure with conventional MLBS. Therefore, the optimal design of the COS is case dependent. In general, the generation frequency of the first sequence (that is, the base MLBS) can be designed similarly than when a single MLBS is applied; the generation frequency should be twice the highest frequency-of-interest, as the measurement bandwidth is limited to half of the generation frequency. However, the length of the first sequence is chosen so that the resolution in the high-frequency range is sufficient, in contrast to conventional approach with a single MLBS where the frequency resolution must satisfy also the low-frequency-range requirements. Then, additional OBS can be added (with respect to design rules in the steps above) to reinforce the perturbation at specific frequency ranges, for example by enhancing the frequency resolution at the low-frequency range. The amplitude of the COS, which is the summation of OBS amplitudes, should be designed similarly than the amplitude of a single MLBS injection which is discussed in [33]. The amplitudes of individual OBS should be chosen so that the frequency ranges that have the lowest frequency-response magnitude or the highest noise content should have the highest amplitude.

B. EXAMPLE IMPLEMENTATION OF COS

Fig. 3 presents an implementation of the proposed method for three orthogonal sequences that are generated with different frequencies. The OBS have sequence lengths of 63, 126, and 252, while the respective generation frequencies are 8000 Hz, 1000 Hz, and 125 Hz. The COS shown in red is obtained by summing up the three orthogonal sequences. The orthogonality is preserved as seen from the spectral lines that never occur at the same frequency. A -6 dB is considered to be the threshold for excitation power, below which the excitation power is insufficient and ignored. The COS has a relatively low number of different signal levels (two times the number of the applied orthogonal sequences) making it straightforward to be generated even with a low-cost controller. The sequence is periodic and can be averaged over multiple periods to increase the signal-to-noise ratio. The measurement duration is determined by the length and generation frequency of the longest sequences, similarly than with a single MLBS.

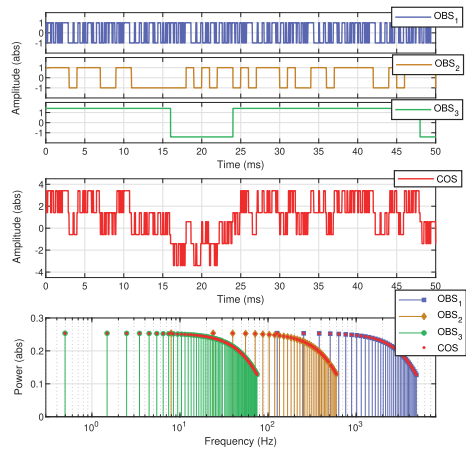


FIGURE 3. Three orthogonal sequences in the time and frequency domain.

Fig. 4 shows a conventional MLBS for a comparison to the combined sequence. The MLBS is designed so that the injection amplitude and resolution at low frequencies are equal to the combined sequence, so a 8191-bit-long MLBS generated at 8 kHz is applied. While the maximum amplitude is equal in both sequences, the combined sequence has lower total power as the time-domain signal includes levels below the maximum amplitude. Therefore, the combined sequence produces less disturbances to the measured system. Despite the lower total power, the COS has up to 230 % more excitation power on each frequency harmonic due to lower total number of spectral power harmonics, which is the main advantage of the proposed sequence.

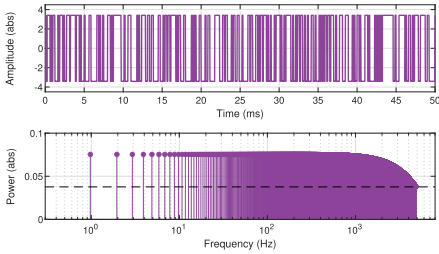


FIGURE 4. Conventional 8191-bit-long MLBS.

IV. EXPERIMENTS

Fig. 5 shows the experimental setup that is used to perform the measurements, and a photograph of the setup is shown in Fig. 6. A four-quadrant linear amplifier (*Spitzenberger Spies PAC 15000*) is set to emulate the grid voltages for a grid-connected three-phase inverter (*Myway Plus MWINV-9R144*). The inverter control system is implemented in a dSPACE real-time simulator, and the DC power is provided by a photovoltaic emulator (*Spitzenberger Spies PVS 7000*). An external CL-filter and isolation transformer are used to interface the inverter to the grid. In the grid impedance measurements, an additional inductor is connected between the transformer and the grid to emulate the grid impedance. The setup parameters are shown in Table 1.

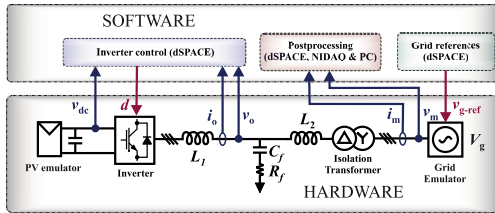


FIGURE 5. Experimental setup for impedance measurements.



FIGURE 6. Photograph of the experimental setup.

Fig. 7 presents the detailed schematics of the subsystems that control the devices and perform the postprocessing. The inverter is operated in a cascaded control scheme, where the outer DC voltage controller is responsible for the DC volt-

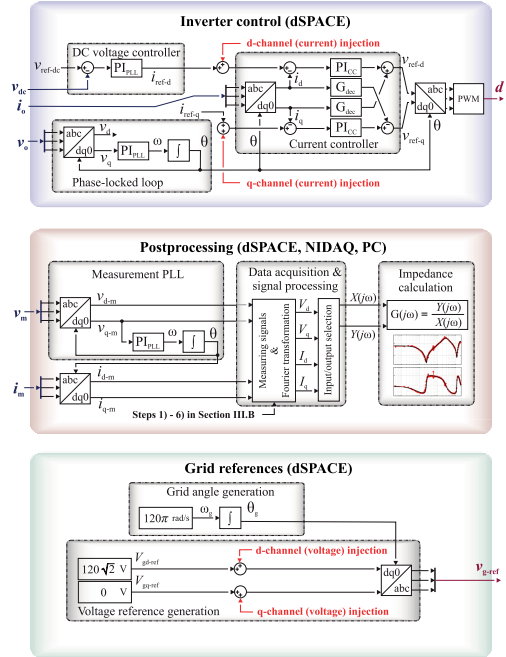


FIGURE 7. Detailed schematics of the control and postprocessing blocks.

TABLE 1. Parameters of the experimental setup.

Parameter	Symbol	Value
Grid frequency	f_n	60 Hz
Grid phase voltage	V_g	120 V
Inverter nominal power	S_n	2.7 kVA
Switching frequency	f_{sw}	8 kHz
Power factor	$\cos\phi$	1.0
Switching deadtime	T_{dt}	4.0 μ s
DC voltage	V_{dc}	414.3 V
DC input current	I_{dc}	6.577 A
DC capacitor capacitance	C_{dc}	1.5 mF
L-filter inductance	L_1	2.2 mH
L-filter resistance	R_1	100 m Ω
CL-filter inductance	L_2	0.6 mH
CL-filter resistance	R_2	40 m Ω
CL-filter capacitance	C_f	10 μ F
CL-filter damping resistance	R_d	1.8 Ω
Transformer inductance	L_{tf}	0.3 mH
Transformer resistance	R_{tf}	400 m Ω
Additional inductance	L_g	4 mH
Additional resistance	R_g	100 m Ω
AC current control proportional gain	$K_{P,CC}$	0.0149
AC current control integral gain	$K_{I,CC}$	23.442
DC voltage control proportional gain	$K_{P,VC}$	0.0962
DC voltage control integral gain	$K_{I,VC}$	1.2092
PLL control proportional gain	$K_{P,PLL}$	2.3280
PLL control integral gain	$K_{I,PLL}$	351.720

age control of the DC link that connects the inverter to the PV emulator. The innermost current controller controls the

output currents, where the reference for the d-component is the output of the outer voltage controller and the q-component reference is set to zero (that is, the inverter operates at unity power factor). The voltage references for the grid emulator are also formed in the dq-domain. The perturbation signal can be injected to either inverter current controller (d- or q-channel) or the grid voltage references (d- or q-channel). Consequently, the configuration enables impedance measurement on any of the impedance component for the inverter or the grid. Moreover, the complete 2×2 matrices can be extracted for both subsystems by applying four sequential measurements and applying Eq. (3). In the postprocessing, the measured signals are transformed into dq-domain by an additional low-bandwidth phase-locked loop.

The effectiveness of the proposed method is demonstrated by performing grid impedance measurements and output terminal admittance measurements on a grid-connected inverter. The measurements are performed both with the proposed COS and conventional MLBS. Both sequences are designed so that they have approximately the same time-domain amplitude, measurement duration, measurement bandwidth, and low-frequency frequency resolution. In the first set, the grid impedance is measured by utilizing the inverter in the current-type excitation injection. In the second set, a voltage-type injection from the grid emulator is applied in the measurements of inverter's output admittance. The measurements are performed in the dq-domain for the impedance d component. Finally, the complete 2×2 impedance matrices are measured for both the inverter and the grid, and an impedance-based stability analysis is performed.

A. GRID IMPEDANCE MEASUREMENTS

In the first experiment set, the three-phase inverter is utilized in the grid impedance measurement of the interfacing system. Fig. 8 presents a simplified schematic of the experiment, where the interfacing impedance consists of an external CL-filter, an isolation transformer, and an additional inductor that emulates the grid impedance. The perturbation signal is injected to the current references of the inverter resulting in a current-type excitation to the system. The inverter operates at the nominal setpoint feeding 2.7 kW to the grid, and the perturbation is superimposed to the fundamental current. The three-phase voltages and currents are measured at the grid interface and transformed to the dq-domain. Then, the signals are Fourier transformed and the impedance is obtained from the ratio of voltage and current.

The grid impedance measurements are performed by applying both the conventional MLBS and the COS. The perturbations are designed to have an equal bandwidth, measurement duration (T_m), and time-domain amplitude (A). In addition, the low-frequency resolution (f_{res}) is set to be equal. Due to characteristics of orthogonal sequences in COS, the MLBS is averaged over two periods to achieve equal measurement duration. The signal parameters are summarized in Table 2, where the number of averaged periods is denoted by P . The proposed COS is formed by summing

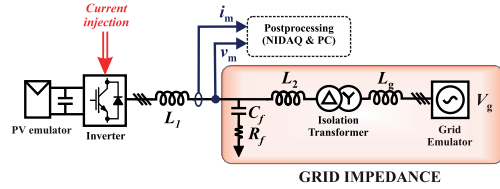


FIGURE 8. Schematic of the grid impedance measurements.

TABLE 2. Sequence parameters for grid-impedance measurements.

	N	f_{gen} (Hz)	A (A)	f_{res} (Hz)	P	T_m (s)
OBS ₁	127	4000	0.05	31.5	32	1.016
OBS ₂	254	250	0.15	1.97	1	1.016
COS	381	250..4000	0.2	1.97..31.5	1	1.016
MLBS	2047	4000	0.2	1.95	2	1.024

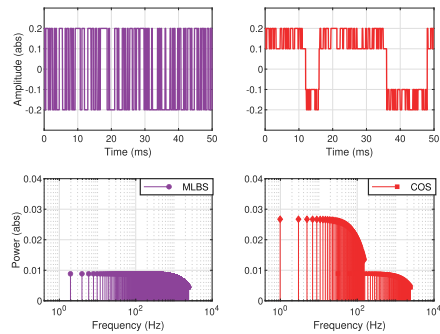


FIGURE 9. Time domain waveform and frequency domain spectrum for the MLBS (purple) and the COS (red) in grid impedance measurement.

up the two OBS. To improve the measurement performance at low frequencies, the COS design is weighted towards the low-frequency range by increasing the amplitude of the second OBS and simultaneously decreasing the amplitude of the first OBS.

Fig. 9 shows the time-domain waveforms and frequency spectra of the MLBS and the COS. Despite the equal total amplitude, the COS is designed to have significantly higher power in the low-frequency range to tackle the challenges related to the weak voltage response in low frequencies of an inductive grid. The injection amplitude is set to 0.2 A, which is approximately 2 % of the nominal current (10 A). The phase currents at the inverter point-of-common-coupling (PCC) are shown without perturbation and with the MLBS and COS perturbations in Fig. 10. Fig. 11 presents the PCC voltages showing that the injection has a very small effect on the voltages. The disturbance from the excitation to the fundamental currents and voltages is negligible, which makes the perturbations highly suitable in, for example, online identification of grid-connected systems.

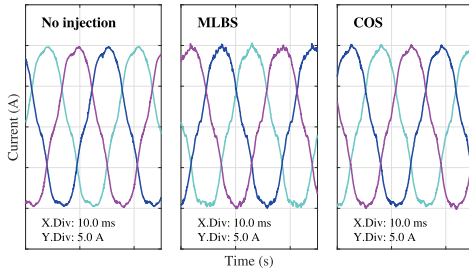


FIGURE 10. Phase currents without injection and with MLBS and COS perturbation.

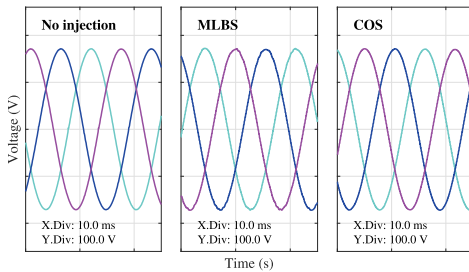


FIGURE 11. Phase voltages without injection and with MLBS and COS perturbation.

Fig. 12 shows the measured grid impedance by applying both the MLBS and the COS. The COS demonstrates drastically improved accuracy resulting from the higher frequency-specific excitation power, especially in the high-frequency range. With the COS, also the high-frequency resonant peak is still adequately identified, despite the lower frequency resolution at these frequencies. On the other hand, similar low-frequency resolution to the MLBS ensures that the low-frequency dynamics are accurately captured. As both the injection amplitude and measurement duration are chosen very small for both perturbations, the measurement accuracy is adversely affected. The accuracy could be increased by increasing either the injection amplitude or measurement duration. However, this trade-off is not possible in some applications where fast measurements of sensitive systems are required. By applying the the proposed combined orthogonal sequences, the accuracy can be improved without increasing the duration or injection amplitude.

B. INVERTER OUTPUT ADMITTANCE MEASUREMENTS

In the second experiment set, the total terminal admittance of the inverter, filter, and transformer is measured as seen from the grid-side. Fig. 13 presents the measurement configuration for inverter admittance measurements. The measurements are performed with a voltage-type injection by superimposing the perturbation signal to the grid voltages through the grid emulator. The measurements are performed

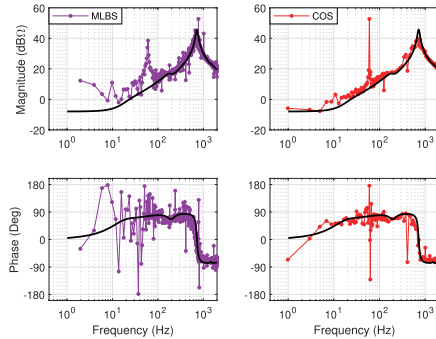


FIGURE 12. Grid impedance measurements by applying the MLBS (purple) and the COS (red).

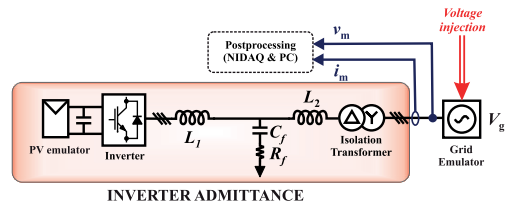


FIGURE 13. Schematic of the inverter terminal admittance measurements.

both by the COS and the conventional MLBS. The inverter admittance is expected to have multiple resonant peaks resulting from the controllers and LCL-interactions, and the inverter admittance measurements at low frequencies typically requires a relatively high SNR compared to higher frequencies. Consequently, the COS is designed to consist of three orthogonal sequences. The signal parameters are summarized in Table 3. As the third orthogonal sequence (OBS₃) covers the low-frequency region, the injection amplitude is set to a higher value compared to the other two sequences. Fig. 14 presents the time-domain waveforms and power spectra of the applied perturbations. As the figure shows, the combined sequence can be designed to have a significantly higher spectral power at specific frequencies compared to the MLBS when the time-domain amplitudes are similar.

TABLE 3. Sequence parameters for inverter measurements.

	<i>N</i>	<i>f</i> _{gen} (Hz)	<i>A</i> (V)	<i>f</i> _{res} (Hz)	<i>P</i>	<i>T</i> _m (s)
OBS ₁	63	4000	0.1	63.5	128	2.016
OBS ₂	126	500	0.2	7.94	8	2.016
OBS ₃	252	125	0.7	0.99	1	2.016
COS	411	125..4000	1	0.99..64	1	2.016
MLBS	4095	4000	1	0.98	2	2.048

Fig. 15 shows the measured output admittance of the inverter when both the MLBS and the proposed perturbation is applied (the analytically obtained admittance is shown

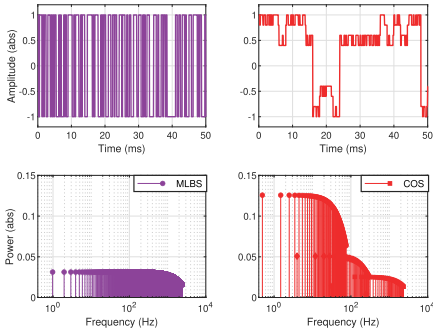


FIGURE 14. Time domain waveform and frequency domain spectrum for the MLBS (purple) and the COS (red).

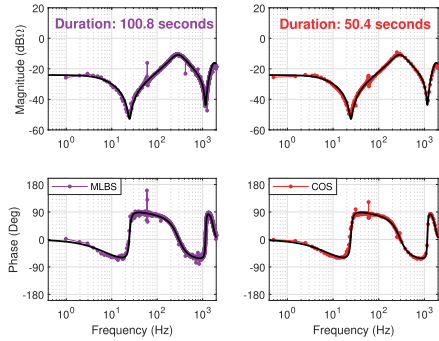


FIGURE 16. Long-duration admittance measurements by applying 100 periods of the MLBS (purple) and 25 periods of the COS (red).

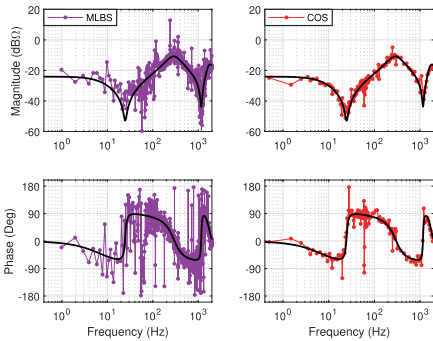


FIGURE 15. Admittance measurements by applying the MLBS (purple) and the COS (red).

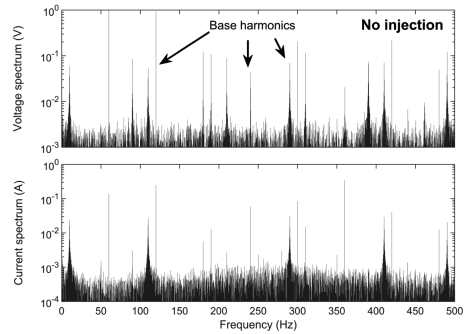


FIGURE 17. Spectra of d-channel voltages and current with no injection.

as a reference). The figure shows the superiority of the combined sequence compared to the MLBS, as the measurement obtained by the combined sequence follows the reference much more accurately through the whole frequency band, including the resonant peaks. With the combined sequence, the SNR can be increased to overcome the effects of noise, harmonic currents, and nonlinearities that corrupt the MLBS measurement.

The measurement results can be further improved by averaging the results over multiple injection periods. Fig. 16 presents long-duration measurements of the output admittance of the inverter, where the MLBS has been applied with 100 periods and the COS with 25 periods. The durations of the measurements are 100.8 s and 50.4 s, respectively. As the figure shows, similar (or even better) accuracy can be achieved in significantly shorter measurement duration when the proposed COS is applied. Consequently, the proposed method can also be applied to reduce the measurement duration in applications where a high accuracy is required, such as stability analysis of grid-connected systems.

C. SPECTRAL ANALYSIS

In order to validate the superiority of the COS, a spectral analysis is performed to show the effect of the applied perturbation in the measured voltages and currents. Fig. 17 shows the d-component voltage and current spectra in the nominal operation conditions when no injection is applied. In the phase-domain, the current harmonics have magnitudes of 1.2 % for the 3rd harmonic, 5.4 % for the 5th harmonic, and 2.0 % for the 7th harmonic. However, in the dq-frame the harmonics are shifted by the fundamental frequency $\pm f_n$ due to rotating reference frame. The harmonic currents result mostly from the inverter switching and system nonlinearities, such as saturation in the isolation transformer. The inverter switches have a high deadtime of 4 μ s with respect to the 8 kHz switching frequency degrading the current quality.

Fig. 18 shows the corresponding spectra when the voltage-type MLBS perturbation applied in the inverter output admittance measurements is injected to the grid voltages. The excited frequencies at the voltage spectrum have an even power distribution. At the low-frequency anti-resonance, however, the current response is very small drastically degrading the measurement performance. Fig. 19 shows

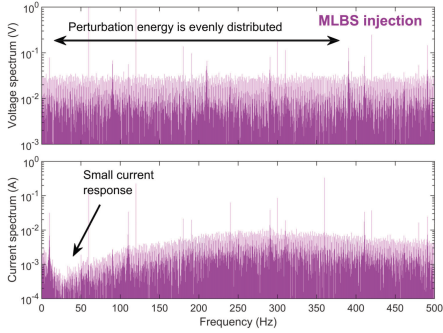


FIGURE 18. Spectra of d-channel voltages and current with the MLBS.

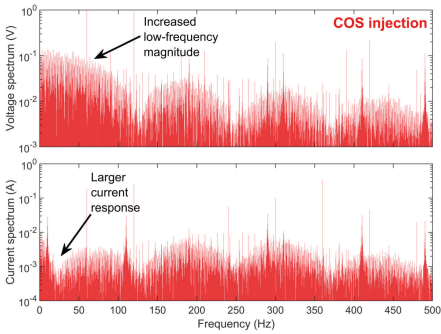


FIGURE 19. Spectra of d-channel voltages and current with the COS.

the corresponding spectra when the proposed COS is injected. With the COS, the excitation spectrum is weighted towards the low frequencies in the perturbation design. Consequently, also the current response spectrum is enhanced at the critical frequencies.

Fig. 20 shows the low-frequency spectra for both perturbation signals, where the excited frequencies have been highlighted. The comparison between the inherent noise and excited frequencies when both the MLBS and the COS are applied explains the superior performance of the COS. The adjustable amplitude spectrum of the COS allows improving the SNR at certain frequency ranges. In this case, the admittance at the anti-resonant peak is approximately $-50 \text{ dB}\Omega$, so the current response is only 0.3 % of the voltage excitation. Therefore, enhancing the excitation amplitude near these frequencies is critical for high-performance measurements.

In order to quantify the disturbance of the perturbation injection for the system operation, the total harmonic distortions (THDs) are measured. The phase current and voltage THDs are shown in Table 4 for the three cases. As the excitation amplitude is chosen small, the perturbation has only a minor impact on the THDs, as the base level without

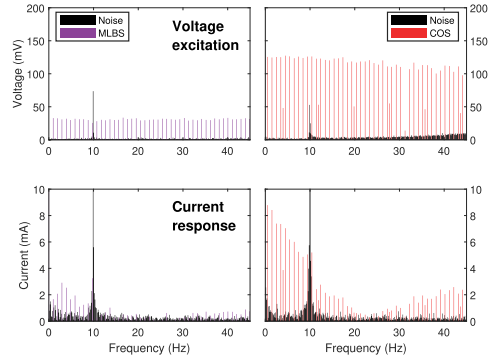


FIGURE 20. Low-frequency current and voltage spectra for the MLBS and the COS injection with highlight on excited frequencies.

TABLE 4. Total harmonic distortions in phase currents and voltages.

	Voltage THD	Current THD
No excitation	0.3 %	6.47 %
MLBS excitation	0.54 %	6.91 %
COS excitation	0.45 %	6.60 %

perturbations is close to the THD during the measurements. Although the impact is low for both perturbation signals, the COS disturbs the system even less than the MLBS.

D. STABILITY ANALYSIS

The stability analysis of grid-connected devices is a common utilization for the impedance measurements [34], [35]. In this section, an impedance-based stability analysis is performed by applying the impedance measurements obtained with the COS and the MLBS. Multivariable impedances (2×2 matrix in dq-domain) are obtained by two independent measurements where the perturbation is first injected to the d-channel and then to the q-channel and applying Eq. (3). The stability experiments are performed with a 9 mH inductor as the grid impedance and by tuning the bandwidth of the inverter’s phase-locked loop, as the high PLL bandwidth is known to deteriorate system stability [23]. The setup configuration is shown in Fig. 21 and the stability analysis is performed as follows

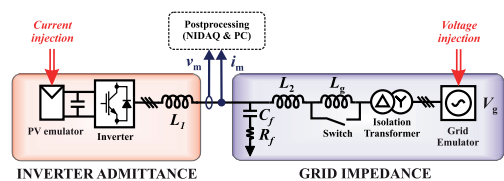


FIGURE 21. Measurement setup diagram for the stability analysis.

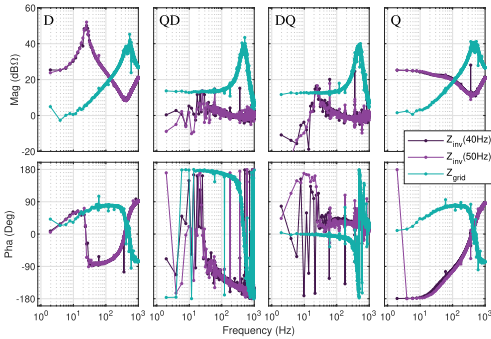


FIGURE 22. Complete impedance matrices measured with the MLBS.

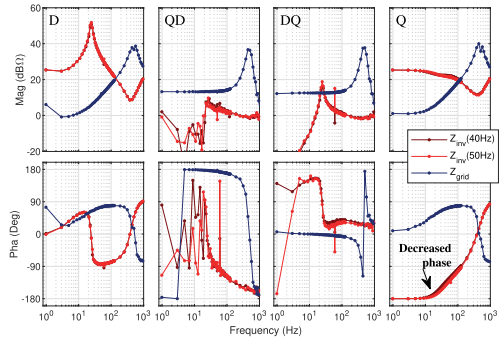


FIGURE 23. Complete impedance matrices measured with the COS.

- 1) The PLL is set to very low bandwidth (1 Hz) and the grid impedance measurements are performed by applying current injection from the inverter
- 2) The grid impedance is disconnected, and the inverter output admittance is measured for two sets of PLL parameters (40 Hz and 50 Hz) by applying voltage injection from the inverter
- 3) The multivariable impedances are calculated for each measurement set and the stability analysis is performed by assessing the impedance ratio of the grid and the inverter (for both PLL parameter sets).

The measurements are performed both by MLBS and COS, and the obtained results are compared. The PLL controller parameters are shown in Table 5.

TABLE 5. Phase-locked loop parameters for the stability experiments.

Bandwidth	Proportional gain	Integral gain
1 Hz	0.0388	0.0977
40 Hz	1.5520	156.32
50 Hz	1.9400	244.25

Performing the stability analysis relies on the impedance ratio of the subsystems, and consequently, both the subsystems must be measured at the same frequencies. Therefore, the measurements are performed with the same COS design for both the grid and the inverter. The sequence designed for the grid impedance measurements is selected and also the MLBS is designed similarly (Table 2). The total injection amplitude is set to 0.2 A for current injection and 2 V for voltage injection. The measurements are averaged over 50 periods for the COS and 100 periods for the MLBS, and the total measurement duration for each set of measurements is 51 seconds.

Fig. 22 presents the measured impedance matrix of the grid impedance and inverter output impedance (shown as impedance instead of admittance) measured by applying the MLBS. In Fig. 23, the impedances measured with the COS are shown. It should be noted that the change in

PLL bandwidth has only a minor impact on the impedances besides the phase decrease in the q-channel impedance. In order to assess the system stability, the generalized Nyquist criterion is applied to the impedance ratio [36]. Fig. 24 presents the eigenloci for both system configurations (40 Hz and 50 Hz PLL bandwidth) measured with both the MLBS and the COS. As seen from the figure, both measurements indicate stability for the 40 Hz PLL and instability for the 50 Hz PLL (as the locus encircles the critical point). The measurements with COS show superior accuracy over the MLBS.

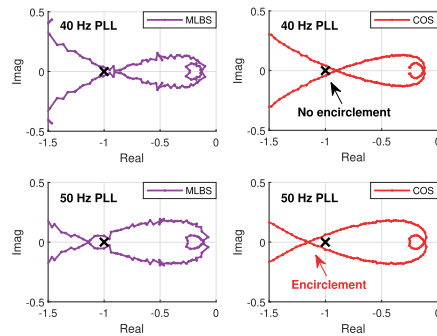


FIGURE 24. Nyquist loci of the 40 Hz (upper) and 50 Hz (lower) PLL systems measured with MLBS (purple) and COS (red).

In order to validate the predicted system stability, an experiment is performed where the PLL controller bandwidth is abruptly changed from 40 Hz to 50 Hz by changing the controller gains. Fig. 25 presents the three-phase current waveforms measured from the grid. In prior to changing the PLL bandwidth, the current waveforms are smooth and sinusoidal. However, increasing the PLL bandwidth provokes an increasing oscillation to the currents, which indicates an unstable system. This experiment validates the performed stability analysis.

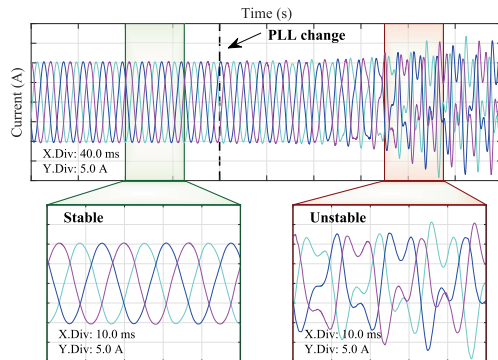


FIGURE 25. Three-phase currents when the PLL bandwidth is increased from 40 Hz to 50 Hz and the stability is lost.

V. CONCLUSION

Impedance measurements are important in the design and analysis of power-electric systems. Recently, significant research effort has been directed to the design of perturbation sequences, as the measurement quality is strongly dependent on the applied perturbation signal. Pseudo-random broadband sequences have demonstrated multiple desirable characteristics, but the linear power distribution of those sequences causes challenges especially in systems that have a wide frequency-range of interest. This work proposed a novel method for the perturbation design. In the method, multiple orthogonal binary sequences are summed up forming a near-binary signal. As the orthogonal sequences can be independently designed, the produced signal can have much higher power at certain frequency bands compared to the conventional MLBS with a similar time-domain amplitude. Additionally, the frequency resolution of the sequences can be selected differently, allowing sufficient resolution over a wide frequency range. Experimental measurements based on a grid-connected inverter system were presented to demonstrate the effectiveness of the proposed method. The results clearly showed the superiority of the proposed combined sequence compared to the conventional MLBS. An experimental stability analysis was performed based on the impedance measurements to present an example utilization for the measured impedances. It is also emphasized, that the proposed method can be applied not only in grid-connected systems but in a wide range of systems where pseudo-random sequences are used for system identification.

REFERENCES

- [1] B. K. Bose, "Global energy scenario and impact of power electronics in 21st century," *IEEE Trans. Ind. Electron.*, vol. 60, no. 7, pp. 2638–2651, Jul. 2013.
- [2] R. Luhtala, T. Roinila, and T. Messo, "Implementation of real-time impedance-based stability assessment of grid-connected systems using MIMO-identification techniques," *IEEE Trans. Ind. Appl.*, vol. 54, no. 5, pp. 5054–5063, Sep. 2018.
- [3] Y. Tang, R. Burgos, B. Wen, D. Boroyevich, J. Verhulst, D. Vrtachnik, and M. Belkhatay, "A novel DQ impedance measurement method in three-phase balanced systems," in *Proc. 20th Workshop Control Modeling Power Electron. (COMPEL)*, Jun. 2019, pp. 1–5.
- [4] T. Roinila, T. Messo, and E. Santi, "MIMO-identification techniques for rapid impedance-based stability assessment of three-phase systems in DQ domain," *IEEE Trans. Power Electron.*, vol. 33, no. 5, pp. 4015–4022, May 2018.
- [5] H. Alenius and T. Roinila, "Impedance-based stability analysis of parallel grid-connected rectifiers: Experimental case study in a data center," *Energies*, vol. 13, no. 8, p. 2109, Apr. 2020.
- [6] B. Wen, D. Boroyevich, R. Burgos, P. Mattavelli, and Z. Shen, "Small-signal stability analysis of three-phase AC systems in the presence of constant power loads based on measured d-q frame impedances," *IEEE Trans. Power Electron.*, vol. 30, no. 10, pp. 5952–5963, Oct. 2015.
- [7] T. Messo, A. Aapro, T. Suntio, and T. Roinila, "Design of grid-voltage feedforward to increase impedance of grid-connected three-phase inverters with LCL-filter," in *Proc. IEEE 8th Int. Power Electron. Motion Control Conf. (IPEMC-ECCE Asia)*, May 2016, pp. 2675–2682.
- [8] R. Luhtala, T. Messo, and T. Roinila, "Adaptive control of grid-voltage feedforward for grid-connected inverters based on real-time identification of grid impedance," in *Proc. Int. Power Electron. Conf. (IPEC-Niigata-ECCE Asia)*, May 2018, pp. 1–8.
- [9] A. Riccobono, M. Cupelli, A. Monti, E. Santi, T. Roinila, H. Abdollahi, S. Arrua, and R. A. Dougal, "Stability of shipboard DC power distribution: Online impedance-based systems methods," *IEEE Electr. Mag.*, vol. 5, no. 3, pp. 55–67, Sep. 2017.
- [10] M. Cespedes and J. Sun, "Online grid impedance identification for adaptive control of grid-connected inverters," in *Proc. IEEE Energy Convers. Congr. Exposit. (ECCE)*, Sep. 2012, pp. 914–921.
- [11] H. Alenius, T. Messo, T. Reinikka, and T. Roinila, "Aggregated modeling and power Hardware-in-the-Loop emulation of grid impedance," in *Proc. IEEE Energy Convers. Congr. Exposit. (ECCE)*, Sep. 2018, pp. 4179–4186.
- [12] R. Luhtala, H. Alenius, T. Messo, and T. Roinila, "Online frequency response measurements of grid-connected systems in presence of grid harmonics and unbalance," *IEEE Trans. Power Electron.*, vol. 35, no. 4, pp. 3343–3347, Apr. 2020.
- [13] T. Roinila and T. Messo, "Online grid-impedance measurement using ternary-sequence injection," *IEEE Trans. Ind. Appl.*, vol. 54, no. 5, pp. 5097–5103, Sep. 2018.
- [14] T. Roinila, T. Messo, T. Suntio, and M. Vilkkö, "Pseudo-random sequences in DQ-domain analysis of feedforward control in grid-connected inverters," *IFAC-PapersOnLine*, vol. 48, no. 28, pp. 1301–1306, 2015, doi: 10.1016/j.ifacol.2015.12.311.
- [15] D. Martin, E. Santi, and A. Barkley, "Wide bandwidth system identification of AC system impedances by applying perturbations to an existing converter," in *Proc. IEEE Energy Convers. Congr. Exposit.*, Sep. 2011, pp. 2549–2556.
- [16] J. Siegers, E. Santi, and A. Barkley, "Wide bandwidth system identification of MVDC distribution system by applying perturbations to an existing converter," in *Proc. IEEE Electr. Ship Technol. Symp. (ESTS)*, Apr. 2013, pp. 434–441.
- [17] A. Riccobono, M. Mirz, and A. Monti, "Noninvasive online parametric identification of three-phase AC power impedances to assess the stability of grid-tied power electronic inverters in LV networks," *IEEE J. Emerg. Sel. Topics Power Electron.*, vol. 6, no. 2, pp. 629–647, Jun. 2018.
- [18] J. Koppinen, J. Kukkola, and M. Hinkkanen, "Plug-in identification method for an LCL filter of a grid converter," *IEEE Trans. Ind. Electron.*, vol. 65, no. 8, pp. 6270–6280, Aug. 2018.
- [19] H. Alenius, T. Roinila, R. Luhtala, T. Messo, A. Burstein, E. de Jong, and A. Fabian, "Hardware-in-the-loop methods for stability analysis of multiple parallel inverters in three-phase AC Systems," *IEEE J. Emerg. Sel. Topics Power Electron.*, early access, Aug. 16, 2020. [Online]. Available: <https://doi.org/10.1109/JESTPE.2020.3014665>
- [20] W. D. T. Davies, "Using the binary maximum length sequence for the identification of system dynamics," *Proc. Inst. Electr. Eng.*, vol. 114, no. 10, p. 1582, 1967.
- [21] A. H. Tan and K. Godfrey, *Industrial Process Identification—Perturbation Signal Design and Applications*, 1st ed. Cham, Switzerland: Springer, 2019.
- [22] M. Liserre, R. Teodorescu, and F. Blaabjerg, "Stability of photovoltaic and wind turbine grid-connected inverters for a large set of grid impedance values," *IEEE Trans. Power Electron.*, vol. 21, no. 1, pp. 263–272, Jan. 2006.

- [23] L. Harnefors, M. Bongiorno, and S. Lundberg, "Input-admittance calculation and shaping for controlled voltage-source converters," *IEEE Trans. Ind. Electron.*, vol. 54, no. 6, pp. 3323–3334, Dec. 2007.
- [24] T. Roinila, M. Vilkkö, and J. Sun, "Online grid impedance measurement using discrete-interval binary sequence injection," *IEEE J. Emerg. Sel. Topics Power Electron.*, vol. 2, no. 4, pp. 985–993, Dec. 2014.
- [25] D. Reigosa, F. Briz, C. B. Charro, P. Garcia, and J. M. Guerrero, "Active islanding detection using high-frequency signal injection," *IEEE Trans. Ind. Appl.*, vol. 48, no. 5, pp. 1588–1597, Sep. 2012.
- [26] A. Rygg and M. Molinas, "Apparent impedance analysis: A small-signal method for stability analysis of power electronic-based systems," *IEEE J. Emerg. Sel. Topics Power Electron.*, vol. 5, no. 4, pp. 1474–1486, Dec. 2017. [Online]. Available: <http://ieeexplore.ieee.org/document/7986961/>
- [27] M. Jaksic, Z. Shen, I. Cvetkovic, D. Boroyevich, R. Burgos, C. DiMarino, and F. Chen, "Medium-voltage impedance measurement unit for assessing the system stability of electric ships," *IEEE Trans. Energy Convers.*, vol. 32, no. 2, pp. 829–841, Jun. 2017.
- [28] J. Schoukens, K. Godfrey, and M. Schoukens, "Nonparametric data-driven modeling of linear systems: Estimating the frequency response and impulse response function," *IEEE Control Syst.*, vol. 38, no. 4, pp. 49–88, Aug. 2018. [Online]. Available: <https://ieeexplore.ieee.org/document/8412623/>
- [29] P. Guillaume, J. Schoukens, R. Pintelon, and I. Kollar, "Crest-factor minimization using nonlinear chebyshev approximation methods," *IEEE Trans. Instrum. Meas.*, vol. 40, no. 6, pp. 982–989, Dec. 1991.
- [30] J. Sun, "Small-signal methods for AC distributed power systems—A review," *IEEE Trans. Power Electron.*, vol. 24, no. 11, pp. 2545–2554, Nov. 2009.
- [31] G. Francis, R. Burgos, D. Boroyevich, F. Wang, and K. Karimi, "An algorithm and implementation system for measuring impedance in the D-Q domain," in *Proc. IEEE Energy Convers. Congr. Exposit.*, Sep. 2011, pp. 3221–3228.
- [32] J. Huang, K. A. Corzine, and M. Belkhaty, "Small-signal impedance measurement of Power-Electronics-Based AC power systems using line-to-line current injection," *IEEE Trans. Power Electron.*, vol. 24, no. 2, pp. 445–455, Feb. 2009.
- [33] H. Alenius, R. Luhtala, and T. Roinila, "Amplitude design of perturbation signal in frequency-domain analysis of grid-connected systems," *IFAC-PapersOnLine*, vol. 2020, pp. 1–6, Jul. 2020.
- [34] J. Sun, "Impedance-based stability criterion for grid-connected inverters," *IEEE Trans. Power Electron.*, vol. 26, no. 11, pp. 3075–3078, Nov. 2011.
- [35] Y. Hu, S. Bu, B. Zhou, Y. Liu, and C.-W. Fei, "Impedance-based oscillatory stability analysis of high power electronics-penetrated power systems—A survey," *IEEE Access*, vol. 7, pp. 120774–120787, 2019.
- [36] M. Belkhaty, "Stability criteria for AC power systems with regulated loads," Ph.D. dissertation, Dept. Elect. Eng., Purdue Univ., West Lafayette, IN, USA, 1997.



HENRIK ALENIUS (Graduate Student Member, IEEE) received the M.Sc. degree in electrical engineering from the Tampere University of Technology, Tampere, Finland, in 2018. He is currently pursuing the Ph.D. degree with the Faculty of Information Technology and Communication Sciences, Tampere University. His research interests include impedance-based interactions in grid-connected systems, broadband methods in impedance measurements, and stability analysis of multi-parallel inverters.



RONI LUHTALA (Graduate Student Member, IEEE) received the M.Sc. degree in electrical engineering from the Tampere University of Technology, Tampere, Finland, in 2017. He is currently pursuing the Ph.D. degree with the Faculty of Engineering and Natural Sciences, Tampere University. His main research interests include real-time identification and adaptive control of grid-connected systems.



TOMI ROINILA (Member, IEEE) received the M.Sc. (Tech.) and Dr.Tech. degrees in automation and control engineering from the Tampere University of Technology, Finland, in 2006 and 2010, respectively. He is currently an Assistant Professor with the Faculty of Information Technology and Communications Sciences, Tampere University, Finland. His main research interests include modeling and control of grid-connected power-electronics systems and modeling of multiconverter systems.

...

PUBLICATION

III

**”Impedance-Based Stability Analysis of Paralleled Grid-Connected Rectifiers:
Experimental Case Study in a Data Center”**

H. Alenius and T. Roinila

Energies, no. 8, vol. 13, pp. 1–15, 2020

Publication reprinted with the permission of the copyright holders

Article

Impedance-Based Stability Analysis of Paralleled Grid-Connected Rectifiers: Experimental Case Study in a Data Center

Henrik Alenius *  and Tomi Roinila

Faculty of Information Technology and Communication Sciences, Tampere University, 33720 Tampere, Finland; tomi.roinila@tuni.fi

* Correspondence: henrik.alenius@tuni.fi

Received: 20 March 2020; Accepted: 17 April 2020; Published: 24 April 2020



Abstract: Grid-connected systems often consist of several feedback-controlled power-electronics converters that are connected in parallel. Consequently, a number of stability issues arise due to interactions among multiple converter subsystems. Recent studies have presented impedance-based methods to assess the stability of such large systems. However, only few real-life experiences have been previously presented, and practical implementations of impedance-based analysis are rare for large-scale systems that consist of multiple parallel-connected devices. This work presents a case study in which an unstable high-frequency operation, caused by multiple paralleled grid-connected rectifiers, of a 250 kW data center in southern Finland is reported and studied. In addition, the work presents an experimental approach for characterizing and assessing the system stability by using impedance measurements and an aggregated impedance-based analysis. Recently proposed wideband-identification techniques based on binary injection and Fourier methods are applied to obtain the experimental impedance measurements from the input terminals of a single data center rectifier unit. This work provides a practical approach to design and implement the impedance-based stability analysis for a system consisting of multiple paralleled grid-connected converters. It is shown that the applied methods effectively predict the overall system stability and the resonant modes of the system, even with very limited information on the system. The applied methods are versatile, and can be utilized in various grid-connected applications, for example, in adaptive control, system monitoring, and stability analysis.

Keywords: grid-connected power electronics; stability analysis; impedance-based stability criterion; system instability; case study

1. Introduction

Grid-connected power-electronics systems have become an essential part of the modern power system. A large share of electricity consumption is processed in power electronics, and also the production has started to shift towards power-electronic interfaced renewable alternatives. Consequently, the number of inverters and rectifiers in the electrical system is increasing rapidly, and it is expected that eventually 100% of the electricity in modern countries will flow through power-electronic devices [1].

Along with the transformation of the energy system, information technology and data processing, such as cloud storages, centralized servers and data mining, are experiencing a revolution. The energy demand for these activities has continuously increased in the past few years, and the data centers are becoming a significant energy consumer [2]. For example, maintaining the blockchain for the cryptocurrency Bitcoin has a yearly energy demand of approximately 43 TWh [3]. The majority

of the required data mining takes place in data centers, where grid-connected power-supplying units (PSUs) feed the processing units. The processors are often graphical processing units (GPUs), central processing units (CPUs) or application-specific integrated circuits (ASICs). To achieve required power levels for high processing capability, multiple modular units are connected in parallel.

The high power consumption of a data center may cause issues in power quality, such as high total harmonic distortion (THD) or flicker in grid voltages [4,5]. In addition, the grid interface of power-electronic devices is prone to adverse interactions, which may lead to dramatic stability issues [6]. The threat of instability increases as more power-electronic units are connected in parallel [7]. Consequently, data centers that can have up to thousands of paralleled PSUs may encounter very low stability margins leading to unstable operation, as already encountered in systems that have multiple parallel inverters [8–10].

Past studies have shown methods that can be applied in stability analysis of grid-connected systems based on eigenvalue modeling [11–13] and impedance-based stability criterion [7,14–17]. Recently, the impedance-based analysis was applied also for a data center [18]. The work in [18] assessed the stability of a large-scale data center through modeling approach, where system topology is known in detail and the results are derived applying considerable modeling effort. However, often the detailed structure of the PSUs is not known, and the analysis must rely at least partially on black-box models. In such systems, modeling-based approaches are not applicable, and impedance measurements are imperative in order to predict the system stability margins.

Methods for measuring the terminal impedance of power-electronic devices have become popular, as the impedance measurements can be directly applied in the stability analysis [17,19–21]. This tackles the issues related to small-signal modeling and black-box nature of many commercial devices. In the methods, a perturbation signal is injected to the terminals and the currents and voltages are measured and Fourier transformed to extract the spectral information. Binary wideband sequences have shown prominent characteristics as perturbation signals, as they possess multiple desirable characteristics, such as controllable frequency content, minimal crest factor, and fast measurement time [21,22].

This work reports an unstable operation experienced in 250 kW data center in southern Finland. Multiple parallel connected power-factor correcting (PFC) rectifiers produced sustained high-frequency oscillation, which distorted the voltages of local low-voltage (LV) grid and damaged nearby electric loads. The main oscillatory frequency manifested in the range of 7–8 kHz and had root-mean-square (RMS) amplitude of approximately 71 V, corresponding to 30.7% of the nominal phase voltage (230 V at 50 Hz). The detailed topology and control scheme of the rectifiers were unknown, and therefore, modeling-based analysis methods are unsuitable for assessing the instability. Additionally, the measurements on the internal dynamics of the rectifiers are unavailable. Thus, the only viable stability analysis method is the impedance-based analysis by applying terminal impedance measurements.

In this work, a 2400 W single-phase PSU (shown in Figure 1) obtained from the data center is examined and the input impedance is measured in varying load range applying pseudo-random binary excitation signal and Fourier methods. The impedance data is utilized in aggregated impedance-based stability analysis, which is used to explain the origin of the experienced instability of the data center. Consequently, the work provides a real-life example of instability in paralleled PSUs in a data center, and explains the origin of this instability based on known grid impedance and impedance-measurements of a single PSU.

The rest of the work is organized as follows. Section 2 provides the fundamental background on impedance-based stability analysis and broadband impedance measurements. Section 3 presents the detailed case description of the instability that occurred in the data center. Section 4 shows the impedance measurements of a single PSU and performs the stability analysis based on aggregated total load impedance of parallel PSUs. In Section 5, a brief discussion on the results of the work is presented. Finally, Section 6 concludes the work.

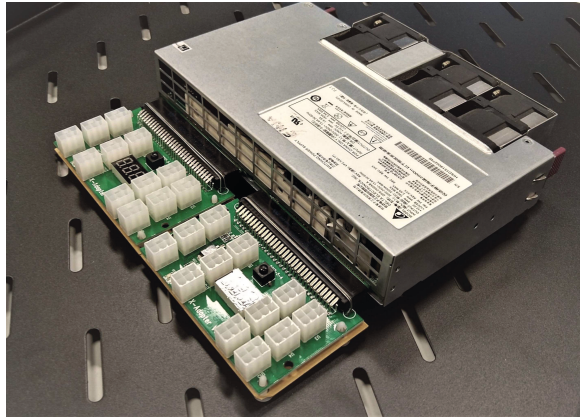


Figure 1. 2400 W single-phase power-supplying unit.

2. Background

2.1. Impedance-Based Stability Criterion

Although switched-mode power-electronics converters are nonlinear systems, the small-signal stability can be accurately assessed based on linearized small-signal-model. A grid-connected converter can be examined as an interconnected source-load system, where the impedance ratio of the subsystems indicates the stability [14]. Figure 2 presents a generalized source-load configuration of Thevenin and Norton equivalents, which is applicable for a grid-connected rectifier.

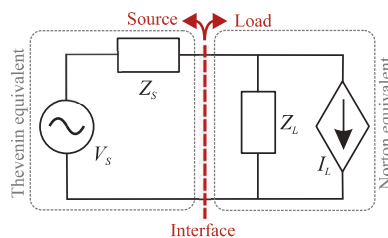


Figure 2. Source-load equivalent circuit for a grid-connected rectifier.

The current flowing from the source subsystem can be given as

$$I(s) = \frac{V_s(s)}{Z_1(s)} H(s) \quad (1)$$

where $V_s(s)$ is the source voltage, $Z_1(s)$ is the load impedance, and $H(s)$ is given as

$$H(s) = \frac{1}{1 + Z_s(s)/Z_1(s)} \quad (2)$$

where $Z_s(s)$ is the source impedance. $H(s)$ resembles the transfer function of a negative feedback control system, where the forward path has a unity gain and the feedback is the impedance ratio. Thus, the stability can be analysed based on the impedance ratio, which is also known as the minor loop gain [23]. The Thevenin and Norton equivalents are interchangeable, and choosing Norton equivalent for source and Thevenin equivalent for load inverts the minor loop gain to be $Z_1(s)/Z_s(s)$. As discussed in [24], the stability analysis can be performed similarly for $Z_1(s)/Z_s(s)$ and $Z_s(s)/Z_1(s)$, and the ratio should be chosen so that it has no right-half plane (RHP) poles.

Conventional control theory tools, such as sensitivity function and Nyquist criterion, can be used in the stability analysis once the impedance-ratio is obtained. Nyquist criterion states that the stability can be analyzed from the Nyquist contour, which is the loop gain (in this case, impedance ratio) in complex plane. The system is stable if the open-loop transfer function is

- Stable and the contour does not encircle the critical point;
- Unstable and the contour encircles the critical point in a counter-clockwise direction once for each RHP pole of the loop gain.

Consequently, the stability of the open-loop transfer function must be known. Additionally, if the contour passes through the critical point $(-1, 0)$, the system is marginally stable. The system sensitivity to disturbances can be assessed through maximum peak criterion (MPC), which interprets the system sensitivity from the minimum distance of the Nyquist contour to the critical point. The distance to the critical point corresponds to the disturbance attenuation at that frequency. The sensitivity function for the impedance-based analysis can be derived straightforwardly from

$$S(s) = \left| \frac{1}{1 + Z_s(s)/Z_l(s)} \right| \quad (3)$$

However, the MPC alone cannot be utilized for stability analysis, as the distance of the contour to the critical point does not consider the stability of the system. Thus, the MPC is only applicable for sensitivity analysis of stable systems.

2.2. Stability Analysis of Paralleled Devices

Originally, the impedance-based stability criterion was derived for systems that have a single source and load subsystem. However, the majority of large-scale systems consist of multiple paralleled devices in order to reach suitable power levels. This is the case also in data centers, where multiple PSUs are connected in parallel to feed the data processing units. To address the stability issue of paralleled devices, the impedance-based stability analysis has been extended to multi-paralleled devices [7]. Figure 3 presents a source-load equivalent of n parallel connected units, similar to Figure 2. Based on the figure, the parallel sources (or loads) can be aggregated to an equivalent source (or load) that has an equivalent impedance of

$$Z_{\text{tot}}(s) = \left(\sum_{n=1}^n 1/Z_n(s) \right)^{-1} \quad (4)$$

A necessary requirement for the aggregation method is that the subsystems are connected to the same point-of-common coupling; that is, the impedance in between the separate units is negligible [7]. In data centers, the PSUs are typically located nearby, so the interconnecting impedances between the PSUs can be assumed to be small. The analysis can be further simplified for parallel-connected systems where the devices are identical. The total aggregated admittance of n identical parallel-connected rectifiers can be obtained straightforwardly from

$$Y_{l,\text{tot}}(s) = n * Y_l(s) \quad (5)$$

In this case study, the PSUs were identical and connected to the same feeding transformer, which makes (5) applicable.

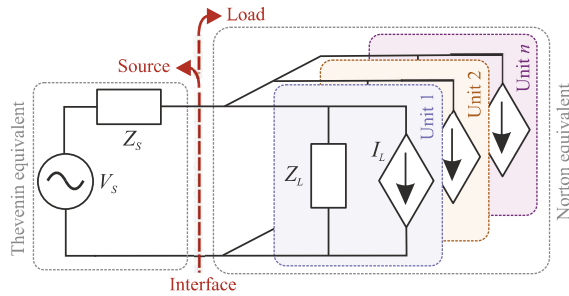


Figure 3. Source-load equivalent circuit for parallel-connected rectifier.

2.3. Impedance Measurements with Broadband Excitations

Typically, the systems under analysis are either complex or partially unknown, and the analytical methods become inadequate. In these cases, the most used approach is the impedance-based analysis, which often relies on practical impedance measurements of the subsystems. The impedance measurements generally require a perturbation signal to be injected to the system, which can be either voltage- or current-type, and the resulting currents and voltages are measured. Then Fourier transform is applied to extract the spectral information (impedance) from the measured signals. Multiple different perturbation signals have been discussed, such as sine sweep, multi-sine sweep, impulse response, or broadband sequences [25].

In this work, a maximum-length binary sequence (MLBS) is applied as the excitation signal. Figure 4 presents a 31-bit-length MLBS generated at 1 kHz. The MLBS is a periodic broadband excitation with a controllable frequency content and minimal peak-factor, which result in fast measurement time and possibility to average over multiple excitation periods [26]. Additionally, the MLBS is easy to generate and implement using a simple shift-register structure. As the signal is binary, it is very easy to implement even with a low-cost device, whose output can only cope with a small number of signal levels. The comparison of the MLBS to other measurement designs has been thoroughly reported in [22]. The sequence length N , frequency resolution f_{res} , and measurement time T_{meas} can be given as

$$N = 2^n - 1 \quad (6)$$

$$f_{res} = \frac{f_{gen}}{N} \quad (7)$$

$$T_{meas} = \frac{PN}{f_{gen}} \quad (8)$$

where n is the length of shift-register system, f_{gen} is the generation frequency, and P is the number of averaged periods. A logarithmic averaging procedure is an effective method for decreasing the effect of noise in periodic signals, which can be given as

$$Z(j\omega) = \left(\prod_{k=1}^P \frac{U_k(j\omega)}{I_k(j\omega)} \right)^{(1/P)} \quad (9)$$

where $U(j\omega)$ and $I(j\omega)$ are the Fourier-transformed voltages and currents [26].

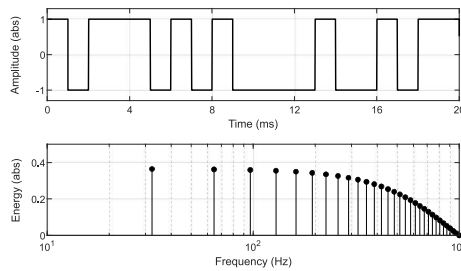


Figure 4. Maximum-length binary sequence in time-domain and frequency-domain.

3. Case Description: Sustained Harmonic Resonance in a Data Center

In November 2017, a new data center in southern Finland expressed unstable behavior, which produced dramatic sustained harmonic resonance in system currents and voltages causing breakdown of electric equipment for nearby consumers. Figure 5 presents the measured grid voltages at the point-of-common coupling of the data center. A drastic harmonic distortion is observed at around 7–8 kHz frequency range, with peak-to-peak amplitude of 200 V (that is, 31% of nominal peak-to-peak voltage). This sustained resonance corresponds to a total harmonic distortion (THD) of 31%, which is approximately four times the THD limitation set by standards (maximum 8% THD given in SFS-EN 50160 standard) [27]. In addition, the upper limit for grid voltages in the standard is +10% of the nominal phase voltage (360 V peak value) [27]. However, the sustained resonance introduced temporary phase voltages up to 420 V peak value, that is, 29% above normal peak voltages. The initial attempt to remove the harmonics was to decrease the data center power from 263 kW to 140 kW. However, the harmonic resonance persisted and was not removed until the data center replaced the PSUs with devices from a different manufacturer.

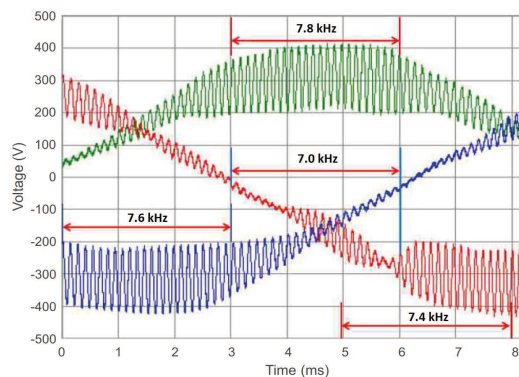
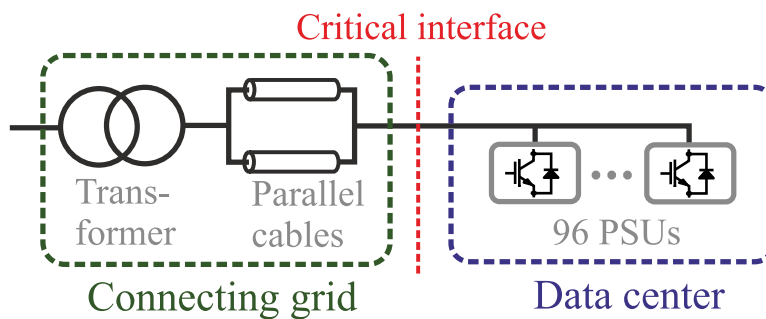


Figure 5. Unstable operation in a data center: distorted phase voltages.

The data center connects to the grid through a 500 kVA transformer (20.5/0.41 kV) and two parallel underground cables (AXMK-Plus 2). The parameters are given in Table 1. The effect of other local electric loads such as fans is assumed to be negligible, and left out from the analysis. Figure 6 presents the overview of the grid connection of the data center.

Table 1. Parameters of grid connection.

Parameter		Value
Cable	Length	88 m
	Resistance	0.20 Ω /km
	Capacitance	0.28 μ F/km
	Inductance	0.26 mH/km
Transformer	Nominal power	500 kW
	Voltage	20.5/0.41 kV
	Resistance	1.064%
	Reactance	4.420%

**Figure 6.** Schematic diagram of the data center and the grid.

4. Experimental Impedance-Based Stability Analysis

The stability analysis is performed based on impedance measurements of a single PSU acquired from the data center and known grid parameters. The equivalent parallel impedance of multiple PSUs is approximated from the impedance measurements, and the stability margins are examined using impedance-based stability criterion. The replacement PSUs could not be obtained for measurements, so a comparison of terminal impedances of the different type PSUs is not available.

4.1. Experimental Setup

An experimental setup shown in Figure 7 was built for measuring the PSU input impedance. The setup consists of a linear 4-quadrant voltage amplifier (Spitzenberger&Spies PAS 15000) controlled using dSPACE real-time simulator (model 1103, GmbH, Germany), the PSU, I/O measurement card (National Instruments data acquisition card USB-6363), and a custom passive load for output power consumption. The voltage amplifier is set to emulate 230 V phase voltage at 50 Hz frequency, which provides the input power to the PSU. Additionally, a preprocessed broadband MLBS excitation is added to the grid voltage reference in order to provide the perturbation for the PSU impedance measurements.

The operation conditions of the PSU, such as loading state, affect the input impedance. Thus, multiple impedance measurements are required so that more reliable analysis on the system behavior can be obtained. However, the low PSU output voltage of 12.5 V paired with high single-phase power output of 2.4 kW results in very high current (that is, 200 A). To tackle this issue, a modular passive load was built from 10 paralleled ceramic power resistors ($R = 0.8 \Omega$), each of which rated for 300 W dissipation. The actual power dissipation at 12.5 V voltage is approximately 200 W for each resistor. The experimental power resistor load for the PSU is shown in Figure 8. The measurements

are performed to the powers up to 80% of the maximum load, which is assumed to be approximately the typical loading state. Further increases of the loading above 50% change the impedance only marginally, and consequently, the obtained results can be assumed to valid for loading conditions between 50% and 100% of the nominal load. In a data center, the PSUs can be assumed to be operated in this range all the time.

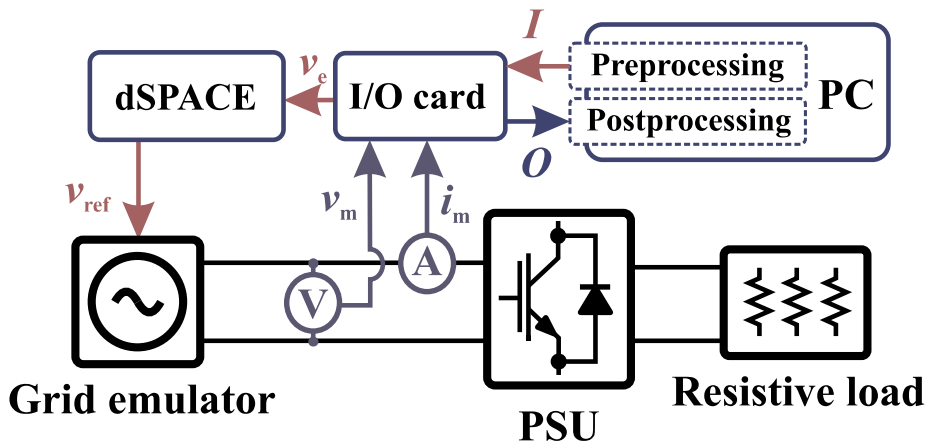


Figure 7. Schematic diagram of the experimental measurement setup.



Figure 8. Modular passive load for emulating DC power consumption.

4.2. Impedance Measurements

The input impedance of the PSU was measured by applying a 2047-bit-length MLBS injection generated at 140 kHz. These parameters yielded a frequency resolution of approximately 68 Hz and an injection time of approximately 14.6 ms (for a single-period injection). In order to increase the signal-to-noise ratio, the injection was applied with 2000 periods and the results averaged using (9). The total injection time was therefore approximately 29.2 s. The excitation is voltage-type with an amplitude of 2 V, and therefore, the measurement provides admittance data. However, in this work all the measurements are shown as impedances for consistency.

The input impedance of the PSU was measured during varying PSU output powers, ranging from 0 to 10 paralleled resistors, corresponding to power range of 0–2000 W. Figure 9 shows the measured

input impedances. The impact of the power level has a drastic impact on the measured input impedance, as a distinct resonant shape appears as the output power is increased. In addition, the phase experiences a sudden shift of 360 degrees at the resonant frequency when the PSU operates above 30% of the nominal power. This indicates a shift of a system pole from left-hand plane (LHP) to right-hand plane (RHP). In order to verify this observation, an analytical transfer function based on the measured frequency-response data is estimated by using a least-square fitting function. Figure 10 presents the corresponding pole pair as a function of output power. The path of the pole pair crosses the imaginary axis at 600 W power, explaining the phase behavior at the resonance frequency. The presence of a RHP pole in the input impedance of the PSU indicates that the minor loop gain should be examined as $Z_{\text{grid}}/Z_{\text{PSU}}$ so that the RHP poles can be avoided (the grid impedance is passive and contains no RHP poles or zeros). Although the input impedance has RHP poles, the grid-connected PSU is inherently a voltage-input type device and the zeros and poles of input admittance describe the internal stability of the device. Consequently, the admittance has only RHP zeros and no RHP poles, and the device is internally stable as assumed.

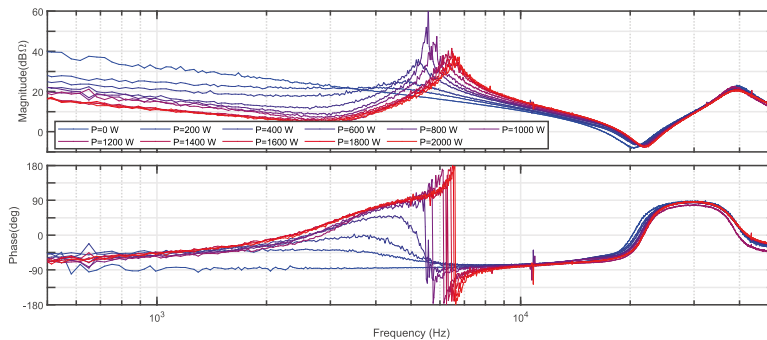


Figure 9. Measured PSU input impedance with input powers varying from 0 to 2000 W (blue to red, from 0% to 80%).

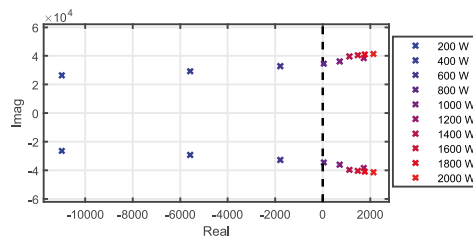


Figure 10. Pole-pair that shifts from LHP to RHP as the output power increases.

4.3. Stability Analysis

The stability analysis is performed by applying the presented impedance-based stability criterion (Section 2.1) and aggregation of identical parallel devices (Section 2.2). The PSU impedance is obtained through experimental measurements, and the grid impedance is analytically derived from the known grid parameters. The single-phase PSUs are assumed to be evenly distributed in the three phases. Figure 11 presents the modeled grid impedance (left, black) and the total impedance of parallel PSUs ranging from 3 to 96 units (right, blue to red). The PSUs operate at 80% loading conditions (2000 W) and all the units are assumed to be identical to the experimentally measured unit. The total impedance is obtained using (5).

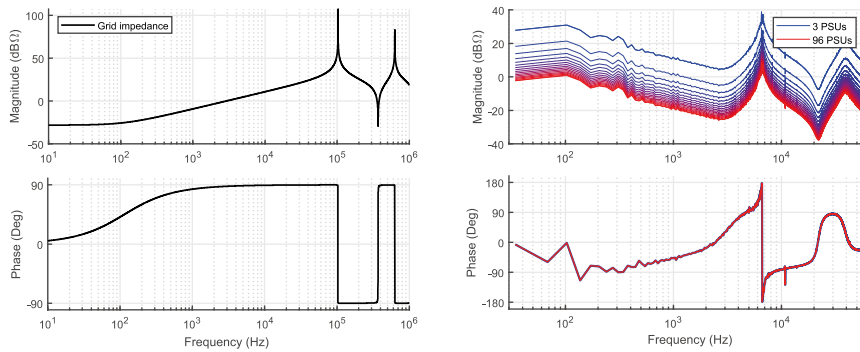


Figure 11. Modeled grid impedance (left, black) and aggregated measured PSU impedance (left, blue to red).

The first method applied for the stability analysis is Nyquist criterion where the minor loop gain (the impedance ratio) is drawn in complex plane. The system is stable if the contour does not encircle the critical point $(-1, 0)$. Figure 12 presents the Nyquist contours for the paralleled PSUs. As seen from the figure, increasing the number of PSUs from 9 to 12 shifts the contour to left resulting in encirclement of the critical point. Thus, the maximum number of paralleled devices is only 9 based on the impedance-based Nyquist analysis.

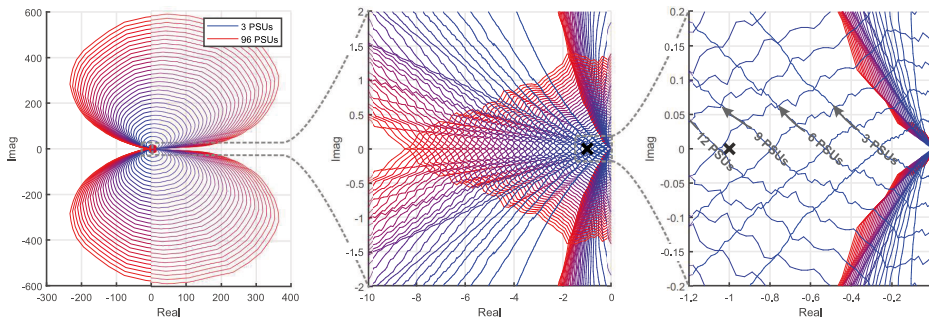


Figure 12. Nyquist contour of the minor loop gain when the number of paralleled PSUs is increased.

As a complementary method, a closed-loop stability of the system can be assessed through transfer function fitting and pole-zero analysis. The closed-loop poles of the system correspond to the eigenvalues of the system and describe the resonant modes by yielding the resonance frequencies and damping factors. Consequently, in addition to the absolute stability illustrated in the Nyquist contours, the modal analysis of closed-loop poles yield also the stability margins of the system. A linear time-invariant transfer function can be fitted to the aggregated PSU input impedance. Based on the fitted transfer functions, the closed-loop poles of the system are obtained by using (2). The poles shift as the number of parallel PSUs is increased, which corresponds to the changing stability margins of the system. Figure 13 shows the root loci of the system closed-loop poles, which show that the right-most pole pair (critical pole pair) shifts from LHP to RHP as the number of parallel devices increases from 12 to 15. The prediction of the stability boundary differs from the Nyquist analysis by 3 converters (1 per phase), which results from the slight inaccuracies in the transfer-function fitting performed for the closed-loop pole analysis. However, the eigenvalue analysis is an auxiliary method that aims to obtain the resonant modes and dampings, and the absolute stability should be assessed applying the unmodified measurement data in Nyquist analysis.

The critical poles have frequencies in the range of 6–8 kHz for multiple paralleled PSUs as showed in detail in Table A1 in Appendix A. This frequency corresponds accurately to the frequency of oscillation observed in the data center shown in Figure 5. Thus, the performed stability analysis predicted both the instability of the data center and the resonance frequency.

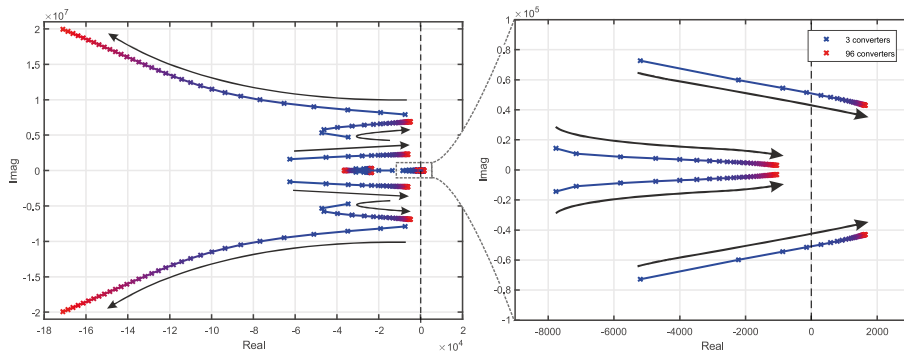


Figure 13. Pole path for critical system poles as the number of paralleled PSUs is increased.

5. Discussion

While the dynamics of grid-connected converters and related stability analysis methods are widely studied, real-life cases and applications of the methods still remain rare. This study presented a practical implementation of an impedance-based stability analysis, where the instability of a commercial data center is explained directly from the black-box impedance measurements of a single PSU. The steps of this process are

1. Model the grid impedance at the point-of-common coupling;
2. Measure the input impedance of a converter;
3. Aggregate the parallel devices;
4. Calculate the impedance ratio and avoid RHP poles;
5. Perform the stability analysis through Nyquist contours or closed-loop eigenvalues..

In this study, only a limited amount of information was available from the data center: the parameters of the grid connection and the number of paralleled PSUs were known, and a PSU acquired from the data center. The detailed wiring schematics, topology of the PSUs, and control schemes of the PSUs were all unknown or unavailable. Consequently, the impedance-based stability analysis utilizing the terminal impedance measurements of a PSU is the only method that can cope with these limitations. The impedance measurements were performed for a single PSU, and the rest were assumed identical. While all the PSUs were the same model, a variation is possible in the component values of the units. The detailed connection configuration of the PSUs and resonance frequency spectrum were unavailable. In addition, the PSU could not be measured in natural operation, where the load is graphical or central processing units. Instead, a resistive load was built to consume the output power, so that the PSUs can be measured at a nominal power. The output load may have impact on the input impedance through load effect, which may result in slight inaccuracies in the impedance measurements. Despite these challenges, the applied stability analysis predicted both the instability and the resonant frequencies, and the unstable operation could have been avoided if a similar analysis had been performed prior to commissioning the data center.

Mitigating the stability issues post-commissioning can be tedious or expensive, as it is significantly easier to avoid the stability issues instead of attempting to fix them. In general, the main contributor for stability issues in systems that consist of multiple parallel converters is a high grid impedance,

that increases the interaction between the converters. In an ideal grid, an arbitrary number of converters can be connected in parallel, as all the current is directed to the zero-impedance grid and the bus voltages are rigid, and consequently, the converters cannot interact with each other. Consequently, the most straightforward method for resolving stability issues in such systems is to decrease the grid impedance by strengthening the grid through investments such as increasing the power rating of the grid-interfacing transformer or adding parallel cables from the transformer to the converters. However, these are often costly investments, and the viability should be carefully assessed by utilizing, for example, the presented measurement-based impedance analysis. In the presented data center, the PSUs were highly unsuited for multi-parallel operation due to the drastic resonant peak and present RHP zero pair. Very significant grid investments would have been required to decrease the grid impedance enough to stabilize the system, and thus, the most applicable solution was to completely replace the PSUs. Again, the replacement PSUs should be assessed beforehand to ensure the compatible operation.

6. Conclusions

Impedance-based stability criterion is a valuable tool in analysis of grid-connected systems. This work has shown a practical approach and a case study in which the stability criterion was applied to explain the instability occurred in a new data center in Southern Finland. The instability was observed as a sustained high-frequency resonance that had amplitude of 31% of nominal grid voltages measured at the grid-coupling transformer. The instability originated from paralleled rectifiers used in power supplying that had total power capacity of 250 kW.

In this work, the input impedance of a single power-supplying rectifier acquired from the data center was measured and the impedance-based stability analysis was extended to multi-converter systems, where the analysis was performed based on aggregated impedance-based stability criterion. The analysis revealed decreasing stability margins as more units were connected in parallel, until the stability was lost when the number of paralleled devices was increased to 12 (total power of 30 kW). In addition, system eigenvalue analysis accurately predicted the resonance frequency to the range of 6–8 kHz, which was the resonant frequency in the initial on-site measurements at the data center. To conclude the findings, the instability of the data center along with resonant modes could have been predicted by measuring the input impedance of a single rectifier and applying aggregated impedance-based stability criterion.

Author Contributions: Conceptualization, H.A.; Methodology, H.A.; Software, H.A. and T.R.; Validation, H.A.; Formal Analysis, H.A.; Investigation, H.A.; Resources, T.R.; Data Curation, H.A.; Writing – Original Draft Preparation, H.A.; Writing – Review & Editing, T.R.; Visualization, H.A.; Supervision, T.R.; Project Administration, T.R.; Funding Acquisition, T.R. All authors have read and agreed to the published version of the manuscript.

Funding: This research was funded by Business Finland.

Conflicts of Interest: The authors declare no conflict of interest.

Appendix A. Critical Poles of Paralleled PSUs

Table A1 shows the detailed characteristics of the critical pole pair for varying number of parallel PSUs, as shown in Figure 13. Increasing the number of paralleled PSUs above 12 results in pole-shift to RHP, which indicates unstable system described by the negative damping factors shown in red.

Table A1. Critical pole pairs.

Parallel PSUs	Critical Pole Pair (1000 rad/s)	Frequency (Hz)	Damping Factor
3	$-5.197 \pm 72.761i$	11,609.8	0.0714
6	$-2.216 \pm 59.83i$	9528.8	0.0370
9	$-0.871 \pm 54.448i$	8666.8	0.0160
12	$-0.147 \pm 51.515i$	8198.9	0.0029
15	$0.293 \pm 49.674i$	7906	-0.0059
18	$0.583 \pm 48.412i$	7705.6	-0.0120
21	$0.786 \pm 47.493i$	7559.8	-0.0166
24	$0.936 \pm 46.794i$	7449.0	-0.0200
27	$1.049 \pm 46.246i$	7362.2	-0.0227
30	$1.139 \pm 45.803i$	7292.0	-0.0249
33	$1.210 \pm 45.439i$	7234.4	-0.0266
36	$1.269 \pm 45.134i$	7186.1	-0.0281
39	$1.317 \pm 44.874i$	7145.0	-0.0294
42	$1.358 \pm 44.651i$	7109.7	-0.0304
45	$1.393 \pm 44.458i$	7079.2	-0.0313
48	$1.424 \pm 44.287i$	7052.1	-0.0321
51	$1.450 \pm 44.137i$	7028.4	-0.0328
54	$1.473 \pm 44.003i$	7007.2	-0.0335
57	$1.494 \pm 43.883i$	6988.2	-0.0340
60	$1.512 \pm 43.775i$	6971.2	-0.0345
63	$1.528 \pm 43.677i$	6955.7	-0.0350
66	$1.543 \pm 43.588i$	6941.6	-0.0354
69	$1.556 \pm 43.506i$	6928.6	-0.0358
72	$1.568 \pm 43.431i$	6916.8	-0.0361
75	$1.579 \pm 43.362i$	6905.9	-0.0364
78	$1.590 \pm 43.299i$	6895.9	-0.0367
81	$1.599 \pm 43.239i$	6886.4	-0.0370
84	$1.608 \pm 43.185i$	6877.9	-0.0372
87	$1.616 \pm 43.134i$	6869.8	-0.0375
90	$1.623 \pm 43.086i$	6862.2	-0.0377
93	$1.630 \pm 43.041i$	6855.1	-0.0379
96	$1.636 \pm 42.999i$	6848.5	-0.0381

References

1. Bose, B. Global Energy Scenario and Impact of Power Electronics in 21st. Century. *IEEE Trans. Ind. Electron.* **2013**, *60*, 2638–2651. [CrossRef]
2. Koomey, J. Worldwide electricity use in data centers. *Environ. Res. Lett.* **2008**, *3*, 220–236. [CrossRef]
3. Kosharnaya, Y.; Yanchenko, S.; Kulikov, A. Specifics of Data Mining Facilities as Energy Consumers. In Proceedings of the 12th International Scientific and Technical Conference on Dynamics of Systems, Mechanisms and Machines, Omsk, Russia, 13–15 November 2018; pp. 1–4. [CrossRef]
4. Harinath, P.; Kamaleswaran, K.; Venkateshwaran, M.; Sreenath, C.; Prabhakaran, S.; Kirubakaran, V. A critical analysis of Power Quality issues in Data Center. In Proceedings of the 2016 Biennial International Conference on Power and Energy Systems: Towards Sustainable Energy (PESTSE), Bengaluru, India, 21–23 January 2016; pp. 1–6.
5. Nassif, A.B.; Wang, Y.; Rahimi Pordanjani, I. Power Quality Characteristics and Electromagnetic Compatibility of Modern Data Centres. In Proceedings of the 2018 IEEE Canadian Conference on Electrical Computer Engineering (CCECE), Québec City, QC, Canada, 13–16 May 2018; pp. 1–4.
6. Suntio, T.; Messo, T.; Berg, M.; Alenius, H.; Reinikka, T.; Luhtala, R.; Zenger, K. Impedance-Based Interactions in Grid-Tied Three-Phase Inverters in Renewable Energy Applications. *Energies* **2019**, *12*. [CrossRef]
7. Alenius, H.; Berg, M.; Luhtala, R.; Roinila, T.; Messo, T. Impedance-Based Stability Analysis of Multi-Parallel Inverters Applying Total Source Admittance. In Proceedings of the 2019 20th Workshop on Control and Modeling for Power Electronics (COMPEL), Toronto, ON, Canada, 16–19 June 2019; pp. 1–8. [CrossRef]

8. Li, C. Unstable Operation of Photovoltaic Inverter from Field Experiences. *IEEE Trans. Power Deliv.* **2017**, *33*, 1013–1015. [CrossRef]
9. Buchhagen, C.; Rauscher, C.; Menze, A.; Jung, J. BorWin1—First Experiences with harmonic interactions in converter dominated grids. In Proceedings of the International ETG Congress 2015; Die Energiewende—Blueprints for the New Energy Age, Bonn, Germany, 17–18 November 2015; pp. 27–33.
10. Wang, L.; Xie, X.; Jiang, Q.; Liu, H.; Li, Y.; Liu, H. Investigation of SSR in Practical DFIG-Based Wind Farms Connected to a Series-Compensated Power System. *IEEE Trans. Power Syst.* **2015**, *30*, 2772–2779. [CrossRef]
11. Amin, M.; Molinas, M. Small-Signal Stability Assessment of Power Electronics based Power Systems: A Discussion of Impedance- and Eigenvalue-based Methods. *IEEE Trans. Ind. Appl.* **2017**, *53*, 5014–5030. [CrossRef]
12. Wang, Y.; Wang, X.; Blaabjerg, F.; Chen, Z. Harmonic instability assessment using state-space modeling and participation analysis in inverter-fed power systems. *IEEE Trans. Ind. Electron.* **2017**, *64*, 806–816. [CrossRef]
13. Zhou, J.Z.; Ding, H.; Fan, S.; Zhang, Y.; Gole, A.M. Impact of short circuit ratio and phase locked loop parameters on the small signal behavior of a VSC HVDC converter. *IEEE Trans. Power Deliv.* **2014**, *29*, 2287–2296. [CrossRef]
14. Sun, J. Impedance-based stability criterion for grid-connected inverters. *IEEE Trans. Power Electron.* **2011**, *26*, 3075–3078. [CrossRef]
15. Vesti, S.; Suntio, T.; Oliver, J.A.; Prieto, R.; Cobos, J.A. Impedance-based stability and transient-performance assessment applying maximum peak criteria. *IEEE Trans. Power Electron.* **2013**, *28*, 2099–2104. [CrossRef]
16. Rygg, A. Impedance-Based Methods for Small-Signal Analysis of Systems Dominated by Power Electronics. Ph.D. Thesis, NTNU, Trondheim, Norway, 2018.
17. Roinila, T.; Messo, T.; Santi, E. MIMO-identification techniques for rapid impedance-based stability assessment of three-phase systems in DQ Domain. *IEEE Trans. Power Electron.* **2018**, *33*, 4015–4022. [CrossRef]
18. Sun, J.; Xu, M.; Cespedes, M.; Wong, D.; Kauffman, M. Modeling and analysis of data center power system stability by impedance methods. In Proceedings of the 2019 IEEE Energy Conversion Congress and Exposition, ECCE 2019, Baltimore, MD, USA, 29 September–3 October 2019; pp. 107–116. [CrossRef]
19. Cespedes, M.; Sun, J. Three-phase impedance measurement for system stability analysis. In Proceedings of the IEEE 14th Workshop on Control and Modeling for Power Electronics (COMPEL), Salt Lake City, UT, USA, 23–26 June 2013; pp. 1–6.
20. Tang, Y.; Burgos, R.; Wen, B.; Boroyevich, D.; Verhulst, J.; Vrtachnik, D.; Belkhat, M. A Novel DQ Impedance Measurement Method in Three-Phase Balanced Systems. In Proceedings of the 2019 20th Workshop on Control and Modeling for Power Electronics (COMPEL), Toronto, ON, Canada, 16–19 June 2019; pp. 1–5. [CrossRef]
21. Roinila, T.; Messo, T.; Suntio, T.; Vilkkko, M. Pseudo-Random Sequences in DQ-Domain Analysis of Feedforward Control in Grid-Connected Inverters. In Proceedings of the 17th IFAC Symposium on System Identification SYSID 2015, Beijing, China, 19–21 October 2015; Volume 48, pp. 1301–1306. [CrossRef]
22. Tan, A.H.; Godfrey, K. *Industrial Process Identification—Perturbation Signal Design and Applications*; Springer: Berlin, Germany, 2019; p. 217.
23. Middlebrook, D. Input filter considerations in design and applications of switching regulators. In Proceedings of the IEEE Industry Applications Society Annual Meeting, Chicago, IL, USA, 11–14 October 1976; pp. 91–107.
24. Liao, Y.; Wang, X. General Rules of Using Bode Plots for Impedance-Based Stability Analysis. In Proceedings of the 2018 IEEE 19th Workshop on Control and Modeling for Power Electronics (COMPEL), Padova, Italy, 25–28 June 2018; pp. 1–6. [CrossRef]
25. Roinila, T.; Vilkkko, M.; Sun, J. Broadband methods for online grid impedance measurement. In Proceedings of the IEEE Energy Conversion Congress and Exposition (ECCE), Denver, CO, USA, 15–19 September 2013; pp. 3003–3010. [CrossRef]

26. Godfrey, K. *Perturbation Signals for System Identification*; Prentice Hall: London, UK, 1993.
27. Standard EN 50160. *Voltage Characteristics of Electricity Supplied by Public Distribution System*; EN: Brussels, Belgium, 2004.



© 2020 by the authors. Licensee MDPI, Basel, Switzerland. This article is an open access article distributed under the terms and conditions of the Creative Commons Attribution (CC BY) license (<http://creativecommons.org/licenses/by/4.0/>).

PUBLICATION

IV

**”Amplitude Design of Perturbation Signal in Frequency-Domain Analysis of
Grid-Connected Systems”**

H. Alenius, R. Luhtala and T. Roinila

in Proc. *IFAC World Congress*, pp. 1–6, 2020

Publication reprinted with the permission of the copyright holders

Amplitude Design of Perturbation Signal in Frequency-Domain Analysis of Grid-Connected Systems

Henrik Alenius* Roni Luhtala** Tomi Roinila*

* Faculty of Information Technology and Communication Sciences, Tampere University, Finland, (e-mail: henrik.alenius@tuni.fi; tomi.roinila@tuni.fi).

** Faculty of Engineering and Natural Sciences, Tampere University, Finland, (e-mail: roni.luhtala@tuni.fi).

Abstract: The rise of renewable electricity production has driven the power grid to a remarkable transformation, where a large share of the electricity production is integrated to the grid through power-electronic inverters. The inverters have fast internal dynamics and no inherent inertia, which makes the power grid prone to stability issues. The stability analysis to ensure system robustness can be performed based on the impedance ratio of the inverter and power grid. The grid impedance is often an unknown parameter, and methods for grid impedance measurements are required. Past studies have presented a number of measurement methods based on a broadband perturbation, such as pseudo-random binary sequence (PRBS), and Fourier techniques for obtaining the grid impedance. However, only a little attention has been paid to the injection-amplitude design, and most often, the amplitude has been selected based on trial and error. This work presents an algorithm based on the total harmonic distortion (THD) levels of grid currents and voltages for choosing a suitable perturbation amplitude. The proposed method makes it possible to fully automate the stability analysis of a grid-connected system. Experimental results based on a three-phase grid-connected inverter are presented and used to demonstrate the effectiveness of the proposed method.

Keywords: Power Electronics, Grid-Connected Systems, Frequency-Response Measurements, Broadband Sequences, Perturbation Design, Excitation Amplitude.

1. INTRODUCTION

The rise of renewable electricity production has started to change the power grid (Bose (2013)). Unlike conventional centralized synchronous generators, the renewable energy production is often distributed in the system. Additionally, the majority of wind and solar power is interfaced to the grid through a grid-connected three-phase inverter, which accommodates the produced power to the grid frequency and voltage. Fig. 1 presents a schematic of an inverter interfacing a renewable power source to the grid. The inverters typically have fast internal dynamics and no inherent inertia, which makes the system prone to stability issues. One issue that has been studied is the harmonic resonance between the inverter and power grid, which occurs in systems that have high penetration of grid-connected inverters (Li (2017); Liu et al. (2017)). The harmonic resonance may appear to be a power quality problem, but it is actually an indication of lack of system stability margin and may lead to instability and disruption of inverter operation if the grid impedance or the inverter power level further increases.

Recent studies have presented multiple methods for stability analysis of grid-connected inverters (Sun (2011); Amin and Molinas (2017); Wang et al. (2017b,a); Rygg and Molinas (2017); Alenius et al. (2019a,b)). The most ap-

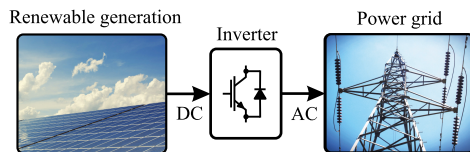


Fig. 1. Power-electronic interface between renewable generation and power grid.

plied approach is the impedance-based stability criterion, which analyzes the inverter output impedance and grid impedance at the common interface, where a Nyquist stability criterion is applied to the ratio of these impedances (Sun (2011); Suntio et al. (2019); Alenius and Roinila (2020)). In general, the inverter impedance can be obtained by impedance modeling (Wang et al. (2018)). However, the grid impedance seen from the interface is often either unknown or highly complex and, therefore, difficult to model. Thus, in many cases the grid impedance is a black-box model and accurate analysis requires measurements or estimates. Additionally, the grid conditions may fluctuate along with system power flows, which affects the impedance (Jessen et al. (2015)). The grid impedance is a crucial variable as the stability issues emerge mostly in high-impedance grids typical for remote locations or systems that have high penetration of distributed generation.

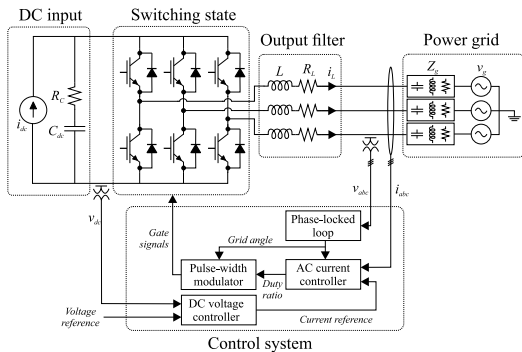


Fig. 2. Three-phase grid-connected inverter.

Recently, a number of measurement techniques for obtaining the grid impedance for stability analysis have been presented (Cespedes and Sun (2013); Roinila et al. (2018); Luhtala et al. (2020)). In most of the presented methods, a current excitation is applied to perturb the system. In grid impedance measurements, the excitation can be injected to the current references of a grid-connected inverter, and the currents and voltages are measured from the output terminals of the inverter. The frequency response of the impedance can be obtained by applying Fourier methods to these currents and voltages. Broadband signals have become popular for excitation as they allow measurements from multiple frequencies simultaneously, resulting in significantly shorter measurement times in comparison to conventional sine sweep (Godfrey (1993); Roinila et al. (2018)). Particularly attractive characteristics have been demonstrated in pseudo-random binary sequences (PRBS), which have tunable frequency spectrum, minimal crest factor, and they are easy to generate. In addition, the signals are periodic, which allows averaging over multiple periods to increase the signal-to-noise ratio (SNR).

One of the challenges of the previously presented measurement techniques of the grid impedance has been the selection of the excitation amplitude. The excitation amplitude determines the SNR in the measurements, and a sufficiently large amplitude is required to overcome the noise in the system. On the other hand, the excitation appears as harmonic pollution in the power grid, and too large excitation amplitude may trigger system nonlinearities. Consequently, the amplitude should be selected as a tradeoff between these two colliding requirements. While previously introduced methods have been able to measure the grid impedance accurately, the excitation amplitude has been often selected by trial and error, and no straightforward guidelines or methods have been presented for the amplitude selection. The lack of methods for simple/automated amplitude selection not only increases the total measurement time for obtaining the impedance, but also affects the measurement quality as the system parameters typically vary over time and, therefore, a varying value for the amplitude may be required.

This work presents a method for amplitude selection for impedance measurements of grid-connected systems. The proposed method considers the effect of perturbation injection on grid-side voltage and current total harmonic distortion (THD), and tunes the amplitude with respect to the THD limits. The impact of averaging and amplitude selection on measurement accuracy is demonstrated for grid-impedance measurements applying a grid-connected inverter. Experimental power hardware-in-the-loop (PHIL) measurements are performed with a 2.7 kW three-phase inverter for grids with varying impedance.

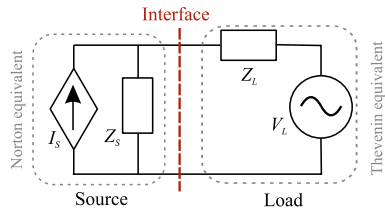


Fig. 3. Equivalent source-load model of grid-connected inverter.

The remainder of the paper is organized as follows. Section II presents the impedance-based stability criterion for grid-connected inverter. Section III considers system identification with maximum-length binary sequence (MLBS) and presents the proposed algorithm for injection amplitude selection. In Section IV, the experimental setup and measurement results are shown. Section V discusses the use of the proposed method and suggests general guidelines for the amplitude selection. Finally, conclusions are drawn in Section VI.

2. IMPEDANCE-BASED STABILITY CRITERION

Fig. 2 shows a simplified diagram of a grid-connected three-phase inverter. The system can be analyzed as a simplified source-load equivalent, where the inverter represents a source and the grid acts as a load, as shown in Fig. 3. The source is modeled by a Norton equivalent circuit, as a current source I_S in parallel with the source impedance Z_S . The load voltage is denoted by V_L , and the load impedance by Z_L . Assuming the source is stable when unloaded and the load is stable when powered by an ideal source, the stability and other dynamic characteristics of the interconnected system can be determined from the transfer function

$$G(s) = \frac{1}{1 + Z_L(s)/Z_S(s)} \quad (1)$$

where $Z_L(s)$ is the load impedance and $Z_S(s)$ is the source impedance. The impedance ratio $Z_L(s)/Z_S(s)$ must satisfy Nyquist criterion for the system to be stable (Sun (2011)). For three-phase devices, similar analysis can be performed applying impedance matrices, for example in dq frame, and generalized Nyquist criterion (GNC) applicable for multi-input-multi-output (MIMO) systems (Belkhaty (1997)). The source impedance of an inverter can be acquired from small-signal model, data sheet, or by measurements from output terminals. The load impedance (grid impedance), however, is typically unknown and can vary over a wide range. Thus, the grid impedance measurements are often required for stability analysis of grid-connected devices.

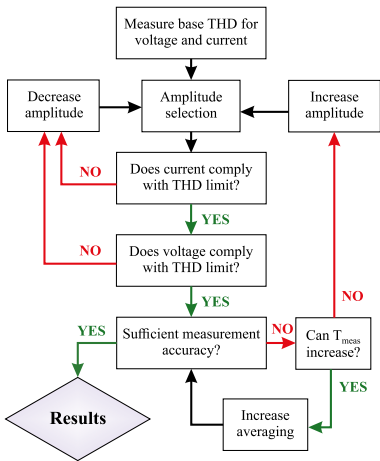


Fig. 4. Flowchart of the amplitude selection algorithm.

3. BROADBAND SYSTEM IDENTIFICATION

In steady state, a grid-connected system can be considered as a linear time-invariant system for small disturbances. According to basic control theory, such system can be fully characterized by its impulse response in the time domain, which can be transformed to the frequency domain and presented as a frequency-response function (Godfrey (1993)). A method to obtain the frequency-response function of the grid impedance is to apply a broadband perturbation such as the pseudo-random binary sequence (PRBS). In the method, the perturbation is injected into the network (for example, by using the inverter), and Fourier analysis is applied to extract the frequency-domain voltages and currents to obtain the impedance.

3.1 Maximum-Length Binary Sequence

Maximum-length binary sequence (MLBS) is a type of pseudo-random sequence that has been successfully applied in grid-impedance measurements (Roinila et al. (2018)). The MLBS has multiple characteristics that are suitable for identification of grid-connected systems; it has a largely adjustable frequency spectrum for both bandwidth and resolution, and its binary nature results in an ideal crest factor. Additionally, binary sequences are easy to generate and inject using switched-mode devices, and the periodic sequences can be averaged over arbitrary number of periods.

The MLBS is deterministic and periodic over sequence length N , which can be chosen freely for $N = 2^n - 1$, where n is an integer. The sequence can be easily generated by a XOR-feedback shift register, which produces a binary signal between 0 and 1 repeating after N steps. In order to produce a symmetrical excitation that has average close to zero, the injection is usually mapped to vary between -1 and 1. The amplitude of the injection can be chosen freely, and it is a trade-off between measurement accuracy and system disturbance. The measurement time for P averaged periods is given as

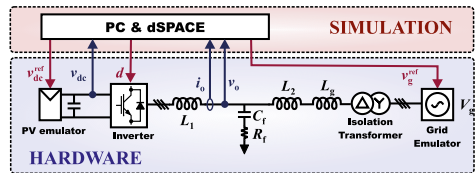


Fig. 5. Experimental PHIL setup schematic diagram.

$$T_{\text{meas}} = NP/f_{\text{gen}} \quad (2)$$

where f_{gen} is the generation frequency. In this work, a logarithmic averaging is applied (Pintelon and Schoukens (2001)), where the measured signal is averaged based on

$$X(j\omega) = \left(\prod_{k=1}^P x_k(j\omega) \right)^{(1/P)} \quad (3)$$

where $x_k(j\omega)$ is a signal in frequency domain. The logarithmic averaging reduces the uncorrelated noise in the measurements to the power of $x^{(1/P)}$.

3.2 Design of Injection Amplitude

The selection of the injection amplitude plays important role in the grid-impedance measurement, particularly in online applications where the impedance is measured in real time. The amplitude must be high enough in order to provide good signal-to-noise ratio (SNR) but low enough to avoid too high nonlinear distortions.

In this work, the value of total harmonic distortion (THD) is used as an indicator for iteratively selecting the appropriate injection amplitude. The THD is the most used indicator for power quality, and consequently, standards and regulations have been widely imposed on THD values of grid currents and voltages. As the excitation signal from the inverter inevitably distorts the currents and voltages in the grid, the THD can be applied as a feedback for the amplitude selection.

Fig. 4 presents the suggested amplitude selection algorithm as a flowchart, where the injection amplitude is tuned iteratively. The THD limits for currents and voltages can either be set by a standard, or by the user. The selection depends on the application and the base THD level, and the designer of a grid-connected system usually has good insight on the desired THD. The algorithm prioritizes amplitude selection over averaging, so the injection amplitude is increased to the THD limit first, and then if necessary, the number of averaged periods is increased. If a sufficient measurement accuracy is not met even with maximum allowable injection amplitude and measurement time, one of the requirements must be loosened until sufficient accuracy is met.

4. EXPERIMENTS

The experiments are performed with a power hardware-in-the-loop (PHIL) setup, where a kW-scale three-phase inverter (*Myway Plus MWINV-9R144*) is connected to a linear voltage amplifier (*Spitzenberger & Spies PAC 15000*) that emulates three-phase grid voltages. A real-time simulator (*dSPACE model 1103*) provides the voltage references for the voltage amplifier. In addition, the

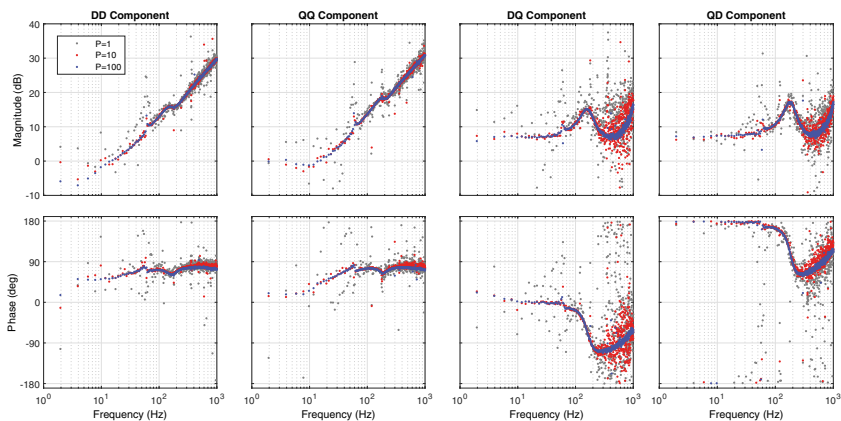


Fig. 6. Measured MIMO impedance with either 1, 10, or 100 averaged periods.



Fig. 7. Picture of the laboratory setup.

inverter control scheme is implemented on the dSPACE, which produces the driving gate signals for the IGBT switches in the inverter. A photovoltaic emulator (*Spitzberger & Spiess PVS 7000*) provides the DC input power for the inverter by emulating the voltage-current profile of a photovoltaic system. An external hardware inductor and isolation transformer are connected between the inverter and the voltage amplifier (grid emulator), which here act as the grid impedance. Fig. 5 presents a block diagram of the experimental setup, and a picture of the setup is shown in Fig. 7.

The experiments consist of grid-impedance measurements performed with the grid-connected inverter. The MLBS excitation signal is added to the current references of the inverter current controller, so the inverter produces a current-type injection to the system. The three-phase currents and voltages are measured from the output terminal of the inverter, and these measurements are applied in the grid-impedance measurements. These measurements are required also for the control system, so no additional sensors are required. The current and voltage quality are assessed from these measurements in both time domain (waveforms) and frequency domain (THD and power spectrum). The measurements are performed for three different grid impedances; in addition to the isolation transformer, the grid connection had either no additional inductance,

a 4 mH inductor, or a 9 mH inductor. The corresponding short-circuit ratios (SCR) are 22, 7.1, and 3.9, respectively. The grid with lowest impedance (highest SCR) represents a robust grid where stability issues are rare, and the highest impedance grid (lowest SCR) corresponds to a high-impedance system prone to stability issues. In order to obtain the full-order impedance in the dq-domain, two separate measurements are performed to different channels (d-injection yields dd- and dq-components, q-injection yields qq- and qd-components).

4.1 Impedance Measurements

In practice, a high-resolution broadband measurement requires averaging over multiple periods in order to increase the SNR to a sufficient level. In this work, the maximum number of averaged periods for each measurement is 100. Fig. 6 presents the measured impedances from the SCR = 22 grid, and shows the results with logarithmic averaging over different number of periods with excitation amplitude of 3 % of nominal current (approximately 300 mA). It is apparent that with low number of averaged periods, the measurements are noisy, and especially the crosscouplings (QD and DQ) are very scattered due to low magnitude. However, increasing the averaging to 10 periods already illustrates the shape of the impedance accurately. With 100 averaged periods, the measurements can be applied for example in impedance-based analysis without considerable loss of accuracy. In all measurements, the frequencies closest to the fundamental frequency (60 Hz) are corrupted by the fundamental currents and voltages.

Another approach to enhance the measurement accuracy is to increase the excitation amplitude, which results in higher SNR. However, in online measurements the excitation pollutes the grid currents and voltages increasing the system THD. Although the perturbation is injected as a current excitation, it depends on the grid impedance whether currents or voltages are more corrupted. In strong grids (low impedance), the grid voltages remain ideally uncorrupted as the current produces insignificant voltage response in low grid impedance. In weak grids (high

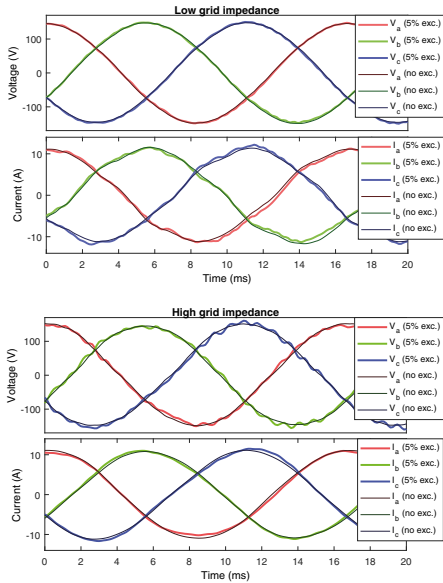


Fig. 8. Time-domain currents and voltages with no excitation and 5% excitation in strong grid (upper) and in weak grid (lower).

impedance), on the other hand, the current produces larger voltage response. However, as the grid impedance is typically inductive, it increases the filtering effect resulting in smoother current waveforms. Consequently, the perturbation corrupts the current THD in strong grids and the voltage THD in weak grids. Fig. 8 shows the measured three-phase time-domain currents and voltages in two cases; in strong grid connection (upper, SCR = 22) and in weak grid connection (lower, SCR = 3.9). In both experiments, the injection amplitude was 5 % of the nominal current. Table 1 presents the measured current and voltage THDs in grids with different impedances for five different injection amplitudes. Based on the table, the following conclusions can be given

- low grid impedance results in high current THD and low voltage THD
- high grid impedance results in low current THD and high voltage THD
- excitation amplitude below 1 % has no effect on current or voltage THD (in these systems)
- even 5 % excitation has a moderate effect on the THD (in these systems).

4.2 Measurement Variance

The quality of the measurements can be characterized by measurement variance to reference. In this case, no analytical reference is available, so the reference is constructed from the measurement with maximum averaging and excitation amplitude by fitting a transfer function to the obtained data. The variance is given by

Table 1. Measured THD values of currents and voltages.

	Injection amplitude					
	0.0 %	0.5 %	1.0 %	3.0 %	5.0 %	
0 mH	5.41 %	5.42 %	5.47 %	6.03 %	7.03 %	Current
4 mH	2.91 %	2.90 %	2.96 %	3.50 %	4.41 %	
9 mH	2.15 %	2.15 %	2.19 %	2.70 %	3.54 %	
0 mH	1.17 %	0.99 %	1.11 %	1.42 %	1.29 %	Voltage
4 mH	2.02 %	1.94 %	2.05 %	2.33 %	3.21 %	
9 mH	2.38 %	2.45 %	2.17 %	2.99 %	3.74 %	

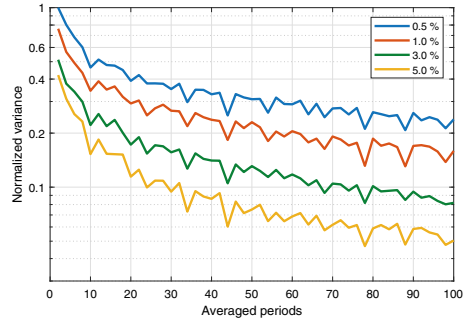


Fig. 9. Measurement variance as a function of number of averaged periods.

$$\sigma^2 = \sum_{f=1}^{f_{\max}} [Z_{\text{fit}}(f) - Z(f)]^2 \quad (4)$$

where $Z_{\text{fit}}(f)$ is the fitted impedance and $Z(f)$ is the measured impedance. The total variance of the measurement is the sum of component variances. To illustrate the impact of both amplitude and averaging, Fig. 9 shows the variance from reference as a function of number of averaged periods for different excitation amplitudes, measured from the strongest grid. The variance is normalized, where the variance is compared to measurement that has the highest variance. The figure shows a clear increase in measurement quality when the excitation amplitude is increased, and on the other hand, when the number of averaged periods increases. Based on the trends shown in the figure, it is apparent that lower injection amplitude can be compensated only partially by increasing the averaging. This supports the proposed algorithm, where the injection amplitude is increased to the THD limit first.

5. DISCUSSION

A proper amplitude design requires thorough consideration of the desired measurement accuracy, grid under measurement, and base level of the THD for grid voltages and currents. Sufficient measurement accuracy can be obtained with small excitation amplitude by allowing long measurement time for averaging over multiple periods. Yet, increase in excitation amplitude is shown to enhance the measurement accuracy, which can not be achieved by simply increasing the averaging and measurement time. Fig. 10 illustrates the inherent trade-offs between measurement quality (indicated by SNR) against grid THDs and

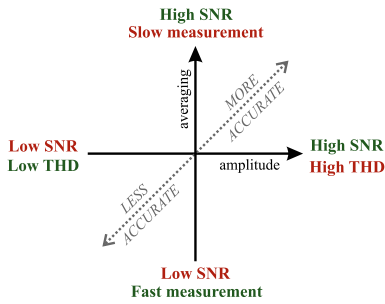


Fig. 10. Inherent trade-offs in measurement accuracy.

measurement duration. The optimal perturbation design depends on the application and grid conditions, and a generalized optimal design can not be derived. However, the proposed algorithm can be utilized as a procedure to find a design that optimizes the amplitude and averaging to a specific application.

6. CONCLUSION

Wideband identification methods based on broadband perturbation and Fourier techniques have become popular in stability analysis of grid-connected systems. This work has presented a method for tuning the perturbation amplitude and measurement duration with respect to the given limitations in grid-side THD levels. In impedance measurements of grid-connected systems, the perturbation signal pollutes the grid currents and voltages with harmonic content. Consequently, the perturbation amplitude should be designed carefully to provide sufficient signal-to-noise ratio and to minimize the disturbance to normal system operation. This work has illustrated the impact of perturbation amplitude on measurement accuracy and grid current and voltage total harmonic distortions in impedance measurements of grid-connected systems. Experimental results based on a three-phase grid-connected inverter operating under varying conditions were shown to demonstrate the proposed method.

REFERENCES

- Alenius, H., Berg, M., Luhtala, R., and Roinila, T. (2019a). Stability and Performance Analysis of Grid-Connected Inverter Based on Online Measurements of Current Controller Loop. In *Proc. Industrial Electronics Conference (in press)*, 7 pages.
- Alenius, H., Berg, M., Luhtala, R., Roinila, T., and Messo, T. (2019b). Impedance-Based Stability Analysis of Multi-Parallel Inverters Applying Total Source Admittance. In *Proc. 20th Workshop on Control and Modeling for Power Electronics (COMPEL)*, 8 pages.
- Alenius, H. and Roinila, T. (2020). Impedance-Based Stability Analysis of Paralleled Grid-Connected Rectifiers: Experimental Case Study in a Data Center. *Energies*, 13(2109). doi:10.3390/en13082109.
- Amin, M. and Molinas, M. (2017). Small-Signal Stability Assessment of Power Electronics based Power Systems: A Discussion of Impedance- and Eigenvalue-based Methods. *IEEE Transactions on Industry Applications*, 53(5), 5014–5030.
- Belkhat, M. (1997). *Stability criteria for AC power systems with regulated loads*. Doctoral thesis, Purdue University.
- Bose, B. (2013). Global Energy Scenario and Impact of Power Electronics in 21st Century. *IEEE Transactions on Industrial Electronics*, 60(7), 2638–2651.
- Cespedes, M. and Sun, J. (2013). Three-phase impedance measurement for system stability analysis. *Proc. IEEE 14th Workshop on Control and Modeling for Power Electronics (COMPEL)*, 6 pages.
- Godfrey, K. (1993). *Perturbation Signals for System Identification*. Prentice Hall, UK.
- Jessen, L., Gunter, S., Fuchs, F.W., Gottschalk, M., and Hinrichs, H.J. (2015). Measurement results and performance analysis of the grid impedance in different low voltage grids for a wide frequency band to support grid integration of renewables. In *Proc. IEEE Energy Conversion Congress and Exposition*, 1960–1967.
- Li, C. (2017). Unstable Operation of Photovoltaic Inverter from Field Experiences. *IEEE Transactions on Power Delivery*, 33, 1013–1015.
- Liu, H., Xie, X., He, J., Xu, T., and Yu, Z. (2017). Sub-synchronous Interaction Between Direct-Drive PMSG Based Wind Farms and Weak AC Networks. *IEEE Transactions on Power Systems*, 32(6), 4708–4720.
- Luhtala, R., Alenius, H., Messo, T., and Roinila, T. (2020). Online Frequency Response Measurements of Grid-Connected Systems in Presence of Grid Harmonics and Unbalance. *IEEE Transactions on Power Electronics*, 35(4), 3343–3347.
- Pintelon, R. and Schoukens, J. (2001). *System Identification - A Frequency Domain Approach*. John Wiley & Sons.
- Roinila, T., Messo, T., and Santi, E. (2018). MIMO-identification techniques for rapid impedance-based stability assessment of three-phase systems in DQ Domain. *IEEE Transactions on Power Electronics*, 33(5), 4015–4022.
- Rygg, A. and Molinas, M. (2017). Apparent impedance analysis: A small-signal method for stability analysis of power electronic-based systems. *IEEE Journal of Emerging and Selected Topics in Power Electronics*, 5(4), 1474–1486.
- Sun, J. (2011). Impedance-based stability criterion for grid-connected inverters. *IEEE Transactions on Power Electronics*, 26(11), 3075–3078.
- Suntio, T., Messo, T., Berg, M., Alenius, H., Reinikka, T., Luhtala, R., and Zenger, K. (2019). Impedance-Based Interactions in Grid-Tied Three-Phase Inverters in Renewable Energy Applications. *Energies*, 12(464).
- Wang, X., Harnefors, L., and Blaabjerg, F. (2018). Unified Impedance Model of Grid-Connected Voltage-Source Converters. *IEEE Transactions on Power Electronics*, 33(2), 1775–1787.
- Wang, Y., Wang, X., Blaabjerg, F., and Chen, Z. (2017a). Harmonic instability assessment using state-space modeling and participation analysis in inverter-fed power systems. *IEEE Transactions on Industrial Electronics*, 64(1), 806–816.
- Wang, Y., Wang, X., Blaabjerg, F., and Chen, Z. (2017b). Small-Signal Stability Analysis of Inverter-Fed Power Systems Using Component Connection Method. *IEEE Transactions on Smart Grid*, 9(5), 5301–5310.

PUBLICATION

V

**”Stability and Performance Analysis of Grid-Connected Inverter Based on Online
Measurements of Current Controller Loop”**

H. Alenius, M. Berg, R. Luhtala and T. Roinila

in Proc. *45th Annual Conference of the IEEE Industrial Electronics Society*, pp. 2013–2019, Lisbon,
Portugal, 2019

Publication reprinted with the permission of the copyright holders

Stability and Performance Analysis of Grid-Connected Inverter Based on Online Measurements of Current Controller Loop

1st Henrik Alenius

Faculty of Information Technology
and Communication Sciences
Tampere University
Tampere, Finland
henrik.alenius@tuni.fi

2nd Matias Berg

Faculty of Information Technology
and Communication Sciences
Tampere University
Tampere, Finland
matias.berg@tuni.fi

3rd Roni Luhtala

Faculty of Engineering
and Natural Sciences
Tampere University
Tampere, Finland
roni.luhtala@tuni.fi

4th Tomi Roinila

Faculty of Engineering
and Natural Sciences
Tampere University
Tampere, Finland
tomi.roinila@tuni.fi

Abstract—The amount of grid-connected three-phased inverters is increasing rapidly. In a weak grid, the non-ideal grid impedance decreases the control performance and can even compromise the system stability through load effect. The stability assessment of the inverter-grid interface has been assessed extensively through state-space and impedance-based methods. The current work presents stability analysis method based on the load-affected loop gain of the innermost control loop, which includes the effect of phase-locked loop and grid impedance. The stability analysis is carried out by assessing modeled and measured loop gains using the Nyquist criterion, step responses, and system closed-loop poles. The stability issues originating from grid impedance or too high phase-locked loop bandwidth are accurately predicted by examining the innermost control loop.

Index Terms—Grid-connected inverter, Stability analysis, Control system analysis, Online measurement

I. INTRODUCTION

THREE-PHASE grid-connected inverters have been widely adopted for power processing in modern power systems. The share of grid-connected inverters has increased rapidly over the past decade, mainly driven by tightened requirements for more precise power processing and the rise of renewable energy production [1], [2]. As the inverters have fast and complex control dynamics and often exhibit non-passive impedance characteristics, stability issues have become an important design factor in power-electronic-based systems [3]–[5]. Power quality and stability issues emerging from the unintentional interactions between the inverters and the grid have been studied extensively [6]–[8].

The grid impedance affects the operation of grid-connected devices, and may deteriorate the control performance and robustness. The most commonly used approaches for stability assessment are the impedance-based methods [3], [9], [10] as well as the conventional control-theory methods such as state-space analysis [11]–[13]. However, the dq-domain impedance measurements are often inaccurate or impractical [3], [14] and the state-space analysis requires significant modeling effort [15].

The transfer functions of the inverter control loops are used to describe the dynamic behavior. The load effect imposed by the grid impedance can be included in the transfer functions through small-signal modeling [3]. The most practical control loop for a stability assessment of the internal stability of an inverter is the innermost control loop with highest control bandwidth, which is typically the AC-current-control loop in grid-feeding inverters. The effect of other control loops on the current-control loop will take place through the load effect, which consists of the ratio of inverter and grid impedances.

This paper presents a small-signal model of a load-affected AC-current-control loop, which includes the grid impedance and the impact of synchronous reference-frame phase-locked loop (SRF-PLL). In addition, the loop gain is shown to predict accurately the control performance of the inverter and the stability margins related to the small-signal interactions. The model is validated with simulation measurements, and the performance and robustness indications are verified with simulations and experiments on kW-scale three-phase inverter.

The remainder of this paper is organized as follows. Section II presents the small-signal modeling of the load-affected current-controller loop gain. Section III shows the simulation validation of the modeled current controller loop and the effect of grid impedance and PLL bandwidth on the stability margins. In Section IV, experiments with power hardware-in-the-loop setup show online measurements of the current loop, based upon which the stability margin is indicated accurately. Section V draws the conclusion.

II. DYNAMIC MODELING OF CF-CO INVERTER

In renewable energy systems, the inverter is typically in grid-feeding mode, where a phase-locked loop is used to synchronize the inverter to grid voltages. In photovoltaic (PV) applications, the DC voltage must be controlled in order to achieve maximum-power-point operation of the PV panels. A single-stage PV inverter, which also controls the DC-link voltage, has been widely adopted as it removes the need for an additional DC-DC converter. The single-stage

$$\begin{bmatrix} \hat{v}_{in} \\ \hat{i}_o \end{bmatrix} = \begin{bmatrix} \mathbf{Z}_{in} + \mathbf{T}_{oi}[\mathbf{I} + \mathbf{Y}_o\mathbf{Z}_L]^{-1}\mathbf{Z}_L\mathbf{G}_{io} & \mathbf{T}_{oi}[\mathbf{I} + \mathbf{Y}_o\mathbf{Z}_L]^{-1} & \mathbf{Z}_{ci} + \mathbf{T}_{oi}[\mathbf{I} + \mathbf{Y}_o\mathbf{Z}_L]^{-1}\mathbf{Z}_L\mathbf{G}_{co} \\ [\mathbf{I} + \mathbf{Y}_o\mathbf{Z}_L]^{-1}\mathbf{G}_{io} & -[\mathbf{I} + \mathbf{Y}_o\mathbf{Z}_L]^{-1}\mathbf{Y}_o & [\mathbf{I} + \mathbf{Y}_o\mathbf{Z}_L]^{-1}\mathbf{G}_{co} \end{bmatrix} \begin{bmatrix} \hat{i}_{in} \\ \hat{v}_o \\ \hat{\mathbf{d}} \end{bmatrix} \quad (1)$$

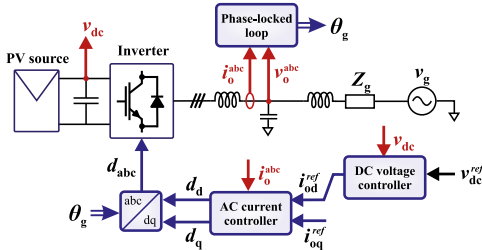


Fig. 1: Schematic of cascaded control system in CF-CO inverter.

inverter typically operates in cascaded control scheme, which consists of outer DC voltage control loop, inner output current control loop, and phase-locked loop for grid synchronization. An inverter with this configuration is known as current-fed current-output (CF-CO) inverter. Fig. 1 presents the simplified block diagram of the control system.

A. Open-loop dynamics on dq-domain

A common approach for control theory and stability assessment is small-signal analysis, where the system response to a small-signal variation around steady-state operation point is considered. Nonlinear systems can be approximated with linear equations by linearizing the system around a steady-state operation point. The small-signal approach is feasible when the superimposed AC signal has significantly lower amplitude than the steady-state DC signal.

In three-phase AC systems, the signals become matrices, instead of scalars found in DC systems. In addition, no small-signal equilibrium point exists as the variables fluctuate with the fundamental frequency. The inherent complexity of three-phase AC systems has led to introduction of advanced modeling techniques, in order to reduce the complexity of modeling and control design. The complexity can be decreased by, for example, approaches based on sequence domain or synchronous reference frame (dq domain). In the dq-domain analysis, the three phases are described as direct, quadrature, and zero components in rotating reference frame. As the frame rotates with fundamental frequency, the fundamental AC component is removed from the signals. Additionally, the system is usually assumed to be balanced, so the zero component can be neglected. The system is reduced to two DC signals, which allows straightforward Jacobian linearization.

The modeling of CF-CO inverter in the dq domain has been widely presented in previous work [3], [16]. The linearized multi-input multi-output (MIMO) open-loop transfer matrices can be given in the dq domain as

$$\begin{bmatrix} \hat{v}_{in} \\ \hat{i}_o \end{bmatrix} = \begin{bmatrix} \mathbf{Z}_{in} & \mathbf{T}_{oi} & \mathbf{G}_{ci} \\ \mathbf{G}_{io} & -\mathbf{Y}_o & \mathbf{G}_{co} \end{bmatrix} \begin{bmatrix} \hat{i}_{in} \\ \hat{v}_o \\ \hat{\mathbf{d}} \end{bmatrix} \quad (2)$$

B. Load effect of grid impedance

A non-ideal grid-connection of the inverter has grid impedance, which results in load effect and alters the transfer functions shown in (2). Fig. 2 presents the origin of load effect as a two-port model. The inclusion of load impedance \mathbf{Z}_L changes the dynamics, as the original ideal-load output voltage is replaced by

$$\hat{v}_o = \hat{v}_o^L + \mathbf{Z}_L \hat{i}_o \quad (3)$$

where superscript L denotes the load-affected variable. Substituting lower row of (2) to (3) yields

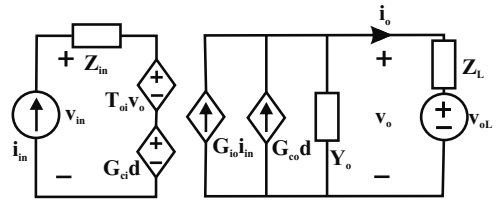


Fig. 2: Load-affected multivariable equivalent circuit of CF-CO inverter.

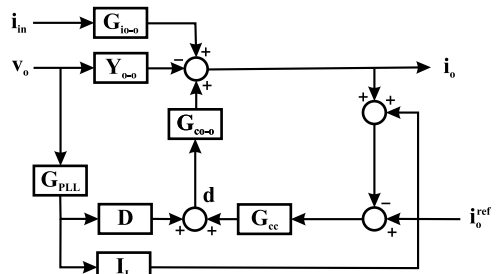


Fig. 3: Small-signal block diagram of output dynamics with current control and PLL.

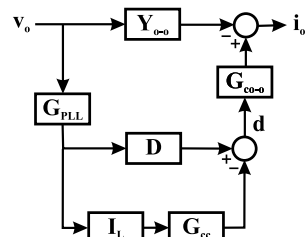


Fig. 4: Small-signal block diagram of PLL-affected output impedance.

$$\begin{aligned} \hat{\mathbf{v}}_o = & [\mathbf{I} + \mathbf{Y}_o \mathbf{Z}_L]^{-1} \hat{\mathbf{v}}_o^L \\ & + [\mathbf{I} + \mathbf{Y}_o \mathbf{Z}_L]^{-1} \mathbf{Z}_L \mathbf{G}_{io} \hat{\mathbf{i}}_{in} \\ & + [\mathbf{I} + \mathbf{Y}_o \mathbf{Z}_L]^{-1} \mathbf{Z}_L \mathbf{G}_{co} \hat{\mathbf{d}} \end{aligned} \quad (4)$$

Substituting (3)-(4) into (4) yields the load-affected multi-variable transfer functions shown in (1). In order to accurately model the load effect, the impact of grid-synchronization by PLL should be considered, as it affects the output admittance of the inverter. Fig. 3 presents the small-signal block diagram for the inverter output dynamics, where the PLL and current controller are included. The PLL adds a parallel signal paths from \mathbf{v}_o to $\hat{\mathbf{i}}_o$, which affects the total output admittance. Fig. 4 shows the PLL-affected output impedance derived from Fig. 3. The small-signal modeling of the PLL has been considered in [16]. The PLL-affected total output admittance is given by

$$\mathbf{Y}_{o-c} = \mathbf{Y}_o + \mathbf{Y}_{pll} \quad (5)$$

where \mathbf{Y}_{pll} is the PLL-induced admittance component, which can be given as

$$\mathbf{Y}_{pll} = \mathbf{G}_{co} \mathbf{G}_{cc} \mathbf{I}_L \mathbf{G}_{pll} - \mathbf{G}_{co} \mathbf{D} \mathbf{G}_{pll} \quad (6)$$

where

$$\mathbf{D} = \begin{bmatrix} 0 & -D_q \\ 0 & D_d \end{bmatrix} \quad \mathbf{G}_{pll} = \begin{bmatrix} 0 & 0 \\ 0 & \frac{L_{pll}}{V_{od}(1+L_{pll})} \end{bmatrix} \quad (7)$$

$$\mathbf{I}_L = \begin{bmatrix} 0 & I_{Lq} \\ 0 & -I_{Ld} \end{bmatrix} \quad \mathbf{G}_{cc} = \begin{bmatrix} G_{pld} & 0 \\ 0 & G_{plq} \end{bmatrix} \quad (8)$$

$$L_{pll} = (K_{p-pll} + K_{I-pll}/s) * V_{od}/s. \quad (9)$$

Finally, the load affected control-to-output transfer function, which is the plant for the current controller, is given by

$$\mathbf{G}_{co}^L = [\mathbf{I} + \mathbf{Y}_{o-c} \mathbf{Z}_L]^{-1} \mathbf{G}_{co} \quad (10)$$

In this analysis, the outer DC voltage controller is omitted, as the impact can be considered negligible due to significantly lower bandwidth.

C. Full-order current control loop

A typical controller choice for the AC current controller is the PI-type compensator, which is usually identical for both channels. The cross-couplings are often assumed to be small and neglected, which results in simplified analysis as the d- and q-channels can be separated. The reduced-order current controller loop gain is

$$L_{cc-d}^{RO} = G_{codd}^L G_{PWM} G_{PI-d} H_d \quad (11)$$

where G_{codd-o} is the open-loop control to output of d-channel, G_{PWM} is the pulse-width modulator, G_{PI-d} is the current controller, and H_d is the sensing gain. However, ignoring the cross-couplings may lead to inaccurate models. Fig. 5 shows the full-order control block diagram of the current control loop gain, which includes the cross-couplings. The dashed red lines indicate the interface where the loop is calculated or measured. Based on the block diagram, the full-order control loop can derived

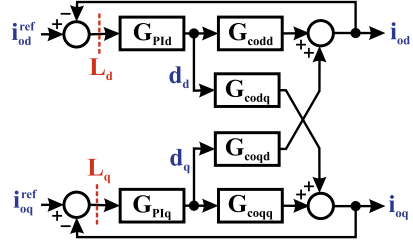


Fig. 5: Control block diagram of the current control loops.

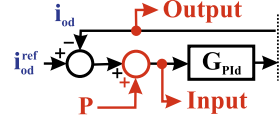


Fig. 6: Excitation injection diagram for d-channel loop measurement.

$$L_{cc-d}^{FO} = G_{codd}^L G_{PI-d} - \frac{G_{codd}^L G_{cocoqd}^L G_{PIq} G_{PI-d}}{1 + G_{PIq} G_{cocoqd}^L} \quad (12)$$

where G_{PWM} and H_d are incorporated into G_{PI-d} and G_{PIq} . The system control characteristics can be predicted based on the closed-loop transfer function from input to output, where the control feedback loops are closed. The closed-loop transfer function from d-current reference to output d-current of the current controller can be given as

$$G_{c-cod} = \frac{L_{cc-d}^{FO}}{1 + L_{cc-d}^{FO}} \quad (13)$$

and similarly for G_{c-coq} of the q-channel.

III. SIMULATIONS

The simulations are performed in MATLAB/Simulink environment with a three-phase grid-connected CF-CO inverter shown in Fig. 1. The nominal output voltage is 120 V and the output power is 2.7 kW, which match the parameters used in the experimental setup. The output current measurements are taken from the middle of the LCL-filter so that the CL-part appears in grid impedance. Table I in Appendix presents the controller parameters used in the simulation experiments.

A. Loop-gain measurements

Frequency-response measurements have been widely used for model verification and assessment of system behavior. In general, the measurements are performed by injecting an excitation signal to the system and measuring the response [17]. In this work, a broadband ternary pseudo-random excitation was used to measure the current controller loop gains in varying operation conditions. The system was perturbed by a ternary sequence with length of $N = 1999$ generated at $f_{gen} = 4$ kHz. Thus, the frequency resolution and the lowest obtainable frequency are 2 Hz [17]. The feasible highest frequency of the measurement is approximately 2 kHz, due

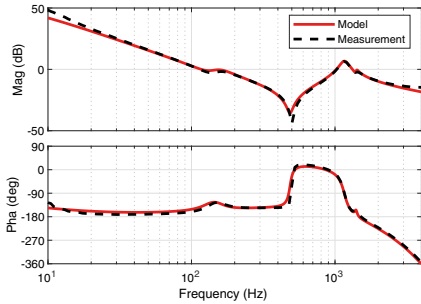


Fig. 7: Modeled and measured load-affected loop gain transfer function from the q-channel of current controller.

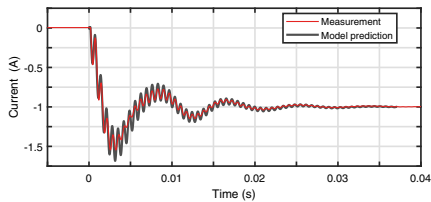


Fig. 8: Modeled (grey) and measured (red) q-channel current response to a step change in current reference (from 0 to -1 A at 0 s).

to decreasing power of the excitation. Fig. 6 schematically presents the measurement implementation, supplementing the full-order block diagram of the control loops shown in Fig. 5. The ternary sequence is injected to the current controller loop, and the input and output signals are measured and Fourier-transformed, which yields the current-control-loop transfer function. The presented load-affected current-controller loop gain model was verified with measurements from the simulation. Fig. 7 presents the measured and modeled loop gain transfer function of the current controller q-channel for a grid inductance of 10 mH.

The control performance can be predicted from the closed loop transfer function derived in (13). To further verify the presented modeling method and predictions of the system behavior, a step-change to q-channel current reference was performed in simulation and the current response was measured. Fig. 8 presents the current response predicted from the modeled transfer function (grey) and the simulated current response (red) for the system with 10 mH grid inductance. The modeled transfer function predicts the system response to the transient with high accuracy, as the overshoot, oscillation frequency, and settling time are accurately captured.

B. Load-affected control performance

The sensitivity of the current controller loop gain to the varying grid impedance is illustrated by measuring the load-affected current loop with different grid inductance values. Fig. 9 presents the measured q-channel loop gain with the grid inductance ranging from 0 to 20 mH, which corresponds to a

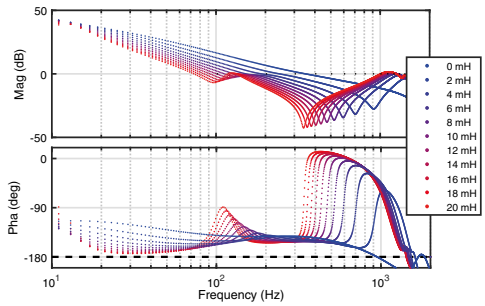


Fig. 9: Measured load-affected loop gain from q-channel with varying grid impedance.

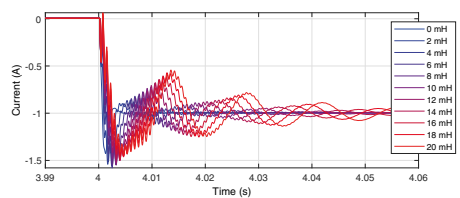


Fig. 10: Current q-component response to step change with varying grid inductance values.

short-circuit ratio (SCR) decrease from 40 to 2. The increase in grid inductance magnifies the load effect, which results in decreased magnitude and phase margin. This decreases the control bandwidth, thus reducing the stability margins and control performance. Fig. 10 presents a set of step responses showing the output current q-component when the reference value is stepped from 0 to -1 A. Increasing the grid inductance deteriorates the control performance, validating the hypothesis. Thus, modeled load-affected control loop can be used to assess the performance and stability of an inverter in a weak grid.

C. PLL impact on current loop robustness

A high control bandwidth of PLL is known to cause stability issues in weak grids, due to the negative-resistance-like behavior of the inverter output admittance q-component [13], [18]. Previous research has mostly assessed the stability impact of the PLL based on the impedance-based stability criterion [18], [19]. The PLL affects the output admittance of the inverter, which is included in the load-affected control-to-output transfer function in (10). The proposed current-control-loop model incorporates the load effect and, consequently, the effect of the PLL.

Fig. 11 shows the q component of the PLL-affected current-control loop when the PLL-controller settings are varied. The phase margin reduces significantly when the PLL-control bandwidth is increased. The Nyquist criterion can be applied for the stability assessment of the control loop. Fig. 12 provides an overview of the Nyquist contour. Based on the modeled loop, the open-loop transfer function has a RHP pole,

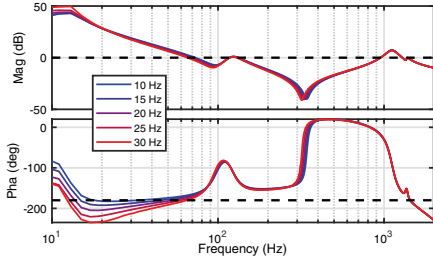


Fig. 11: Measured q-channel current control loop gain with different PLL control bandwidths.

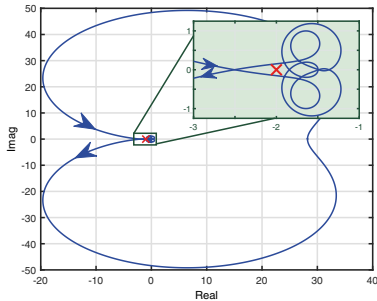


Fig. 12: Nyquist contour of the q-channel current controller open-loop gain (zoomed figure on green background).

so the locus must encircle the critical point once counter-clockwise in order for the closed-loop system to be stable. Increasing the PLL bandwidth shifts the crossing point on the real axis towards the critical point, as shown in Fig. 13. With control bandwidths above 31 Hz, the open-loop locus no longer encircles the critical point, indicating that the closed-loop system would be unstable.

The prediction is verified by simulations. The PLL-induced stability issues were tested by changing the PLL bandwidth by adjusting the PI-controller gains during simulation. Three cases were considered: the PLL bandwidth was changed from 20 Hz to 27, 31, or 35 Hz. Nyquist criterion (see Fig. 13) predicts that the systems will be stable, marginally stable, and unstable, respectively. Fig. 14 presents the time-domain waveforms of the output current d-component for the three

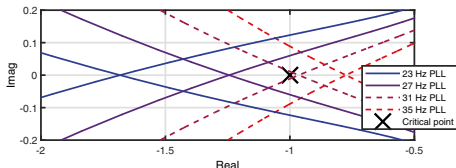


Fig. 13: Nyquist loci of the current controller loop for varying PLL bandwidths, where the unstable closed-loops are shown with dashed line.

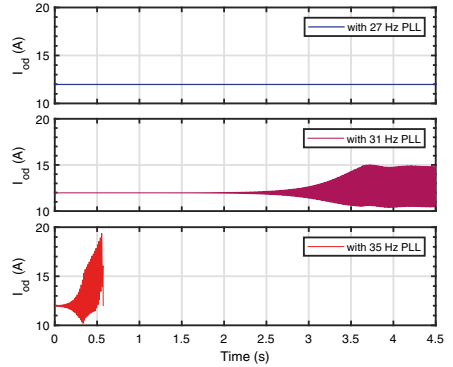


Fig. 14: Output current d-component when the PLL bandwidth is changed from 20 Hz to 27 Hz (blue), 31 Hz (purple), or 35 Hz (red) at $t = 0$ s.

experiments. The response is dominated by the pole pair, which causes oscillation at the main oscillatory frequency around 70 Hz. When the PLL bandwidth is changed to 27 Hz, the stability margins are sufficient and no visible transient occurs. When the bandwidth is changed to 31 Hz, the system initially appears stable. However, after a few seconds the oscillation has increased to the state of sustained resonance, which indicates marginal stability. In the third scenario, the PLL controller is changed to bandwidth of 35 Hz, which instantly results in unstable oscillation and the system shuts down at $t = 0.6$ s. Consequently, the Nyquist contours in Fig. 13 predicted the system stability with high accuracy.

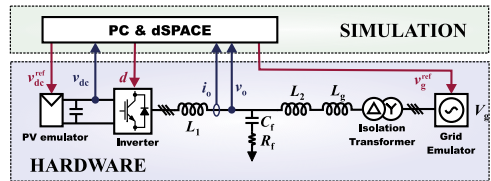


Fig. 15: Experimental power hardware-in-the-loop setup.

IV. EXPERIMENTS

The experimental power hardware-in-the-loop setup consists of a PV emulator (*Spitzenberger Spies PVS 7000*), a 10 kW three-phase inverter (*Myway Plus MWINV-9R144*), and a voltage amplifier (*Spitzenberger Spies PAC 15000*). An isolation transformer connects the inverter to the grid voltages, and inductors (12 mH) are connected before the voltage amplifier to emulate the grid impedance (see Fig. 1). The inverter control system is implemented to a dSPACE real-time simulation. Fig. 15 provides an overview of the experimental setup. The parameters are shown in Table I in Appendix.

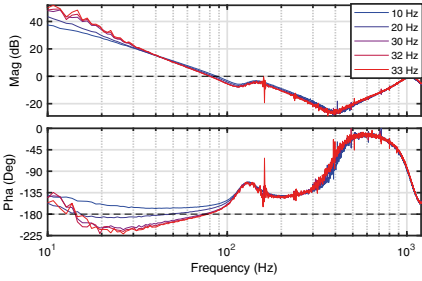


Fig. 16: Measured experimental current controller q-channel loops with different PLL bandwidths.

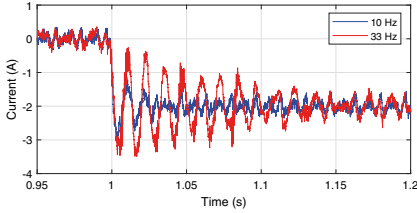


Fig. 17: Current step responses with different PLL controller tunings.

A. Stability and performance analysis

Fig. 16 shows the measured current-controller loop q components with PLL control bandwidths of 10, 20, 30, 32, and 33 Hz. As predicted from models and simulation, the phase decreases significantly when the PLL bandwidth increases. With 33 Hz control tuning, the measured loop indicates a phase margin of only 1.0 degrees, and the high sensitivity produces noise to the loop measurements. Fig. 17 shows the q-current step tests with PLL tunings of 10 and 33 Hz, where the highly oscillatory response validates the very low phase margin. Fig. 18 shows the Nyquist loci calculated from the measured loop gains, which clearly indicate that increasing bandwidth shifts the contour closer to the critical point. Based on 32 and 33 Hz contours, tuning the PLL to 34 Hz bandwidth would result in marginal stability. Fig. 19 shows the phase A output current waveforms in steady state for PLL tunings with 33 Hz and 34 Hz. As predicted from the current-controller loop measurements and the Nyquist analysis, the 34 Hz PLL results in marginal stability with highly distorted waveforms. Despite the very low stability margins for 33 Hz PLL, the steady-state current waveform shows no signs of stability issues. However, the low margins manifest in system transients, such as the step responses shown previously.

B. Discussion

The impedance-based stability criterion has been widely applied for stability analysis of grid-connected inverters. However, measuring the grid and inverter impedances is not always possible, as special hardware may be required. This work

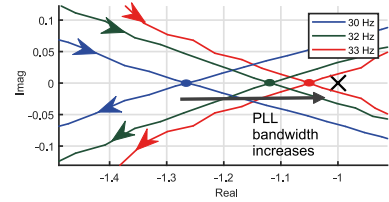


Fig. 18: Nyquist loci of measured current-controller loops with different PLL bandwidths.

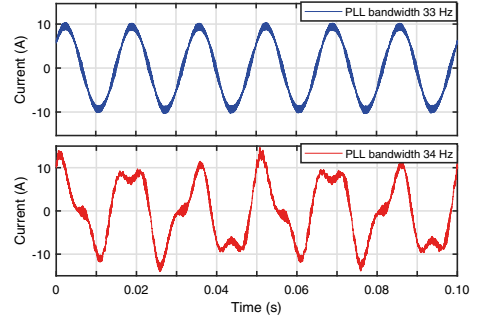


Fig. 19: Steady-state phase A currents with PLL tunings of 33 and 34 Hz.

presents a method to access the stability margins directly from the online measurements of the AC current controller loop. The implementation of the method is straightforward and can be directly included in the current controllers of inverters. In addition, the use of wideband-identification techniques makes it possible to perform the required frequency-response measurements, typically within few seconds. Thus, the proposed method can be used for real-time stability assessment or adaptive control of inverters.

V. CONCLUSION

The grid impedance affects the grid-connected inverters through the load effect, which may deteriorate system performance and robustness. This paper proposes a method for assessing the stability of a grid-connected inverter based on the current controller loop gain. The loop gain can be modeled accurately to include the effect of the grid impedance and the PLL, which are known to compromise the stability in weak grids. Another approach is to measure the current controller loop gain online in normal operation conditions. The inverter robustness can be assessed by calculating the Nyquist contour or directly from the indicated phase margin. The presented methods were verified by simulations and power hardware-in-the-loop experiments.

APPENDIX

TABLE I: Parameters for inverter and grid in simulations and experiments.

Parameter	Symbol	Value
Grid frequency	f_n	60 Hz
Nominal power	P_n	2.7 kVA
Nominal phase voltage	V_n	120 V
Switching frequency	f_{sw}	8 kHz
DC voltage reference	V_{dc}^*	414 V
D-current reference	i_d^*	10.6 A
Q-current reference	i_q^*	0 A
DC capacitance	C_{dc}	1.5 mF
Inverter-side inductance	L_1	2.2 mH
Inverter-side resistance	R_{L1}	100 m Ω
Filter capacitance	C_f	10 μ F
Filter capacitor resistance	R_{Cf}	1.8 Ω
Grid-side inductance	L_2	0.9 mH
Grid-side resistance	R_{L2}	400 m Ω
Grid inductance	L_g	0...20 mH
AC current control P gain	K_{P-CC}	0.0149
AC current control I gain	K_{I-CC}	23.442
DC voltage control P gain	K_{P-VC}	0.0962
DC voltage control I gain	K_{I-VC}	1.2092
PLL control P gain	K_{P-PLL}	0.39...1.36
PLL control I gain	K_{I-PLL}	9.77...119.7

REFERENCES

- [1] B. Bose, "Global Energy Scenario and Impact of Power Electronics in 21st. Century," *IEEE Transactions on Industrial Electronics*, vol. 60, no. 7, pp. 2638–2651, 2013.
- [2] F. Blaabjerg, Y. Yang, D. Yang, and X. Wang, "Distributed Power-Generation Systems and Protection," *Proceedings of the IEEE*, vol. 105, no. 7, pp. 1311–1331, 2017.
- [3] T. Suntio, T. Messo, M. Berg, H. Alenius, T. Reinikka, R. Luhtala, and K. Zenger, "Impedance-Based Interactions in Grid-Tied Three-Phase Inverters in Renewable Energy Applications," *Energies*, vol. 12, no. 464, 2019.
- [4] T. Suntio, T. Messo, and J. Puukko, *Power Electronics Converters - Dynamics and Control in Conventional and Renewable Energy Applications*. Wiley-VCH, 2017.
- [5] X. Wang, L. Harnefors, and F. Blaabjerg, "Unified Impedance Model of Grid-Connected Voltage-Source Converters," *IEEE Transactions on Power Electronics*, vol. 33, no. 2, pp. 1775–1787, 2018.
- [6] C. Li, "Unstable Operation of Photovoltaic Inverter from Field Experiences," *IEEE Transactions on Power Delivery*, vol. 8977, no. c, pp. 1–1, 2017.
- [7] C. Buchhagen, C. Rauscher, A. Menze, and J. Jung, "BorWin1 - First Experiences with harmonic interactions in converter dominated grids," *International ETG Congress 2015: Die Energiewende - Blueprints for the new energy age*, pp. 27–33, 2015.
- [8] C. Zou, H. Rao, S. Xu, Y. Li, W. Li, J. Chen, X. Zhao, Y. Yang, and B. Lei, "Analysis of Resonance between a VSC-HVDC Converter and the AC Grid," *IEEE Transactions on Power Electronics*, vol. 33, no. 12, pp. 10157–10168, 2018.
- [9] J. Sun, "Impedance-based stability criterion for grid-connected inverters," *IEEE Transactions on Power Electronics*, vol. 26, no. 11, pp. 3075–3078, 2011.
- [10] A. Rygg, M. Molinas, C. Zhang, and X. Cai, "On the equivalence and impact on stability of impedance modelling of power electronic converters in different domains," *IEEE Journal of Emerging and Selected Topics in Power Electronics*, vol. 5, no. 4, pp. 1–1, 2017.
- [11] M. Amin, A. Rygg, and M. Molinas, "Impedance-based and eigenvalue based stability assessment compared in VSC-HVDC system," *ECCE 2016 - IEEE Energy Conversion Congress and Exposition, Proceedings*, 2016.
- [12] Y. Wang, X. Wang, F. Blaabjerg, and Z. Chen, "Harmonic instability assessment using state-space modeling and participation analysis in inverter-fed power systems," *IEEE Transactions on Industrial Electronics*, vol. 64, no. 1, pp. 806–816, 2017.
- [13] J. Z. Zhou, H. Ding, S. Fan, Y. Zhang, and A. M. Gole, "Impact of short circuit ratio and phase locked loop parameters on the small signal behavior of a VSC HVDC converter," *IEEE Transactions on Power Delivery*, vol. 29, no. 5, pp. 2287–2296, 2014.
- [14] H. Gong, D. Yang, and X. Wang, "Impact of Synchronization Phase Dynamics on DQ Impedance Measurement," *2018 IEEE 19th Workshop on Control and Modeling for Power Electronics (COMPEL)*, no. 1, pp. 1–7, 2018.
- [15] J. Sun, "Small-signal methods for AC distributed power systems-A review," *IEEE Transactions on Power Electronics*, vol. 24, no. 11, pp. 2545–2554, 2009.
- [16] T. Messo, R. Luhtala, A. Aapro, and T. Roinila, "Accurate Impedance Model of Grid-Connected Inverter for Small-Signal Stability Assessment in High-Impedance Grids," in *2018 International Power Electronics Conference (IPEC-Niigata 2018 - ECCE Asia)*, no. 1. IEEE Industry Application Society, 2018, pp. 3156–3163.
- [17] K. Godfrey, *Perturbation Signals for System Identification*. Prentice Hall, UK, 1993.
- [18] T. Messo, J. Jokipii, A. Mäkinen, and T. Suntio, "Modeling the grid synchronization induced negative-resistor-like behavior in the output impedance of a three-phase photovoltaic inverter," *2013 4th IEEE International Symposium on Power Electronics for Distributed Generation Systems, PEDG 2013 - Conference Proceedings*, pp. 1–7, 2013.
- [19] D. Dong, B. Wen, D. Boroyevich, P. Mattavelli, and Y. Xue, "Analysis of phase-locked loop low-frequency stability in three-phase grid-connected power converters considering impedance interactions," *IEEE Transactions on Industrial Electronics*, vol. 62, no. 1, pp. 310–321, 2015.

PUBLICATION

VI

”Analysing the Damping of Grid-Connected Inverter by Applying Impedance-Based Sensitivity Function”

H. Alenius and T. Roinila

in Proc. *46th Annual Conference of the IEEE Industrial Electronics Society*, pp. 1249–1254, Singapore, 2020pp. 1249–1254, Singapore, 2020

Publication reprinted with the permission of the copyright holders

Analysing the Damping of Grid-Connected Inverter by Applying Impedance-Based Sensitivity Function

1st Henrik Alenius

*Faculty of Information Technology
and Communication Sciences*

Tampere University, Tampere, Finland

henrik.alenius@tuni.fi

2nd Tomi Roinila

*Faculty of Information Technology
and Communication Sciences*

Tampere University, Tampere, Finland

tomi.roinila@tuni.fi

Abstract—Stability issues have emerged in the grid interfaces of power electronics when the grid impedance is high or multiple devices are connected in parallel. Impedance-based stability criterion has demonstrated high applicability in the stability assessment, as the analysis can be performed based on the terminal impedances of the grid and the converter. Typically, impedance measurements are required to obtain the terminal impedances. However, extracting the stability margins and predicting the system dynamics from the measured impedances typically requires complex methods, such as transfer function fitting. This work proposes an extension to the impedance-based stability criterion, where the critical system damping and the critical resonant mode are extracted from the impedance data. An impedance-based sensitivity function is constructed from the terminal impedances, and the system damping factor is calculated from the sensitivity function. A second-order transfer function is constructed from the obtained damping factor and resonant frequency, which captures the critical resonant mode of the system. The method is validated in experimental stability analysis of a 2.7 kW grid-connected three-phase inverter, where the method accurately predicts the resonant dynamics of the system when the stability margins are low.

Index Terms—Stability analysis, Sensitivity function, Impedance-based stability criterion, Impedance measurements.

I. INTRODUCTION

The rapid increase in the amount of grid-connected power electronics has disrupted the dynamics of modern power systems and exposed challenges in the control and stability of the system. The interactions of power-electronic devices in the grid interface have been shown to expose the system to instability [1]–[5]. To predict the stability issues, impedance-based stability analysis has been proposed. In the method, the interface stability is assessed through impedances of both subsystems [6].

This work extends the conventional impedance-based stability criterion by proposing a straightforward method for predicting the critical system dynamics and resonant modes from the impedance measurements. In the method, the system damping factor and critical frequency are obtained from the impedance-based sensitivity function. Then, a second-order transfer function estimate is constructed from the damping factor and frequency, which accurately captures the critical resonant mode of the system. As a result, the system stability margins and transient dynamics can be predicted.

The performance of the proposed method is verified through stability analysis of a grid-connected three-phase inverter. The q-components of the inverter output admittance and the grid impedance are measured, and the presented method is applied. The obtained estimate is shown to accurately predict the system robustness and stability margins.

Performing the impedance-based analysis requires the terminal impedances of the subsystems. However, the detailed structure of a power system is often unknown due to very high number of electronic devices and high system complexity. Additionally, the precise internal dynamics of commercial devices are often protected by the manufacturer. Consequently, measurements have been widely applied to obtain the terminal impedances of systems [2]–[5], [7], [8].

Recently, broadband excitation sequences have been applied in the impedance measurements, as they exhibit multiple desirable characteristics, such as fast measurement duration, controllable frequency bandwidth and resolution, low crest factor, and they are easy to generate [8]–[13]. One of the most widely applied broadband sequence is the maximum-length binary sequence (MLBS). However, the MLBS suffers from very limited number of available signal lengths, which are available for $N = 2^n - 1$, where n is a positive integer. Therefore, the signal length is approximately doubled each time when a signal of higher length is required. This may cause issues in practical implementations which are often characterized by tight constraints in computing power.

As a second contribution, this work applies a quadratic-residue binary sequence (QRBS), originally introduced in [14], in the impedance measurements of a power electric system. The QRBS has similar favorable characteristics than the MLBS, but the sequence length has drastically more options as the sequence is available for lengths $N = 4k - 1$, where k is a positive integer and N is a prime.

The remainder of the work is organized as follows. Section II reviews the theoretical background of the impedance-based stability analysis. Section III discusses the impedance measurements and presents the quadratic-residue binary sequence (QRBS). In Section IV, the proposed method for estimating the critical system dynamics is presented. Section V shows the experimental measurements and validation of the presented method. Finally, Section VI concludes the work.

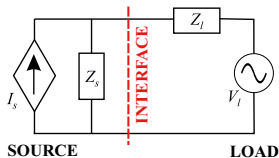


Fig. 1. Source-load equivalent of interconnected subsystems

II. IMPEDANCE-BASED STABILITY ANALYSIS

Fig. 1 shows the equivalent circuit for the system, where a grid-connected inverter is modeled as a Norton equivalent and the grid as a Thevenin equivalent. The stability of the interconnected subsystems can be assessed directly from the impedance-based characteristic equation

$$C(s) = \frac{1}{1 + Y_o(s)Z_g(s)} = \frac{1}{1 + Z_g(s)/Z_o(s)} \quad (1)$$

where $Y_o(s) = 1/Z_o(s)$ is the output admittance of the power-electronic device $Z_g(s)$ is the grid impedance [6]. The stability analysis can be performed by applying Nyquist criterion to the impedance ratio $Z_g(s)/Z_o(s)$.

A. DQ-Domain Impedance

Power-electric devices are often controlled in the dq-domain, where the three AC signals of a three-phase system can be reduced to two DC valued signals through Park's transformation [15]. Consequently, the impedance measurements are often performed in the same dq-frame to allow straightforward analysis. The direct components (d and q) are coupled through crosscouplings (dq and qd) and the system impedance (admittance) is defined as

$$\begin{bmatrix} V_d(s) \\ V_q(s) \end{bmatrix} = \begin{bmatrix} Z_{dd}(s) & Z_{qd}(s) \\ Z_{dq}(s) & Z_{qq}(s) \end{bmatrix} \begin{bmatrix} I_d(s) \\ I_q(s) \end{bmatrix} \quad (2)$$

where V is the voltage, Z is the impedance, I is the current, and the subscripts indicate the component in the dq-domain.

In the dq-domain analysis, accurate stability assessment requires the use of multivariable models, where both the d- and q-components, as well as crosscouplings, are taken into account. Thus, the impedances become 2x2-matrices and the stability analysis must be performed by applying the generalized Nyquist criterion (GNC), where two eigenvalue contours are drawn in the complex plane [16], [17]. However, in grid-feeding inverters the origin of the stability issues is often the phase-locked loop which affects the qq-component of the impedance [18]. Therefore, without significant loss of accuracy, the stability analysis can be performed by assessing the qq-components of the grid impedance and inverter output admittance.

B. Sensitivity Function

The stability analysis based on Nyquist contour shows the absolute stability of the system. However, the stability margins of the system are typically as important as the absolute stability. For stable systems, the stability margins can be deduced from the distance from the Nyquist contour to the

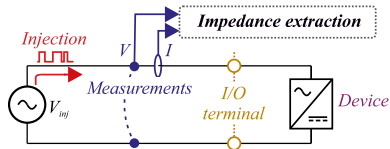


Fig. 2. Simplified diagram of an impedance measurement.

critical point. To quantify the stability margins, impedance-based sensitivity function has been applied [19], which shows the frequency-dependent distance of the contour to the critical point. The sensitivity function can be given as

$$S(\omega) = |1/(1 + Y_o(\omega)Z_g(\omega))| \quad (3)$$

where $Y_o(\omega)$ is the output admittance of the inverter and $Z_g(\omega)$ is the grid impedance. The sensitivity peak is defined as $M_s = \max(S)$, where the peak occurs at the critical frequency ω_c .

III. PERTURBATION DESIGN

To facilitate the use of impedance-based stability criterion, methods for measuring the terminal impedance have been presented [2], [7], [8]. Typically, the impedance measurements are performed by injecting a perturbation signal to the system, measuring the voltages and currents, and obtaining the frequency-response through Fourier techniques. The perturbation is injected to the system as a voltage- or current-type excitation, for example by applying the current references of an inverter or grid voltage references. Fig. 2 shows a simplified diagram of a terminal impedance measurement of a grid-connected device.

A. Broadband Perturbations

Recently, broadband sequences have shown many desirable characteristics for impedance measurements, and especially maximum-length binary sequence (MLBS), originally introduced in [20], has been widely adopted [7], [11], [21], [22]. The MLBS is a periodic and deterministic binary sequence that has a length of N and is generated at f_{gen} . The frequency spectrum is linearly spaced with a resolution of $f_{\text{res}} = f_{\text{gen}}/N$, and the measurement duration of a period is $T_{\text{meas}} = 1/f_{\text{res}}$.

B. Quadratic-residue binary sequence

Quadratic-residue binary sequence (QRBS) is a form of periodic pseudo-random signal originally introduced in [14]. The QRBS has the following properties:

- 1) the length of the signal can be chosen as $N = 4k - 1$
- 2) the signal alternates between two levels with almost uniform distribution between the levels
- 3) the signal value can change only at discrete times every $1/f_{\text{gen}}$
- 4) the signal is deterministic, allowing repeatable experiments
- 5) the signal is periodic over $t_m = N/f_{\text{gen}}$, allowing averaging over multiple periods

where N is a prime number, k is a positive integer, f_{gen} is the generation frequency, and t_m the duration of one period [12].

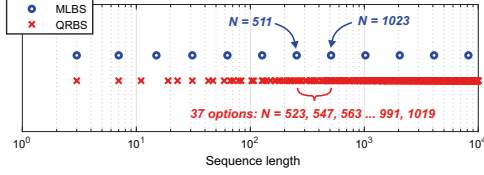


Fig. 3. Available signal lengths for MLBS (blue) and QRBS (red).

The characteristics of the QRBS are similar to the MLBS, but a significant difference is found from the available signal lengths. As the MLBS is available only for $N = 2^n - 1$, where n is a positive integer, it is apparent that the length of the QRBS has drastically more options. Fig. 3 presents the available signal lengths for both the MLBS and QRBS up to 10000.

The design of the QRBS is well documented [12], and can be summarized as follows

- 1) Choose a signal length of $N = 4k - 1$, where N is a prime and k a positive integer
- 2) Form a sequence up to $(N - 1)/2$,
 $[1 \ 2 \ \dots \ (N - 1)/2]$
- 3) Square the sequence,
 $[1^2 \ 2^2 \ \dots \ ((N - 1)/2)^2]$
- 4) Take mod- N of all the values,
 $[1_{\text{mod}N} \ 2_{\text{mod}N} \ \dots \ ((N - 1)/2)_{\text{mod}N}]$
- 5) Generate a sequence of zeros with a length of N
- 6) Set the values in empty sequence to one based on the modulo sequence (that is, if the modulo sequence in (4) contains a number 1, the 1st element of the sequence full of zeros is replaced by one).
- 7) From the obtained sequence, map values of 0 to -1.

A design example for QRBS that has $N = 7$ is presented in the Appendix A.

IV. SYSTEM DAMPING FACTOR ESTIMATION

In this work, the impedance-based stability criterion is extended by extracting the system damping and resonant frequency from the impedance data through the use of the impedance-based sensitivity function. Fig. 4 presents the method this work proposes for extending the impedance-based stability criterion. The steps of the method are as follows

- 1) Measure the terminal impedances, Y_{o-qq} and Z_{g-qq}
- 2) Calculate the sensitivity function S
- 3) Obtain the corresponding minimum phase margin Φ_m from the sensitivity function
- 4) Calculate the damping factor ζ from the Φ_m
- 5) Extract the critical frequency ω_c from the peak value of the sensitivity function
- 6) Calculate the natural resonant frequency ω_n
- 7) Formulate a second-order estimate from ζ and ω_n .

The minimum phase margin can be defined from the sensitivity function peak by applying

$$\Phi_m = 2 * \sin\left(\frac{1}{2M_s}\right) \quad (4)$$

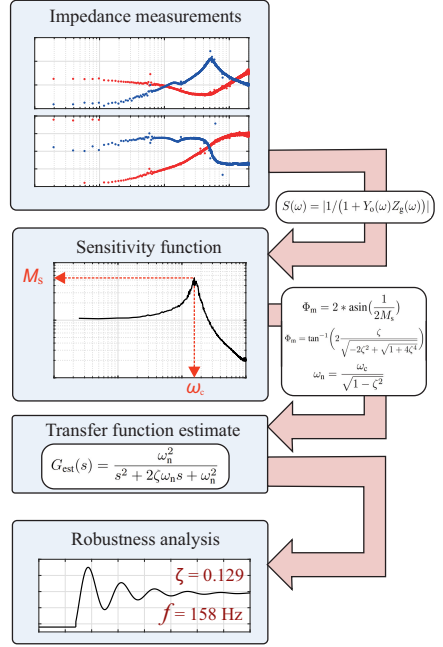


Fig. 4. Flowchart of the proposed method.

where M_s is the sensitivity peak (maximum of the sensitivity function). Additionally, the phase margin and damping factor are related through

$$\Phi_m = \tan^{-1}\left(2 \sqrt{-2\zeta^2 + \sqrt{1 + 4\zeta^4}}\right) \quad (5)$$

which can be simplified as $\zeta \approx 0.01\Phi_m$ for low values of damping factor. Moreover, the critical resonant frequency ω_c can be directly obtained from the frequency of the sensitivity function maximum. The natural resonant frequency of the system can be given as

$$\omega_n = \frac{\omega_c}{\sqrt{1 - \zeta^2}} \quad (6)$$

Finally, when the damping factor and frequency are known, a second-order transfer function can be built to approximate the critical system dynamics given as

$$G_{\text{est}}(s) = \frac{\omega_n^2}{s^2 + 2\zeta\omega_n s + \omega_n^2} \quad (7)$$

This transfer function can be directly used to approximate the system dynamics based on the critical frequency. In system that has low stability margins, the transfer function shows the shape of the transient response. Additionally, the damping factor can be used as a quantitative measure for system robustness, and the critical frequency can be utilized in the system design to strengthen the system by, for example, controller re-design.

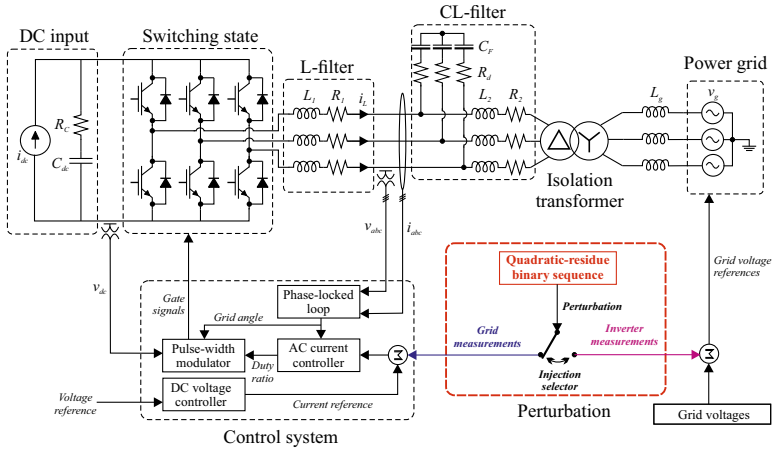


Fig. 5. Experimental setup configuration.

V. EXPERIMENTS

The performance of the proposed method is verified with an experimental setup that consists of a 2.7 kW three-phase inverter (*Myway Plus MWINV-9R144*), a linear voltage amplifier (*Spitzenberger & Spies PAC 15000*), and a PV emulator (*Spitzenberger & Spies PVS 7000*). Fig. 5 presents the detailed configuration of the experimental setup. The controller of the inverter is implemented in a dSPACE real-time simulation. The inverter has an L-filter, and is interfaced to the grid (voltage amplifier) through an external CL-filter, an isolation transformer, and an additional inductor that emulates the grid impedance. The system parameters are shown in Table II in Appendix B.

A. Impedance measurements

In this work, the stability analysis is performed based on the q-channel impedances of the interconnected inverter and grid. First, the inverter output admittance is measured by injecting a broadband perturbation to the grid voltages and obtaining the admittance through Fourier methods. Then, an additional inductor is connected to the system to emulate the grid impedance, and the grid impedance is measured by performing the perturbation injection through the current reference of the inverter. The parameters of the QRBS perturbation are shown in Table I. Fig. 6 presents the measurement configuration for (a) grid impedance measurements and (b) inverter admittance measurements. Fig. 7 shows the measured grid impedance q-component and Fig. 8 shows the inverter output admittance q-component.

TABLE I
PERTURBATION PARAMETERS FOR MEASUREMENTS.

Parameter	Value	Parameter	Value
Sequence length	1999	Generation frequency	8 kHz
Average periods	50	Frequency resolution	2.0 Hz
Amplitude (V-type)	3 V	Amplitude (I-type)	0.2 A

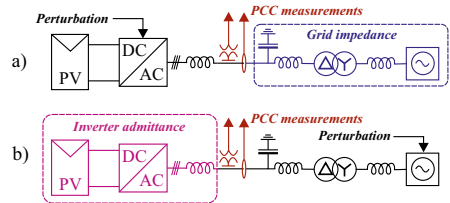


Fig. 6. Measurement configuration for (a) grid impedance and (b) inverter admittance measurements.

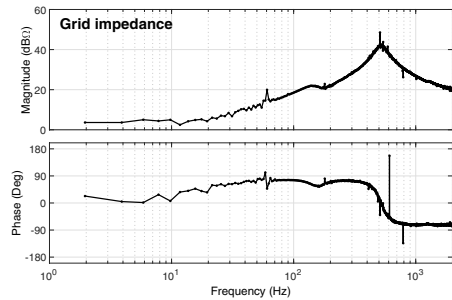


Fig. 7. Measured grid impedance q-component.

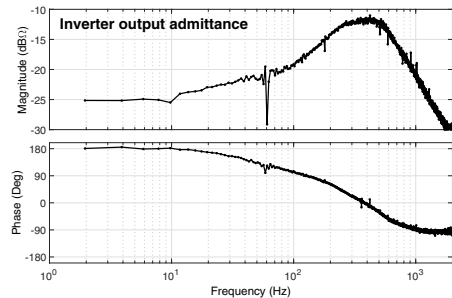


Fig. 8. Measured inverter output admittance q-component.

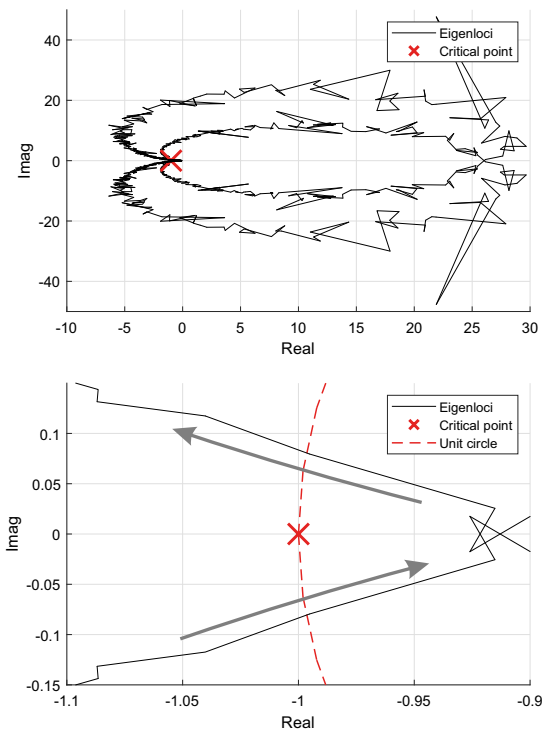


Fig. 9. Nyquist contour of the impedance ratio (upper) and zoomed contour around critical point (lower).

B. Stability analysis

The stability analysis is performed based on the measured impedances by applying Nyquist criterion and the proposed method. Fig. 9 shows the Nyquist contour (eigenlocus) which is calculated from the impedance ratio. The contour does not encircle the critical point, which indicates stable operation. However, the contour passes close to the critical point, which suggests the possibility of low stability margins.

To assess the stability margins quantitatively, the proposed method is applied. First, the impedance-based sensitivity function shown in Fig. 10 is calculated by applying (3). From the sensitivity function, the peak can be identified to have a magnitude of $M_s = 13.1$ and an angular frequency of $\omega_c = 626.2$ rad/s. Next, the minimum phase margin and corresponding damping factor are calculated by applying (4) and (5), which yield $\Phi_m = 4.36$ degrees and $\zeta = 0.0381$. Applying (6), the natural resonant frequency is ω_n . Finally, the second-order estimate of the system can be calculated from (7), yielding

$$G_{\text{est}}(s) = \frac{392700}{s^2 + 47.71s + 392700} \quad (8)$$

The obtained transfer function can be applied to predict the system transient responses, where the damping factor gives

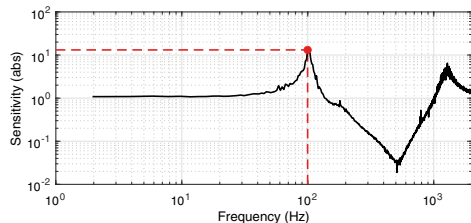


Fig. 10. Impedance-based sensitivity function (sensitivity peak indicated with red).

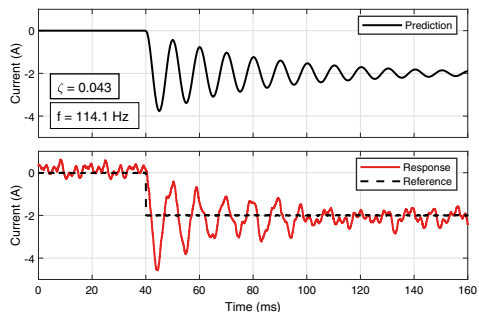


Fig. 11. Predicted dynamic performance (black) and actual system response (red).

a quantitative value for the system robustness. To verify the prediction, the operation of the system is disturbed with a step change of q-channel current reference. Fig. 11 presents the predicted current response to the reference change (black, upper) and the measured step response (red, lower). Ideally, the current should follow the reference closely and have a similar shape. However, due to the low stability margins resulting from the high-impedance grid, the system damping factor is low and the response is highly resonant. As seen from the figure, the second-order estimation that was obtained by applying the proposed method gives an accurate prediction of the response, and thus, describes the system damping factor. The estimation indicates slightly lower damping factor compared to the actual value. This can be explained by examining Equation (4). The equation yields the minimum phase margin, so the actual phase margin of the system can be slightly higher. However, the error is negligible and always in the manner where a worst-case robustness is predicted. Therefore, the method can be considered to ensure the stability with a safety factor.

VI. CONCLUSION

The impedance-based stability criterion has become a widely applied method for stability analysis of grid-connected systems. This work has extended the stability criterion, and presented a method for quantifying the stability margins obtained through the impedance measurements. In

addition, in order to improve the conventional impedance-measurement technique based on the maximum-length binary sequence (MLBS), the quadratic-residue binary sequence (QRBS) was applied. Compared to the MLBS, the QRBS has a significantly higher number of available signal lengths, thus making it possible to more efficiently optimize the practical measurement setup. The method was shown to accurately capture the damping factor and to predict the system responses to transients in experimental system of a grid-connected inverter.

APPENDIX A: GENERATING 7-BIT-LONG QRBS

This appendix shows the design of 7-bit-long QRBS as an example, where the steps are

- 1) $N = 4k - 1 = 7$, where $k = 2$ and N is prime
- 2) Form basic sequence: [1 2 3]
- 3) Square the sequence: [1 4 9]
- 4) Take mod-7 of the sequence: [1 4 2]
- 5) Generate zero sequence: [0 0 0 0 0 0]
- 6) Set 1st, 2nd, and 4th bit to 1: [1 1 0 1 0 0 0]
- 7) Map zeros to -1: [1 1 -1 1 -1 -1 -1].

Similarly, sequences with different lengths can be designed for $N = 4k - 1$, where N is a prime number and k is a positive integer.

APPENDIX B: SYSTEM PARAMETERS

TABLE II
PARAMETERS OF THE EXPERIMENTAL SETUP.

Parameter	Symbol	Value
Grid frequency	f_n	60 Hz
Grid phase voltage	V_g	120 V
Inverter nominal power	S_n	2.7 kVA
Switching frequency	f_{sw}	8 kHz
Power factor	$\cos\phi$	1.0
Switching deadtime	T_{dt}	4.0 μ s
DC voltage	V_{dc}	414.3 V
DC input current	I_{dc}	6.577 A
DC capacitor capacitance	C_{dc}	1.5 mF
L-filter inductance	L_1	2.2 mH
L-filter resistance	R_1	100 m Ω
CL-filter inductance	L_2	0.6 mH
CL-filter resistance	R_2	100 m Ω
CL-filter capacitance	C_f	10 μ F
CL-filter damping resistance	R_d	1.8 Ω
Transformer inductance	L_{tf}	0.3 mH
Transformer resistance	R_{tf}	400 m Ω
Grid inductance	L_g	9 mH
AC current control proportional gain	$K_{P,CC}$	0.0149
AC current control integral gain	$K_{I,CC}$	23.442
DC voltage control proportional gain	$K_{P,VC}$	0.0962
DC voltage control integral gain	$K_{I,VC}$	1.2092
PLL control proportional gain	$K_{P,PLL}$	2.3280
PLL control integral gain	$K_{I,PLL}$	351.720

REFERENCES

[1] C. Li, "Unstable Operation of Photovoltaic Inverter from Field Experiences," *IEEE Transactions on Power Delivery*, vol. 8977, no. c, pp. 1–1, 2017.

[2] Y. Tang, R. Burgos, B. Wen, D. Boroyevich, J. Verhulst, D. Vrtachnik, and M. Belkhatay, "A Novel dq impedance measurement method in three-phase balanced systems," in *2019 IEEE 20th Workshop on Control and Modeling for Power Electronics, COMPEL 2019*, 2019.

[3] T. Roinila, T. Messo, and E. Santi, "MIMO-identification techniques for rapid impedance-based stability assessment of three-phase systems in DQ Domain," *IEEE Transactions on Power Electronics*, vol. 33, no. 5, pp. 4015–4022, 2018.

[4] T. Suntio, T. Messo, M. Berg, H. Alenius, T. Reinikka, R. Luhtala, and K. Zenger, "Impedance-Based Interactions in Grid-Tied Three-Phase Inverters in Renewable Energy Applications," *Energies*, vol. 12, no. 464, 2019.

[5] H. Alenius and T. Roinila, "Impedance-Based Stability Analysis of Paralleled Grid-Connected Rectifiers: Experimental Case Study in a Data Center," *Energies*, vol. 13, no. 2109, 2020.

[6] J. Sun, "Impedance-based stability criterion for grid-connected inverters," *IEEE Transactions on Power Electronics*, vol. 26, no. 11, pp. 3075–3078, 2011.

[7] R. Luhtala, T. Roinila, and T. Messo, "Implementation of Real-Time Impedance-Based Stability Assessment of Grid-Connected Systems Using MIMO-Identification Techniques," *IEEE Transactions on Industry Applications*, vol. 54, no. 5, pp. 5054–5063, 2018.

[8] A. Riccobono, M. Cupelli, A. Monti, E. Santi, T. Roinila, H. Abdollahi, S. Arrua, and R. A. Dougal, "Stability of shipboard dc power distribution: Online impedance-based systems methods," *IEEE Electrification Magazine*, vol. 5, no. 3, pp. 55–67, 2017.

[9] R. Luhtala, H. Alenius, T. Messo, and T. Roinila, "Online Frequency Response Measurements of Grid-Connected Systems in Presence of Grid Harmonics and Unbalance," *IEEE Transactions on Power Electronics*, vol. 35, no. 4, pp. 3343–3347, 2020.

[10] T. Roinila and T. Messo, "Online Grid-Impedance Measurement Using Ternary-Sequence Injection," *IEEE Transactions on Industry Applications*, vol. 54, no. 5, pp. 5097–5103, 2018.

[11] T. Roinila, T. Messo, T. Suntio, and M. Vilkkö, "Pseudo-Random Sequences in DQ-Domain Analysis of Feedforward Control in Grid-Connected Inverters," *IFAC-PapersOnLine*, vol. 48, no. 28, pp. 1301–1306, 2015.

[12] A. H. Tan and K. Godfrey, *Industrial Process Identification - Perturbation Signal Design and Applications*, 1st ed. Springer, 2019.

[13] H. Alenius, T. Roinila, R. Luhtala, T. Messo, A. Burstein, E. de Jong, and A. Fabian, "Hardware-in-the-Loop Methods for Stability Analysis of Multiple Parallel Inverters in Three-Phase AC Systems," *IEEE Journal of Emerging and Selected Topics in Power Electronics*, pp. 1–10, 2020. [Online]. Available: <https://dx.doi.org/10.1109/JESTPE.2020.3014665>

[14] D. Everett, "Periodic digital sequences with pseudonoise properties," *G.E.C Journal*, vol. 33, no. 115–126, 1966.

[15] T. Suntio, T. Messo, and J. Puukko, *Power Electronics Converters - Dynamics and Control in Conventional and Renewable Energy Applications*. Wiley-VCH, 2017.

[16] M. Belkhatay, "Stability criteria for AC power systems with regulated loads," Doctoral thesis, Purdue University, 1997.

[17] A. G. J. Macfarlane and I. Postlethwaite, "The generalized nyquist stability criterion and multivariable root loci," *International Journal of Control*, vol. 25, no. 1, pp. 81–127, 1977.

[18] T. Messo, J. Jokipii, A. Mäkinen, and T. Suntio, "Modeling the grid synchronization induced negative-resistor-like behavior in the output impedance of a three-phase photovoltaic inverter," *2013 4th IEEE International Symposium on Power Electronics for Distributed Generation Systems, PEDG 2013 - Conference Proceedings*, pp. 1–7, 2013.

[19] S. Vesti, T. Suntio, J. A. Oliver, R. Prieto, and J. A. Cobos, "Impedance-based stability and transient-performance assessment applying maximum peak criteria," *IEEE Transactions on Power Electronics*, vol. 28, no. 5, pp. 2099–2104, 2013.

[20] W. Davies, "Using the binary maximum length sequence for the identification of system dynamics," *Proceedings of the Institution of Electrical Engineers*, vol. 114, no. 10, p. 1582, 1967.

[21] T. Messo, R. Luhtala, A. Aapro, and T. Roinila, "Accurate Impedance Model of Grid-Connected Inverter for Small-Signal Stability Assessment in High-Impedance Grids," in *2018 International Power Electronics Conference*, no. 1, 2018, pp. 3156–3163.

[22] Y. Han, M. Yang, H. Li, P. Yang, L. Xu, E. A. A. Coelho, and J. M. Guerrero, "Modeling and Stability Analysis of LCL-Type Grid-Connected Inverters: A Comprehensive Overview," *IEEE Access*, vol. 7, pp. 114975–115001, 2019.

PUBLICATION

VII

”Impedance-Based Stability Analysis of Multi-Parallel Inverters Applying Total Source Admittance”

H. Alenius, M. Berg, R. Luhtala, T. Roinila and T. Messo

in Proc. *20th Workshop on Control and Modeling for Power Electronics*, pp. 1–8, Toronto, Canada, 2019

Publication reprinted with the permission of the copyright holders

Impedance-Based Stability Analysis of Multi-Parallel Inverters Applying Total Source Admittance

1st Henrik Alenius

Faculty of Information Technology
and Communication Sciences
Tampere University
Tampere, Finland
henrik.alenius@tuni.fi

2nd Matias Berg

Faculty of Information Technology
and Communication Sciences
Tampere University
Tampere, Finland
matias.berg@tuni.fi

3rd Roni Luhtala

Faculty of Engineering
and Natural Sciences
Tampere University
Tampere, Finland
roni.luhtala@tuni.fi

4th Tomi Roinila

Faculty of Engineering
and Natural Sciences
Tampere University
Tampere, Finland
tomi.roinila@tuni.fi

5th Tuomas Messo

Faculty of Information Technology
and Communication Sciences
Tampere University
Tampere, Finland
tuomas.messo@tuni.fi

Abstract—The utility-scale wind and solar electricity production is typically connected to the power grid through multiple parallel three-phase inverters. One of the main issues in such grid-connected systems is the harmonic resonance caused by interactions between the grid and inverters. A common method for the analysis of these systems has been the impedance-based stability criterion. However, in systems that have multiple parallel inverters, the system complexity and challenges in obtaining the required impedance measurements may deteriorate the accuracy of the impedance-based approach. This paper discusses the aggregation of parallel inverters and the stability analysis of such grid-connected system. A simple method, based on impedance measurements, is shown for defining the allowable number of paralleled inverters so that the system remains stable. Experimental results are shown from power hardware-in-the-loop setup recently developed at DNV GL Flexible Power Grid Lab.

Index Terms—Stability analysis, Impedance measurement, Grid-connected inverter, Parallel inverters, Power hardware-in-the-loop

I. INTRODUCTION

The electrical power system is changing rapidly, as the electricity production shifts towards inverter-interfaced sustainable options, such as solar and wind power [1]. This causes inherent change in power system dynamics, as the inverters operate over a wide frequency range with little to no internal inertia. This has shown to cause stability and power-quality issues especially in weak grid conditions and in grids with high power-electronics penetration [2]–[4].

The stability assessment of systems that have high number of grid-connected inverters are usually carried out either by state-space based methods [5]–[7] or by applying impedance-

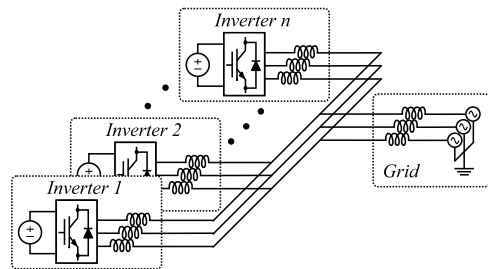


Fig. 1. Schematic of parallel-connected inverters.

based stability criterion [8]–[11]. The methods have different approach; state-space methods permit the complete assessment of the global system, while the impedance-based stability criterion is limited to the local interface [12], [13]. The impedance-based stability analysis is based on the ratio of the equivalent grid impedance and inverter output impedance. However, as the method is interface-dependent, the selection of the interface affects the indicated stability margins [10], [14]. The implementation of the impedance-based stability assessment is simple for single inverters, but in multi-inverter systems the interface selection is not as intuitive and the impedance measurements are more difficult to obtain.

The large-scale solar and wind power plants consist of multiple inverters, as the unit power is limited to a few megawatts. Consequently, the plants typically have complex structures, which introduces new challenges in using the impedance-based stability criterion. Fig. 1 shows a schematic diagram of n parallel three-phase inverters connected to the

power grid through a common bus. In such a system, assessing the impedance-based stability at the output interface of a single inverter may be insufficient. The absolute stability in the system is mutual, but the indicated stability margins at different interfaces may differ drastically. For a system shown in Fig. 1, the sources can be aggregated, and the stability analysis can be carried out for source-load subsystems.

This paper applies the impedance-based stability criterion for systems comprising multiple paralleled inverters. Experimental results are provided by using power hardware-in-the-loop experiments performed at DNV GL Flexible Power Grid Lab in high power range (73 kW). Additionally, a simple method is shown for predicting the system robustness for n parallel inverters based on measurements of a single device, which can be used as a guideline for designing plants with multiple inverters. The stability is assessed based on multi-input multi-output (MIMO) impedance measurements [15] and applying sensitivity function, generalized Nyquist criterion (GNC), and closed-loop system poles.

The remainder of the paper is organized as follows. Section II briefly reviews the theory of the impedance-based stability analysis of grid-connected inverters in synchronous reference frame. In Section III, a MATLAB/Simulink case study demonstrates the presented stability assessment methods for paralleled inverters connected to a shared point of common coupling (PCC). Section IV presents the experimental power hardware-in-the-loop setup (DNV GL Flexible Power Grid Lab, Arnhem, Netherlands) and impedance measurements of parallel devices. In addition, the stability margins of a system that has n identical inverters are evaluated and discussed. Finally, Section V concludes this paper.

II. THEORY

A. Synchronous Reference Frame

Synchronous reference frame has been widely applied to simplify control of three-phased AC system, where the frame of reference rotates at the grid frequency describing the balanced three-phased sinusoids as two constant values (d and q components). The transformation is carried out by a multiplication with Park's matrix to direct, quadrature and zero-components, respectively. In balanced systems, the zero component is omitted. The DC-valued signal has a steady-state value, and can be linearized for small-signal analysis and controlled with conventional PID-controllers. The synchronous reference frame voltage, current, and impedance are matrices given as

$$\mathbf{V}_{dq}(s) = \begin{bmatrix} V_d(s) \\ V_q(s) \end{bmatrix} \quad \mathbf{I}_{dq}(s) = \begin{bmatrix} I_d(s) \\ I_q(s) \end{bmatrix} \quad \mathbf{Z}_{dq}(s) = \begin{bmatrix} Z_{dd}(s) & Z_{dq}(s) \\ Z_{dq}(s) & Z_{qq}(s) \end{bmatrix}$$

where the off-diagonal elements in the impedance matrix represent the cross-couplings $Z_{qd}(s)$ and $Z_{dq}(s)$ between the d and q components. For the remainder of this paper, the Laplace variable s is omitted from the equations.

B. Impedance-based stability criterion

Fig. 2 shows an example in which a single inverter (source) is connected to a power grid (load). The source is modeled

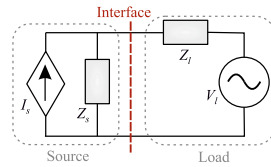


Fig. 2. Source-load system presented as Norton and Thevenin equivalents.

by a Norton equivalent circuit, as a current source I_s in parallel with the source impedance Z_s . The load voltage is denoted by V_l and the load impedance by Z_l . This combination applies for a grid-parallel inverter in which the grid acts as a voltage type load and the inverter resembles a controlled current source. Assuming that the source is stable when unloaded and that the load is stable when powered by an ideal source, the stability and other dynamic characteristics of the interconnected system can be determined by applying the impedance ratio of the source and load [8]. The impedance-based characteristic equation for the interface can be written as

$$[\mathbf{I} + \mathbf{Y}_o \mathbf{Z}_g]^{-1} \quad (1)$$

where \mathbf{Y}_o is the inverter output admittance, \mathbf{Z}_g is the grid impedance, and their product $\mathbf{Y}_o \mathbf{Z}_g$ is the minor loop gain [16]. The small-signal characteristics of the interface between the systems resemble a feedback system, and the small-signal stability of such three-phase AC system can be assessed by examining its closed-loop poles and the characteristic loci [17].

C. Dq-domain impedance measurements

The impedances of the load and source subsystems can be measured by either voltage- or current-type injection. Recent studies have presented methods in which an excitation signal is injected to the system (for example, to controller reference) and the output currents and voltages are measured and Fourier-transformed [15], [18]. The frequency-dependent dq-domain impedance is defined as

$$\mathbf{V}_{dq} = \mathbf{Z}_{dq} \mathbf{I}_{dq} \quad (2)$$

The impedance (or admittance) matrix can be calculated from the Fourier transformed voltages and currents. In order to reliably measure the impedance of an inverter, the device should operate at nominal operation conditions.

Orthogonal broadband binary signals have been proposed for efficient impedance measurements of power-electronic systems in the dq domain, as the signals are easy to generate and can obtain the complete impedance matrix directly with a single measurement cycle [15]. In this work, two orthogonal binary injections are applied for obtaining the complete impedance matrix. The injections are generated by applying a Hadamard modulation, presented in detail in [15]. The first signal is injected into d channel and the second signal into q channel, while the frame angle is aligned to the local reference frame. The combination of orthogonal injections allows MIMO measurement, where all components are obtained

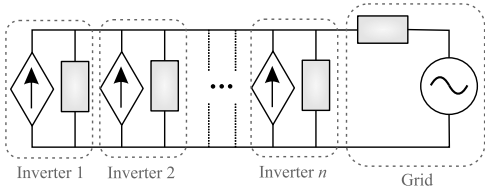


Fig. 3. Norton equivalents of n parallel inverters connected to a Thevenin equivalent of the grid.

simultaneously. In shunt injection, the interconnected load and source subsystems affect the impedance measurements of each other, as the current perturbation to source causes voltage response, which acts as a perturbation for load subsystem (and vice versa). This is an inherent phenomenon when measuring interconnected systems with shunt injection. The same occurs in series injection unless the injection is made with ideal device with negligible impedance.

D. Admittance aggregation of parallel inverters

The impedance-based assessment does not work straightforwardly in systems that have multiple inverters; the system may contain multiple possible choices for interface selection on which the analysis is performed [12]. In addition, the required impedance measurements and models may be very difficult to obtain due to complex system topology. A system that has multiple parallel inverters can be simplified if the impedances between the inverters can be assumed small. In this case, the inverters are connected to the same PCC with zero interconnection impedance. The inverters share the same synchronous reference frame, so they can be aggregated by adding the inverter admittances together. Fig. 3 shows the equivalent circuit for n parallel inverters connected to the same PCC, where the inverters are depicted as Norton equivalents and the grid is Thevenin equivalent (see Fig. 2). The paralleled current sources and impedance elements can be joined to a single current source and parallel impedance, which is the conventional source-load system for impedance-based stability analysis. Thus, the impedance-based stability criterion can be directly applied for parallel inverters at the same PCC with the aggregated total source admittance given as

$$\mathbf{Y}_o^{\text{tot}} = \sum_{n=1}^n \mathbf{Y}_o^n \quad (3)$$

E. Stability analysis based on minor loop gain

As the impedance ratio resembles a feedback system, the impedance-based dynamics are similar to conventional closed-loop systems. The equivalent loop gain is the minor loop gain $\mathbf{Y}_o \mathbf{Z}_g$ (source-load impedance ratio). Thus, multiple methods can be used for stability analysis, which all describe the same stability interpretation, but have differences in the areas of emphasis. A conventional approach is to use Nyquist criterion, where a graphical presentation shows the absolute

stability of a single-input-single-output (SISO) system. In [17], a generalized Nyquist criterion was applied for impedance-based stability analysis in the dq-frame (MIMO system). The path of Nyquist contour related to the critical point $(-1, 0)$ shows the absolute stability. Another widely used method is the sensitivity function of a control loop, which can be extended to MIMO systems. In order to describe the sensitivity of a MIMO system, singular value decomposition (SVD) can be used to obtain the singular values (SV) of the sensitivity matrix [6]. As the interest is on maximal SV, only the upper SV is applied in this work. The MIMO sensitivity function is given by

$$S = \overline{\text{svd}}[(\mathbf{I} + \mathbf{Y}_o \mathbf{Z}_g)^{-1}] \quad (4)$$

The stability assessment can also be carried out based on system transfer functions. The transfer functions are usually obtained by analytical small-signal modeling, which may be difficult or time consuming. Another approach is to fit the measured data to a parametric model. The transfer functions can be acquired by matrix fitting [19], [20], where the frequency-dependent impedance-ratio is approximated by matrices equivalent to state-space representation given by

$$\mathbf{Y}_o \mathbf{Z}_g = \mathbf{C}(s\mathbf{I} - \mathbf{A})^{-1}\mathbf{B} + \mathbf{D} + s\mathbf{E} \quad (5)$$

which can be expressed with residual matrix representation

$$\mathbf{Y}_o \mathbf{Z}_g = \sum_{m=1}^N \left(\mathbf{R}_m \frac{1}{s - a_m} \right) + \mathbf{D} + s\mathbf{E} \quad (6)$$

The system eigenvalues, equal to closed-loop poles of the impedance-based feedback system, can be obtained from the estimated MIMO transfer function. The poles give an analytical representation of the impedance-based dynamics by providing resonant frequencies and corresponding system damping factors. In this work, the transfer functions are estimated for providing an auxiliary stability analysis by assessing the system eigenvalues.

III. SIMULATIONS

The simulations are performed in MATLAB/Simulink with averaged models of identical current-fed inverters shown in Fig. 4. The inverters operate in a cascaded control scheme with a DC-voltage controller, AC-current controller, and phase-locked loop (PLL). A case of four parallel inverters without interconnection impedance is considered. Table I presents the control parameters of the inverters.

The measurements are performed with a shunt injection at the common PCC interface. The grid impedance and the inverters' total impedance are obtained by measuring the node voltages and the currents to the grid and to inverters. The minor loop gain is given by a ratio of grid impedance and inverter impedance. The impedance was measured for systems that had either 1, 2, 3, or 4 identical parallel inverters.

The stability of the system under study is assessed based on the shunt impedance measurements with GNC where the eigenvalue trajectories (eigenloci) indicate the stability margins. The minor loop gain is a 2x2 matrix and has two

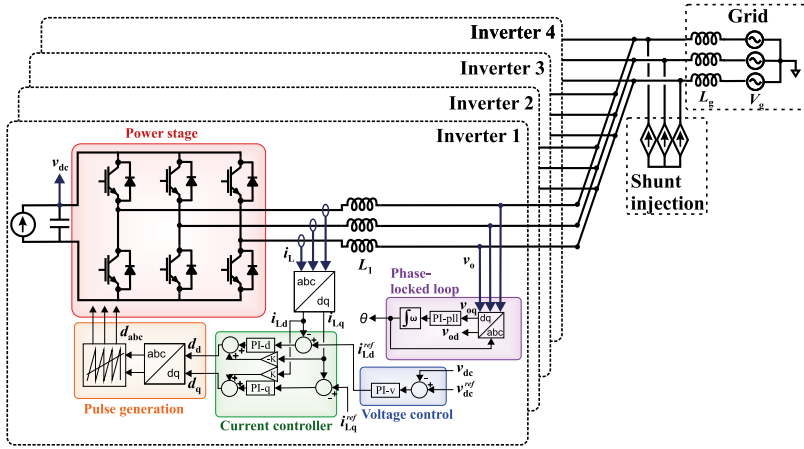


Fig. 4. Overview of system that has four paralleled inverters.

TABLE I
SIMULATION PARAMETERS FOR INVERTER AND GRID.

Parameter	Symbol	Value
Grid frequency	f_n	60 Hz
Base power	S_b	2.7 kVA
Base voltage	V_b	207 V
Power factor	$\cos\phi_{\text{conv}}$	1.0
Switching frequency	f_{sw}	8 kHz
Nominal power	S_{conv}	1.0 p.u.
DC capacitor reactance	X_{Cdc}	0.11 p.u.
L-filter reactance	X_{L1}	0.052 p.u.
L-filter resistance	R_{L1}	0.006 p.u.
DC voltage	V_{dc}	2.0 p.u.
Grid reactance	X_g	0.071
AC current control proportional gain	$K_{\text{P-CC}}$	0.0149
AC current control integral gain	$K_{\text{I-CC}}$	23.442
DC voltage control proportional gain	$K_{\text{P-VC}}$	0.0962
DC voltage control integral gain	$K_{\text{I-VC}}$	1.2092
PLL control proportional gain	$K_{\text{P-PLL}}$	1.5520
PLL control integral gain	$K_{\text{I-PLL}}$	156.32

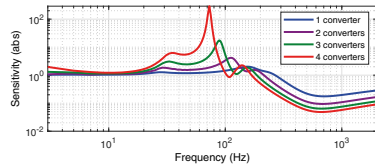


Fig. 6. Maximum singular values for systems with different number of parallel inverters.

eigenvalues. In the analysis, the eigenlocus which bypasses closer to the critical point is considered the critical eigenlocus. Fig. 5 presents the GNC loci of the minor loop gain for systems that have different number of inverters. The figure shows that increasing the number of paralleled inverters drastically reduces the stability margins of the system, as the locus approaches the critical point. In addition, it can be predicted that a fifth parallel inverter would destabilize the system. The same conclusion can be drawn from the sensitivity function shown in Fig. 6, which shows peaking in system sensitivity when more inverters are connected.

In order to test the predicted system robustness, simple step tests are performed for varying number of paralleled inverters. The q-channel current reference of a single inverter is stepped from 0 to -2 A (corresponds to $Q = 0.2$ p.u. reactive power) at 1.0 s for systems that have 1 to 4 inverters. Fig. 7 shows the transient responses to PCC voltages in phase domain (upper envelope). A clear deterioration in the response appears when additional parallel inverters are added.

IV. EXPERIMENTS

The experiments are performed with power hardware-in-the-loop (PHIL) setup developed at DNV GL Flexible Power Grid Lab. Fig. 8 shows the setup diagram, which consists of

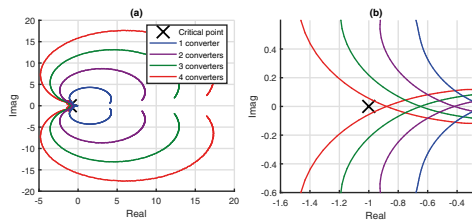


Fig. 5. (a) Critical eigenloci and (b) zoomed critical eigenloci of the system with 1, 2, 3, or 4 parallel inverters.

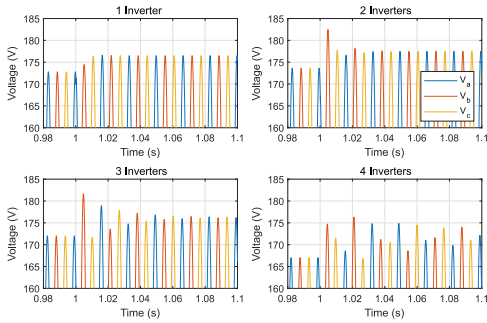


Fig. 7. PCC voltage responses to current reference step test.

an OPAL-RT real-time digital simulator and 200 kVA Egston digital power amplifier, which has four groups of four single-phase units. The units contain six interleaved parallel half-bridge inverters (equivalent switching frequency is 125 kHz) and have closed-loop bandwidth of 5 kHz. A high-speed communication link feeds the references from OPAL-RT to Egston, and the current and voltage measurements are sent to OPAL-RT every 4 μ s from the amplifier. In this work, one group provided stiff grid voltages and groups 2, 3 and 4 were configured to emulate a three-phase grid-connected inverter with current controller (CC) and phase-locked loop (PLL) (see [21]). The three parallel inverters had a total nominal power of 73 kW shared evenly. Table II presents the setup parameters.

TABLE II
EXPERIMENTAL SETUP PARAMETERS.

Parameter	Symbol	Value
Grid frequency	f_g	50 Hz
Egston amplifier maximum power	S_{max}	200 kVA
Nominal phase voltage (RMS)	V_n	230 V
Power set point for inverters	P_{sp}	24.4 kW
Power factor for inverters	$\cos(\phi)$	1.00
D-current reference	i_d^*	50 A
Inverter 1 L-filter	L_1	2.0 mH
Inverter 2 L-filter	L_2	0.5 mH
Inverter 3 L-filter	L_3	3.2 mH
PLL proportional gain	K_{PLL-P}	0.3482
PLL integral gain	K_{PLL-I}	21.88
Inverter 1 CC proportional gain	K_{CC1-P}	6.4247
Inverter 1 CC integral gain	K_{CC1-I}	2019
Inverter 2 CC proportional gain	K_{CC2-P}	1.6514
Inverter 2 CC integral gain	K_{CC2-I}	518.8
Inverter 3 CC proportional gain	K_{CC3-P}	10.070
Inverter 3 CC integral gain	K_{CC3-I}	3162

A. Total admittance of parallel devices

The PHIL setup is capable of admittance measurements, where the voltage perturbation is injected to the grid voltages through voltage references of the grid-emulating group. A multi-input-multi-output (MIMO) measurement scheme is used, where the first orthogonal sequence is injected into

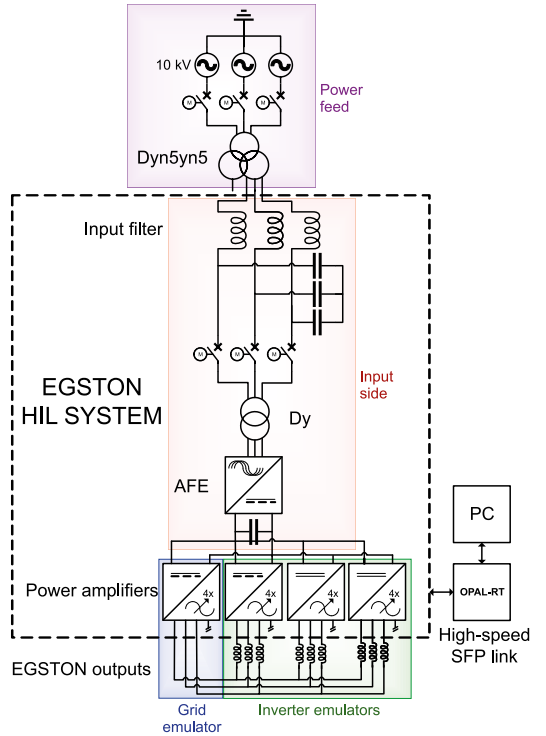


Fig. 8. PHIL setup at DNV GL Flexible Power Grid Lab.

d component and the second orthogonal sequence into q component of the grid voltages. The first injection was 2047-bit length and the second 4094 bits. Both sequences were generated at 5 kHz. The injection amplitudes were selected to be 1 % of the nominal current or voltage values. The measurements using the first injection was averaged over 100 periods, and the measurements using the second injection over 50 periods (because the length of the second sequence is, by definition, doubled compared to the first sequence). Thus, the measurement time for obtaining the complete 2x2 impedance matrix was 41 seconds. Fig. 9 shows the measured MIMO admittances for each inverter. The inverters are not equal due to differently sized output L-filters (0.5, 2, and 3.2 mH) and different current controller parameters (the PLL controllers are identical).

In order to validate the admittance aggregation of parallel devices, the three inverters are measured together. This is compared to the calculated sum of inverter admittances. Fig. 10 shows the measured total impedance (orange) and calculated reference from the separate measurements (black). The measurement accurately follows the predicted sum of admittances, except for the distorted low-frequency cross-couplings. The result verifies the hypothesis of admittance

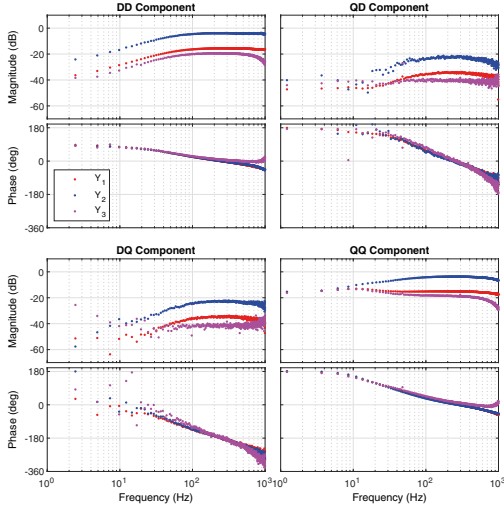


Fig. 9. Complete 2x2 admittances of three inverters measured separately.

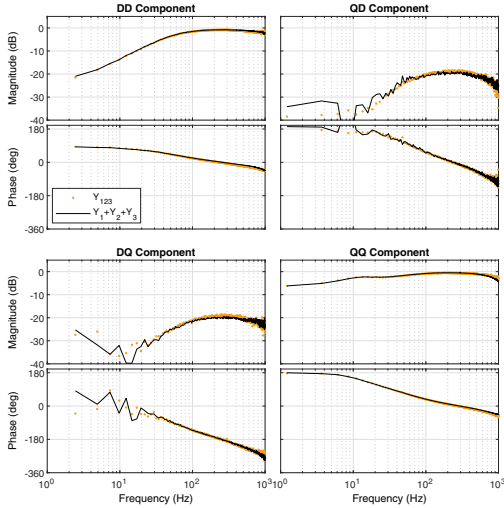


Fig. 10. Measured (orange) and calculated (black) total admittance of three parallel inverters.

aggregation of distinct devices connected to the same point of common coupling. When the impedances of transmission cables and transformers between the inverters can be assumed small, the stability analysis can be performed based on the aggregated total admittance and grid impedance. Thus, the stability margins and limitation to maximum number of parallel devices can be straightforwardly obtained.

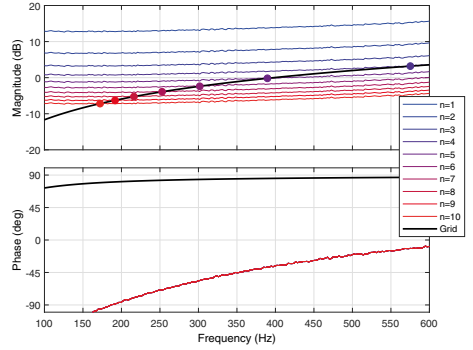


Fig. 11. Grid impedance and aggregated inverters' impedance for $n = 1 \dots 10$ paralleled inverters (qq-component).

B. Stability prediction for parallel identical devices

In many cases, a large-scale plant consists of multiple identical inverters connected to a grid. Impedance measurements of the complete system are usually difficult to obtain, and more convenient analysis methods are required. This section presents a method for assessing the stability and robustness of multiple parallel inverters based on admittance data from a single inverter and grid impedance. Based on the proposed method, guidelines for system design can be derived by considering the required stability margins. The uncertainty of impedances in connections inside the system and possible inaccuracy or variance in grid impedance can be accounted for with simple sensitivity analysis, where, for example, an error margin of $\pm 10\%$ is given to grid impedance.

The deterioration of system robustness is demonstrated by calculating the stability margins for n parallel identical inverters. The grid impedance in this example is $Z_g = 0.08 + j\omega 0.0004 \Omega$. Fig. 11 shows the grid impedance q-component (black) and aggregated inverter impedance (blue to red) for $n = 1 \dots 10$ parallel inverters (the measurements and analysis are performed for complete 2x2 matrices, but only one component is shown here for simplicity). The simplified reduced-order impedance comparison shows that the crossing point in impedances shifts to lower frequencies where the phase difference is greater when n increases.

Based on generalized Nyquist criterion (GNC), the stability analysis for MIMO systems can be performed by examining the characteristic loci. If the loci encircles the critical point and the system has no RHP zeros, the system is unstable. Fig. 12 shows the characteristic loci obtained by solving minor loop eigenvalues for systems that have $n = 1 \dots 10$ parallel devices, where only the critical contour (that is, closer to the critical point) is shown. The figure clearly shows that the critical contour approaches the critical point when n increases. The same information can be extracted from the MIMO sensitivity function (4) shown in Fig. 13.

In order to evaluate the system time-domain properties

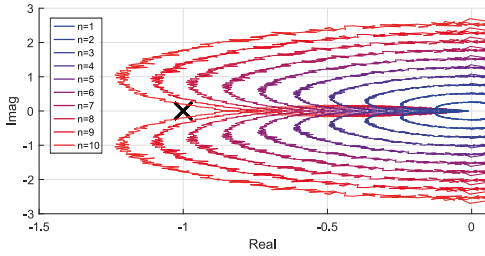


Fig. 12. Critical generalized Nyquist contour of $n = 1...10$ paralleled inverters.

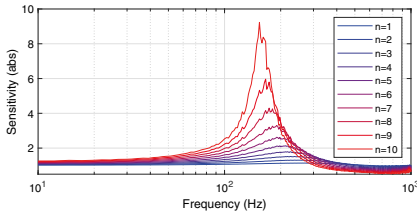


Fig. 13. MIMO sensitivity function of $n = 1...10$ paralleled inverters.

more comprehensively, the system transfer function can be estimated by fitting a pre-defined model to the measured closed-loop return ratio. Once the transfer function is acquired, the poles and zeros of the closed-loop system can be solved analytically. In this example the fitting was performed by MATLAB *tfest()*-tool. Fig. 14 shows the critical poles of the MIMO system, which are located in the (2,2)-component of the full-order matrix for varying number of inverters. The pole-zero map confirms that introducing more parallel inverters shifts the system poles towards imaginary axis, which changes the frequency and damping of the resonant modes present in the system. Based on the pole-zero map and GNC loci, it can be predicted that 11th parallel inverter would destabilize the system as the damping of the critical resonant mode would be almost zero. Table III shows the frequencies and dampings of the critical pole pairs as a function of number of paralleled inverters.

TABLE III
CRITICAL POLE CHARACTERISTICS OF n PARALLEL INVERTERS.

n	Critical pole pair	Frequency (rad/s)	Damping ratio
1	$-268.01 \pm 180.66j$	323.214	0.829
2	$-202.14 \pm 209.87j$	291.386	0.694
3	$-152.89 \pm 214.96j$	263.786	0.580
4	$-116.00 \pm 210.82j$	240.626	0.482
5	$-87.96 \pm 203.05j$	221.284	0.398
6	$-66.24 \pm 194.01j$	205.007	0.323
7	$-49.13 \pm 184.74j$	191.160	0.257
8	$-35.46 \pm 175.65j$	179.194	0.198
9	$-24.4 \pm 166.82j$	168.594	0.145
10	$-15.0 \pm 158.51j$	159.218	0.094

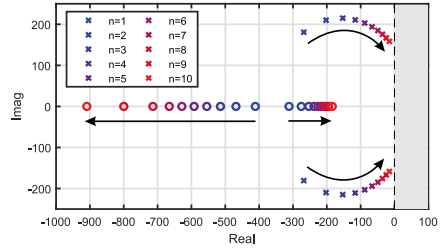


Fig. 14. Pole-zero paths of the closed-loop system when the number of parallel inverters increases from 1 to 10.

C. Discussion

The stability analysis of a grid-connected system that has multiple parallel inverters often becomes complex and even unfeasible. While it is possible to accurately model all components of the system and analyze the stability with state-space models or with impedance models, the computational requirements are very high and time-consuming. When the impedances between the paralleled inverters can be assumed small, a more straightforward approach can be taken as shown in this work. However, the uncertainties in the analysis should be taken into account when defining the minimum stability margins. A simple sensitivity analysis on variance in grid impedance or additional impedance from transformers can be performed as an additional method.

V. CONCLUSION

The impedance-based stability analysis has been extensively applied to stability assessment of grid-connected inverters. This work has studied the stability analysis for grid-connected systems that have multiple parallel inverters. The complete modeling of such complex systems is often infeasible and obtaining accurate impedance measurements at relevant interface may be difficult. If the impedances between the parallel connected inverters can be assumed small, the inverters share the synchronous reference frame, and the total source admittance can be calculated based on measurements or impedance models of separate devices. This work has presented admittance summation of parallel devices and demonstrated the deterioration in stability margins as more parallel devices are connected to a shared point of common coupling. Based on impedance measurements of a single device, the stability margins are predicted for systems that have n identical inverters. The stability is assessed by applying generalized Nyquist criterion, sensitivity function, and closed-loop poles of the source-load impedance ratio. The method indicates the maximum number of paralleled devices at a given grid interface, as well as the system damping ratio at the main resonant frequency. The presented methods can be used for stability prediction for systems that have multi-parallel inverters.

ACKNOWLEDGEMENTS

This research and testing has been performed using the ERIGrid Research Infrastructure and is part of a project that has received funding from the European Union's Horizon 2020 Research and Innovation Programme under Grant Agreement No. 654113. The support of the European Research Infrastructure ERIGrid and its partner DNVGL is very much appreciated. The work was also supported in part by the Academy of Finland.

REFERENCES

- [1] B. Bose, "Global Energy Scenario and Impact of Power Electronics in 21st. Century," *IEEE Transactions on Industrial Electronics*, vol. 60, no. 7, pp. 2638–2651, 2013.
- [2] C. Li, "Unstable Operation of Photovoltaic Inverter from Field Experiences," *IEEE Transactions on Power Delivery*, vol. 8977, no. c, pp. 1–1, 2017. [Online]. Available: <http://ieeexplore.ieee.org/document/7827164/>
- [3] C. Buchhagen, C. Rauscher, A. Menze, and J. Jung, "BorWin1 - First Experiences with harmonic interactions in converter dominated grids," *International ETG Congress 2015; Die Energiewende - Blueprints for the new energy age*, pp. 27–33, 2015.
- [4] J. Adams, C. Carter, and S. Huang, "ERCOT Experience with Sub-Synchronous Control Interaction and Proposed Remediation," in *2012 IEEE Transmission and Distribution Conference and Exposition*, 2012, pp. 1–5.
- [5] X. Wang, F. Blaabjerg, and P. C. Loh, "Passivity-Based Stability Analysis and Damping Injection for Multiparalleled VSCs with LCL Filters," *IEEE Transactions on Power Electronics*, vol. 32, no. 11, pp. 8922–8935, 2017.
- [6] A. Rodríguez-Cabero and M. Prodanovic, "Stability analysis for weak grids with power electronics interfaces," *IECON Proceedings (Industrial Electronics Conference)*, pp. 2402–2407, 2016.
- [7] G. O. Kalcon, G. P. Adam, O. Anaya-lara, S. Lo, and K. Uhlen, "Small-Signal Stability Analysis of Multi-Terminal VSC-Based DC Transmission Systems," *IEEE Transactions on Power Electronics*, vol. 27, no. 4, pp. 1818–1830, 2012.
- [8] J. Sun, "Impedance-based stability criterion for grid-connected inverters," *IEEE Transactions on Power Electronics*, vol. 26, no. 11, pp. 3075–3078, 2011.
- [9] X. Zhang, H. S. H. Chung, L. L. Cao, J. P. W. Chow, and W. Wu, "Impedance-based stability criterion for multiple offshore inverters connected in parallel with long cables," in *2017 IEEE Energy Conversion Congress and Exposition, ECCE 2017*, vol. 2017-Janua, 2017, pp. 3383–3389.
- [10] S. Vesti, T. Suntio, J. A. Oliver, R. Prieto, and J. A. Cobos, "Impedancebased stability and transient-performance assessment applying maximum peak criteria," *IEEE Transactions on Power Electronics*, vol. 28, no. 5, pp. 2099–2104, 2013.
- [11] B. Wen, D. Boroyevich, P. Mattavelli, Z. Shen, and R. Burgos, "Experimental verification of the Generalized Nyquist stability criterion for balanced three-phase ac systems in the presence of constant power loads," *2012 IEEE Energy Conversion Congress and Exposition, ECCE 2012*, no. 1, pp. 3926–3933, 2012.
- [12] M. Amin and M. Molinas, "Small-Signal Stability Assessment of Power Electronics based Power Systems: A Discussion of Impedanceand Eigenvalue-based Methods," *IEEE Transactions on Industry Applications*, vol. 53, no. 5, pp. 1–1, 2017. [Online]. Available: <http://ieeexplore.ieee.org/document/7940030/>
- [13] M. Amin, A. Rygg, and M. Molinas, "Impedance-based and eigenvalue based stability assessment compared in VSC-HVDC system," *ECCE 2016 - IEEE Energy Conversion Congress and Exposition, Proceedings*, 2016.
- [14] S. D. Sudhoff and S. F. Glover, "Admittance space stability analysis of power electronic systems," *IEEE Transactions on Aerospace and Electronic Systems*, vol. 36, no. 3 PART 1, pp. 965–973, 2000.
- [15] T. Roinila, T. Messo, and E. Santi, "MIMO-identification techniques for rapid impedance-based stability assessment of three-phase systems in DQ Domain," *IEEE Transactions on Power Electronics*, vol. 33, no. 5, pp. 4015–4022, 2018.
- [16] D. Middlebrook, "Input filter considerations in design and applications of switching regulators," in *IEEE Ind. Appl. Soc. Annu. Meeting*, 1976, pp. 91–107.
- [17] M. Belkhatay, "Stability criteria for AC power systems with regulated loads," Doctoral thesis, Purdue University, 1997.
- [18] M. Cespedes and J. Sun, "Three-phase impedance measurement for system stability analysis," *2013 IEEE 14th Workshop on Control and Modeling for Power Electronics, COMPEL 2013*, 2013.
- [19] B. Gustavsen and A. Semlyen, "Rational Approximation of Frequency Domain Responses by Vector Fitting," *IEEE Transactions on Power Delivery*, vol. 14, no. 3, pp. 1052–1061, 1999.
- [20] B. Gustavsen and A. Semlyen, "A Robust Approach for System Identification in the Frequency Domain," *IEEE Transactions on Power Delivery*, vol. 19, no. 3, pp. 1167–1173, 2004.
- [21] T. Messo, R. Luhtala, T. Roinila, E. D. Jong, R. Scharrenberg, T. Caldognetto, P. Mattavelli, Y. Sun, and A. Fabian, "Using High-Bandwidth Voltage Amplifier to Emulate Grid-Following Inverter for AC Microgrid Dynamics Studies," *Energies*, vol. 12, no. 3, 2019.

PUBLICATION

VIII

**”Online Frequency Response Measurements of Grid-Connected Systems in Presence
of Grid Harmonics and Unbalance”**

R. Luhtala, H. Alenius, T. Messo and T. Roinila

IEEE Transactions on Power Electronics, vol. 35, pp. 3343–3347, 2020

Publication reprinted with the permission of the copyright holders

Online Frequency-Response Measurements of Grid-Connected Systems in Presence of Grid Harmonics and Unbalance

Roni Luhtala, Henrik Alenius, Tuomas Messo, and Tomi Roinila

Abstract—Grid characteristics have a drastic impact on the stability and control performance of grid-connected systems. Because the grid conditions typically vary over time, online measurements are most desirable for the stability assessment, protection design, and control-system optimization of the systems. Previous studies have presented methods based on Fourier techniques and broadband sequences with which the frequency responses of the grid-connected systems, such as the grid impedance or inverter control loops, can be measured. However, online measurements under unbalanced grids with harmonic voltages have not been comprehensively considered. The present paper demonstrates how the previously applied online-measurement methods fail in the presence of unbalanced grid and voltage harmonics due to the spectral leakage caused by Fourier transform. This work also proposes a simple signal-design method to avoid the leakage. Experimental results based on a high-power grid-connected system are shown to demonstrate the effectiveness of the proposed method.

I. INTRODUCTION

The performance and stability of grid-connected power-electronics applications are significantly affected by the interfaced grid [1]–[4]. Since the grid conditions vary over time, online measurements of the grid impedance and the load-affected converter AC-side dynamics are most desirable for obtaining the system stability margins in the grid-connection point. Additionally, online measurements acquired in real time allow novel control strategies such as adaptive control or adjustment of the protection parameters. Such measurements have become popular in power-electronics applications, including grid-connected converters [5]–[8]. In most of the presented methods, a broadband perturbation such as pseudo-random binary sequence (PRBS) is injected into the system, and Fourier analysis is applied to extract the corresponding frequency components in the responses.

A single converter may face unpredictable grid conditions such as a weak grid or poor grid voltages [2], [9]. The disturbances in grid voltages, such as voltage harmonics, may cause errors in the frequency-response measurements. Although the issues related to unbalanced or harmonic-polluted grid voltages are widely known, the impact of the voltage waveforms on the online measurements has not been previously considered. The present study discusses the measurement issues under the unbalanced grid with a high harmonic content and introduces a design procedure of the perturbation signal to suppress the issues.

The grid harmonics appear as periodic oscillations in the measured samples. When the discrete Fourier transform (DFT)

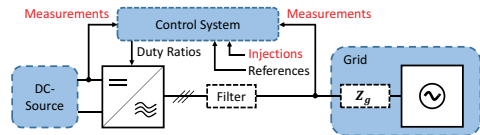


Fig. 1: Grid-connected inverter.

is applied, the periodic oscillations may leak to other frequencies through two undesired features known as spectral leakage and the picket-fence effect (PFE) [5], [10]. The PFE appears if the discrete spectrum, produced by the DFT, does not include exactly the frequencies of periodic oscillations. This results in leaking to the nearest available frequency bins [11]. The spectral leakage occurs when the DFT is applied on samples that contain non-integer periods of periodic signals, causing those frequencies to leak over a wide frequency band [12].

The grid fundamental and its harmonics appear at specific frequencies. This means they can be taken into account when adjusting the measurement time so that each measured sample contains integer periods of the grid fundamentals, and thereby, also its harmonics. This suppresses the spectral leakage caused by grid harmonics and unbalance.

This paper shows how the spectral leakage deteriorates the online frequency-response measurements under grid harmonics and unbalance. It also introduces a design procedure to remove the spectral leakage from the measurements.

The remainder of the paper is organized as follows. Section II reviews the online frequency-response measurements and issues related to the spectral leakage. Section III introduces the applied broadband perturbations that are suitable for the dq-domain measurements and proposes a design procedure for measurements under the grid unbalance and harmonics. Section IV shows high-power experimental results in which spectral leakage occurs and how the proposed design procedure can be used to remove the leakage. Section V draws conclusions.

II. ONLINE MEASUREMENTS OF GRID-CONNECTED SYSTEMS

Fig. 1 shows a three-phase grid-connected inverter. The inverter is controlled based on measurements from the DC- and AC-side waveforms. The same measurements can be used for frequency-response identification, which usually requires an excitation signal to be injected into the system. A typical frequency-response measurement setup for multi-input-multi-output (MIMO) identification is illustrated in Fig. 2. In this

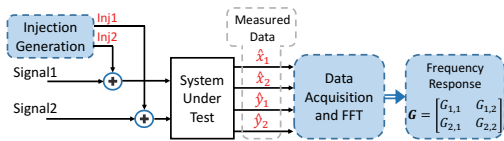


Fig. 2: Typical frequency-response measurement setup.

example, two signals are perturbed, the system responses are measured, and the frequency response is computed using Fourier techniques [7]. The online measurements can be performed either for the grid- or the inverter-side transfer functions, thus obtaining, for example, the grid impedance or inverter control loops.

Three-phase grid-connected systems are often analyzed in the dq domain, where three-phase AC quantities can be transformed into two DC quantities, d and q components [1]. In the dq domain, full-order transfer functions are represented as 2×2 matrices that include direct (dd and qq) and crosscoupling (dq and qd) components. The dq-domain measurements can be performed in accordance with the setup shown in Fig. 2, where Signal1 and Signal2 correspond to the d and q components. In the computed frequency-response matrix, the diagonal components ($G_{1,1}$ and $G_{2,2}$) usually refer to direct components (G_{dd} and G_{qq}) and the off-diagonal components ($G_{1,2}$ and $G_{2,1}$) refer to crosscouplings (G_{dq} and G_{qd}).

In online measurements of the grid-connected systems, the grid cannot be considered as an ideal three-phase voltage source, due to the occurrence of non-idealities such as harmonics, unbalance, or noise. The measurement noise is usually relatively low and can be mitigated by simply increasing the signal-to-noise ratio (SNR) of the measurements by applying higher perturbation amplitude or by averaging the measurements over multiple measurement cycles [10].

The grid harmonics and unbalance appear as periodic oscillations in the measured data. When the discrete Fourier transformation (DFT) is applied, two unwanted features may appear: spectral leakage and picket-fence effect (PFE) [12]. These features deteriorate the spectral estimation and may cause drastic errors in the frequency-response measurements [5], especially at frequencies near the grid-voltage harmonics. The PFE results from non-coherent sampling as a discrete spectrum of the DFT does not include exactly the same frequencies that appear in the measured data, causing these frequencies to leak to the nearest frequency bins. The spectral leakage appears if the measured time-domain data does not include exact integer periods of each periodic signal components, such as the grid-voltage fundamental and its harmonics. If the DFT sample contains fractional periods of periodic signals, the DFT interprets them as discontinuities that cause spectral leakage over a wide frequency band.

III. MEASUREMENT DESIGN

A. Orthogonal Pseudo-Random Sequences

A maximum-length binary sequence (MLBS) is a widely applied broadband excitation in the frequency-response measurements of power-electronics systems [5]. The MLBS can be

easily modified, the sequence has lowest possible crest factor, and is periodic over its length $N = n^2 - 1$, where n is an integer [10]. Considering the measurement setup shown in Fig. 2, one can apply orthogonal binary sequences for simultaneously measuring the full impedance matrix [6], [7]. In the method, two orthogonal sequences are simultaneously injected into d and q channels. As the injections have energy at different frequencies, several (coupled) impedance components can be measured during a single measurement cycle.

The work in [6] and [7] applied a method based on Hadamard modulation for generating orthogonal binary sequences. In the method, the conventional MLBS is used as a first injection. The second (orthogonal) injection is obtained by doubling the MLBS and inverting every other digit. Due to inverse-repeated characteristics of the second injection, the power of the even-order harmonics equals to zero, and thus, must be neglected from the frequency-response measurements [6].

B. Measurement Parameters

The optimal online-measurement design avoids unnecessarily long measurement time and high injection amplitude, while still providing sufficient SNR. Averaging reduces the effect of the noise, but the spectral leakage may still remain. The leakage can be minimized by designing the measurement setup so that an integer number of the grid fundamental cycles (and, thereby, also its harmonics) occurs in the measured sample. The number of the grid fundamental cycles that occur during the measurement time can be given as

$$\frac{N}{f_{\text{gen}}} P f_g = (R + r) \quad (1)$$

where P is a number of averaged MLBS (generated at f_{gen}) periods, and f_g is a grid fundamental frequency. The number of grid fundamental cycles is separated to its integer part (R) and fractional part (r), from which the non-zero r causes the spectral leakage. The time difference ΔT between the measurement time and the nearest multiple of the periodic cycle can be given as

$$\Delta T = \text{abs} \left[\frac{N}{f_{\text{gen}}} P f_g - \text{round} \left(\frac{N}{f_{\text{gen}}} P f_g \right) \right] \frac{1}{f_g} \quad (2)$$

where the operator *round* gives the nearest integer of the grid fundamental. By varying the averaged periods, the local minimum of the spectral leakage is expected when $\Delta T(P)$ (and r) is minimized, representing the proposed measurement design. The following design procedure yields parameters to minimize the spectral leakage.

- 1) Adjust $f_{\text{gen}} = m(2f_g)$, where m is an integer.
 - Converter switching frequency f_{sw} restricts the possible choices as $f_{\text{gen}} = f_{\text{sw}}/e$, where e is an integer.
- 2) Choose $P = f_{\text{gen}}/f_g$ or multiple of it.
 - $T_{\text{meas}} = P(N/f_{\text{gen}}) = a(1/f_g)$, where a is an integer.
 - This results in $a = N$, and thus, T_{meas} includes exactly $R = N$ fundamental grid cycles and $r = 0$.
- 3) N can be chosen without restrictions to satisfy the desired measurement characteristics.

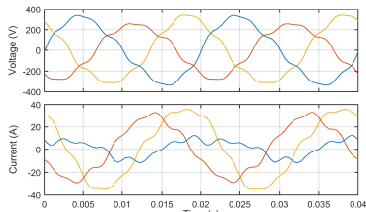


Fig. 3: Polluted grid waveforms without injection.

As a result of the proposed design procedure, an integer amount of the grid fundamental cycles (and consequently, its harmonics) is measured. Therefore, the spectral leakage caused by grid-voltage harmonics is avoided.

C. Measurement Accuracy

The measurement accuracy can be assessed by its variance σ^2 . Higher values indicate increased variability between consecutive measurements and errors around the reference, thus making the measurement system unreliable. In this paper, a smooth impedance Z_{Fit} is used as a reference, produced by a MATLAB's curve-fitting tool from a measurement under ideal grid voltages. The variance can be computed as

$$\sigma^2 = \sum_{f=1}^{\infty} [Z_{\text{Fit}}(f) - Z_{\text{meas}}(f)]^2 \quad (3)$$

where the variance of the reference is considered as zero. It may be assumed that each dq-domain channel (including crosscouplings) has approximately equal SNR during measurements, and they can be taken equally into account when comparing the measurement results to each other. Thus, the total variance of measurement is computed over the entire dq-domain impedance matrix as

$$\sigma_{\text{dq}}^2 = \sigma_{\text{di}}^2 + \sigma_{\text{dq}}^2 + \sigma_{\text{qd}}^2 + \sigma_{\text{qq}}^2 \quad (4)$$

IV. EXPERIMENTS

The experiments are performed using a high-power PHIL setup in accordance with Fig. 1. The system is implemented by two 200 kVA Egston voltage amplifiers and the grid impedance by three-phase inductors. The amplifiers are used to emulate a three-phase grid and a grid-connected converter. The measurement system is described in detail in [8]. In the following experiments the grid impedance is measured in the dq domain. The currents and voltages are measured from the output terminal of the inverter emulator and the data is captured by a measurement card (NI USB-6363). The data is operated by the MATLAB/Data Acquisition Toolbox.

Fig. 3 shows samples of the highly-distorted grid voltages (230 V, 50 Hz) under which the experiments are performed. One of the phases is in 20 % unbalance and all phases include 5 % of the positive sequence 2^{nd} and 7^{th} harmonics as well as negative sequence 2^{nd} and 5^{th} harmonics.

A. Grid-Impedance Measurements

Two orthogonal sequences were designed and injected into the references of the current controller. The first sequence

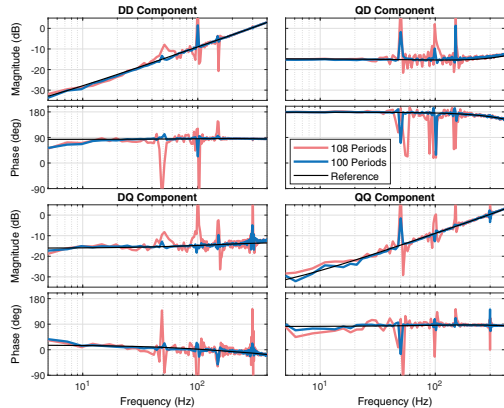


Fig. 4: MIMO-measurements of the grid impedance with different averaging.

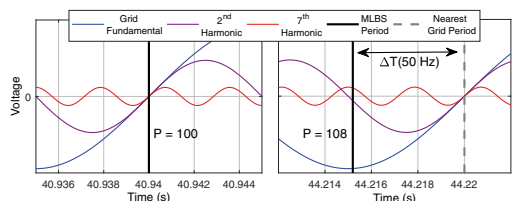


Fig. 5: Time difference between applied MLBS periods $P = 100$ (left), $P = 108$ (right), and grid-voltage components.

had 2047 bits and the second had 4094 bits. Both sequences were generated at 5 kHz, providing 2.44 Hz (5000/2047 Hz) frequency resolution. The number of averaged periods varied between the measurements in order to achieve desired measurement time that minimizes ΔT . The unbalance occurs at 50 and 100 Hz in the dq domain, and the present harmonics at 50, 150, and 300 Hz. As the frequency resolution of the measurements does not produce the discrete spectral line at 50 Hz, the PFE occurs and the harmonics leak to the nearest discrete spectrum frequencies, given in Table I.

TABLE I: Nearest discrete spectrum frequency points to the grid harmonics.

f (Hz)	50	100	150	300
Below	48.85	97.70	149.00	298.00
Above	51.29	100.15	151.44	300.44

Fig. 4 shows the measured grid impedance with two different number of averaged periods. The blue line represents one of the proposed measurement designs ($P = 100$), where the measured data includes an integer amount of the fundamental grid cycles ($R = 2047$, $r = 0$, $\Delta T = 0$). Therefore, the grid-impedance measurement does not show any spectral leakage, only the PFE distort the measurement near the grid harmonics, which can be predicted. Red line ($P=108$) represents design without considering the spectral leakage minimization as the fractional part of grid fundamental cycle occurs in the measured data ($R = 2210$, $r = 0.76$, $\Delta T = 4.8$ ms). Fig. 5 illustrates the time difference between the measurement time for different number of averaged periods and the nearest full period of fundamental grid voltage. When $P = 100$ (left), the time difference equals to zero and no spectral leakage occurs.

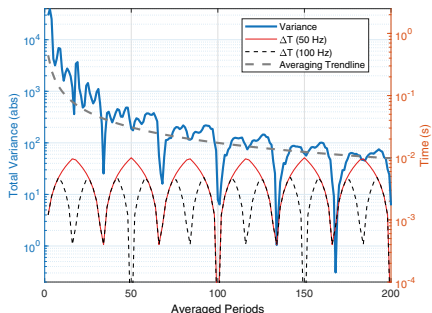


Fig. 6: Variance over different averaging periods.

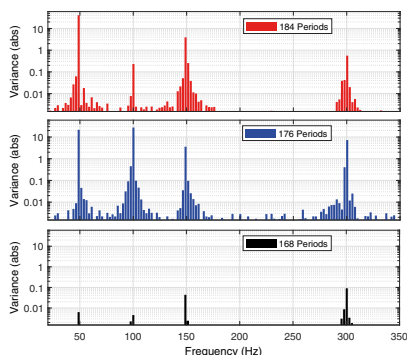


Fig. 7: Variance over frequency spectrum for different numbers of averaged periods.

The time difference with $P = 108$ (right) produces spectral leakage which deteriorates the measurements, as shown in Fig. 4.

Fig. 6 shows the variance, averaging trend line, and the time difference to the grid fundamental cycle $\Delta T(50 \text{ Hz})$ and its second harmonic $\Delta T(100 \text{ Hz})$ with varying number of averaged periods. The local minimums of $\Delta T(50 \text{ Hz})$ give the proposed parametrization to minimize the spectral leakage. The variance follows the averaging trend line otherwise, but the variance is significantly decreased at the local minimums of $\Delta T(50 \text{ Hz})$.

To illustrate the appearance of the spectral leakage, Fig. 7 shows the measurement variance as a function of frequency with three different P , given as

- $P = 184$ (red bars), chosen from local minimum of $\Delta T(100 \text{ Hz})$, which mitigates the spectral leakage of even-order grid harmonics (here 100 and 300 Hz).
- $P = 176$ (blue bars) representing design not considering the spectral leakage.
- $P = 168$ (black bars), chosen from local minimum of both $\Delta T(50 \text{ Hz})$ and $\Delta T(100 \text{ Hz})$, which mitigates the spectral leakage from all grid-harmonic frequencies.

V. CONCLUSIONS

Wideband identification methods have become popular in the analysis of grid-connected systems. However, recent studies have not considered the undesired spectral leakage that

deteriorates the measurements under unbalanced grid conditions or under high harmonic content in the grid voltages. The unbalance and harmonics occur as periodic oscillations in the measured data and leak over a wide frequency band during the signal post-processing. This paper has presented methods to mitigate the spectral leakage by adjusting the measurement parameters such that an integer amount of grid-fundamental cycles is included in the measured data. Consequently, the spectral leakage caused by signal processing is avoided, and the frequency responses are obtained with significantly more accuracy. The proposed method is well applicable both in dq- and sequence-domain measurements. Experimental measurements based on a high-power PHIL system were shown to demonstrate the effectiveness of the proposed method.

ACKNOWLEDGMENT

This research and testing has been performed using the ERIGrid Research Infrastructure and is part of a project that has received funding from the European Union's Horizon 2020 Research and Innovation Programme under Grant Agreement No. 654113. The support of the European Research Infrastructure ERIGrid and its partner DNVGL is much appreciated. The work was also supported by the Academy of Finland.

REFERENCES

- [1] A. Rygg and M. Molinas, "Apparent impedance analysis: A small-signal method for stability analysis of power electronic-based systems," *IEEE Journal of Emerging and Selected Topics in Power Electronics*, vol. 5, no. 4, pp. 1474–1486, Dec 2017.
- [2] T. Messo, R. Luhtala, A. Aapro, and T. Roinila, "Accurate impedance model of grid-connected inverter for small-signal stability assessment in high-impedance grids," in *IEEJ Journal of Industry Applications*, vol. 8, 2019, pp. 488–492.
- [3] L. Jessen and F. W. Fuchs, "Modeling of inverter output impedance for stability analysis in combination with measured grid impedances," in *2015 IEEE 6th International Symposium on Power Electronics for Distributed Generation Systems (PEDG)*, 2015.
- [4] M. Cespedes and J. Sun, "Online grid impedance identification for adaptive control of grid-connected inverters," in *2012 IEEE Energy Conversion Congress and Exposition (ECCE)*, 2012, pp. 914–921.
- [5] J. Schoukens, K. Godfrey, and M. Schoukens, "Nonparametric data-driven modeling of linear systems: Estimating the frequency response and impulse response function," *IEEE Control Systems Magazine*, vol. 38, no. 4, pp. 49–88, Aug 2018.
- [6] T. Roinila, T. Messo, and E. Santi, "Mimo-identification techniques for rapid impedance-based stability assessment of three-phase systems in dq domain," *IEEE Transactions on Power Electronics*, vol. 33, no. 5, pp. 4015–4022, 2018.
- [7] R. Luhtala, T. Roinila, and T. Messo, "Implementation of real-time impedance-based stability assessment of grid-connected systems using mimo-identification techniques," *IEEE Transactions on Industry Applications*, 2018.
- [8] T. Roinila, T. Messo, R. Luhtala, R. Scharrenberg, E. de Jong, A. Fabian, and Y. Sun, "Hardware-in-the-loop methods for real-time frequency-response measurements of on-board power distribution systems," *IEEE Transactions on Industrial Electronics*, 2018.
- [9] C. Li, "Unstable operation of photovoltaic inverter from field experiences," *IEEE Transactions on Power Delivery*, vol. 33, no. 2, 2018.
- [10] K. R. Godfrey, *Perturbation Signals for System Identification*. Prentice Hall, UK, 1993.
- [11] G. W. Chang, C. I. Chen, Y. J. Liu, and M. C. Wu, "Measuring power system harmonics and interharmonics by an improved fast fourier transform-based algorithm," *IET Generation, Transmission Distribution*, vol. 2, no. 2, pp. 193–201, March 2008.
- [12] H. Wen, Z. Teng, Y. Wang, B. Zeng, and X. Hu, "Simple interpolated fit algorithm based on minimize sidelobe windows for power-harmonic analysis," *IEEE Transactions on Power Electronics*, vol. 26, no. 9, pp. 2570–2579, Sep. 2011.

